



UNIVERSITÉ DE
SHERBROOKE

FACULTÉ DE GÉNIE
DÉPARTEMENT DE GÉNIE MÉCANIQUE

**GEOMETRIC CHARACTERIZATION AND SIMULATION OF CELL-MEDIATED
RESORPTION FOR POROUS BONE SUBSTITUTES USING MICRO COMPUTED
TOMOGRAPHY AND ADVANCED FUZZY METHOD**

**CARACTÉRISATION GÉOMÉTRIQUE PAR LA LOGIQUE FLOUE ET
SIMULATION DE LA RÉSORPTION CELLULAIREMENT ASSISTÉE DE
SUBSTITUTS POREUX POUR TISSUS OSSEUX PAR MICROTOMOGRAPHIE À
RAYONS X**

By

Mahdieh Bashoor Zadeh

A Dissertation Submitted in Partial Fulfillment of the requirement for the degree of Doctor of
Philosophy
Spécialité: GÉNIE MÉCANIQUE

Jury committee:

1- Gamal Baroud (directeur)

4- Saïd Elkoun

2- Stephan Becker

5- Hassan Serhan

3- Marc Bohner

Sherbrooke (Québec), Canada

January, 2011

IV-2105



Library and Archives
Canada

Published Heritage
Branch

395 Wellington Street
Ottawa ON K1A 0N4
Canada

Bibliothèque et
Archives Canada

Direction du
Patrimoine de l'édition

395, rue Wellington
Ottawa ON K1A 0N4
Canada

Your file *Votre référence*
ISBN: 978-0-494-75057-5
Our file *Notre référence*
ISBN: 978-0-494-75057-5

NOTICE:

The author has granted a non-exclusive license allowing Library and Archives Canada to reproduce, publish, archive, preserve, conserve, communicate to the public by telecommunication or on the Internet, loan, distribute and sell theses worldwide, for commercial or non-commercial purposes, in microform, paper, electronic and/or any other formats.

The author retains copyright ownership and moral rights in this thesis. Neither the thesis nor substantial extracts from it may be printed or otherwise reproduced without the author's permission.

In compliance with the Canadian Privacy Act some supporting forms may have been removed from this thesis.

While these forms may be included in the document page count, their removal does not represent any loss of content from the thesis.

AVIS:

L'auteur a accordé une licence non exclusive permettant à la Bibliothèque et Archives Canada de reproduire, publier, archiver, sauvegarder, conserver, transmettre au public par télécommunication ou par l'Internet, prêter, distribuer et vendre des thèses partout dans le monde, à des fins commerciales ou autres, sur support microforme, papier, électronique et/ou autres formats.

L'auteur conserve la propriété du droit d'auteur et des droits moraux qui protègent cette thèse. Ni la thèse ni des extraits substantiels de celle-ci ne doivent être imprimés ou autrement reproduits sans son autorisation.

Conformément à la loi canadienne sur la protection de la vie privée, quelques formulaires secondaires ont été enlevés de cette thèse.

Bien que ces formulaires aient inclus dans la pagination, il n'y aura aucun contenu manquant.


Canada

*This thesis is dedicated to my beautiful daughter, Kiana, and my husband, Ali,
for their love, support and patience,*

And

to my parents for their unconditional love and encouragement.

PUBLICATION DISSERTATION OPTION

This dissertation consists of the following three manuscripts that have been accepted or prepared for submission as follows: The third chapter presented the first manuscript that it has been published in *Acta Biomaterialia* 6 (2009), p. 864-875. The fourth and the fifth chapters demonstrated two manuscripts that are prepared for submission in one of the field journals. The first one is entitled “Geometric analysis of porous bone substitutes using micro-computed tomography and fuzzy distance transform” and the second one is entitled “Effect of subvoxel process on non-destructive characterization of bone substitutes”.

Summary

Repairing of large bone defects with the use of scaffolds has received significant attention from both the medical and scientific communities because of its potential to accelerate the bone healing process. From the literature, it is known that the scaffold architecture is a key factor in the biological response of the bone to the substitute. The architectural properties include, among others, the pore and interconnection sizes.

Pores provide the space for cells to reside and form new bone tissue while pore interconnections are crucial for cell migration, vascularization and transport of waste products and nutrients. It is therefore important to provide accurate characterization of the porous structure of the scaffold to better understand its biological response. With this understanding, a better design of bone substitute becomes possible.

Generally, an efficient characterization method should be accurate and non-destructive and provides comprehensive information of scaffold architecture. Micro-computed tomography as a non-destructive technique provides access to 3D structure of scaffold, but there are limitations such as how to extract the relevant information from large amount of data. Various methods have been established to quantify the architectural properties from micro-computed tomography data. The main goal of these methods is to enhance the precision of geometric characterization.

The broader objective of this thesis is to provide an improved characterization of the porous scaffolds. A more focused objective is to provide a computational model simulating the cell mediated resorption process of resorbable bone substitutes. Therefore, this study combined both novel image treatments and algorithms to meet these objectives.

The thesis is structured in three scientific manuscripts. The first manuscript used fuzzy-based image treatment methods to analyse images generated by micro-computed tomography. From the literature, it is known that the fuzzy-based method helps to improve the accuracy of the characterization, in particular for scaffolds featuring a relatively small pore size. In addition, a new algorithm was introduced to determine both pore and interconnection sizes. The

surface area of bone substitutes was quantified by using marching cube algorithm. Besides, the so-called Lattice Boltzmann method was used to characterize the permeability of the investigated scaffolds. Scaffolds made of β -tricalcium phosphate (β -Ca₃(PO₄)₂) and presenting a constant porosity and four variable pore sizes were examined. The average pore size (diameter) of the four bone substitute groups (denominated with a letter from group A to D) was measured to be 170.3 ± 1.7 , 217.3 ± 5.2 , 415.8 ± 18.8 and 972.3 ± 10.9 μm . Despite this significant change in pore size, the pore interconnection size only increased slightly, in the range of 61.7 to 85.2 μm . The average porosity of the four groups was 52.3 ± 1.5 %. The surface density of scaffolds decreased from 11.5 to 3.3 mm^{-1} , when the pore size increased. The results revealed that the permeability of scaffolds is in the same order of magnitude and increased from $1.1 \cdot 10^{-10}$ to $4.1 \cdot 10^{-10}$ m^2 with increasing the pore size.

The second manuscript was devoted to the use of subvoxelization algorithm and high-resolution scanner, in an attempt to further improve the accuracy of the results, in particular, of the small pore scaffolds. As expected, an increase of the image resolution from 15 to 7.5 μm significantly eased the segmentation process and hence improved scaffold characterization. Subvoxelization also improved the results specifically in terms of interconnection sizes. Specifically, much smaller interconnection sizes were yielded after applying the subvoxelization process. For example, the mean interconnection size of small pore size groups, group A and B, dropped from 63 to 20 and 30 μm , respectively. Furthermore, due to more details obtained from subvoxelization and high-resolution scanning, additional effects so called “boundary effects” were observed. The boundary effects can yield misleading results in terms of interconnection sizes. The means to reduce these effects were proposed.

The third manuscript focused on the simulation and understanding of cell mediated resorption of bone graft substitutes. A computer model was developed to simulate the resorption process of four bone substitute groups. μCT data and new “image processing” tools such as labelling and skeletonization were combined in an algorithm to perform the steps of resorption simulation algorithm. The proposed algorithm was verified by comparing simulation results with the analytical results of a simple geometry and biological in vivo data of bone substitutes. A correlation coefficient between the simulation results and both

analytical and experimental data, was found to be larger than 0.9. Local resorption process revealed faster resorption in external region specifically at earlier resorption time. This finding is in agreement with the in vivo results. Two definitions were introduced to estimate the resorption rate; volume resorption rate and linear resorption rate. The volume resorption rate was proportional to accessible surface and decreased when the pore size increased, while the linear resorption rate was proportional to thickness of material and increased with increasing the pore size. In addition, the simulation results revealed no effect of resorption direction on resorption behaviour of substitutes. However, the resorption rate of small pore size samples was decreased with increasing the minimum interconnection size required for cell ingrowth, to 100 μm .

This thesis combined novel “image processing” tools and subvoxelization method to improve the characterization of porous bone substitutes used in the bone repair process. The improved characterization allowed a more accurate simulation process. The simulation data were consistent with previously obtained biological data of the same group and allows understanding the local resorption process. The available tools and results are expected to help with the design of optimal substitute for bone repair.

Keywords: Bone substitutes, scaffold, μ -computed tomography, image analysis, subvoxelization, image resolution, resorption simulation, resorption rate

Résumé

L'utilisation de greffons osseux synthétiques pour réparer les défauts osseux prononcés est un procédé qui a reçu de plus en plus l'attention de la part de la communauté scientifique, étant donné qu'il présente un potentiel d'accélération du processus de guérison des os. Il est mentionné dans la littérature que l'architecture du greffon osseux synthétique est un facteur clé dans l'acceptation de l'os biologique à son substitut. Ces propriétés architecturales incluent, entre autres, la taille des pores et des interconnexions.

Les pores constituent un espace dans lequel les cellules peuvent se régénérer pour former de nouveaux tissus osseux, alors que les interconnexions sont cruciales pour la migration des cellules, la vascularisation et le transport des déchets produits et des nutriments. Dans le but de mieux comprendre la réponse biologique de l'os à son substitut, la caractérisation de la microstructure poreuse est donc indispensable.

Généralement, une méthode de caractérisation idéale se doit d'être précise, non-destructive et de fournir une information complète sur l'architecture du greffon osseux synthétique. La tomographie assistée par ordinateur est non-destructive et conduit à une caractérisation tridimensionnelle du greffon osseux. Toutefois, cette technique a quelques limitations dont l'extraction de l'information utile depuis une grande quantité de données. Diverses méthodes ont été mises au point afin de quantifier les propriétés architecturales à partir des données issues de la tomographie assistée par ordinateur.

L'objectif général de cette thèse est de fournir une méthode améliorée de caractérisation du greffon osseux poreux. Un des objectifs spécifiques consiste à proposer un modèle de caractérisation de la structure poreuse capable de simuler la résorption des cellules par les substituts osseux. Afin d'atteindre cet objectif, un modèle combinant à la fois des traitements d'images et des algorithmes novateurs est proposé.

La thèse est structurée autour de trois articles scientifiques. Le premier manuscrit a utilisé une méthode de traitement d'images dite « fuzzy-based » pour l'analyse d'images générées par tomographie assistée par ordinateur. Dans la littérature, il est dit que la cette méthode

améliore la précision de la caractérisation, particulièrement pour une greffe osseuse présentant des pores relativement petits. La surface de substitut osseux a été quantifiée en utilisant l'algorithme « marching cubes ». De plus, la méthode dite « Lattice Boltzmann » a été utilisée pour caractériser la perméabilité de la structure poreuse de la greffe. Dans cet article, des résultats de caractérisation de différents substituts osseux en phosphate de β -tricalcium (β -Ca₃(PO₄)₂) d'une même porosité mais de quatre tailles de pores différentes ont été présentés. La taille moyenne (diamètre) des pores pour chacun des quatre groupes de substituts testés (identifiés de A à D) était de 170,3±1,7, 217,3±5,2, 415,8±18,8 et 972,3±10,9 μ m. Malgré cette variation importante de la taille des pores, celle des interconnexions entre les pores n'a que légèrement augmenté, passant de 61,7 à 85,2 μ m. La porosité moyenne des quatre groupes se trouvait à 51,3±1,5%. Lorsque la taille des pores augmente, la densité surfacique est réduite passant de 11,5 à 3,3 mm⁻¹. Les résultats ont montré que la perméabilité des structures poreuses étaient du même ordre de grandeur : de 1,1·10⁻¹⁰ à 4,1·10⁻¹⁰ m² avec l'augmentation de taille des pores.

Dans le but d'améliorer la précision des mesures pour des greffes qui présentent des pores de taille relativement petite, le second manuscrit a été dédié à l'utilisation d'un algorithme dit de sous-voxelisation et d'un analyseur haute résolution. Tel qu'attendu, l'amélioration de la résolution de 15 à 7,5 μ m a facilité le processus de segmentation des images et a ainsi amélioré la caractérisation des greffons. La sous-voxelisation a notamment amélioré les résultats au niveau de la taille des interconnexions. Plus spécifiquement, des tailles d'interconnexions beaucoup plus petites ont été obtenues suite à l'application de la sous-voxelisation. Par exemple, la taille moyenne des interconnexions mesurée pour les groupes A et B s'est trouvée réduite de 60 à 20 et 30 μ m respectivement. De plus, l'augmentation de la résolution obtenue par l'utilisation de l'analyseur haute résolution et de la sous-voxelisation a révélé l'existence « d'effets de bord ». Ces effets de bords peuvent mener à des mesures de taille d'interconnexion erronées. Des moyens de réduire ces effets ont été proposés.

Le troisième manuscrit est consacré à la simulation et la compréhension du processus de résorption assistée par les cellules pour des substituts de greffe osseuse. Un modèle a été développé pour simuler le processus de résorption de quatre groupes de substituts osseux. Les données μ CT ainsi que des nouveaux outils de traitement d'images tels que

l'identification des pores et la squelettisation ont été combinés dans un premier algorithme qui effectue les incréments destinés à un deuxième algorithme de simulation de la résorption. L'algorithme proposé a été vérifié en comparant les résultats simulés aux résultats analytiques d'une géométrie simple et aux résultats biologiques *in vivo* de substituts osseux. Un coefficient de corrélation supérieur à 0,9 a été obtenu entre les résultats simulés, analytiques et expérimentaux. Le processus de résorption locale s'est révélé plus rapide dans la région externe, particulièrement au début du processus. Cette découverte est en accord avec les résultats *in vivo*. Pour estimer la résorption, le taux de résorption volumique et le taux de résorption linéaire ont été introduits. Le taux de résorption volumique est proportionnel à la surface accessible et inversement proportionnelle à la taille des pores. Quant au taux de résorption linéaire, il est à la fois proportionnel à l'épaisseur du matériau et à la taille des pores. D'un autre côté, la simulation révèle que la direction de résorption n'a aucun effet sur le comportement des substituts. Cependant, le taux de résorption pour les échantillons à petits pores a diminué avec l'augmentation de la taille minimale d'interconnexion requise pour la croissance des cellules.

Cette thèse propose de combiner un nouvel outil de traitement d'images à la méthode de sous-voxelisation dans le but d'améliorer la caractérisation des substituts poreux utilisés pour la réparation des défauts osseux. Cette caractérisation précise a donné lieu à des simulations plus réalistes qui se révèlent cohérentes avec des données biologiques préalablement prises pour un même groupe de substitut. Les outils de caractérisation et de simulation mis en œuvre dans ces travaux apportent, d'une part, une modélisation réaliste du phénomène de résorption et, d'autre part, ouvrent des perspectives dans la conception et l'optimisation des substituts pour la réparation osseuse.

Mots clés : Substitut osseux, greffon osseux synthétique, micro tomographie (μ CT) par rayons X, Traitement d'images, subvoxelization, résolution d'une image, taux de résorption osseuse, simulation de la résorption osseuse.

Acknowledgment

These four years of research have been a truly enjoyable experience in my life. I would like to take this opportunity to thank all the people who have made this possible for me.

First of all, I would like to express my deepest appreciation to my PhD supervisor, Professor Gamal Baroud, for his guidance and support during these years. It has been a great chance and pleasure to work with him and learn from him. I am heartily grateful to him for his valuable advice, enlightening discussions and positive and encouraging words. I also would like to express my appreciation to him for making it possible for me to attend international conferences inside and outside of Canada.

Furthermore, this research project and direction wouldn't have been possible without the generous support from the Canada Research Chairs Program (CRC), the National Sciences and Engineering Research Council of Canada (NSERC), the Canadian Institute of Health Research (CIHR) and the Robert Mathys Stiftung (RMS).

I would like to sincerely thank Professor Marc Bohner for his critical yet very fruitful advices, discussions and for his attentive curiosity. It has been a great opportunity for me to work with him. I am really grateful to him and his colleagues in 'Robert Mathys foundation' (RMS) in Switzerland for preparing the calcium phosphate porous scaffolds used in this study.

I also wish to express my appreciation to Dr. Steve Allen from 'Centre de calcul scientifique de l'Université de Sherbrooke' (CCS) for his generous help and the great work he has done in parallelization and modification of my code to accelerate the implementation strategies. I further appreciate a lot Dr. Thomas Zeiser for providing the 'Lattice Boltzmann code' and for his excellent support during the computational analysis. Also I am thankful to Dr. Akbar Darabi for highlighting the use of fuzzy logic in medical imaging and the many useful discussions. I would like to thank Mrs. Irène Kelsey from 'Institut des matériaux et systèmes intelligents' (IMSI) center at Université de Sherbrooke for her patience to teach me how to use μ -computed tomography and to scan

the samples. Many thanks to my colleagues and friends at Université de Sherbrooke, their kindness supported and streamlined my studies.

Last, but not least, I am grateful to my husband Ali and my daughter Kiana for their great support and patience throughout these years. And finally I thank my parents who taught me valuable lessons about humanity, life and world and for their unconditional support and continuous encouragement during the whole period of my studies.

Table of contents

Summary	ii
Acknowledgement	viii
Table of contents.....	x
Abbreviation and symbol list.....	xiv
Tables list	xviii
Figures list.....	xix
CHAPTER 1 Introduction	1
1.1 Context of the doctorate.....	1
1.2 Questions of research	4
1.3 Hypothesis.....	5
1.4 Objectives	6
1.5 Block diagram of the doctorate work.....	6
CHAPTER 2 Literature survey.....	8
2.1 Bone defects and repair procedure.....	8
2.2 Bone substitute and its role in bone healing	9
2.2.1 Ideal scaffold for bone substitute	9
2.3 Bone substitute material.....	11
2.3.1 Autografts	11
2.3.2 Allografts	11
2.3.3 Xenografts.....	12
2.3.4 Synthetic bone graft substitutes	12
2.3.4.1 Metal	13
2.3.4.2 Polymer	13
2.3.4.3 Ceramics	14

2.3.4.4	Composites.....	15
2.4	Bone substitute and structural parameters	16
2.4.1	Definition of porous structure.....	16
2.4.2	Geometrical characteristics of porous structure.....	16
2.5	Bone substitute paradigms	18
2.5.1	Biological paradigms	18
2.5.2	Structural paradigms	19
2.5.3	Physical and mechanical paradigms	22
2.6	Characterization of structural parameters	24
2.6.1	Traditional methods to measure Porosity and Pore size	25
2.6.2	Recent methods to measure Porosity and Pore size.....	27
2.6.2.1	Micro Computed tomography (μ CT).....	27
2.6.2.2	Thresholding	29
2.6.2.3	Distance transform (DT).....	31
2.6.2.4	Fuzzy distance transform (FDT).....	32
2.6.2.5	Skeletonization.....	34
2.6.2.6	3-D Geometric analysis of μ CT images: The Hildebrand Method.....	38
2.6.3	Methods to measure specific surface	42
2.7	Fluid flow analysis and lattice Boltzmann method.....	43
2.7.1	Methods to measure permeability	43
2.7.2	Lattice Boltzmann Method	45
 CHAPTER 3 Geometric analysis of porous bone substitutes using micro-computed tomography and fuzzy distance transform.....		 49
3.1	Abstract.....	50
3.2	Introduction.....	50
3.3	Material and Method.....	54
3.3.1	Scaffold production and preparation.....	54
3.3.2	Micro-computed tomography	54
3.3.3	Geometric analysis.....	55

3.3.4	Fuzzy Distance Transform computation	55
3.3.5	Analysis of pore size and interconnection size	57
3.3.6	Skeletonization and Reconstruction.....	58
3.3.7	Computing specific surface by marching cube algorithm	59
3.4	Results.....	59
3.5	Discussion	69
3.6	Reference	76
CHAPTER 4	Effect of subvoxel process on non-destructive characterization of bone substitutes.....	81
4.1	Abstract	82
4.2	Introduction.....	83
4.3	Material and Method.....	86
4.3.1	Scaffold fabrication and preparation.....	86
4.3.2	Image acquisition	86
4.3.3	Subvoxelization process.....	87
4.3.4	Thresholding	87
4.3.5	Geometric analysis and verification.....	88
4.4	Results.....	91
4.5	Discussion	106
4.6	Conclusion	109
4.7	Reference	110
CHAPTER 5	Simulation of cell-mediated resorption of porous bone substitutes	114
5.1	Abstract.....	115
5.2	Introduction.....	115
5.3	Material and Method.....	117
5.3.1	Scaffold fabrication and Image acquisition	117
5.3.2	Application of the model on the in vivo data.....	119
5.3.3	Geometric analysis.....	120
5.3.4	Skeletonization and Reconstruction.....	121

5.3.5	Creating models with FCC lattice of pores.....	121
5.3.6	Resorption simulation analysis	122
5.3.7	Prony Method and Resorption Rate	125
5.3.8	Study design.....	126
5.3.9	Effect of voxel size on resorption simulation	126
5.3.10	Computational platform	127
5.3.11	Provided in vivo data	127
5.4	Results.....	128
5.5	Discussion	136
5.6	Conclusion	141
5.7	Reference	142
CHAPTER 6 General discussion and conclusion		147
6.1	Image processing and geometric analysis.....	147
6.2	Fluid flow analysis.....	149
6.3	Effect of voxel size on geometric parameters.....	150
6.4	Cell-mediated resorption process.....	152
6.5	Methodology-synthesis diagram.....	154
6.6	Contributions.....	155
6.7	Current limitation.....	155
6.8	Future work.....	157
6.9	Discussion et conclusion (Français).....	159
Reference		172
Annexe A Additional scientific contributions		187
A.1	Journal publications	187
A.2	Conference/Proceeding publications	187

Abbreviation and symbol list

A	Cross sectional area of the samples
AGV	Average gray level value
A_i	Rate coefficients of Prony's series
c	Lattice speed
C	Kozeny constant
CFD	Computational fluid dynamic
c_s	Speed of sound
CVF	Ceramic volume fraction
Df_q	Previously determined fuzzy distance of an adjacent voxel q to p
D_{map}	Distance map
$d_{material}$	Density of scaffold material
D_{min}	Minimum interconnection size required for vascularization
$D(q)$	Previously determined distance of an adjacent voxel q to p
$d_{scaffold}$	Apparent density of porous scaffold
DT	Distance transform
$DT(p)$	Distance transform value at p
$f^{(0)}$	Equilibrium distribution function
FCC	Face-centered cubic
FDT	Fuzzy distance transform
$FDT(p)$	Fuzzy distance transform of voxel p
$f_i(\mathbf{x}, t)$	Distribution function of the i -th velocity \mathbf{e}_i
$f_i^{(eq)}$	Equilibrium distribution function of the i -th discrete velocity \mathbf{e}_i
$f(p)$	Intensity of voxel p
$f(t)$	Percentage of ceramic volume fraction at time t
$f(\mathbf{x}, \xi, t)$	Single particle distribution function
HA	Hydroxiapatite
I	Input images

I'	Modifies images
K_i	Constant coefficients of Prony's series
L	Length of the sample
LB	Lattice Boltzmann
L_p	Fuzzy distance from object voxel, p , to the background
MR	Magnetic resonance
MVF	Material volume fraction
N	Space dimension
$N-b$	Number-based
$NeighP$	Adjacent voxel of P
P, p	Pressure
p_{close}	Close porosity
p_{open}	Open porosity
p_{total}	Total porosity
$PSvb$	Volume-base average pore size
Q	Set of object voxels
q	Volumetric flow rate
Q_{in}	Accessible ports
R	Radius of pores
R^2	Correlation coefficient
$ROI1$	External zone of cylindrical sample
$ROI2$	Middle zone of cylindrical sample
$ROI3$	Internal zone of cylindrical sample
S	Skeleton point, Fuzzy set, Pore surface area
SD	Standard deviation
SE	Skeleton voxels with FDT value less than $(D_{min} / 2)$
SEM	Scanning electron microscopy
$skelet(\Omega)$	Skeleton of structure Ω
SP	Set of n points in the plan
$sph(x,r)$	Set of points in a sphere with center x and radius r
S_s	Nearest skeleton points to Q_{in}

t	Time
TCP	Tricalcium phosphate
THC	Cavity threshold value
THM	Material threshold value
\mathbf{u}	Flow velocity
V-b	Volume based
$V_{intrusion}$	Total intrusion volume
$V_{scaffold}$	Scaffold volume
VOI	Volume of interest
w_i	Weighting factor for different directions
X	Set of image voxels
\mathbf{x}	Space position (coordinate vector of a point in the space)
X(p)	Set of center points of all spheres with a radius equal to their corresponding DT value and including the point p
α -TCP	α -Tricalcium phosphate
β -TCP	β -Tricalcium phosphate
Δp	Pressure drop across the specimen
$\delta(p_i, p_{i+1})$	Integer weight related to membership values and Euclidean distance between p_i and p_{i+1}
ε	Porosity
θ	Contact angle
κ	Permeability
λ	Relaxation time
λ_i	Eigenvalues of FDT Hessian matrix
μ	Dynamic viscosity
$\mu(\mathbf{x})$	Membership value of object's voxel \mathbf{x}
μCT	Micro computed tomography
$\mu(p)$	Membership value of voxel p
ν	Kinematic viscosity
ζ	Particle velocity
ρ	Fluid density

σ	Surface tension
τ	Tortuosity, Dimensionless relaxation time
$\tau(p)$	Local thickness at point p
v_i	Eigenvectors of FDT Hessian matrix
Ω	An arbitrary structure in space
Ω_R	Distance ridge points
$\omega(p)$	Volume of sphere at voxel p
$\ p-q\ $	Euclidean distance between p and q
$ \text{skelet}(\Omega) $	Number of points in the skeleton
∇D_f	Gradient of FDT map
$\nabla^t \cdot \nabla D_f$	Hessian of FDT map

Tables list

Table 2-1 Common biomaterial used for bone repair [Di Silvio, 2007].....	16
Table 3-1 Geometrical properties of bone substitutes obtained from introduced image processing tools.....	68
Table 3-2 Geometric properties before and after subvoxelization process.....	71
Table 3-3 Summary of average, standard deviation and variation of permeability values of samples in each group.....	72
Table 4-1 Geometrical properties of bone substitutes presented as a function of resolution and method.....	96
Table 4-2 Comparing voxel size dependency of structural parameters obtained from scan and artificial datasets. Arrows (▲, ▼) indicate direction of change in parameters as voxel size decreased.....	97
Table 5-1 Geometrical parameters of bone substitutes obtained from μ CT data. The pore size calculated according to two definitions, number-base and volume-base. The surface density was calculated as the ratio of material surface to total volume, this parameter was computed by using CT-Analyzer software (CTAN).	130
Table 5-2 Volume and linear resorption rate at different remaining ceramic volume fractions (CVF), to investigate the pattern of resorption rate over time the resorption rate was calculated at different CVFs (30%, 20% and 10%). The calculation was done on 30 μ m resolution images.	133
Table 5-3 Volume and linear resorption rate at different remaining ceramic volume fractions (CVF). To investigate the pattern of resorption rate over time the resorption rate was calculated at different CVFs (30%, 20% and 10%). The calculation was done on 15 μ m resolution images.	136
Table 6-1 The porosity calculated based on fuzzified images and reconstructed images. ...	149

Figures list

Figure 1-1 (a) 2-D fuzzy image and (b) 2-D FDT map, local maxima as a representative of pore size are shown with white points and local saddles as a representative of interconnection size are shown with black point. The diameter of corresponding circles is equal to the pore and interconnection sizes.....	6
Figure 2-1 2-D image as representative of pores and interconnections.....	17
Figure 2-2 Schematic representation of Liquid displacement method.	26
Figure 2-3 Representative SEM images of scaffolds with different pore sizes, the white bar corresponds to 0.5 mm [Bohner et al., 2005].....	27
Figure 2-4 (a) Sketch of μ -Computer Tomography.....	28
Figure 2-5 The steps to generate 2-D cross section images from radiographic images.	29
Figure 2-6 2-D representative of (a) original μ CT image, (b) binary image and (c) DT map.32	
Figure 2-7 Thinning skeleton, the darkest pixels represent the skeleton of object.....	35
Figure 2-8 Voronoi skeleton, (a) Some border points of a rectangle form the set of generating points, (b)The Voronoi diagrams are displayed as dashed lines and the skeleton (black lines) is estimated based on the Voronoi diagrams.....	36
Figure 2-9 2-D representative of distance transform skeleton (dotted line), as the locus of maximal disks (2-D) or spheres (3-D) which are set into the object.	36
Figure 2-10 (a) The original binary image and (b) The DT map of binary image, the bright points are local maxima in DT map and considered as skeleton of object.	37
Figure 2-11 Local thickness $\tau(p)$ of a structure Ω determines by fitting maximal spheres to the structure [Hildebrand and Rüegsegger, 1997].	39
Figure 2-12 Typically μ CT reconstructed structure [Bohner et al., 2005]	41
Figure 2-13 (a) 2D FDT map, local maxima as a representative of pore size are shown with dark points.(b) Corresponding circles at local maxima with radius equal to their FDT. 41	
Figure 2-14 15 unique cube configurations	43
Figure 2-15 Discrete velocity set for the D3Q19 model.....	46
Figure 3-1 Sigmoidal fuzzy membership function	56

Figure 3-2 Four 3-D reconstructed structure of bone substitutes produced by different emulsifier concentrations. These structures were extracted from the middle of the samples..... 60

Figure 3-3 2-D fuzzified images selected from first specimen of each group, the threshold values, Th_C and Th_M , are (a) sample A, $Th_C=35$ and $Th_M=50$, (b) sample B, $Th_C=30$ and $Th_M=55$, (c) sample C, $Th_C=30$ and $Th_M=55$ and (d) sample D, $Th_C=30$ and $Th_M=50$.. 61

Figure 3-4 FDT maps of (a) Sample A, (b) Sample B, (c) Sample C and (d) Sample D. The FDT values are in voxel unit..... 62

Figure 3-5 Number-based pore size distribution of bone substitute structures (before applying exclusion conditions) derived from max-min operation and FDT values, (a) Group A; (b) Group B; (c) Group C; (d) Group D..... 64

Figure 3-6 Number-based pore size distribution of bone substitute structures after applying exclusion criteria, (a) Group A; (b) Group B; (c) Group C; (d) Group D. 65

Figure 3-7 Volume-based pore size distribution of bone substitute structures, (a) Group A; (b) Group B; (c) Group C; (d) Group D..... 66

Figure 3-8 Interconnection size distribution of bone substitute structures derived from max-min operation and FDT values, (a) Group A; (b) Group B; (c) Group C; (d) Group D. 67

Figure 3-9 Velocity map of bone substitute (sample D-1) with stream lines show the flow direction through the bone substitute structure 73

Figure 3-10 (a) Bone substitute average pore and interconnection size versus four different bone substitute groups. (b) Bone substitute permeability and surface density versus four different bone substitute groups..... 75

Figure 4-1 (a) Fuzzified image of an individual void space. (b) 2-D fuzzy distance transform map; The pore size and interconnection size is defined as the diameter of circles in 2-D (or spheres in 3-D) centered at local maxima (white points) and saddle voxels (black points), respectively 90

Figure 4-2 (a) Representative illustration of 2-D fuzzified image (left) and fuzzy distance transform (FDT) map (right) of individual void space extracted from images of 30 μm resolution. The local maximums are shown as white points in FDT map. (b) Corresponding illustration of 2-D fuzzified image (left) and FDT map (right) after applying subvoxel process. The surface irregularities are appeared by decreasing the

voxel size. These irregularities caused generating local saddle point as representative of virtual interconnections in FDT map (black point).....	91
Figure 4-3 2-D representative μ CT slices of samples A, B, C and D scanned at 30, 15 and 7.5 μ m resolutions.....	93
Figure 4-4 Intensity histograms of μ CT images of samples A, B, C and D at various resolutions (Continue on next page).	94
Figure 4-5 Number-based pore size distributions of (a) Sample A, (b) Sample B, (c) Sample C and (d) Sample D derived from max-min operation and FDT values at different scan and artificial resolutions.....	99
Figure 4-6 Interconnection size distributions of (a) Sample A, (b) Sample B, (c) Sample C and (d) Sample D derived from max-min operation and FDT values at different scan and artificial resolutions.	100
Figure 4-7 Average interconnection size versus intersected volume (a) Sample A, (b) Sample B, (c) Sample C and (d) Sample D. in each point, the virtual interconnection with intersected volume larger than X% (60-90%) were removed and average interconnection size was calculated.....	102
Figure 4-8 The impact of numerical effect on interconnection size distribution of (a) Sample D-15 μ m scan, (b) Sample D-15 μ m artificial and (c) Sample D-30 μ m scan. Removing the virtual interconnections considerably affect on distribution of interconnections larger than 300 μ m (Continue on next page). OV is overlapping volume.....	103
Figure 4-9 Percent errors relative to high resolution datasets versus four different bone substitute samples. Voxel size/pore size ratio calculated based on voxel size of 30 μ m and corresponding computed pore size. E1 (30-15): represent the percent error between the pore size analysis at 30 μ m and 15 μ m. E2 (15-7.5): represent the percent error between the pore size analysis at 15 μ m and 7.5 μ m. E3 (30-7.5): represent the percent error between the pore size analysis at 30 μ m and 7.5 μ m.....	105
Figure 5-1 Representative SEM photos of the macropore structure of four groups of β -TCP scaffolds with different macropore sizes. (a) group A, (b) group B, (c) group C and (d) group D. The scale bar corresponds to 0.5 mm [23].....	118

- Figure 5-2 Representative SEM photos of the micropore structure of four groups of β -TCP scaffolds with different macropores sizes. (a) group A, (b) group B, (c) group C and (d) group D. The scale bar corresponds to 50 μm [23]. 119
- Figure 5-3 (a) Porous blocks with isolated spherical pores that are ordered in FCC lattice. (b) Schematic representation of blocks resorption. Resorption occurred from both sides of the blocks with perpendicular direction to block surface (arrows direction). The large circles, which were drawn by break lines, represent the pores that have been enlarged by resorption. r is the pore radius, d is the inter-pore distance and D_{min} is defined as the minimum interconnection size required for vascularization and migration of the cells into the porous structure..... 122
- Figure 5-4 2-D representative of resorption steps, (a) Pores are labeled, (b) The skeleton point are extracted, S_E are skeletons with FDT value less than $D_{\text{min}}/2$, (c) Pores and interconnections with diameter less than D_{min} are blocked by growing the circles (or spheres in 3D) centered at S_E with the radius equal to FDT value of that point, (d) Skeleton branches corresponding to open pores with appropriate FDT value (i.e. larger than $D_{\text{min}}/2$), are detected (f) Pores that can be accessed from the outside are defined, (g) One voxel layer is “resorbed” or “removed” from the accessible surface. (The red lines “ ”, in figures (b), (d) and (f), are the skeleton voxels of non-resorbed pores)..... 124
- Figure 5-5 The left axis presents the simulation data (\diamond) and the exponential series approximation (Prony-series) of the simulation results (\square). The right axis presents the resorption rate data (Δ) which was obtained from the first derivative of Prony-series with respect to time. 125
- Figure 5-6 Schematic representation of three zones in cylindrical scaffold, ROI1: outer zone, ROI2: middle zone and ROI3: inner zone. 127
- Figure 5-7 (\blacktriangle)Analytical and (\blacksquare) simulation results of FCC lattice of pores with various pore radius ranging from 100 to 500 μm . The porous blocks had a width of 5mm and inter-pore distance of 22 μm . A voxel size of 10 μm was set to create the blocks. 129
- Figure 5-8 Resorption simulation of the four groups of scaffolds have been presented based on different setting conditions, (a) group A, (b) group B, (c) group C and (d) group D. Depending on the minimum interconnection size required for blood vessel ingrowth and the resorption direction, the resorption process of each group was analyzed four times.

Dmin was either set to be 50 μm or 100 μm . the resorption direction was either set to be unidirectional or pluridirectional.	131
Figure 5-9 Simulation data of four scaffold groups were compared to experimental data. The experimental data were obtained from μCT analysis of samples implanted in bone defects of sheep for 6, 12 and 24 weeks, (a) group A, (b) group B, (c) group C and (d) group D.	132
Figure 5-10 Volume resorption rate (CVF') at three different zones (ROI1, ROI2 and ROI3). of scaffold groups, (a) group A, (b) group B, (c) group C and (d) group D. The CVF'_ROI represents the volume resorption rate as a function of time for various location of scaffold.	134
Figure 5-11 Resorption simulations of substitutes were processed based on two different voxel sizes (15 μm and 30 μm), (a) Sample A, (b) Sample C, (c) Sample D. The resorption simulation of small pore size samples, A and B, were affected by voxel size at earlier resorption time. The resorption simulation of samples C and D were not influenced by voxel size.....	135
Figure 6-1 (a) 2D FDT map, local maxima as a representative of pore size are shown with dark points. (b) 2D FDT map, local saddles as a representative of interconnection size are shown with dark points.	148
Figure 6-2 Gray level histograms of sample A (the small pore size sample) at (a) 30 μm resolution and (b) 7.5 μm resolution.....	150
Figure 6-3 Sensitivity of samples' porosity to threshold values, AGV is the average gray level value. The threshold domains were selected as $\pm 5\%$, $\pm 10\%$, $\pm 15\%$ and $\pm 20\%$ of AGV.....	151
Figure 6-4 Methodology-Synthesis diagram, combination of methods and algorithm used for accurate geometric, fluid flow and resorption simulation analysis of bone substitutes	154

CHAPTER 1

Introduction

1.1 Context of the doctorate

Bone as a living tissue is able to restore its functionality and health. However, in large bone defects, where a critical size of bone is missing or damaged, the bone repair mechanism fails to repair the defects. Large bone defects caused by pathological conditions (e.g. cancer) or rapid degradation because of age and disease (i.e. osteoporosis) or massive trauma as well as diseases of bone quality itself, such as osteoporosis, are still a major problem in orthopedics [Mastrogiacomo et al., 2005; Celil et al., 2007]. In these cases, patient comfort and bone functionality can be surgically restored by reconstructive surgery and bone augmentation. Bone grafting has been considered as a successful therapy for treatment of large bone defects [van Gaalen et al., 2008]. Bone grafting is a surgical procedure to replace missing bone with bone graft or substitutes [Hing, 2005a]. Due to complications of traditional allografts and autografts, such as pain, morbidity, disease transform and limited availability, there was a great demand for developing synthetic bone substitutes to overcome these complications [Hing, 2004a; Hing, 2005a; Goldberg, 1992; Parikh, 2002].

The bone substitute should not only replace the missing bone, but it should favour the new bone formation and provide an adequate framework for bone ingrowth and vascularization into the substitute [Hing, 2005a; van Gaalen et al., 2008]. Therefore, the geometric parameter and the materials used for fabrication of porous bone substitute should provide the biological and biomechanical properties to enhance the functionality of bone substitute.

Metallic porous bone substitutes show excellent mechanical properties. However, their application is limited due to their lack of degradation and limited tissue adhesion

[Karageorgiou and Kaplan, 2005]. In the other hand, the polymeric biomaterials are biocompatible and biodegradable. Natural polymers are highly biodegradable and used in composite biomaterials to improve their degradation rate. The synthetic polymers can be fabricated with controllable degradation rate. Nevertheless, the poor mechanical properties of polymeric biomaterials limit their application [Karageorgiou and Kaplan, 2005; Yang et al., 2001]. Ceramic biomaterials, such as calcium phosphate ceramics, show biocompatible and bioactive properties. Bioceramics are mechanically resistant under compression but weak and largely brittle under tension and shear loads [Moore et al., 2001; Khang et al., 2007]. Hydroxyapatite ceramics exhibits low resorption rate whereas other composition of calcium phosphate ceramics such as β -tricalcium phosphate ceramics are resorbed readily [Ruhe et al., 2007, Wagoner Johnson and Herschler, 2010]. It should be noticed that the rate of degradation can be affected by several factors such as crystallinity and crystal perfection [Karageorgiou and Kaplan, 2005; Yang et al., 2001]. Calcium phosphate ceramics have been considered as promising material for bone substitute due to their excellent biocompatible, bioactive, bioresorbable, osteoconductive and osteointegrative properties [Grynepas et al., 2002; Yuan et al., 1998; Ohura et al., 1996; Dong et al., 2002; Daculsi et al., 2003]. However, they are still in development to enhance their functionality.

Besides the material property, the structure of bone substitute plays an important role in cell attachment, penetration depth and vascularization. There is a common agreement that bone substitutes should have an interconnected porous matrix (so-called 'scaffold') to allow new bone ingrowth and vessel formation [Lu et al., 1999; Mastrogiacomo et al., 2006; Gauthier et al., 1998]. The scaffold properties and characteristics, such as porosity, pore size, interconnection size and surface area, have been considered to be critical factors in functionality of bone substitute [Ho and Hutmacher, 2006; Ma et al., 2006]. In such porous material, pores provide a space for cells to reside and form new bone tissue while the interconnections provide the ways for cell migration, vascularization and transport of waste products and nutrients [Lu et al., 1999; Mastrogiacomo et al., 2006]. It is therefore important to characterize the structure of scaffolds to better understand the biological response. With this knowledge, a better design of scaffold becomes possible. For this purpose, an effective scaffold assessment is required at initial steps of research

and development to select and design scaffolds with appropriate properties [Ho and Hutmacher, 2006]. Various characterization techniques have been developed to evaluate geometric parameters of scaffold. An effective characterization method should be fast, accurate and non-destructive, while providing comprehensive information of all morphological and architectural properties [Ho and Hutmacher, 2006].

Micro-computed tomography (μ CT) has been introduced to provide access to 3-D structure of scaffold and allow for precise quantification of geometric parameters. Moreover, the use of μ CT is non-invasive and non-destructive [Ho and Hutmacher, 2006; van Lenthe et al., 2007]. μ CT also provided an accurate measurement of bone ingrowth inside the scaffold and evaluation of resorption kinetics [van Lenthe et al., 2007; Jones et al., 2009]. Various methods and algorithms have been developed to quantify the geometric parameters from μ CT images.

The first focus of this thesis is to improve the characterization of geometric parameters of calcium phosphate bone substitutes. This study combines novel image treatment techniques and algorithms to support more precise characterization of the porous scaffolds. For this purpose, the fuzzy-based methods are applied on μ CT images to improve the accuracy of the characterization [Saha et al. 2002; Saha and Wehrli, 2004]. Fuzzy-based methods consider the fuzzy nature of μ CT images and preserve more information from original μ CT images and therefore allow accurate characterization, in particular, when the resolution of images is relatively low [Sladoje et al., 2005; Saha and Wehrli, 2004]. In addition, a new algorithm has been developed to determine both pore and interconnection sizes and their corresponding distributions. In an attempt, to further improve in the accuracy of geometric parameters, this study also mentions to decrease the voxel size of μ CT images using subvoxelization algorithm and high resolution scans. Decreasing the voxel size provides more structural information and leads to precise characterization. Moreover, a well-established Lattice Boltzmann method is used to simulate the fluid flow in complex porous structure and measure the permeability of scaffolds.

Furthermore, the calcium phosphate bone substitutes are resorbable. The resorption rate of the calcium phosphate scaffolds should be controlled to match bone ingrowth in vivo and repair process. The resorption rate can be controlled by structural design. A few years ago, an analytical model was proposed by Bohner and Baumgart [Bohner and Bumgart, 2004] to predict the effect of geometric parameters on cell mediated resorption of ceramic bone substitutes. This thesis also aims to study the resorption behavior of resorbable bone substitutes and fulfill the analytical model presented in previous study [Bohner and Bumgart, 2004] by simulating the in vivo behavior of porous bone substitute. Therefore, a numerical algorithm is presented to simulate the resorption process of calcium phosphate bone substitutes. The simulation algorithm uses μ CT images and fuzzy image processing tools to enhance the precision of simulation.

1.2 Questions of research

Q. Scientific

How to improve the characterization of the pore and interconnection sizes of the micro-porous bone substitute?

Is subvoxelization a valid method to improve characterization?

What is the effect of geometric parameters on permeability and fluid flow analysis of bone substitute?

What is the effect of geometric parameters on resorption behavior of bone substitute?

Does interconnection size have any influence on resorption rate of bone substitutes?

Does the resorption direction effect on resorption rate?

Q. practical

How can we enhance the characterization precision of geometric parameters?

What is the relation between the voxel size and segmentation/thresholding of μ CT images?

What is the optimum resolution for analysis of structural parameters?

What is the effect of voxel size on characterization of structural parameters?

Does voxel size have any effect on numerical methods used for quantification of structural parameters?

What is the effect of resolution on resorption analysis of bone substitutes?

Q. biomechanics

How can we explain the biological behavior of porous bone substitute based on its geometric properties?

How can we predict the biological behavior of bone substitute based on its geometric and fluid flow properties, in order to design an efficient scaffold for bone substitute?

1.3 Hypothesis

The main hypothesis in this study is related to the definition of pore size and interconnection size. Due to the shape of pores in the structure of calcium phosphate bone substitutes, it was hypothesized that the fuzzy distance transform (FDT) value of local maxima in FDT map is an appropriate value to represent the pore size. It would be corresponding to the diameter of the largest spheres that was located inside the pores (Figure 1-1). Also, because of the shape of interconnections in the structure of calcium phosphate bone substitutes, it was hypothesized that the FDT value of local saddles in FDT map could be suitable value to define the interconnection size. It would be corresponding to the diameter of the spheres that blocked the fenestration between two or more pores (Figure 1-1).

A second hypothesis relates to the resorption process in that I assume that the pore and interconnection sizes are the key determinants of the cell mediated resorption process. Specifically, an algorithm and a simulation model are to be developed to help understand the resorption process as a function of the pore and interconnection sizes. Therefore, the

skeleton of the structure is used to define the accessible pores and interconnections for resorbing cells.

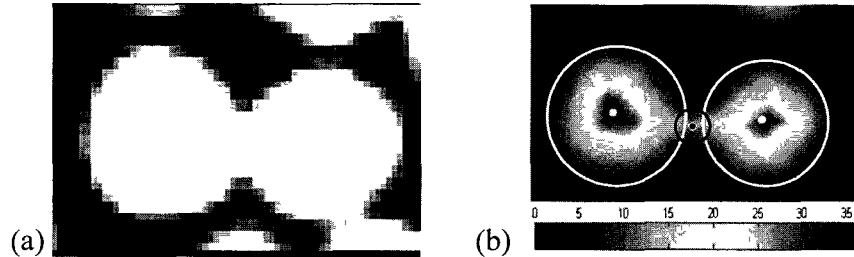


Figure 1-1 (a) 2-D fuzzy image and (b) 2-D FDT map, local maxima as a representative of pore size are shown with white points and local saddles as a representative of interconnection size are shown with black point. The diameter of corresponding circles is equal to the pore and interconnection sizes.

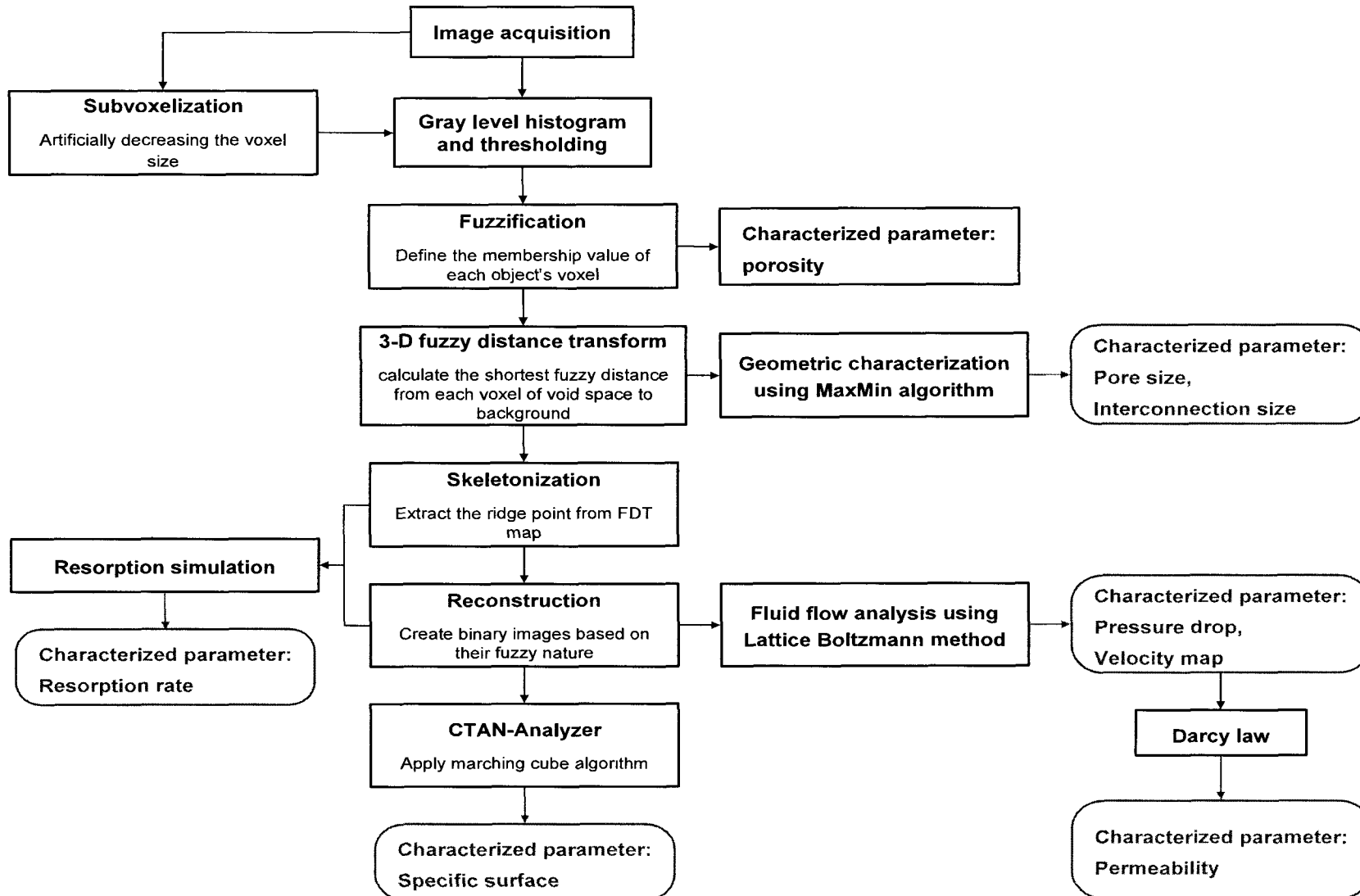
1.4 Objectives

The main objective of this thesis is first to improve the characterization of porous bone substitutes and second to provide a computational model to simulate the cell mediated resorption process of resorbable bone substitutes. Toward the ultimate target, this study combines both novel image treatment and algorithm to reach the objective of the thesis.

Specifically, this study aims to apply the fuzzy image processing technique and developed algorithm to enhance the accuracy of the pore and interconnection size characterization. In addition, subvoxelization algorithm and high resolution μ CT scans will be used to further investigate the accuracy of geometric analysis.

Moreover, this study aims to establish a computer model to simulate the resorption process of resorbable bone substitutes. The effort will be paid to better understand the cell mediated resorption process of calcium phosphate bone substitute. Calculation of resorption rate and investigation of resorption at various locations will be also the targets of this study.

1.5 Block diagram of the doctorate work



CHAPTER 2

Literature survey

2.1 Bone defects and repair procedure

The bone defects can be caused by “missing” or “defective” bone tissue [Celil et al., 2007]. Celil and his colleagues classified the bone defects into two types. First type is the deformities in which tissue elements are not missing, and the defect is caused by abnormal anatomy, like fracture malunion. This case can be repaired by rearranging or augmenting the defected tissue. Second type of defects is occurred by the damage or missing of bone tissue, like cancer. In this case the repair is possible by tissue replacement [Celil et al., 2007].

Generally, as a living tissue, bone is able to restore its functionality and health. For small size fracture (like a crack), after initial stabilization, the healing process begins based on bone repair mechanism [Hing, 2004a]. Simple bone break fractures are usually treated by external or internal fixation of the fracture site using splints and casts or plates and pins, respectively [Hing, 2004a]. These methods provide the local stability required for bone regeneration. However, according to the material used for internal fixation, second surgery is often required to remove the metallic device used for fixation. Spinal fragility fractures, as a result of aging and diseases, such as osteoporotic vertebral fractures, are repaired by injecting acrylic or calcium phosphate cements into weakened vertebrae to augment them [Baroud et al. 2004; Baroud et al. 2005; Baroud et al. 2006]. In large bone defects, where a critical size of bone is missing or damaged [Hing, 2004a], bone repair mechanism fails to restore the defects as a result of fracture size or infection [van Gaalen et al., 2008]. Reconstructive orthopedic surgery highly demands for bone replacement to repair the large bone defects and treat relative diseases such as spinal fusion, bone cancer, accidental trauma cases and hip fracture. Bone grafting has been introduced as a successful therapy for treatment of such large bone defects [van Gaalen et al., 2008].

2.2 Bone substitute and its role in bone healing

Bone reconstructive surgery is the procedure of replacing missing bone with bone grafts or bone substitutes. The bone substitutes should not only fill the bone defects, but also must stimulate the body to repair itself and facilitate the healing procedure [van Gaalen et al., 2008]. Typically, a bone substitute consists of the scaffold (matrix), viable cells and bioactive agents [Hutmacher et al., 2008; Langer and Vicente, 1993]. A scaffold acts as a temporary 3-D support for cells to adhere, proliferate, differentiate and form new bone to restore the functionality of tissue, while the bioactive cells manage the healing process [Yarlagadda et al., 2005; Woźniak and El Haj, 2007]. Thus, a scaffold should provide the biochemical, biomechanical and structural properties to accelerate healing process.

2.2.1 Ideal scaffold for bone substitute

A scaffold is meant to be invaded by cells and should provide chemical and physical properties to ensure adequate bone ingrowth. An ideal scaffold should fulfill specific requirements. Ideally, the biomaterial used for bone substitute application should provide the following biological characteristics [Moore et al., 2001; Celil et al., 2007]:

- (i) Biocompatibility, the ability to match with living cells and tissues without eliciting any undesirable effects in those cells;
- (ii) Osteogenesis, ‘the formation of new bone by osteoblastic cells present within the graft material’ [Moore et al., 2001];
- (iii) Osteoinduction, ‘the ability to induce differentiation of pluripotential stem cells from surrounding tissue to an osteoblastic phenotype’ [Moore et al., 2001];
- (iv) osteoconduction, ‘the ability to support the growth of bone over its surface’ [Moore et al., 2001];
- (v) Osteointegration, ‘the ability to chemically bond to the surface of bone without an intervening layer of fibrous tissue’ [Moore et al., 2001].

Furthermore, many studies have demonstrated that the geometry and architecture of scaffolds also affect their biological response and their ability to remodel to their environment. Therefore, an ideal scaffold should also possess the following properties [Hutmacher, 2000; Agrawal and Ray, 2001].

- (vi) The scaffold structure should be 'three dimensional and highly porous with interconnected pore network' to allow cells ingrowth and transport of nutrients and waste products;
- (vii) The pores in the porous structure should have adequate size for cells;
- (viii) The scaffold should have a surface conducive for cell attachment, proliferation, and differentiation;
- (ix) The scaffold should be bioresorbable with controllable resorption rate to match the bone repair or regeneration process. The resorption rate can be controlled by biomaterial or structural design.

In addition an ideal scaffold should provide specific mechanical and physical properties.

- (x) It should possess adequate mechanical properties like those of the tissue at implantation site;
- (xi) It should have high permeability to allow cell penetration.

At macroscopic level (mm-cm), the shape and composition of scaffold will affect its toxicity, cell penetration and differentiation into the structure. At intermediate level (100 μm), the geometric parameters in terms of pore and interconnection sizes, orientation and surface chemistry will determine the ability of cells to penetrate inside the structure and affect the transport of nutrient and waste products. At microscale level (10 μm), the local surface texture and porosity will affect the protein adsorption and cell adhesion [Griffith, 2002]. Therefore, a comprehensive assessment of scaffold characteristics at each level is critical for understanding its biological behavior.

In the following sections, the current materials used for bone substitute will be reviewed. It will be followed by important geometrical parameters of porous structure and the bone substitute paradigms available in literature.

2.3 Bone substitute material

The bone grafts which are directly derived from real bone are classified into three types; autograft, allograft and xenograft [Baksh, 1999; Woźniak and El Haj, 2007; Laurencin et al., 1999]. In contrary to these types of grafts, the synthetic bone substitutes are produced from biocompatible materials. The properties of each type of grafts and biomaterials used for bone reconstruction are discussed subsequently.

2.3.1 Autografts

Autografts are obtained from the patient's body and transplanted to the damage organ. This type of grafts is still considered as the "gold standard" in bone replacement due to their excellent osteogenic, osteoinductive and osteoconductive properties [Woźniak and El Haj, 2007; Finkemeier, 2002; Hing, 2004a; van Gaalen et al., 2008]. However, their application is limited because of the following reasons: (a) The amount of harvested bone required for defect site is limited [Hing, 2004a; Baksh, 1999; Woźniak and El Haj, 2007; Woźniak and El Haj, 2007], (b) The autograft harvesting lengthens the surgery procedure. [van Gaalen et al., 2008], (c) Post operative complications due to donor-site morbidity, pain, infection and structural weakness [Polly and Kuklo, 2002] and (d) Inability to form the harvested bone shape for optimal function [Goldberg, 1992; Goldberg, 1993; Parikh, 2002].

2.3.2 Allografts

Allografts are harvested from human donor and stored in tissue banks [Woźniak and El Haj, 2007]. Although, using allografts overcomes the autografts limitation, there is still some restriction related to their application. Despite using very strict preparation procedure, there is the possibility of infection, transmission of disease and immunogenicity of the grafts [van Gaalen et al., 2008; Laurencin et al., 1999]. Also in this

case, the blood vessels form very slowly and less extensive than in autografts [van Gaalen et al., 2008; Barriga A, 2004].

2.3.3 Xenografts

Xenografts as another alternative to autografts, are harvested from a species other than human (e.g. Bovine clef bone) [Baksh, 1999; van Gaalen et al., 2008]. These materials are mainly used as mechanical filler to inhibit ingrowth of soft tissue [Baksh, 1999]. The tissue rejection due to immunological problem is the application risk associated with their use [Charalambides et al., 2005; Charles-Harris, 2007].

2.3.4 Synthetic bone graft substitutes

Due to the limitation and complication of the abovementioned grafts, there is an increasing demand for development of synthetic bone graft substitute that would be free from the problems associated to donor site morbidity, disease transfer and inadequate supply of material [Hing, 2004a; Hing, 2005a]. Synthetic bone graft substitutes, fabricated from metals, polymers, ceramics and composites, have been introduced as an alternative to the previous types of grafts. The first generation of synthetic materials for use in the human body was introduced in 1960s and 1970s [Hench and Polak, 2002]. The earlier biomaterials were mainly designed to 'achieve a suitable combination of physical properties to match those of the replaced tissue with a minimal toxic response in the host tissue' [Hench, 1980]. These materials were 'nearly inert' and were separated from the host tissue by growing a thin, fibrous capsule [Hench, 1980]. Finally, due to non-integration between the implant and surrounding tissue, the implants often loosen [Hench, 1980]. In 1980s, the second generation biomaterials were developed to be either bioactive or bioresorbable [Hench and Polak, 2002]. The significant advantage of bioactive materials is forming strong bonds to host tissue [Hench, 1998]. Another advantage of second generation was developing resorbable materials that are replaced by regenerated tissue [Hench and Polak, 2002]. Development of bioactive and bioresorbable material has been a great improvement in orthopedic application. However, the implants' life time analysis revealed that a third to half of implants fail within 10-25 years and revision surgery will be required [Hench and Polak, 2002]. The third generation biomaterials were

designed to motivate specific cellular responses. They were developed to interact with cells and activate certain genes to, specifically, stimulate regeneration of living tissue [Hench and Polak, 2002]. For this type of biomaterials, the bioactive and resorbable properties have been combined to help the body repair itself in a good and rapid way. Potential materials used as bone substitutes can be divided into: metals, polymers, ceramics and composite materials.

2.3.4.1 Metal

Typical metallic implants used for bone reconstruction are stainless steel, titanium alloys and cobalt alloys. An excellent mechanical property is the main advantage of metallic implants. Due to their mechanical stability, they have been widely used as implant material for bone repair (e.g. hip replacement device). However, the lack of degradation and non-integration to surrounding tissue limit their application and second surgery will be required to remove the implant, or in the case of permanent implantation there is the risk of toxicity/ allergic reaction [Karageorgiou and Kaplan, 2005; Yang et al., 2001].

2.3.4.2 Polymer

Polymers are known as the largest group of biomaterials [Charles-Harris, 2007]. Both natural and synthetic polymers are used in orthopedic applications. The natural polymers, such as collagens, glycosaminoglycan, chitosan, etc. [Yang et al., 2001; Meyer and Wiesmann, 2006] offer the advantage of biocompatibility, biodegradability and easy processing [Karageorgiou and Kaplan, 2005; Khang et al., 2007]. However, their application is limited due to their high rate of degradation [Karageorgiou and Kaplan, 2005], poor mechanical properties [Karageorgiou and Kaplan, 2005; Yang et al., 2001] and low reproducibility [Charles-Harris, 2007].

The synthetic polymers, such as polylactic acid and poly (lactic-co-glycolic acid), have been developed to overcome the limitation of natural polymers. They provide a large range of bone substitutes with controlled degradation rate and different geometrical and mechanical properties [Karageorgiou and Kaplan, 2005]. They also have the advantage of high reproducibility and can be fabricated in large-scale [Charles-Harris, 2007]. Synthetic

polymers based on biodegradable polyhydroxyacids, such as poly-lactic-glycolide, have been widely used for bone replacement due to their excellent cell adhesion and cell proliferation [Meyer and Wiesmann, 2006]. The limitations associated with use of synthetic materials are their low mechanical properties (even in solid form) [Karageorgiou and Kaplan, 2005] and their acidic degradation products that may reduce biocompatibility [Yang et al., 2001].

2.3.4.3 Ceramics

Ceramics have been specifically used as artificial matrix for bone repair applications [Yang et al., 2001; Charles-Harris, 2007]. The ceramic biomaterials can be classified into three groups based on their chemical activity [Charles-Harris, 2007; Yang et al., 2001; Khang et al., 2007].

(a) Bioinert ceramics, such as alumina and zirconia, have the great advantage of biocompatibility and high mechanical properties such as excellent compressive strength and high resistance to wear [Thamaraiselvi and Rajeswari S, 2004]. However, they do not show ionic interaction with the surrounding tissue, in other word they have weak osteointegration properties. A relationship between the implant and host bone is formed due to mechanical bonds which are created by the stresses on the implant [Moore et al., 2001].

(b) The second type of bioceramics is the surface bioactive group. This group includes bioglasses, glass-ceramics and synthetic hydroxyapatite ceramics [Charles-Harris, 2007; Yang et al., 2001]. The bioglasses and glass-ceramics show excellent mechanical properties, bioactivity, biocompatibility and no toxicity [Thamaraiselvi and Rajeswari S, 2004]. The hydroxyapatite ceramics have a composition similar to the mineral component of bone. They exhibited excellent biointegration properties and have been used to coat metal implants to improve their osteointegration [Moore et al., 2001]. Hydroxyapatite ceramics are mechanically resistant under compression, but they are weak and brittle under tension and shear loads [Moore et al., 2001; Khang et al., 2007].

(c) The third group of ceramics is bioresorbable ceramics such as, coralline, tricalcium phosphate (TCP), soluble biocompatible glasses, α and β tricalcium phosphate (α -TCP, β -TCP), etc [Khang et al., 2007; Charles-Harris, 2007; Yang et al., 2001]. Calcium phosphate family has the advantages of biocompatibility, osteointegrativity, osteoconductivity and no toxicity [Moore et al., 2001]. The calcium phosphate ceramics are brittle under tensile and shear and strong under compression loads [Moore et al., 2001]. β -TCP ceramics in porous form have compressive strength and tensile strength similar to cancellous bone [Moore et al., 2001; Jarcho, 1981; Miranda et al., 2008]. Although, these ceramics are mechanically brittle and fragile, they should preserve their structure and mechanical stability of their structure during the initial period of implantation [Charles-Harris, 2007; Hing, 2005]. Therefore, the degradation rate must be controlled to match new bone formation [Charles-Harris, 2007].

2.3.4.4 Composites

Composite materials are introduced as the combination of two or more individual materials that are able to act synergistically to enhance the properties provided by each material alone [Thamaraiselvi and Rajeswari S, 2004]. Composites made from bioinert and bioactive ceramics are fabricated to attain bioactive material with mechanical strength. Coating porous titanium scaffolds with calcium phosphate led to earlier and greater bone ingrowth and improved mechanical properties [Tache et al., 2004]. Biphasic calcium phosphate ceramics composed of tricalcium phosphate and hydroxyapatite ceramics were developed to achieve resorbable ceramics with controllable resorption rate. Table 2-1 summarizes the common polymers, ceramics and composites used for bone repair application [Di Silvio, 2007].

Table 2-1 Common biomaterial used for bone repair [Di Silvio, 2007]

Polymer	Ceramics	Composite/natural
<ul style="list-style-type: none"> • Polylactic acid • Polyglycolic acid • Polycaprolactone • Polyanhydrides • Polyphosphazenes • Polymethylmethacrylate (PMMA) • Polytetrafluoroethylene (PTFE) 	<ul style="list-style-type: none"> • Bioglass • Sintered hydroxyapatite • Glass-ceramic A-W • Hydroxyapatite (HA) – calcium phosphate-based ceramic • Bioactive glass • Sol-gel-derived bioactive glass 	<ul style="list-style-type: none"> • Poly(D,Lactide-co-glycolide) + bioactive glass • Extracellular matrix (ECM) • Hyaluronan - linear glycosaminoglycan (GAG) • Demineralized bone matrix (DBM) • Collagraft – commercial graft = HA + tricalcium phosphate ceramic + fibrillar collagen

2.4 Bone substitute and structural parameters

2.4.1 Definition of porous structure

A porous medium is defined as ‘solid body that contains pores’, the pores are void spaces which are frequently distributed through the porous media [Scheidegger, 1960]. Pores or void spaces are classified into two groups, interconnected or effective pore space and non-interconnected or isolated pores [Scheidegger, 1960; Dullien, 1979]. Non-interconnected pores are not able to contribute in fluid transport through porous structure. Fluid flow is possible, only if the pores are connected [Scheidegger, 1960; Dullien, 1979]. The dead-end pores are only interconnected from one side [Dullien, 1979; Kaviani, 1995].

2.4.2 Geometrical characteristics of porous structure

A porous medium can be quantified by different geometrical parameters. ‘Porosity’, the volume fraction of void space, is one of the important parameter in characterization of porous medium. It is calculated as the ratio of void volume to the total volume occupied by solid and void spaces. The porosity is expressed in percent or as a fraction of one [Scheidegger, 1960; Kaviani, 1995]. If the porosity is calculated based on the volume of interconnected pores instead of total pore space, it is entitled as effective porosity.

Other important parameters in the characterization of porous medium are ‘pore size’ and ‘pore size distribution’. There are various definitions of pore size. In general, pore size at any point within the pore space is defined as the diameter of the largest sphere which contains this point and is completely inside the pores [Scheidegger, 1960]. The pore size distribution is also determined as the fraction of total pores which have sizes between δ and $\delta+d\delta$ [Scheidegger, 1960]. When a pore network is interconnected, the pores are linked together by smaller voids. It can be introduced as a ‘neck’ or ‘interconnection’ between the pores [Dullien, 1979] (Figure 2-1). The interconnection size and distribution are other geometric parameters of the porous structure, which allow the fluid flows through the structure.

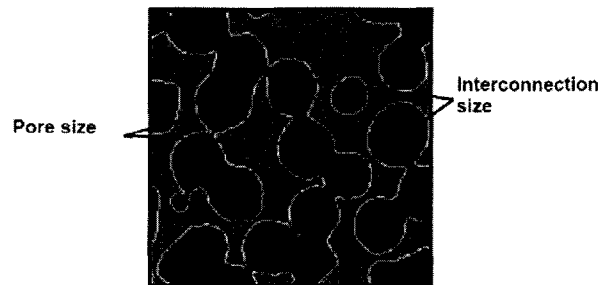


Figure 2-1 2-D image as representative of pores and interconnections

‘Specific surface’ is another geometric parameter of porous medium and is defined as the ratio of the internal surface area of pores to the bulk volume [Scheidegger, 1960]. Specific surface plays an important role in different application of porous media; for example, it is related to cell adhesion and osteointegration into porous scaffold. Finally, tortuosity of porous structure is introduced as another geometric parameter [Scheidegger, 1960]. Tortuosity is defined as a kinematical property equal to the ratio of the actual flow path to the length of the straight line between its starting point and ending point. Tortuosity of porous bone substitute can help understanding how much easy the fluid (nutrient and blood cells) can pass through the scaffolds.

2.5 Bone substitute paradigms

2.5.1 Biological paradigms

Vascularization: The penetration of oxygen and nutrient supplies through bone is highly dependent on the existence of blood vessels [Hing, 2004a, Hing, 2005a]. Vascularization is known as the prerequisite and the preceding step for bone repair and new bone formation [Street et al., 2002]. Specifically, for repair of bone defects with porous biomaterials, formation of a vascular network is significantly important at early stage of implantation [Otsuki et al., 2006]. Vascularization enhances the nutrients transport, waste removal and cells migration. [Klenke et al., 2007]. High porosity and high degree of interconnectivity between pores are essential requirements for vascularization of scaffold and bone formation [Mastrogiacomo et al., 2005].

Further, there is a relation between vascularization and interconnection size. Narrow interconnections inhibit vessel formation inside the porous scaffold [Otsuki et al., 2006]. The degree of interconnectivity between the pores strongly affects the rate and extent of vascularization [Rubin et al., 1994]. The interconnections sizes also influence the quality of vascularization. Two phenomenon due to larger interconnection size have been reported: (a) the formation of multiple blood vessels [Chang et al., 2000] and (b) the formation of larger blood vessels [Mastrogiacomo et al., 2006].

Bone ingrowth: Bone formation is assured by growth of blood vessels inside the pores. Structural features, such as porosity, pore size and interconnectivity between the pores, play critical role in bone formation [Jones et al., 2009; Klenke et al., 2007]. The volume of bone ingrowth and the rate of osteointegration are relying on the available surface for the new bone cells [Mastrogiacomo et al., 2006]. The size of pores that are accessible from the scaffold periphery has a strong correlation with bone ingrowth [Jones et al., 2009]. Furthermore, it was shown that the pore interconnectivity is the controlling factor at the earlier implantation time [Hing et al., 2004b]. Hing et al. demonstrated that the rate and the volume of bone apposition initially depend on pore interconnection rather than the pore size [Hing et al., 2004b].

2.5.2 Structural paradigms

The rate and quality of vascularization, bone formation and degradation inside the scaffold can be affected by structural feature of porous scaffold. Several studies have been done to find optimum geometric parameters to improve scaffold functionality. However, there is no consensus regarding the optimum porosity, pore size and interconnection size. In the following paragraphs, the current paradigms in terms of geometric parameters will be reviewed.

Porosity: Higher porosity is expected to improve osteogenesis. This hypothesis has been proved by many studies [Karageorgiou and Kaplan, 2005]. Roy et al. used polylactic-co-glycolic acid (PLGA) and β -tricalcium phosphate (β -TCP) scaffolds with pore size of 125-150 μ m and porosity gradient of 80-87.5%, then they implanted the samples in rabbit cranium [Roy et al., 2003]. They observed the presence of more bone formation in area with higher porosity. In another study, Kruyt et al. implanted the hydroxyapatite scaffolds with different porosity (70% and 60%) and pore sizes (800 μ m and 400 μ m, respectively) in bilateral paraspinal muscles of goat. More bone formed in samples with higher porosity and pore size (i.e. 70% and 800 μ m) [Kruyt et al., 2003].

There are a few articles that report no effect of porosity on the amount of bone formation. For example, Gauthier et al. implanted macroporous biphasic calcium phosphate scaffolds in distal femoral site of rabbits [Gauthier et al., 1998]. The samples were designed with different pore sizes (300 and 565 μ m) and porosities (40 and 50%). They observed no significant differences in newly formed bone inside the implants with similar pore sizes (565 μ m) and different porosities (40 and 50%). The absence of any reports indicating the positive effect of lower porosity on biological results, confirms the necessity of highly porous scaffold for bone formation [Karageorgiou and Kaplan, 2005].

In addition, the rate of degradation of scaffold material should be considered when porosity is studied. Scaffolds made from biomaterials with high degradable rate should not be highly porous, since rapid reduction of material lead to mechanical and structural instability before replacement by new bone cells. Conversely, scaffolds made from

biomaterials with low degradable rate and good mechanical properties should have high porosity [Karageorgiou and Kaplan, 2005].

Generally, there is no optimal porosity to ensure rapid bone formation inside the porous scaffold, but a level of porosity larger than 50%-60% was widely advised [Hing, 2005a].

Pore size: Pore size would directly affect bone formation, since it provides surface and space for cell attachment and bone formation [Mastrigiocomo et al., 2006; Jones et al., 2009; Lu et al., 1999]. Hulbert et al. proposed the pore size of 100 μm as the minimum size required for osteoconduction, and the pore size of 150 μm as the optimal size for bone ingrowth [Hulbert et al., 1972]. Many studies have explored pore sizes over 100 μm as optimum size for bone ingrowth. Gauthier et al. found that a pore size of 80-100 μm is the minimal size to promote bone formation in the porous HA/ β -TCP scaffolds [Gauthier et al., 1998]. In another study, Kuboki et al. compared honey-comb hydroxyapatite blocks with different pore sizes (106-212, 212-300, 300-400, 400-500 and 500- 600 μm) when subcutaneously implanted in the backs of rats [Kuboki et al., 2001]. They observed that the pore size of 300-400 μm was the optimum size for bone ingrowth.

There are a number of articles that report no effect of pore size on the amount of bone formation. For example, Ayers et al. observed no statistical difference in bone ingrowth in nitinol blocks with different pore size (353, 218, 179 μm) and porosities (43%, 54%, 51%, respectively) when implanted in cranial defect of rabbits [Ayers et al., 1999]. A similar effect was found in the study of Kujala et al. when compared nickel-titanium scaffolds implanted in distal femoral of rat, with porosities of 66.1% and 46.6% and pore sizes of 295 μm and 505 μm , respectively [Kujala et al., 2003]. In another study, β -TCP blocks of four different pore sizes (150, 260, 510 and 1220 μm) and constant macroporosity (~50%) were implanted in bone defect in sheep, there was no significant effect of the pores on bone, ceramic and soft tissue fraction [von Doernberg et al., 2006].

Other factors, such as accessibility to pores and pore shape should be taken into account when pore size is studied. Local pore size does not affect on bone ingrowth. Many unreachable pores have poor accessibility to the periphery of scaffold; however, they have large local pore size [Jones et al., 2007]. In their study, Jones AC et al. showed that

the cells could penetrate to all accessible pores which are connected to the periphery of scaffold with accessible size of 100 μm [Jones et al., 2007; Jones et al., 2009]. Longer and curved pores decrease the rate of cell penetration and delay bone formation [Karageorgiou and Kaplan, 2005].

It is well defined that the rate and volume of bone formation is significantly influenced by macropore size and macroporosity. However, recent studies have reported that micropores and micro porosity in the structure of ceramics can further support the bone ingrowth inside the structure [Lan Levengood et al., 2010; Habibovic et al., 2006; Hing et al., 2005b].

Interconnection size: Pore interconnections are known as the controlling factor for rapid and efficient vascularization and bone formation [Hing et al., 2004b]. Pore interconnections provide the path for cell migration, nutritional diffusion and blood vessel formation [Lu et al., 1999; Mastrogiacomo et al., 2006; Li et al 2007; Jones et al., 2009]. Some researchers have explored minimum interconnection size of 50 μm as adequate size for cell penetration [Lu et al., 1999; Outsuki et al., 2007]. However, some reports in the literature have suggested that a minimum interconnection size of 100 μm is required for bone formation [Jones et al., 2007; Jones et al., 2009].

Outsuki et al. studied the effect of interconnection on bone and tissue differentiation inside the porous titanium blocks with different porosities (50% and 70%) and pore sizes (250-500 μm and 500-1500 μm) [Outsuki et al., 2007]. They demonstrated that the existence of narrow interconnections in the shortest routes from the pores to the outer surface may prevent tissue differentiation.

In another study, HA and β -TCP porous scaffolds with constant porosity (50%), pore size (100-300 μm) and interconnection size (30-100 μm) were compared when implanted in rabbit femurs [Lu et al., 1999]. The results revealed that: (i) interconnection size larger than 50 μm allowed bone formation, (ii) due to the in vivo degradation of β -TCP, deeper vascular penetration occurred more frequently in β -TCP than HA blocks. They also mentioned that 'in resorbable materials, pore and interconnection densities (the number of pores and interconnections per volume) play a more important role than the pore and

interconnection sizes; because sizes are modified by degradation, while in unresorbable material the sizes and densities are equally important' [Lu et al., 1999].

2.5.3 Physical and mechanical paradigms

Permeability: Generally, permeability is quantified as the ability of porous structure to transmit the fluid through its structure. More specifically, the scaffold permeability can be defined as 'a measure of the ease at which fluid passes through the scaffold pores' [Ho and Hutmacher, 2006; Karande et al., 2004]. Hui et al. measured the permeability of cancellous bone grafts before implantation and found that a permeability of $\sim 3 \times 10^{-11}$ m² was required for vascularization and bone formation to occur within the implant [Hui et al. 1996].

A high permeability enhances the diffusion within the scaffolds which promotes the inflow of biological cells, nutrients and waste products [Karande et al., 2004]. The scaffold permeability is influenced by the geometric features. A positive correlation between porosity and permeability could exist when the pores are highly interconnected [Karande et al., 2004]. Agrawal et al. showed that the scaffolds with similar porosity may have different permeabilities [Agrawal et al., 2000]. Highly porous scaffolds with non-connected pores decrease the diffusion efficiency [Ho and Hutmacher, 2006].

The scaffold permeability has been introduced as a representative and comprehensive parameter in describing macroporous scaffolds [Li et al., 2003]. It could reflect a combination of five important parameters of scaffold: (1) porosity, (2) pore size and distribution, (3) interconnectivity, (4) interconnection size and distribution, and (5) orientation of pores [Li et al., 2003, Chor and Li., 2007].

Since mechanical properties are not improved by increasing the porosity, Li Sh et al. proposed that the permeability/porosity ratio as an indication of 'the percolative efficiency per unit porous volume' is a better parameter for characterization of porous scaffolds [Li et al., 2003].

Mechanical properties of material: The mechanical properties of a scaffold should be compatible with the biomechanical properties of the tissue to be replaced [Hollister et al.,

2002; Lin et al., 2002; Moroni et al., 2006]. Specifically, a scaffold should have adequate mechanical strength in reconstruction of load bearing tissue (e.g. bone) [Yang et al., 2001].

The scaffold must allow load distribution and should not be very stiff to produce load concentration [Hing, 2005a]. Stress analysis investigations revealed that the anisotropic structures reduce the stress concentration in comparison with isotropic ones when loaded in one direction [Hing, 2005a]. Therefore, appropriate macroporous structure can improve load distribution and reduce stress concentration.

Mechanical properties are closely related to the porosity of porous structure. Increasing of porosity leads to a reduction in mechanical properties, because high porosity decreases the quantity of material and structural integrity of porous scaffold [Will et al., 2008; Moroni et al., 2006; Huec et al., 1995; Ma et al., 2006; Karageorgiou and Kaplan, 2005]. Dense hydroxyapatite has a compressive strength of 430–920 MPa, significantly higher than that of cortical bone (100–230 MPa), whereas the compressive strength of porous hydroxyapatite samples fabricated by 3D printing, was found to be reduced to 30 MPa at a porosity of 50% [Will et al., 2008]. Dynamic mechanical analysis of copolymer (polyethyleneoxide-terephthalate and polybutylene-terephthalate) scaffolds fabricated by 3D fiber deposition revealed that increase of porosity caused a decrease of elastic properties (e.g. dynamic stiffness and equilibrium modulus) and an increase of viscous properties (e.g. damping factor and creep unrecovered strain) [Moroni et al., 2006]. Bone ingrowth and vascular formation are favored by more porous structures, whereas mechanical strength and stability during the initial period of integration are favored by low porous structures. These conflicting requirements can be balanced by fabricating suitable biomaterials for the scaffold [Karageorgiou and Kaplan, 2005; Hing, 2005a].

Micro mechanical environment: When porous bone substitutes are used to repair load bearing tissues like bone, the interaction with mechanical environment should be considered as an important factor. Bone is a complex tissue that changes its form, mass and internal structure under mechanical loads [Cehreli et al., 2004]. In other words, mechanical loads can influence bone response [van Cleynenbreugel et al., 2006;

Sikavitsas et al., 2001]. Mechanical signals affect the development and differentiation of bone tissue [Cehreli et al., 2004, Sikavitsas et al., 2001].

There is a consensus that bone modeling is based on the ability of bone cells to sense the mechanical loading and adopt accordingly [Cehreli et al., 2004; Jacques et al., 2004; Liebschner and Wettergreen, 2003]. Biomechanical signals, received by the mechanosensing bone cells (osteocytes), would determine whether bone is resorbed by osteoclasts or deposited by osteoblasts. Bone modeling and remodeling theories specified that the dynamic strain levels that exist in bone are the main reason for bone modeling and remodeling process [Liebschner and Wettergreen, 2003; Huiskes et al., 2000]. The dynamic strains can be generated externally by the load or internally by resorption cavities [Huiskes et al., 2000]. In addition, the frequency of mechanical loads can also affect the bone formation, higher frequency loading stimulates bone ingrowth [Liebschner and Wettergreen, 2003]. Experimental results and computational models have revealed that the bone formation will occur in the dominant stress direction [Liebschner and Wettergreen, 2003, Huiskes et al., 2000].

Once the cells colonize the scaffold, they should begin proliferation or differentiation in order to produce the new bone cells. Cells attach onto the scaffold surface and apply traction forces on the attached surface. The interaction between bone cells and bone substitute affects bone cell viability, attachment and penetration [Sikavitsas et al., 2001].

Therefore, due to the effect of bone mechanical environment on new bone formation, the bone substitutes should be considered both biological and mechanical aspects of bone tissue. The scaffolds should also distribute forces at a desirable level of induced strains [Cehreli et al., 2004]. Frost proposed that the bone substitutes used for load bearing application should keep the strain of supporting bone below its micro damage level [Frost, 1994].

2.6 Characterization of structural parameters

According to the above mentioned paradigms, the structure and architecture of scaffolds are considered as crucial factors that affect scaffold functionality. Therefore, effective

characterization methods are required to measure the structural parameters to design a scaffold with appropriate properties. Various techniques have been developed to evaluate these important features. In this section, a brief review of some techniques used for assessment of scaffold properties is presented.

2.6.1 Traditional methods to measure Porosity and Pore size

Gravimetry: Gravimetry method measures the porosity using the following equation:

$$P_{total} = 1 - d_{scaffold} / d_{material} \quad (2.1)$$

Where $d_{material}$ is the density of scaffold material and $d_{scaffold}$ is the apparent density of porous scaffold calculated from weight and volume of scaffold (weight/volume of scaffold) [Karageorgiou and Kaplan, 2005; Hu et al., 2002].

Mercury intrusion porosimetry: This method was used to quantify both porosity and pore size. The scaffolds are placed in a penetrometer and infused with mercury under increasing pressure. The relation between the pressure, P , and the radius of pores, r , is determined by Washburn's equation [Ho and Hutmacher, 2006]:

$$P = 2\sigma \cos \theta / r \quad (2.2)$$

Where σ is the surface tension of Hg and θ is the contact angle. The open porosity (porosity accessible to mercury) is given as:

$$P_{open} = V_{intrusion} / V_{scaffold} \quad (2.3)$$

Where $V_{intrusion}$ and $V_{scaffold}$ are the total intrusion volume and scaffold volume respectively. Then the closed porosity can be measured as follow [Maspero et al., 2002]:

$$P_{close} = P_{total} - P_{open} \quad (2.4)$$

Liquid displacement: The open porosity can be calculated by liquid displacement method. The scaffold is submerged in a graduated cylinder containing a known volume (V_1) of liquid that is not a solvent for the scaffold. The cylinder is then placed in vacuum to force liquid into the pores of the scaffold. Then V_2 is appointed as the total volume of

liquid and liquid-impregnated scaffold. The volume difference ($V_2 - V_1$) is the volume of the scaffold skeleton. When the liquid-impregnated scaffold is removed from the cylinder, the removing liquid volume is recorded as V_3 (Figure 2-2). The void volume of the scaffold is equal to $V_1 - V_3$ and the total volume of the scaffold is equal to $V = (V_2 - V_1) + (V_1 - V_3) = V_2 - V_3$, thus, the open porosity of scaffold is determined as [Karande et al., 2004; Ho and Hutmacher, 2006; Moore et al., 2004]:

$$p_{open} = (V_1 - V_3) / (V_2 - V_3) \quad (2.5)$$

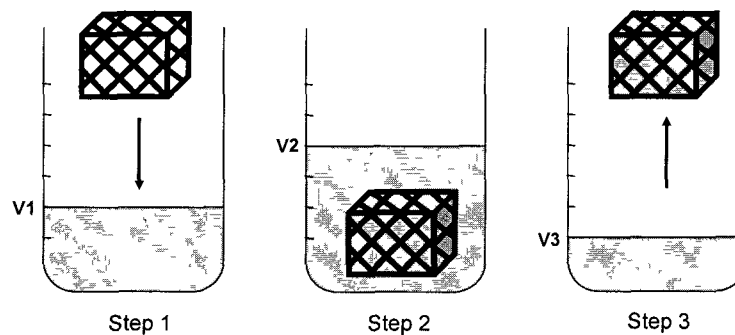


Figure 2-2 Schematic representation of Liquid displacement method.

Optical techniques: Scanning electron microscopy (SEM) as an optical method is widely used for assessment of scaffold structure [Gauthier et al., 2005]. The scanning electron microscopes use electrons rather than light to acquire images of high resolution (Figure 2-3). These images are analyzed with various computer software to measure porosity and particularly pore size [Karageorgiou and Kaplan, 2005; Hu et al., 2002; Moore et al., 2004]. The SEM method is limited to 2D measurements on relatively small fields of view. Therefore, only a small part of the sample can be viewed at each images and it may become difficult to identify pores from interconnections [Moore et al., 2004].

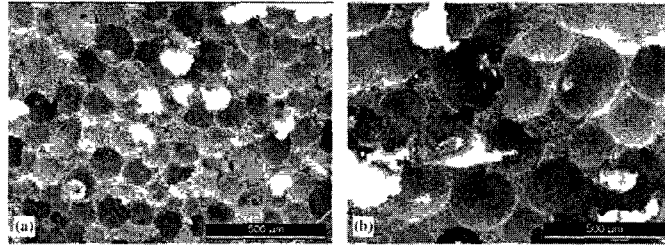


Figure 2-3 Representative SEM images of scaffolds with different pore sizes, the white bar corresponds to 0.5 mm [Bohner et al., 2005]

2.6.2 Recent methods to measure Porosity and Pore size

2.6.2.1 Micro Computed tomography (μ CT)

μ CT is considered as a more recent method for assessment of scaffold morphology. This method provides accurate qualitative and quantitative information of internal structure of scaffold in 3-D. The internal structure of porous scaffolds can be studied in detail without any physical sectioning or chemical process. Therefore, μ CT is known as a non-destructive method, the samples remain intact and can be used for additional investigation [Ho and Hutmacher, 2006; van Lenthe et al., 2007]. The non-destructive aspects of μ CT provide the ability to study the scaffold internal structure before implantation. Thus, the scaffolds that fulfill certain criteria will be selected for bone replacement.

The “Desktop μ CT” systems is a validated technique [Muller and Hildebrand, 1996; Balto et al., 2000] which has been widely used for investigation of scaffold micro structure [Zeltinger et al., 2001; Bohner et al., 2005], bone ingrowth [Guldberg et al., 2004; Tanck et al., 2001] and vascularization [Bentley et al., 2002]. These systems provide high resolution images ranging from 5-100 μ m. The samples with the size ranging from few millimeters to 100 mm can be scanned by this system [van Lenthe et al., 2007].

μ CT allows studying the bone tissue formation in scaffolds. It provides relevant information of the newly formed bone, remaining biomaterial and soft tissue [van Lenthe et al., 2007, Gauthier et al., 2005]. This methodology is useful to control the scaffold structure and architecture and to study the scaffold resorption kinetics.

In addition to assessment of scaffold structure and biological in vivo response, μ CT is used to optimize fabrication process to produce a scaffold with appropriate geometry for bone replacement [Mathieu et al., 2006, Lin et al., 2003, Ho and Hutmacher, 2006, van Lenthe et al., 2007]. Quantification analysis of μ CT data let biomaterial scientists to assess the effects of fabrication parameters on structural features. Based on μ CT data, Lin et al. found a correlation between the structural parameters of polymer-based scaffold and fabrication parameters [Lin et al., 2003].

Mechanical tests are usually destructive; finite element modeling, as an alternative to mechanical test, can be performed to simulate the mechanical analysis of structure nondestructively. Accurate information of 3D structure and architecture of scaffold can be obtained from μ CT data to perform mechanical analysis by finite element model [Jaecques et al., 2004, Sandino et al., 2007]. For example, structural and mechanical properties of three porous scaffolds made from stainless steel, hydroxyapatite and titanium were quantified based on μ CT data and finite element analysis [van Cleynenbreugel et al., 2006].

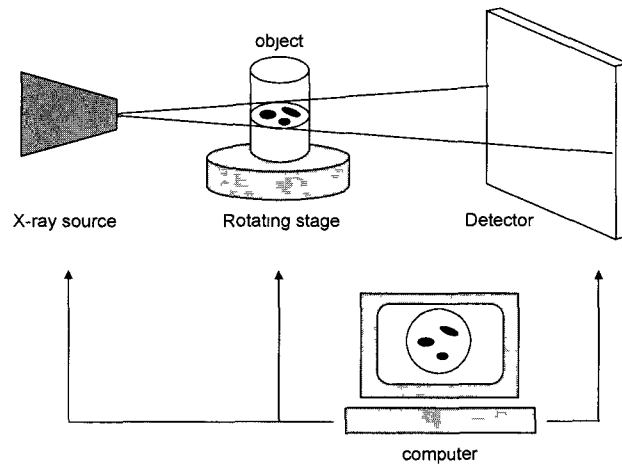


Figure 2-4 (a) Sketch of μ -Computer Tomography

During the scanning, the sample rotates over 180 or 360 degrees with a fixed rotation step. At each angular position, a transmission image will be acquired by X-ray radiation (Figure 2-4). All these radiographic images will be saved as TIFF files on the disk. The number of radiographic images is depending on the rotation step and the total rotation

degree (180 or 360 degree) which are set before acquisition. Assuming, a rotation step of 0.4 degree is selected, for a 360 degree rotation, there will be 900 images acquired. After acquisition the radiographic images, the reconstruction algorithms are applied to generate a raw data cross section which is floating point matrix (i.e. each pixel represents the attenuation value in floating point format). The next step is generating 2-D cross sectional images from raw data cross section. The cross sectional images are generated as 256 gray level images in the format of BMP or TIFF [SkyScan1172_Manuel, 2005]. Figure 2-5 shows all the steps to generate 2-D cross section images [SkyScan1172_Manuel, 2005].

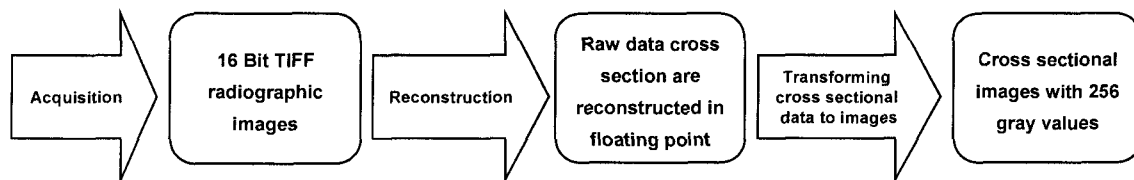


Figure 2-5 The steps to generate 2-D cross section images from radiographic images.

There are associated limitations regarding the uses of μ CT. Specifically, μ CT measures the radiopacity of all the small volumes, called voxels. So, the smaller the voxel size is, the larger the volume of data is. As a result, large amounts of data often need to be produced for adequate accuracy. Accordingly, one main difficulty of the μ CT technique consists of extracting the relevant information from large data files. Furthermore, image thresholding is a critical step that has to be performed before 3-D analysis. Image thresholding can affect the subsequent analysis and visualization. The conventional thresholding is based on gray level histogram and visual inspection [Ho and Hutmacher, 2006]. The problem arises when the resolution of the images is relatively low and when the samples composes of different materials or phases whose thresholding ranges overlap. Therefore, significant research activities have been done in the field of numerical morphology and segmentation techniques to overcome these shortages. In the following sections, some developments in the field of image analysis will be reviewed.

2.6.2.2 Thresholding

Thresholding of gray level images is a process of identifying a value in gray level as object or background [Rajagopalan et al., 2005]. In other words, during the thresholding

process, individual pixels in an image are specified as “object” pixels or as “background” pixels. Image thresholding is a crucial step that has to be performed prior to structural analysis. Accurate thresholding of gray level images is required for precise geometric analysis. Rajagopalan et al. showed that geometric parameters in terms of porosity and the number of connected component were highly sensitive to threshold value [Rajagopalan et al., 2005]. Visual inspection seems to be a preferred approach to select the threshold value [Lin et al., 2003]. However the reliability of visual thresholding is limited by several factors such as room lighting, monitor brightness, contrast setting, randomness in pore solid distribution and other factors [Rajagopalan et al., 2005]. Therefore, different methods were developed to select the appropriate threshold values. Based on the characteristics used for segmentation of images, Rajagopalan et al. classified the thresholding methods as follow [Rajagopalan et al., 2005]:

Histogram shape-based methods: In this method, the thresholding is based on the analysis of gray level histogram of images. For example, Rosenfeld and Torre selected threshold value based on the analysis of concavity points on the convex hull of the image histogram [Rosenfeld and Torre, 1983]. Accordingly, the deepest concavity points of convex hull were selected as threshold value. The iterative thresholding method of Ridler and Calvard was also based on the histogram analysis [Ridler and Calvard, 1978]. In this method, the gray level histogram was modeled by two Gaussian distributions, corresponding to object and background regions, and then an iterative method was established to find optimum threshold value.

Clustering-based methods: In this method, the gray level images are clustered into object and background. For example, the clustering thresholding method of Otsu minimizes the intra-class variance which is defined as a weighted sum of variances of the object and background, to find appropriate threshold value [Otsu, 1979].

Entropy-based methods: In this method, the optimum threshold value is selected based on the entropy of object and back ground regions. The entropy-based thresholding method of Kapur et al. selects the optimum threshold value when the sum of the object entropy and background entropy reaches the maximum level [Kapur et al., 1985].

Global and local methods: the global methods use the correlation between pixels on global scale, whereas the local methods adopt the local threshold value based on the local image characteristics. In the non-linear dynamic thresholding of White and Rohrer, the gray level value of individual pixel is compared with the average grey level values of neighboring pixels and then the pixel is assigned as object or background accordingly [White and Rohrer, 1983].

Fuzzy thresholding methods: The aforementioned thresholding techniques create binary images. In reality, due to the fuzzy nature of μ CT images, the fuzzy segmentation can improve the assessment of porous structure. Specifically, a significant improvement has been found at low resolution images [Sladoje et al., 2005]. In the fuzzy thresholding methods, the area coverage of a pixel is used to determine its belongingness to the object (i.e., its membership value). Based on these methods, the gray level values can be used directly to define the membership value of pixels. Then each pixel is assigned a value in the interval [0, 1]. The pixels which certainly belong to object, are assigned 1, the pixels which certainly belong to background, are assigned 0, and the pixels between these two region make the fuzzy border of object and are assigned a value between 0 and 1. Such segmentation is usually easier to obtain than the binary segmentation.

2.6.2.3 Distance transform (DT)

A distance transform (DT), also known as distance map or field, is a measure of the shortest distance between an object's voxel to the background. It is applied on the binary images that consist of object and non-object (background) voxels [Borgefors and Svensson, 2002]. Thus, DT is suitable for high resolution images that can be easily segmented into object and non-object voxels [Saha and Wehrli, 2004]. The distance between two adjacent voxels can be calculated exactly by using Euclidean distance function or approximately by using chessboard or city block. The DT map looks similar to the input image except that the gray level values of voxels inside the object are changed according to their distance from the background (Figure 2-6). Considering the Euclidean distance function, the distance transform of voxel p is defined as:

$$DT(p) = \min(D(q) + \|p - q\|) \quad (2.6)$$

Where p is the evaluated voxel, $DT(p)$ is the distance transform value at p , $D(q)$ is the previously determined distance of an adjacent voxel q to p (26 adjacent neighbor in 3-D and 8 adjacent neighbor in 2-D), $\|p - q\|$ is the Euclidean distance between p and q .

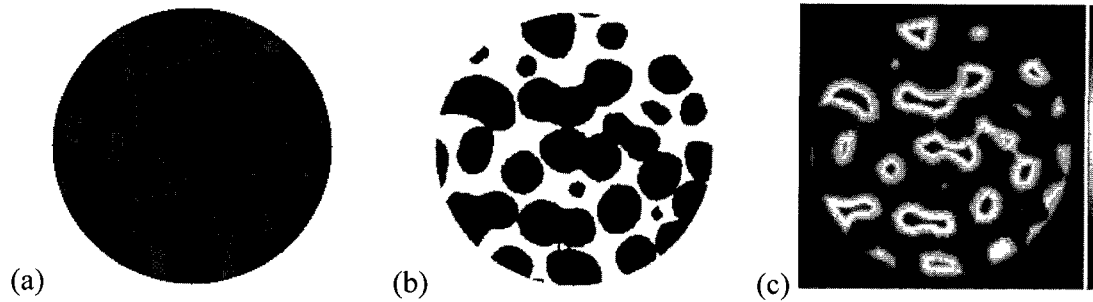


Figure 2-6 2-D representative of (a) original μ CT image, (b) binary image and (c) DT map.

2.6.2.4 Fuzzy distance transform (FDT)

In reality, μ CT images are fuzzy; therefore, the object/background segmentation (binary segmentation) can be an inaccurate way for further analysis. Recently, fuzzy technique has been developed, as an alternative to DT, to analyze gray level medical images [Saha et al., 2002, Wehrli et al., 2006]. FDT is an extended shape of DT and takes into account both distance and pixel gray levels, or membership values, to compute the shortest distance from each object's voxel to the background [Darabi et al., 2009, Saha et al., 2002]. This technique does not require any binarization step. It has been demonstrated that FDT allows more accurate geometric analysis than the traditional DT [Saha and Wehrli, 2004, Darabi et al., 2007].

The FDT calculation usually includes the fuzzification process. As considered above, the μ CT images are gray scale with 256 different levels. Therefore, a membership function is applied to match a gray level value of voxels to the real domain $[0, 1]$. An upper membership value describes a strong belonging to object and a lower membership value

describes a voxel belonging to object. [Sladoje et al., 2004]. The fuzzy set is used to compute the FDT values.

Thus, based on the fuzzy set or the object's voxel membership, the following FDT map was initially introduced by Saha et al. [Saha et al., 2002]:

$$FDT(p) = \min(Df_q + \frac{1}{2}(\mu(p) + \mu(q)) \times \|p - q\|) \quad (2.7)$$

Where p is the evaluated voxel, $FDT(p)$ is the fuzzy distance at p , Df_q is the previously determined fuzzy distance of an adjacent voxel q to p (26 adjacent neighbor in 3-D and 8 adjacent neighbor in 2-D) and $\|p - q\|$ is the Euclidean distance between p and q and $\mu(x)$ is the membership value of object's voxel x . The FDT map calculated based on Saha method is in real space.

In addition, the FDT map can be defined in an integer space [Darabi et al. 2009]:

$$FDT(p) = \min(Df_q + \max(\mu(p), \mu(q)) + \delta(p - q)) \quad (2.8)$$

The new parameter, $\delta(p-q)$ being an integer weight associated to membership values and the Euclidean distance between p and q ((1, $\sqrt{2}$) in 2-D and (1, $\sqrt{2}$, $\sqrt{3}$) in 3-D).

The second FDT equation (Eq. (2.8)) applies the 'max' determination that is fuzzy in its very nature. This procedure was introduced by Darabi et al. to improve the computational performance [Darabi et al., 2009].

In digital space, a dynamic programming-based algorithm was developed to compute the FDT map of fuzzy images [Saha et al., 2002]. Before FDT computation, the input images should be modified to avoid errors caused by even/odd number of voxels across the object thickness. This error misleads the calculation of geometric parameters. Saha et al. proposed the use of modified images to solve this problem [Saha et al., 2002]. The modification is done in two steps [Saha et al., 2002]:

Let I be the input images and I' be the modifies images,

Step1. Set $\mu_I(2i+1, 2j+1) = \mu_I(i, j)$ for all pixels of image I . These points, in I' , are called primary points.

Step2. For non primary points, if $p(i', j')$ is adjacent to non-object primary points, set $\mu_I(i', j') = 0$, otherwise set $\mu_I(i', j') =$ the mean of membership of all adjacent primary object points.

FDT computation Algorithm

1. For all background voxels, set $Df(p) = 0$;
2. For all object voxels, set $Df(p) = \infty$;
3. Push the object contour pixels to queue Q ;
4. While Q is not empty:
 - a. Remove a point p from Q ;
 - b. Find $\text{fuzzy_dist}_{\min} = \min_{q \in N(p)} (Df_q + 0.5 \times (\mu(p) + \mu(q)) \times \|p - q\|)$, or $\text{fuzzy_dist}_{\min} = \min_{q \in N(p)} (Df_q + \max(\mu(p), \mu(q)) \times \|p - q\|)$; where $N(p)$ denotes adjacent neighbors of voxel p ;
 - c. If $\text{fuzzy_dist}_{\min} < D(p)$ then:
 - d. Set $D(p) = \text{fuzzy_dist}_{\min}$;
 - e. Push all voxels $q \in N(p)$, which are object voxels and currently not in Q , into Q
2. Output the FDT of image;

To sum up, it was demonstrated that the FDT is a suitable means for image analysis and generate more accurate geometric characterization [Saha et al., 2002]. In addition, it allows the user to select a range of thresholds for fuzzy border instead of a single threshold value.

2.6.2.5 Skeletonization

The skeleton of an object plays an important role in the morphological analysis and reconstruction of the porous structure [Moon et al., 2002]. Skeleton or medial axis is a

compact shape description of an object [Zhou and Toga, 1999] and skeletonization is a process that reduces the object into a union of surfaces or curves which preserves the topology and the shape of the original object [Saha and Wehrli, 2004]. Basically, the skeleton should be connected, centered and thin [Niblack et al., 1992]. Many algorithms have been developed to extract the skeleton; the most common skeletonization algorithms are discussed below.

Thinning methods: This method repeatedly peels off the border of an object in series of images [Niblack et al., 1992]. Finally, certain points, which are end points, are left unchanged to preserve useful information about the shape of object. Thinning algorithms ensure connected skeletons (Figure 2-7) [Gagvani and Silver, 1997]. In this method the boundary of the object has to be well defined.

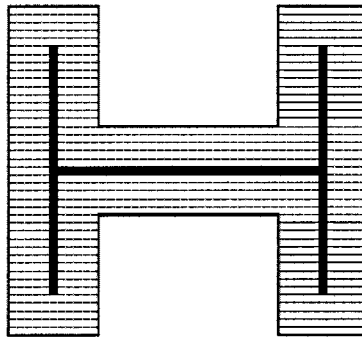


Figure 2-7 Thinning skeleton, the darkest pixels represent the skeleton of object.

Voronoi methods: In this method, a set SP of n points in the plan is given (generating points); the Voronoi polygon of a point P_i is the polygon enclosing all points in a plan that are closer to P_i than to any other point in SP . The Voronoi diagram is the collection of the Voronoi polygons of all the points in SP . This method can provide connected and centered skeleton (Figure 2-8, reproduced based on diagram presented in [Palágyi, 2008]) [Gagvani and Silver, 1997; Ogniewics and Kubler, 1995]. Voronoi method is only applied on binary images.

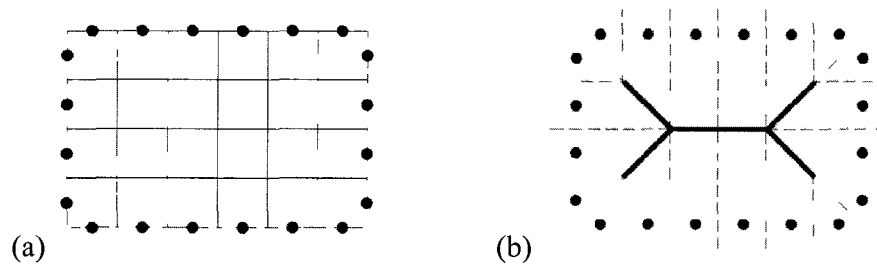


Figure 2-8 Voronoi skeleton, (a) Some border points of a rectangle form the set of generating points, (b)The Voronoi diagrams are displayed as dashed lines and the skeleton (black lines) is estimated based on the Voronoi diagrams.

Distance Transform methods (Ridge of DT map): Distance Transform skeletonization methods are sequential and noniterative methods [Niblack et al., 1992]. The skeleton is requisite to be centered with respect to object boundary, considering that the points located at the center of the object have maximal distance transform; therefore, the skeleton or medial surface/axis can be defined as the locus of the center of maximal disks (2-D) or spheres (3-D) that are set into the object (Figure 2-9)[Gagvani and Silver, 1997].

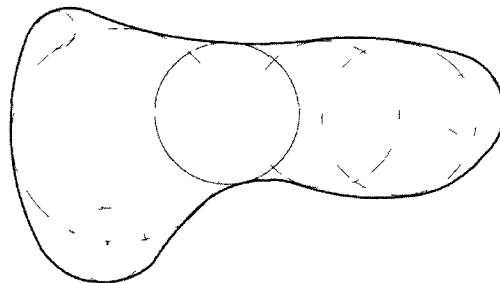


Figure 2-9 2-D representative of distance transform skeleton (dotted line), as the locus of maximal disks (2-D) or spheres (3-D) which are set into the object.

The set of extracted point does not guarantee to be connected; hence Niblack et al. introduced saddle points to get a connected skeleton of 2D images [Niblack et al., 1992]. Figure 2-10 shows a 2-D binary image and the corresponding ridge points of DT map. The ridges have been depicted as bright points, because they have higher DT value than their neighboring pixels.

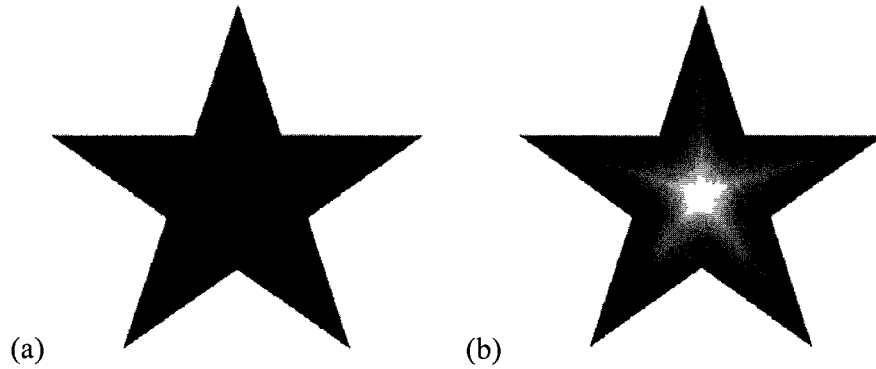


Figure 2-10 (a) The original binary image and (b) The DT map of binary image, the bright points are local maxima in DT map and considered as skeleton of object.

FDT Ridge-based methods: For the skeletonization based on FDT ridges, it is required to define ridge voxels on FDT map. The ridge voxels are the ones at which the first derivative of the FDT map is zero at least in one direction and the second derivative of the FDT map is negative in the same direction [Darabi et al., 2009]. Assuming ∇D_f and $\nabla' \cdot \nabla D_f$ are gradient and Hessian of FDT map respectively, the skeleton points based on ridge detection method are extracted by extending Haralick's idea [Haralick and Shapiro, 1992] to N dimension [López et al., 1999]; therefore, ridge points of the FDT map can be characterized as follow:

$$\nabla D_f \cdot v_i = 0 \quad \text{and} \quad \lambda_i < 0 \quad i=1,2,\dots,N \quad (2.9)$$

Where λ_i are eigenvalues and v_i are eigenvectors. This is the set of local maxima, saddle and peak points in FDT map. Since the images are represented in digital space so localization of ridge point by Eq. (2.9) is impossible, Darabi et al. presented an algorithm to detect the ridge points in FDT map [Darabi et al., 2009]. It includes two steps; in the first step, some primary ridge points are detected, then in the second step, the local maxima points detected in the first step are connected by the steepest uphill climbing path [Niblack et al., 1992 Gagvani and Silver, 1997].

The FDT method based on 'max' determination, introduced by Darabi et al. [Darabi et al., 2009], and skeletonization method based on FDT ridge detection voxels have been

used in this project because of their higher compatibility to the fuzzy nature of images and efficient computational performance.

2.6.2.6 3-D Geometric analysis of μ CT images: The Hildebrand Method

Accurate measurement of morphological parameters is of significant interest in the field of trabecular bone and bone substitutes. The imaging technologies such as μ CT provide access to 3-D structure and require more elaborate techniques for measuring morphological parameters.

Hildebrand and R uegsegger proposed a model-independent approach to calculate the mean structure thickness and thickness distribution of a 3-D object [Hildebrand and R uegsegger, 1997]. This method was initially applied to characterize trabecular bone thickness, and then widely used for characterization of scaffold pore size. The great concept introduced by Hildebrand was volume-based approach, in which they used the definition of maximal inscribed spheres to characterize geometric parameters. Accordingly, the local size of object (void or solid space) at any location was defined as the diameter of the largest spheres containing that location. Assuming that p is an arbitrary point in the structure Ω (Figure 2-11), then based on Hildebrand method [Hildebrand and R uegsegger, 1997], the local thickness at p , $\tau(p)$, is defined as follow:

$$\tau(p) = 2 \times \max(\{r \mid p \in sph(x,r) \subseteq \Omega, x \in \Omega\}) \quad (2.10)$$

Where $sph(x,r)$ is the set of points in a sphere with center x and radius r . Once the local size is defined for all points in the structure, then the average size is calculated as follow:

$$\bar{\tau} = \frac{1}{Vol(\Omega)} \iiint_{\Omega} \tau(x) d^3x \quad Vol(\Omega) = \iiint_{\Omega} d^3x \quad (2.11)$$

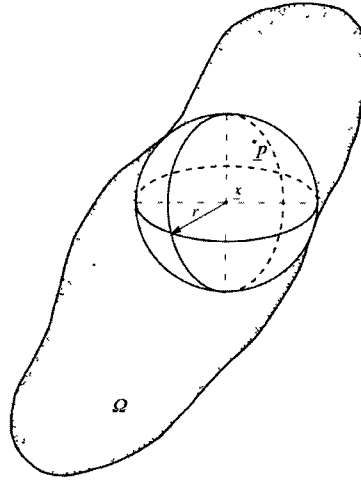


Figure 2-11 Local thickness $\tau(p)$ of a structure Ω determines by fitting maximal spheres to the structure [Hildebrand and Rügsegger, 1997].

To extend this methodology from continuous space to discrete space, Hildebrand provided a discrete implementation based on distance transform and distance ridge methods. Therefore the local size, $\tau(p)$, is defined based on distance transform, as follows:

$$\tau(p) = 2 \times \max_{q \in X(p)} (D_{map}(q)) \quad (2.12)$$

Where the D_{map} is the distance map and $X(p)$ is the set of center points of all spheres with a radius equal to their corresponding DT value and including the point p .

$$X(p) = \{x \in \Omega \mid p \in sph(x, D_{map}(x))\} \quad (2.13)$$

The implementation of this step leads to ‘massive computational overhead’ if performed directly based on $X(p)$ definition. Therefore, Hildebrand defined the distance ridge as a set of central points of all non-redundant spheres, Ω_R .

$$\Omega_R = \{s \in \Omega \mid spr(s, D_{map}(p)) \not\subset spr(x, D_{map}(x)), s \neq x, x \in \Omega\} \quad (2.14)$$

And thus redefined the set $X(p)$ as follows:

$$X(p) = \{x \in \Omega_R \mid p \in sph(x, D_{map}(x))\} \quad (2.15)$$

Hildebrand also noted that ‘the distance ridge correspond to medial axis of a structure does not represent a topological skeleton when derived from a voxel image’ [Hildebrand and Rügsegger, 1997]. In addition, the accuracy of this method depends on the resolution of images. It is well suited for high resolution images; however, in the case of low resolution images, it misleads the results in terms of local and average size of object [Saha and Wehrli, 2004].

Saha and Wehrli introduced a new method based on fuzzy segmentation and FDT map that can effectively overcomes the limitation of low resolution images, in particularly, when the voxel size is comparable to the size of object [Saha and Wehrli, 2004]. The distribution of local thickness over an object was then calculated using the FDT values along its skeleton. The skeleton of object was extracted using the thinning method described in Ref. [Saha et al., 1997] to preserve a topological skeleton. The mean size of object was then calculated as follow:

$$\bar{\tau} = \frac{\sum_{p \in skelet(\Omega)} 2 \times FDT(p)}{|skelet(\Omega)|} \quad (2.16)$$

Where $skelet(\Omega)$ is the skeleton of object and $|skelet(\Omega)|$ is the number of points in the skeleton.

It would be clearly desirable to generate the skeleton of an object directly from its fuzzy representation. This thesis will introduce skeletonization method which extracts the skeleton points based on FDT map and ridge detection algorithm. The porous bone substitutes that will be characterized in this study consist of round pores with side interconnections (Figure 2-12). Therefore, due to the shape of pores in the structure of substitutes, this study introduces a new methodology to calculate the size of pores and interconnections. Accordingly, the local maxima and saddle voxels of the FDT map are extracted as representative of pores and interconnections, respectively. These are the

critical voxels of the skeleton. Therefore, extracting only the critical voxels instead of all skeleton voxels to measure the mean pore and interconnection sizes significantly reduced the computational time without disturbing the accuracy of geometric analysis.



Figure 2-12 Typically μ CT reconstructed structure [Bohner et al., 2005]

Furthermore, due to the shape of pores, one or more maxima are found in the pores, so as illustrated in Figure 2-13, in some pores, the corresponding circles overlap each other (Figure 2-13b). This study therefore introduces volume-base and number-base averaging measures for pore size. The number-base average pore size is equal to the arithmetic average FDT value of maxima voxels (Eq. (2.16)), whereas the volume-base pore size measurement calculates the average value by considering the volume that each pore occupied in the structure.

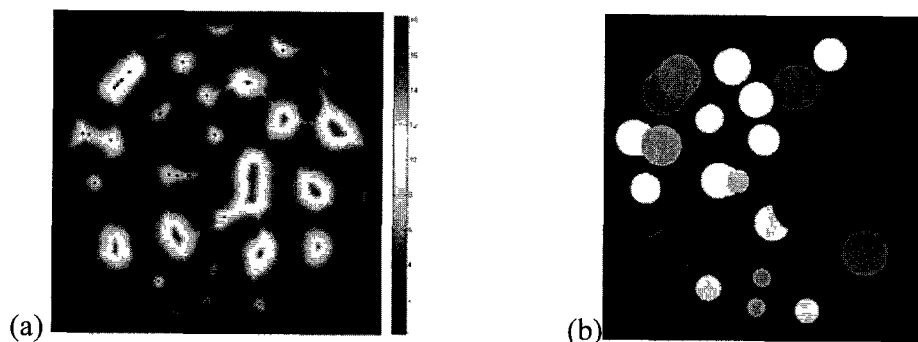


Figure 2-13 (a) 2D FDT map, local maxima as a representative of pore size are shown with dark points.(b) Corresponding circles at local maxima with radius equal to their FDT.

2.6.3 Methods to measure specific surface

Optical methods: These methods use photomicrographs of polished sections of sample. The specific surface is measured by statistical methods [Scheidegger, 1960; Dullien, 1979]. There are several statistical method; for example, in one of them, a needle with the length l falls many times on the picture, then the number of times that two ends of the needle fall inside of the pores (h) and the number of times that the needle intersect the perimeter of the pores (b) are counted, after a large number of throws the following relation is assumed:

$$4 \frac{\text{volume of pores}}{\text{surface of pores}} = \frac{lh}{b} \quad (2.17)$$

If the magnification of the picture is n and V is the volume of pores, the specific surface, S , is equal to $S = 4Vbn / lh$ [Scheidegger, 1960; Dullien, 1979].

Adsorption method: The specific surface is evaluated based on the adsorption of the vapor by the surface of the solid phase [Scheidegger, 1960; Dullien, 1979].

Fluid flow method: Specific surface can be calculated by fluid flow formula such as Kozeny and Kozeny-carman equations which relate the flow rate of fluid through porous media to their specific area [Scheidegger, 1960; Dullien, 1979].

Marching cube method: Marching cube method provides a solution to quantify the volume surface using 3D image processing tools. In digital space, the structure is divided into many cubical parts called voxels. Each voxel contains 8 vertices, and each vertex has two positions (inside or outside of the void space), thus, there are $2^8=256$ ways a surface can intersect the cube, these cases can be reduced to 15 by removing the repeated cases (Figure 2-14). Then the algorithm finds the surface edge intersection via linear interpolation and forms one to four triangles in cube. Finally, the marching cube algorithm calculates a unit normal for each triangle surface. The algorithm uses these normal vectors to produce a smooth surface that estimates the volume surface of object [Lorensen and Cline, 1987].

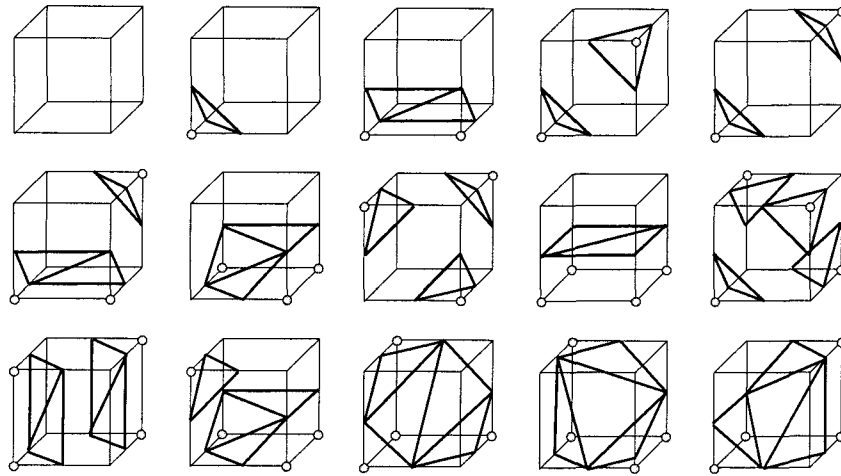


Figure 2-14 15 unique cube configurations

2.7 Fluid flow analysis and lattice Boltzmann method

2.7.1 Methods to measure permeability

The scaffold must be permeable to allow the cells and nutrients to penetrate and diffuse into its structure. There are different theoretical methods to measure the permeability of a porous media at various Reynolds number. The valid methods for laminar flow (low Reynolds number) are Darcy's law and Kozeny-Carman law.

Darcy's law: Darcy's law is the most important relation to describe the fluid transport through porous media at low Reynolds numbers. It relates the volumetric flow rate and induced pressure difference to calculate permeability of porous structure. This relation was introduced as follow:

$$\kappa = -\frac{qL\mu}{\Delta p A} \quad (2.18)$$

Where κ is the permeability, q is volumetric flow rate, L is the length of the sample, μ is dynamic viscosity, Δp is the pressure drop across the specimen and A is the cross sectional area of the samples [Karande et al., 2004; Agrawal et al., 2000, Li et al., 2003]. Darcy's law was introduced initially as an empirical relationship based on experiments on steady flow in beds of particle. Then it has been found that Eq. (2.18) is applicable for

different types of porous media [Aaltosalmi, 2005]. When the flow rate is low, the inertia effect of a flow can be neglected and the relationship between the induced pressure and the flow rate remains linear as described by Darcy's law. For a high flow rate, the nonlinear inertia effect of flow may not be neglected [Chor and Li, 2007]. Therefore, a mathematical model is required to describe both the linear and nonlinear fluid behaviors through a porous media.

Kozeny-Carman law: Kozeny law and Kozeny-Carman law relate permeability to the structural characteristics of the porous media. They have been derived analytically for capillary tube model [Scheidegger, 1960; Bear, 1972]. The Kozeny law expresses the permeability as:

$$\kappa = \frac{\varepsilon^3}{C\tau^2 S^2} \quad (2.19)$$

Where S is the pore surface area in unit volume and C is the Kozeny constant that depends on the geometry of the porous sample and τ is tortuosity. In terms of specific surface $S_0 = S/(1 - \varepsilon)$ the Eq. (2.19) can be rewrite in the form of Kozeny-Carman law as follow [Aaltosalmi, 2005, Dullien, 1979]:

$$\kappa = \frac{\varepsilon^3}{C' S_0^2 (1 - \varepsilon)^2} \quad (2.20)$$

Where ε is porosity and $C' = C\tau^2$. Carman proposed that the best value for the factor C' to fit most experimental data on packed beds is equal to 5 [Dullien, 1979]. Equations (2.18) and (2.19) can be used to predict the qualitative permeable behavior of many porous media, but the accuracy of these relations is generally not very good over an extended interval in ε [Aaltosalmi, 2005].

Theoretical methods include parameters such as pressure drop and velocity which can be measured based on experimental methods or numerical simulations. In this project, Lattice Boltzmann method (LBM) is used to simulate fluid flow in porous scaffolds. LBM is an efficient tool for investigating flow in highly complex porous structures [Bernsdorf et al., 2000]. During last decade, the LBM was developed as an alternative to

classical Navier-Stokes solvers for the numerical simulation of fluid flow [Donath, 2004].

2.7.2 Lattice Boltzmann Method

Historically, the LBM method was developed from the method of lattice gas automata [Donath, 2004; Yu et al., 2003]. The conventional ‘computational fluid dynamic’ (CFD) methods are based on discretization of macroscopic differential equations (in particular Navier-Stokes equations), whereas the LBM follows a bottom-up approach by calculating the evolution of a particle distribution function [Zeiser et al., 2004]. Conventional CFD methods compute relevant flow fields, such as velocity \mathbf{u} and pressure p , by numerically solving the Navier-Stokes equations in space \mathbf{x} and time t . However, the Boltzmann equation deals with the single particle distribution function $f(\mathbf{x}, \boldsymbol{\xi}, t)$, where $\boldsymbol{\xi}$ is the particle velocity, in phase space $(\mathbf{x}, \boldsymbol{\xi})$ and time t [Mei et al., 2000].

One popular kinetic model is the Boltzmann equation with the single relaxation time approximation. This equation is also known as Bhatnagar-Gross-Krook (BGK) [Yu et al., 2003]:

$$\partial_t f + \boldsymbol{\xi} \cdot \nabla f = -\frac{1}{\lambda} [f - f^{(0)}] \quad (2.21)$$

Where $\boldsymbol{\xi}$ is the particle velocity, $f^{(0)}$ is the equilibrium distribution function (Maxwell-Boltzmann distribution function), and λ is the relaxation time.

To solve f numerically, as a first step, Eq. (2.21) is discretized in the velocity space using a finite set of velocity vectors \mathbf{e}_i ($i=0, \dots, N$) which leads to the velocity discrete Boltzmann equation,

$$\partial_t f_i + \mathbf{e}_i \cdot \nabla f_i = -\frac{1}{\lambda} [f_i - f_i^{(eq)}] \quad (2.22)$$

Where $f_i(\mathbf{x}, t) = f(\mathbf{x}, \mathbf{e}_i, t)$ is the distribution function of the i -th velocity \mathbf{e}_i , and $f_i^{(eq)} = f^{(0)}(\mathbf{x}, \mathbf{e}_i, t)$ is the equilibrium distribution function of the i -th discrete velocity \mathbf{e}_i . $f_i^{(eq)}$ depends only on the macroscopic values of the fluid density ρ and the flow velocity \mathbf{u} .

Both can be easily obtained as the first moments of the particle distribution function [Wellein et al., 2006].

A typical set of velocities for 3D simulations is D3Q19 model. It consists of 18 different directions and the center which stands for particles with velocity zero (Figure 2-15). Compared to other common 3D models like D3Q15 and D3Q27 model, the D3Q19 model is a good compromise in terms of stability and computational effort [Mei et al., 2000].

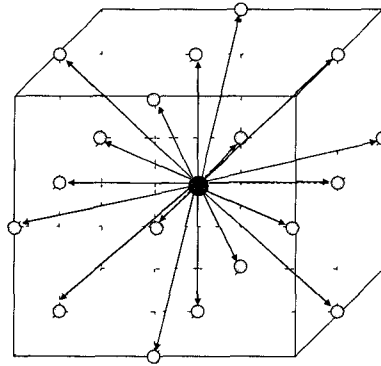


Figure 2-15 Discrete velocity set for the D3Q19 model.

For all these models, a suitable equilibrium distribution function $f_i^{(eq)}$ is:

$$f_i^{(eq)}(\rho, \mathbf{u}) = \rho w_i \left[1 + \frac{3}{c^2} \mathbf{e}_i \cdot \mathbf{u} + \frac{9}{2c^4} (\mathbf{e}_i \cdot \mathbf{u})^2 - \frac{3}{2c^2} \mathbf{u} \cdot \mathbf{u} \right] \quad (2.23)$$

Where w_i is a weighting factor for the different directions and $c = \Delta x / \Delta t$ is so-called lattice speed (Δx and Δt are the cell size and time step).

The D3Q19 model has the following set of discrete velocities:

$$e_i = \begin{cases} (0,0,0) & i = 0 \\ (\pm 1, 0, 0)c, (0, \pm 1, 0)c, (0, 0, \pm 1)c & i = 2, 4, 6, 8, 9, 14 \\ (\pm 1, \pm 1, 0)c, (0, \pm 1, \pm 1)c, (\pm 1, 0, \pm 1)c & i = 1, 3, 5, 7, 10, 11, 12, 13, 15, 16, 17, 18 \end{cases} \quad (2.24)$$

The weighing factor w_i depends on the direction:

$$w_i = \begin{cases} 1/3 & |e_i|^2 = 0 \\ 1/18 & |e_i|^2 = 1 \\ 1/36 & |e_i|^2 = 2 \end{cases} \quad (2.25)$$

To obtain the main equation of the lattice Boltzmann approach, Eq. (2.22) is discretized numerically in a very spatial manner. The discretization of space and time is accomplished by an explicit finite difference approximation and leads to:

$$f_i(\mathbf{x} + \mathbf{e}_i \Delta t, t + \Delta t) - f_i(\mathbf{x}, t) = -\frac{1}{\tau} [f_i(\mathbf{x}, t) - f_i^{eq}(\rho, \mathbf{u})] \quad (2.26)$$

Where $\tau = \lambda / \Delta t$ is the dimensionless relaxation time which determines the rate of approach to locale equilibrium and is related to kinematic viscosity (ν) of the fluid as follow:

$$\nu = (\tau - 1/2) c_s^2 \Delta t \quad (2.27)$$

Where c_s is speed of sound and defined as $c_s = c / \sqrt{3}$.

Each time step ($t \rightarrow t + \Delta t$) consists of the following steps which are repeated for all cells [Wellein et al., 2006]:

- Calculation of the local macroscopic flow quantities ρ and \mathbf{u} from the distribution functions, $\rho = \sum_{i=0}^N f_i$ and $\rho \mathbf{u} = \sum_{i=0}^N f_i \mathbf{e}_i$.
- Calculation of the equilibrium distribution from the macroscopic flow quantities and execution of the “collision” (relaxation) process, $f_i^*(\mathbf{x}, t^*) - f_i(\mathbf{x}, t) = -\frac{1}{\tau} [f_i(\mathbf{x}, t) - f_i^{eq}(\rho, \mathbf{u})]$ where the superscript * denotes the post-collision state.
- “Propagation” of the $i=0, \dots, N$ post-collision states $f_i^*(\mathbf{x}, t^*)$ to the appropriate neighboring cells according to the direction of \mathbf{e}_i , resulting in $f_i(\mathbf{x} + \mathbf{e}_i \Delta t, t + \Delta t)$, i.e. the values of the next time step.

Since the LBM is a kinetic method, macroscopic boundary conditions are not defined as direct values. They have to be replaced by appropriate microscopic rules which induce the desired macroscopic behavior. Therefore, to introduce solid walls boundary condition (i.e. a no-slip), another step called “bounce back” rule is incorporated as additional part of the propagation step [Wellein et al., 2006; Mei et al., 2000]. The bounce back step reflects distribution functions at the interface between fluid and solid cells as:

$$f_i^*(x, t) = f_{\bar{i}}(x, t) \quad \text{With } \mathbf{x} \in \text{wall} \quad (2.28)$$

Where $e_{\bar{i}} = -e_i$ and $f_{\bar{i}}(\mathbf{x}, t) = f(\mathbf{x}, e_{\bar{i}}, t) = f(\mathbf{x}, -e_i, t)$. This rule rotates the distribution functions on the wall nodes and therefore they return back to the fluid with opposite momentum in the next time step. This leads to zero velocities at the wall and ensures that there is no flux across the wall. This is corresponding to the macroscopic boundary condition [Zeiser et al., 2004; Wellein et al., 2006; Korner et al., 2005].

Finally the pressure is given by a simple equation of the state of an ideal gas:

$$P = \rho c_s^2 \quad (2.29)$$

CHAPTER 3

Geometric analysis of porous bone substitutes using micro-computed tomography and fuzzy distance transform

M. Bashoor-Zadeh¹, G. Baroud¹, M. Bohner²

(1) Laboratoire de Biomécanique, Département de Génie, Université de Sherbrooke,
Sherbrooke, QC, Canada J1K 2R1, (2) Dr Robert Mathys Foundation, Bettlach,
Switzerland

Published in *Acta Biomaterialia*, 2009, vol. 6, n° 3, p. 864-875

Corresponding author:

Gamal Baroud, Ph.D., Tenured Professor

Canada Research Chair in Skeletal Reconstruction and Biomedical Engineering

Director, Biomechanics Laboratory

Tel.: (819) 821-8000 ext. 61344

Fax: (819) 821-7163

UNIVERSITE DE SHERBROOKE

Faculté de génie - Département de génie mécanique

2500 boul. Université, Sherbrooke, QC, Canada J1K 2R1

3.1 Abstract

There is an increased interest in resorbable bone substitutes for skeletal reconstruction. Important geometric design measures of bone substitute include pore size, interconnection size, porosity, permeability and surface area of the substitute. In this study, four substitute groups with variable geometric features but with constant porosity were scanned using a micro-computed tomography (μ CT) and their geometric measures were determined using an advanced image-processing algorithm based on fuzzy distance transform and new pore size definition. The substitutes were produced using the calcium phosphate emulsion method. The geometric analysis revealed that the reproducibility of the emulsion method was high, within 5%. The average porosity of the four groups was 52.3 ± 1.5 . The pore diameter of the four bone substitute groups was measured to be 170 ± 1.7 , 217 ± 5.2 , 416 ± 19 , and 972 ± 11 μm . Despite this significant change in pore size, the interconnection size only increased slightly with an increase of pore size. The specific surface decreased with increasing pore size. The permeability increased with the pore size and was inversely proportional to the specific surface. The combination of μ CT and the fuzzy image-processing tool enables accurate geometric analysis, even if pore size and image resolution are in the same range such as in the case of the smallest pore size. Moreover, it is an exciting tool to understand the structure of the substitute with the hope of designing better bone substitutes.

Keywords: Bone substitutes, pore size, scaffold, image analysis, calcium phosphates

3.2 Introduction

Bone grafting is a surgical procedure consisting of filling a bone defect with a bone graft or substitute. The graft should favour the formation of new bone while providing an adequate surface for cell attachment [1, 2]. New bone formation strengthens the grafted area by creating bonds between existing bone and graft material.

In the research community, there is a common agreement that bone grafts should have an interconnected porous structure to allow for tissue regeneration, vascularization and cell ingrowth [3-8]. In such porous structures, pore interconnections act as pathways for cells

transport while pore space provides a location for tissue growth and formation [3, 4]. However, the optimal value of pore size and interconnection size are still open to debate. Generally, it is accepted that the interconnection size must be larger than 50-100 μm to enable blood vessel ingrowth and hence cell invasion, as well as enhanced biological response [3, 4]. Values of ideal pore diameters have been reported between 100 and 500 μm [5-7].

Due to the importance of 3-D scaffold structure on bone formation, great efforts have been made to analyse the geometry of bone substitutes [8-10]. Characterization techniques include gas pycnometry and Archimedes' method to determine the porosity, mercury intrusion porosimetry, gas adsorption, and optical microscopy to estimate the pore size, and more recently, micro-computed tomography (μCT) to quantify 3-D geometric parameters. Among these techniques, μCT is the most advanced tool in that it provides access to the 3-D architecture and hence allows for a more detailed geometric analysis [11-15]. Moreover, the use of μCT is non-invasive and non-destructive [15-16]. This technique has a discrete spatial resolution (linear resolution $>1/2000$ of the sample size, i.e. $>5 \times 5 \times 5 \mu\text{m}^3$ for a $10 \times 10 \times 10 \text{mm}$ cube), and generates very large amounts of data, particularly if the resolution is high.

Specifically, μCT measures the radiopacity of all the small volumes, called voxels, constituting a 3-D structure. So, the higher the resolution (or the smaller the voxel size), the larger the volume of data. For example, a twofold increase in the linear resolution increases the amount of data eightfold. As a result, large amount of data often need to be produced for adequate accuracy. Accordingly, one main difficulty of μCT consists of extracting the relevant information from large data files. This fact explains why significant research activities have been done in the field of numerical morphology for accurate measures and characterization. Further, it has been shown that 2-D analysis leads to overestimation of the characteristic pore sizes and thus the treatment of the 3-D data remain essential for accurate characterization [17].

Two approaches can be used to improve the 3-D analysis of the scaffolds: (i) increasing the resolution, leading to more data and higher scanning costs; and (ii) improving the

numerical segmentation/thresholding algorithm used for the analysis. In addition, readers are advised to pay attention to the definition of the pore size for adequate comparison, as several different methods were used by established authors to define pore and interconnections. Subsequently, corresponding to each definition specific algorithm was developed to calculate pore and interconnection size. Jones et al. [9, 18] used watershed method to divide the void space into individual pores then the diameter of a sphere with the same volume as an individual pore was calculated as a measure for pore size. They also defined each interconnection as the grouped voxel with the same two neighbouring pores and measured the interconnection size as the diagonal of bounding box of that interconnection. For arbitrarily shaped pores; Hildebrand and Ruesgsegger [19], referred to the volume-weighted average size. To achieve a unique average size for such irregular shapes, the local thickness (size) was weighted by volume of the pore. Otsuki et al. [10] used a different algorithm to block the narrow interconnections by dilation of material voxels. The spaces larger than the blocked interconnections were defined as pores and the spaces blocked with a certain number of dilations were defined as interconnections. Mueller et al. [20] computed the average pore size in two and three dimensions by using average distance map values. Peyrin et al. [21] developed their own implementation of a model-independent method to measure the geometric parameters of ceramic scaffolds. According to this method, the average pore size and its distribution were obtained based on the methodology introduced in Ref. [22], in which the 3-D discrete chamfer distance and skeleton of an object were used for geometric analysis. Fierz et al. [17] and Moore et al. [13] did not focus on pore and interconnection definition, but emphasized the interconnectivity of pores or accessibility of scaffold network. The accessible pore volume was estimated using a certain size of a virtual geometry shape, such as a sphere [17] or cube [13]. They defined and calculated the interconnectivity by the regions that were accessible by the virtual geometry. According to these studies, introducing exact definition for pore and interconnection is not an easy task because of the complex shape of pores in a scaffold structure.

In a recent article [8], the distance transform (DT) method introduced by Hildebrand and Ruesgsegger [19] was used for geometric analysis of bone substitutes. In this method, the pore size distribution was obtained by averaging the diameter of non-redundant maximal

spheres which were completely inside the pores [19]. The sphere diameter is defined by DT value of sphere's centre point. It should be noted that DT algorithm applies to the binary images of object and non-object voxels, which requires the segmentation of the images into object and non-object voxels before calculating the DT, which is often a demanding task for the user because of the fuzzy nature of the CT scans [23]. Saha et al. [24] proposed to use a "fuzzy distance transform" (FDT) algorithm to improve the image analysis. The added value reported by Saha et al. [24, 25] on the use of fuzzy distance transform compared to regular distance transform was that it allowed for accurate geometric analysis, even if the resolution of the images was relatively low. Unlike the DT, the new algorithm does not require a binarization of the images and the algorithm uses both distance and gray level values to calculate the shortest distance from each object voxel to the non-object. Darabi et al. [26] proposed a slightly modified FDT algorithm for the computational performance.

In a recent study, four types of β -TCP bone substitutes varying in pore size were implanted in a sheep model [27]. The goal of this study was to assess the validity of a model describing the geometrical changes sustained by a ceramic bone substitute during its cell-mediated resorption [28]. To allow the application of the model on the data, all samples were scanned by μ CT before and after implantation. During the analysis of the μ CT data it appeared that the chosen resolution ($30 \times 30 \times 30 \mu\text{m}^3$) was inadequate to analyse the structure of the scaffolds presenting the smallest mean pore size ($170 \mu\text{m}$). Moreover, the interconnection size was not determined. As the geometric analysis of these blocks is particularly relevant to interpret their biological performance [27], the present work continues the earlier research effort of Böhner et al. [8] by introducing a fuzzy technique for the distance transform method combined with a novel algorithm to analyse the μ CT data which is based on geometrical concepts of 3-D elements. This new approach was expected to allow the analysis of scaffolds with small pores (relative to the μ CT resolution), as well as quantification of the size and distribution of interconnections. Furthermore due to the characteristic properties of the pore, we introduce volume-based and number-based averaging measures for pore size.

To summarize, this study aims at using the advanced image processing algorithms for the analysis of pore size, interconnection size, specific surface area and permeability. Specifically, pore size is defined by the diameter of the maximum sphere that can be completely inscribed in a pore, the interconnection size denotes the bottleneck diameter of interconnections and the surface is defined as the interface surface between the pores and the substitute material. A detailed mathematical definition is given in the next section.

3.3 Material and Method

3.3.1 Scaffold production and preparation

Four groups of porous β -tricalcium phosphate (β -TCP) substitutes of varying pore size but constant porosity were fabricated using calcium phosphate emulsions method [8, 29]. The production method has been described extensively in Ref. [27]. Briefly, a calcium phosphate cement paste was mixed with an oil and an emulsifier, so that small oil droplets were dispersed in the calcium phosphate cement paste. The resultant paste was then poured into a mould and, after hardening; the samples were cleaned, dried and sintered at 1250 °C. The samples were then machined to produce cylinders (diameter = 8mm; height = 13mm). Finally, these cylinders were rinsed in an ultrasonic bath using ethanol to remove small wear particles, and were calcified at 900°C. In this manufacturing method, varying emulsifier concentration led to different pore sizes while maintaining the volume fraction. More specifically, higher emulsifier concentration resulted in smaller pore size [29]. Six specimens were randomly taken from each of the four size groups and their geometric parameters were analysed using FDT tools.

3.3.2 Micro-computed tomography

The μ CT images of the 24 specimens were acquired on a Scanco Medical AG μ CT 40 (Bassersdorf, Switzerland) scanner at 30 μ m isotropic resolution [8]. Further, the images of a cylindrical core (diameter = 7mm; height = 10.5mm) of the samples were selected as volume of interest and the geometric parameters were calculated using the algorithms described in the next sections.

3.3.3 Geometric analysis

The main steps in geometric analysis algorithm are as follow:

- (1) FDT computation;
- (2) analysis of pore size and interconnection size;
- (3) skeletonization and reconstruction.

For geometric analysis, the scanned images were fuzzified and FDT map is determined for each voxel of the pore space. The geometric measures (e.g. pore and interconnection size) are defined by applying the max-min detection algorithm to distance map. Specifically, the average pore size and interconnection size corresponds to the local maxima and saddle point of the FDT map, respectively. In a subsequent separate step, the skeleton of the pore space is determined and then used to reconstruct the 3-D structure of the substitute. In the following sections, each step is discussed.

3.3.4 Fuzzy Distance Transform computation

To compute FDT values, as a first step, the images are fuzzified by a sigmoidal function (Figure 3-1) which is characterized as follow:

$$\mu(p) = \begin{cases} 1 & \rightarrow f(p) \leq TH_C \\ 1 - 2(f(p) - TH_C)^2 / (TH_M - TH_C)^2 & \rightarrow TH_C \leq f(p) \leq (TH_C + TH_M) / 2 \\ 2(f(p) - TH_M)^2 / (TH_M - TH_C)^2 & \rightarrow (TH_C + TH_M) / 2 \leq f(p) \leq TH_M \\ 0 & \rightarrow TH_M \leq f(p) \end{cases} \quad (3.1)$$

Where $f(p)$ is the intensity of voxel p , TH_M and TH_C are the material and cavity thresholds, respectively, and $\mu(p)$ is defined as the membership value of voxel p , which is a measure of the grey value of said voxel. In this study thresholding ranges for each group of scaffolds are selected via histogramics (histogram of images) and visual estimation.

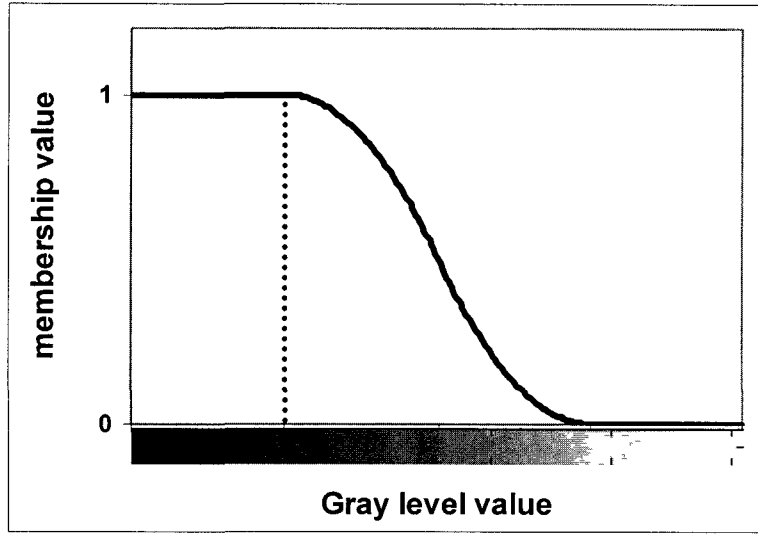


Figure 3-1 Sigmoidal fuzzy membership function

Thus by applying membership function, the fuzzy set S of any set X can be expressed as

$$\{(x, \mu(x)) \mid x \in X, \mu: X \rightarrow [0,1]\} \quad (3.2)$$

The fuzzy set or the object's voxel membership is used to compute the FDT values. For this purpose, it is assumed that the path P from object voxel p to non-object voxel q is a sequence $\langle p = p_1, p_2, \dots, p_n = q \rangle$ of voxels in which all consecutive voxels are adjacent.

The length of the path is defined as follow:

$$L_P = \sum_{i=1}^{n-1} \max(\mu(p_i) + \mu(p_{i+1})) + \delta(p_i, p_{i+1}) \quad (3.3)$$

Where $\delta(p_i, p_{i+1})$ is an integer weight associated with membership values and the Euclidean distance between p_i and p_{i+1} ($(1, \sqrt{2})$ for two dimensions and $(1, \sqrt{2}, \sqrt{3})$ for three dimensions) [26]. This leads to a number of paths between voxel p and q . The FDT value at a voxel p is defined as the shortest fuzzy distance between p and the background (i.e., a set of voxels with zero membership value):

$$FDT(p) = \min_{P \in \text{paths}(p,q)} L_P \quad (3.4)$$

Once the FDT of each voxel has been calculated, an integer number is assigned to each voxel. Using post-processing tools, a colour map, often referred to as a distance map or, in this case, a fuzzy distance map becomes available. Once the FDT map is determined, the next focus point will be characterization of pore size and interconnection size.

3.3.5 Analysis of pore size and interconnection size

Pore size and interconnection size are computed by the so-called max-min detection algorithm, which finds the local maxima and saddle voxels of the FDT map. More specifically, maxima and saddles are particular voxels of the so-called “skeleton”. The voxels are maxima with respect to the FDT value among their neighbours in all direction (maxima voxels) or are at least maximum in one direction and minimum in other directions (saddle voxels). The FDT value at a local maximum corresponds to the radius of the largest spherical sphere that can be placed in that location without impinging on the neighbouring solid structure. In other words, a maximum value of the FDT skeleton is by definition the radius of a pore. Additional conditions, called exclusion criteria, are applied to eliminate the effect of truncated pores at the sample boundaries. Based on these criteria, maxima voxels located in the outer layer of all boundaries with thickness equal to average pore size are examined and then the maxima voxels with an FDT value less than average FDT are excluded. Similarly, the FDT value at a saddle voxel corresponds to the radius of the largest spherical sphere that can be placed at this voxel without impinging on the neighbouring solid structure, i.e. to the interconnections radius. The average pore size is obtained using two definitions: arithmetic average value (number-base) and volume-weighted average value (volume-base). The number-base average pore size is equal to the arithmetic average FDT value of maxima voxels. The volume-base average pore size is computed using the following equation:

$$PS_{vb} = \frac{2 \sum_{p \in \text{Maxima}} \omega(p) FDT(p)}{\sum \omega(p)} \quad (3.5)$$

Where PS_{vb} is volume-base average pore size and $\omega(p)$ is volume of the sphere at voxel p . The average interconnection size is obtained by calculating the average FDT value of saddle voxels.

3.3.6 Skeletonization and Reconstruction

Skeletonization describes the process during which the central voxels of an object (cavity in our study) are extracted. Here, skeletonization was achieved using the so-called ridge detection method which is mainly based on the method and definitions described in Refs. [30, 31]. The ridge peak is found when the first directional derivative is equal to zero and the second derivative has a negative value in the same direction [31]. Analytically, by assuming ∇D_f and $\nabla' \cdot \nabla D_f$ to be the gradient and Hessian of FDT map, respectively, the 3-D skeleton can be extracted as ridge voxels by extending Haralick and Shapiro's idea [31] to N dimension [32].

$$\nabla D_f \cdot v_i = 0 \text{ and } \lambda_i < 0 \quad i=1,2,\dots,N \text{ (} N=3 \text{ for 3-D space)} \quad (3.6)$$

Where λ_i are eigenvalues and v_i are eigenvectors of FDT Hessian matrix. In practice, a dynamic programming-based algorithm was developed to extract ridge voxels on the basis of ridge definition [26]. Details of the algorithm are presented in the following.

Consider 26 adjacent neighbours of any voxel p . The directions are defined as direct paths which link three voxels and connect two neighbours of p by assuming p is the middle voxel of the path [26].

The algorithm for extracting the skeleton of object is summarized as follows:

- (1) compute the FDT of the object;
- (2) push object's voxels into Q (i.e. the voxels with non-zero FDT value);
- (3) repeat steps 4-8 while Q is not empty:
- (4) remove a point p from Q;
- (5) if $FDT(p)$ is maximum in all directions, then p is labelled as a peak;

- (6) if $FDT(p)$ is maximum in one direction and minimum in perpendicular direction then p is labelled as a saddle;
- (7) if $FDT(p)$ is maximum in at least one direction and equal in one or more direction then p is labelled as a flat ridge;
- (8) if $FDT(p)$ is maximum in at least one direction and is not equal in any direction, then p is labelled as a non-flat ridge;
- (9) mark the obtained local maxima voxels (peak, saddle, flat and non-flat ridge) as skeleton voxels;
- (10) output the skeleton of object;

After extracting the skeleton of object, binary images were reconstructed by a union of spheres centred at each skeleton voxel with radius equal to FDT value of that voxel [33]. The skeleton is then used for the reconstruction of scaffolds. Once done, the specific surface can be determined.

3.3.7 Computing specific surface by marching cube algorithm

The reconstructed images were then used as input for the CT-Analyser software (Version 1.5.0.0, SKYSCAN, Belgium). This software computes the surface area of the porous bone substitutes by applying the so-called marching cube algorithm. In this algorithm the interface surface between the cavities and solid phase (volume surface) is covered with triangles. Consequently, the algorithm smoothens the surface and enables an estimation of the volume surface [34].

3.4 Results

Six samples of each of the four scaffold groups were analyzed (Table 3-1). The reconstructed structures of bone substitutes indicate that pore size varied substantially among substitutes as a result of changing the emulsifier concentration (Figure 3-2).

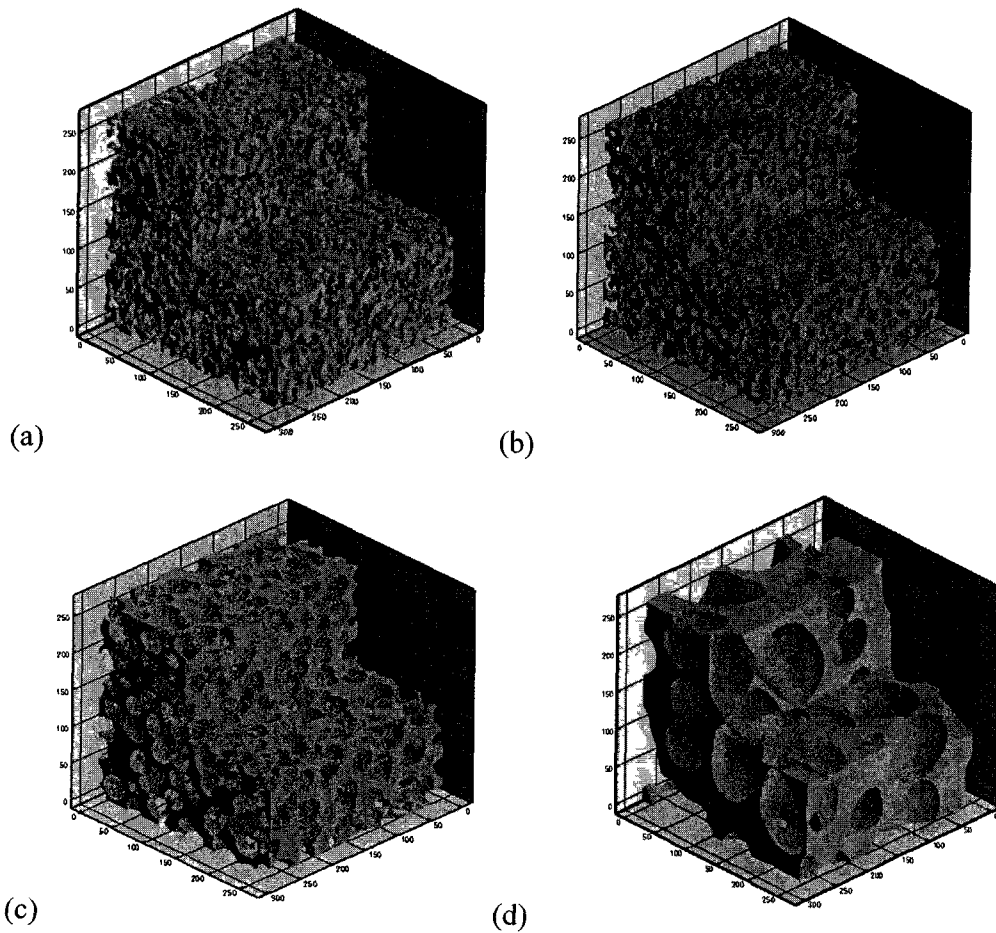


Figure 3-2 Four 3-D reconstructed structure of bone substitutes produced by different emulsifier concentrations. These structures were extracted from the middle of the samples.

The porosity of bone substitutes remains in the range of 48-55% (Table 3-1), which proves the primary hypothesis of fabricating the scaffolds with constant porosity that provides reproducible scaffolds. Specific details on the variability are given in Table 3-1.

Figure 3-3 shows examples of the thresholded images in 2-D and the threshold values used for each bone substitutes. The two threshold values, Th_C and Th_M , were slightly changed between the substitutes, mainly because of the different histograms of each bone substitute group.

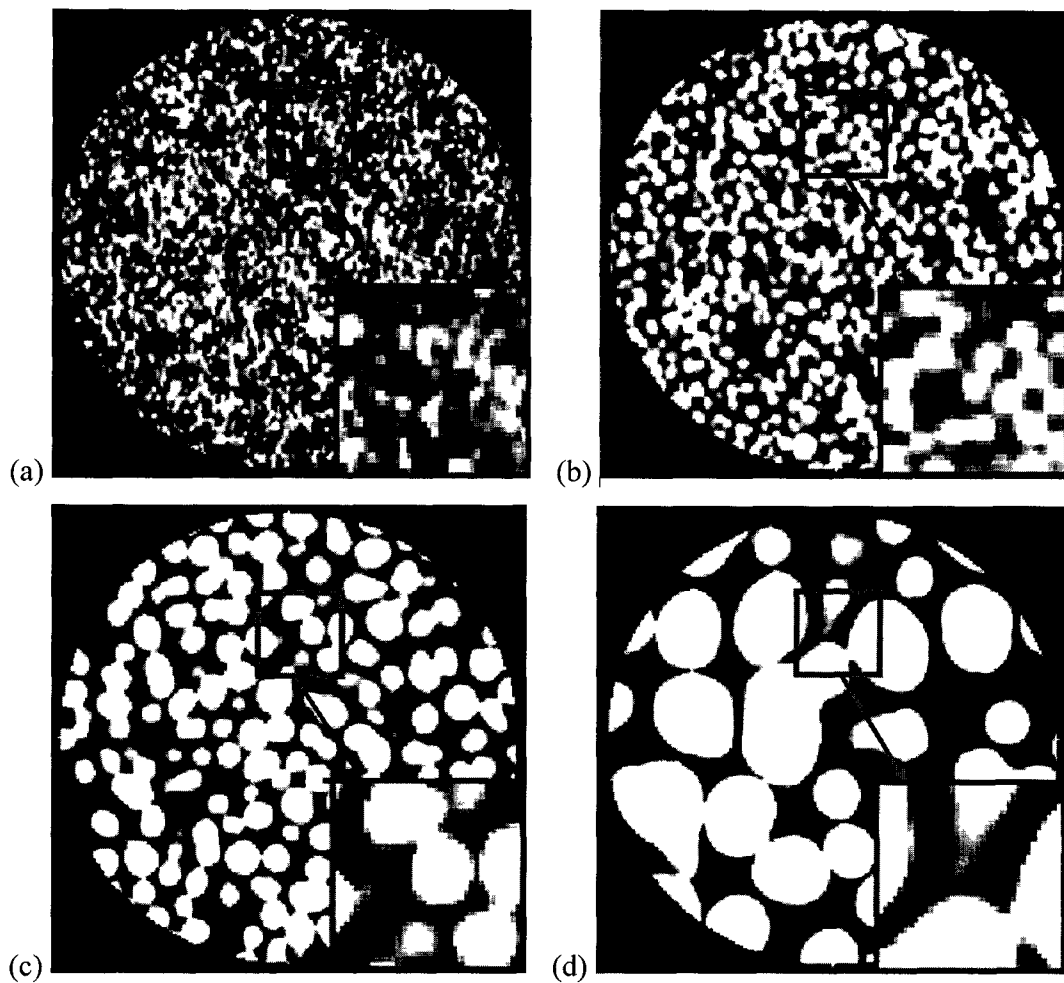


Figure 3-3 2-D fuzzified images selected from first specimen of each group, the threshold values, Th_C and Th_M , are (a) sample A, $Th_C=35$ and $Th_M=50$, (b) sample B, $Th_C=30$ and $Th_M=55$, (c) sample C, $Th_C=30$ and $Th_M=55$ and (d) sample D, $Th_C=30$ and $Th_M=50$.

FDT map of scaffolds are depicted in Figure 3-4. In FDT maps, the colour at one voxel of the pore reveal the shortest distance from this given voxel (in the pore or object) to the pore walls (material or non-object) in voxel units. As the scaffold pore size varies from group A to group D, the maximum FDT value changes for each type of scaffold. The colour scale was adapted accordingly, with the goal of having maximum FDT values in red for all scaffolds. The FDT range is changing from 2-7 voxels for sample A to 2-8 voxels for sample B, 2-14 voxels for sample C and 2-33 voxels for sample D (Figure 3-4). The voxel size was $30 \times 30 \times 30 \mu\text{m}$.

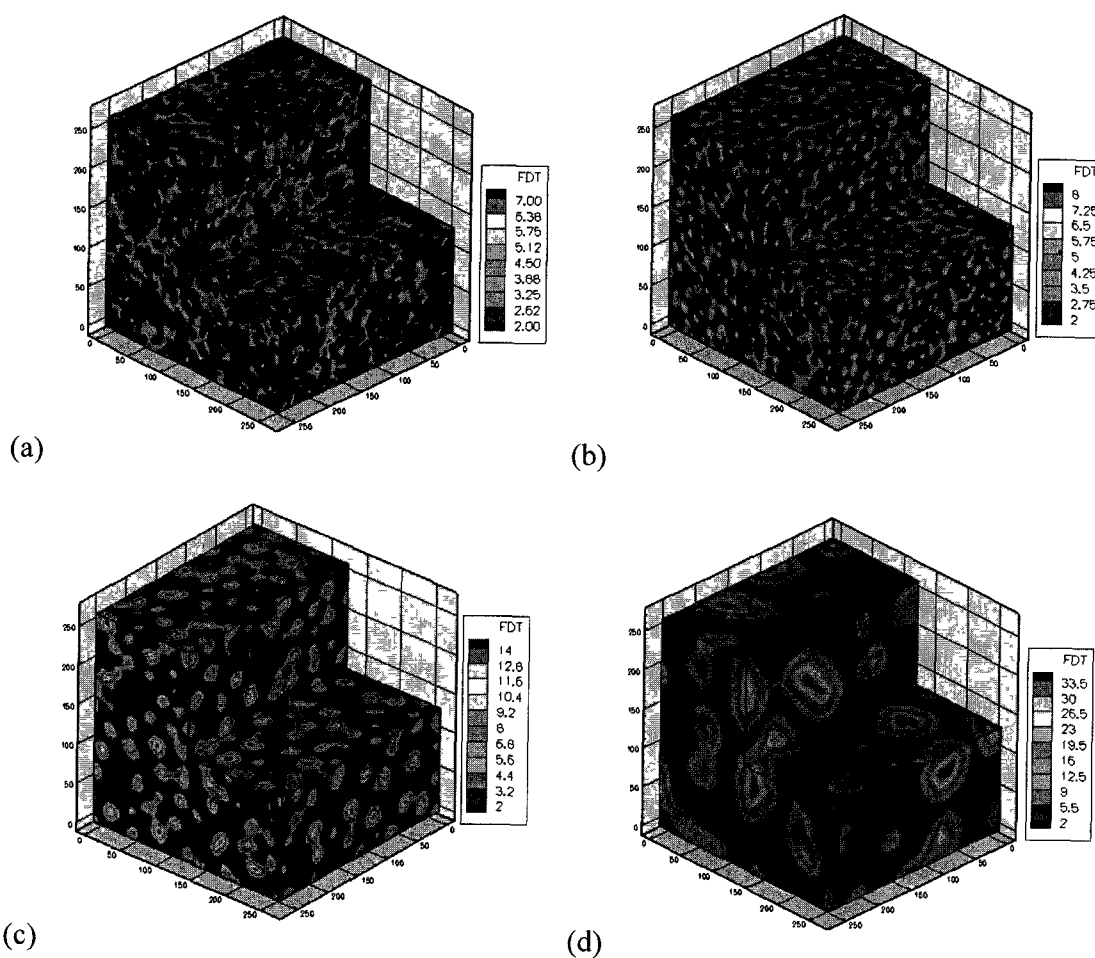


Figure 3-4 FDT maps of (a) Sample A, (b) Sample B, (c) Sample C and (d) Sample D. The FDT values are in voxel unit.

The results of pore size distribution of the four groups based on their frequency are shown in Figure 3-5. For the two smallest pore sizes, groups A and B, the distribution of pore size was narrow, with average diameters of 128 ± 3 and 195 ± 3 μm , respectively. For the two largest pore sizes, group C and D, the pore size distribution was wider, with average diameters of 364 ± 5 and 871 ± 7 μm , respectively. The small ratio between the standard deviation of the pore size and the average pore size shows how small the variation between the samples of each group was (variability < 2.5%).

Figure 3-6 shows the pore size distributions after applying exclusion criteria. The sensitivity of the average pore size and pore size distribution to truncated pores at the boundaries change among the samples. For a constant sample size, due to the number of pores, samples with large pore sizes are more affected by truncated pores than those with small pore sizes. The pore size distributions of samples A and B do not change significantly by excluding the truncated pores. The pore size distributions of samples C and D in Figure 3-6 show that, most of truncated pores are less than 300 μm in size, while most of those in sample D are less than 500 μm .

Figure 3-7 shows the pore size distribution of all samples based on their volume-weighted values. The volume-based distribution of pore size for samples C and D show almost normal distribution. The average volume-based pore size for each sample is listed in Table 3-1. Average volume-based pore size increased from 128 to 170 μm for sample A, 195 to 217 μm for sample B, 364 to 416 μm for sample C and 871 to 972 μm for sample D.

The interconnection size distributions of the bone substitutes are depicted in Figure 3-8. Similar to the pore size distribution, the interconnection size distribution hardly varied within each size group. The average size of interconnections of samples A, B and C were in the range of 61-65 μm but this value increased to 85 μm for sample D (Table 3-1). The interconnection size variability seems to increase with larger pores, reaching up to 8.8%.

The resulting surface density, defined by the surface area divided by the total volume, decreased from $11.5 \pm 0.2 \text{ mm}^{-1}$ for samples A to $3.3 \pm 0.1 \text{ mm}^{-1}$ for samples D (Table 3-1).

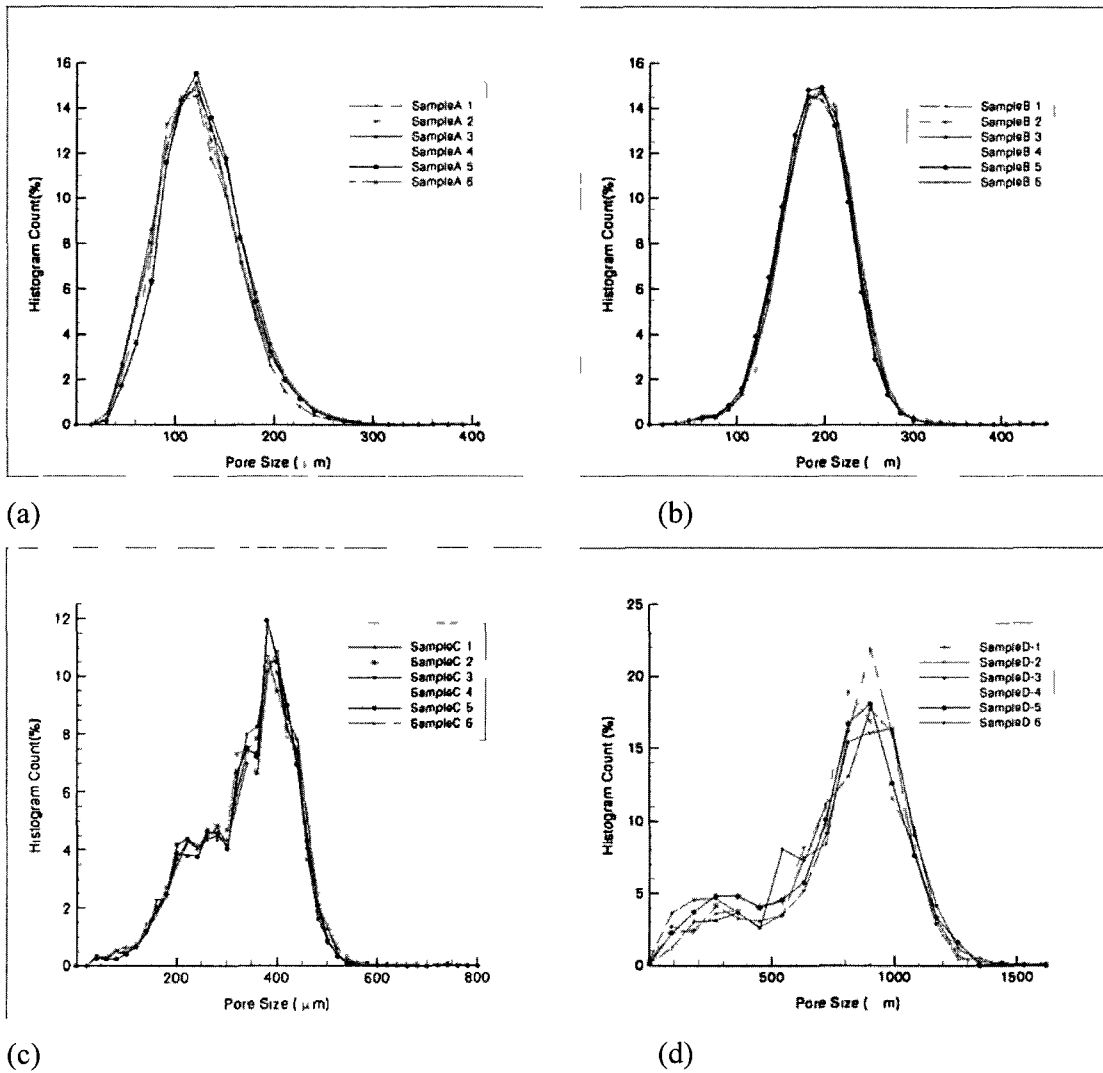


Figure 3-5 Number-based pore size distribution of bone substitute structures (before applying exclusion conditions) derived from max-min operation and FDT values, (a) Group A; (b) Group B; (c) Group C; (d) Group D.

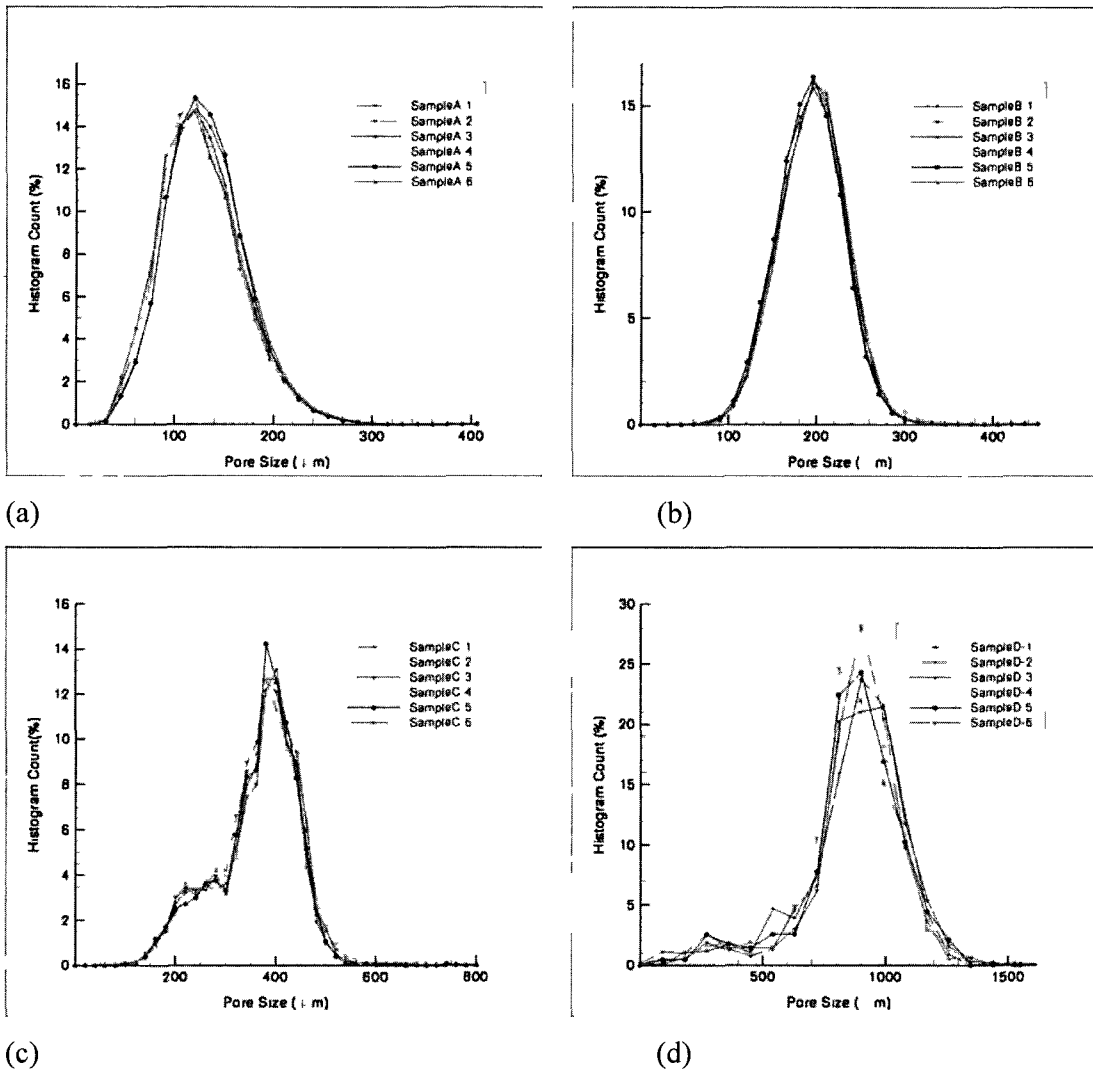


Figure 3-6 Number-based pore size distribution of bone substitute structures after applying exclusion criteria, (a) Group A; (b) Group B; (c) Group C, (d) Group D.

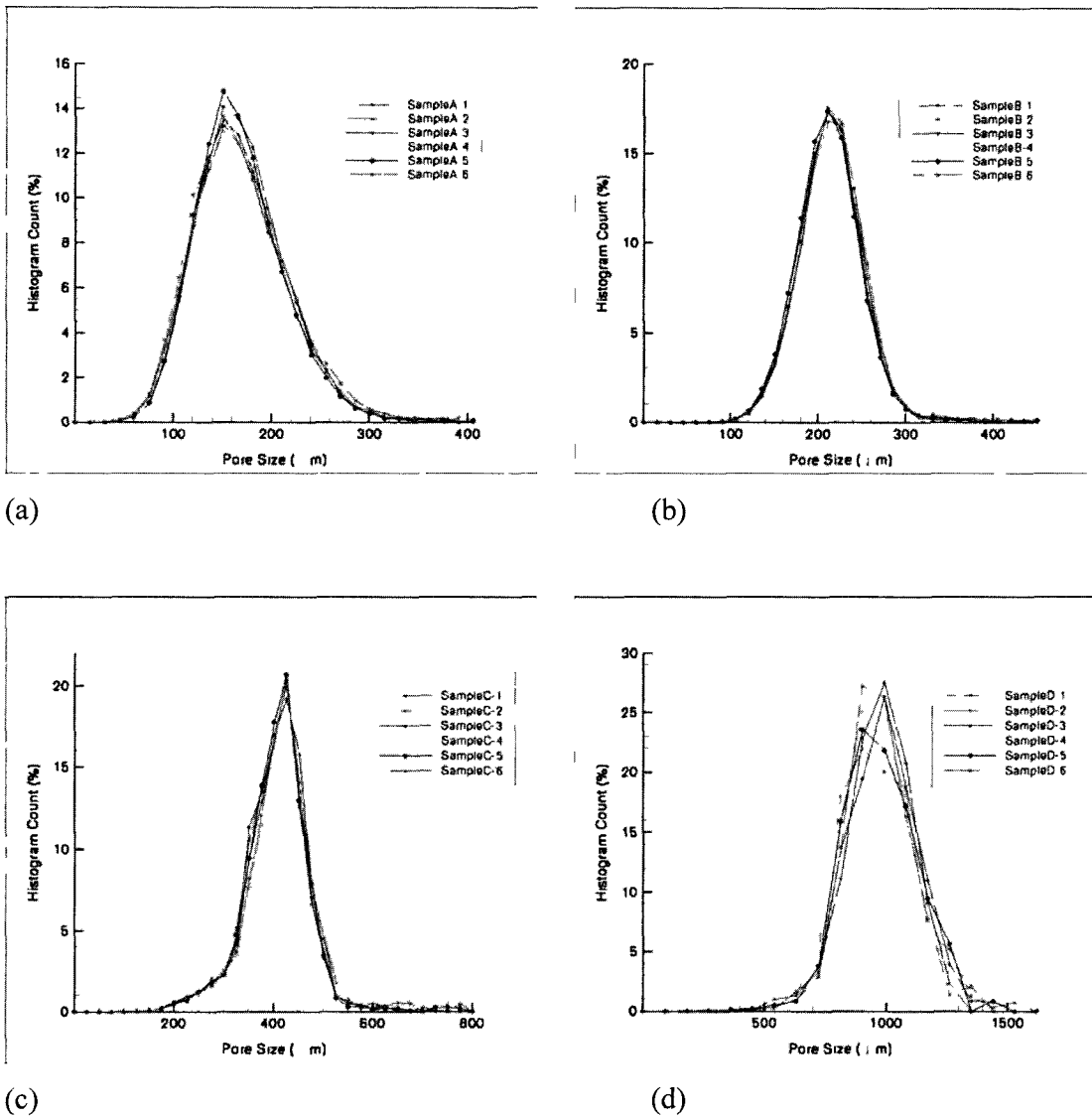


Figure 3-7 Volume-based pore size distribution of bone substitute structures, (a) Group A; (b) Group B; (c) Group C; (d) Group D.

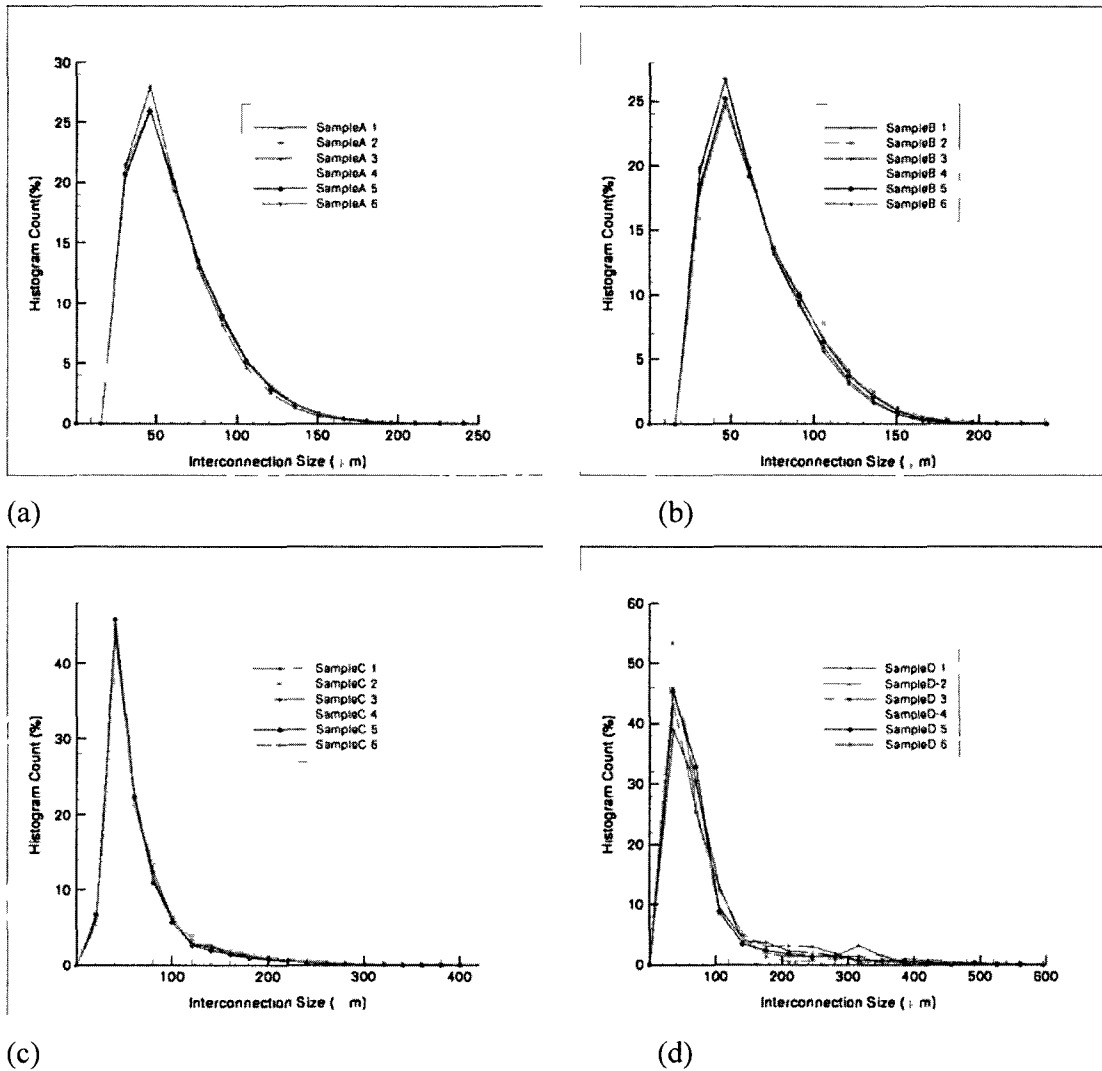


Figure 3-8 Interconnection size distribution of bone substitute structures derived from max-min operation and FDT values, (a) Group A; (b) Group B; (c) Group C; (d) Group D.

Table 3-1 Geometrical properties of bone substitutes obtained from introduced image processing tools.

Sample	Speciment	average pore size (μm)	SD pore size	average pore size (μm) volume base	average Interconnection size (μm)	SD Interconn- ection size	Porosity (%)	Solid Phase surface/volume ratio (BS/BV) 1/mm	surface density (BS/TV) 1/mm
Sample A	SampleA-1	128	42	171	61	28	50	23	12
	SampleA-2	124	42	168	61	28	48	21	11
	SampleA-3	131	41	169	62	28	52	24	12
	SampleA-4	129	43	172	62	29	51	23	12
	SampleA-5	131	40	170	62	28	52	24	11
	SampleA-6	126	43	172	62	28	48	21	11
average		128.1		170.3	61.7		50.2	22.6	11.5
SD		2.6		1.7	0.5		1.6	1.2	0.2
variability		2.1		1.0	0.9		3.2	5.2	1.5
Sample B	SampleB-1	193	38	219	62	28	52	21	10
	SampleB-2	195	38	217	66	30	54	22	10
	SampleB-3	191	38	213	62	27	51	21	10
	SampleB-4	204	39	227	70	33	55	21	9
	SampleB-5	191	37	213	64	29	52	21	10
	SampleB-6	195	37	215	65	29	53	22	10
average		194.8		217.3	64.9		52.7	21.4	10.0
SD		4.8		5.2	2.9		1.3	0.2	0.3
variability		2.5		2.4	4.4		2.5	1.1	2.8
Sample C	SampleC-1	364	81	408	65	40	54	14	7
	SampleC-2	357	81	402	66	41	53	14	6
	SampleC-3	360	81	406	64	37	53	14	7
	SampleC-4	372	94	452	72	45	55	14	6
	SampleC-5	363	80	406	62	37	54	15	7
	SampleC-6	367	85	420	64	39	54	15	7
average		363.7		415.8	65.5		53.7	14.3	6.5
SD		5.1		18.8	3.4		0.7	0.3	0.2
variability		1.4		4.5	5.1		1.2	2.1	2.6
Sample D	SampleD-1	875	198	972	93	84	52	7	3
	SampleD-2	860	199	967	79	87	53	7	3
	SampleD-3	876	225	993	87	95	53	7	3
	SampleD-4	871	190	965	76	84	52	7	3
	SampleD-5	867	205	973	81	81	53	7	3
	SampleD-6	877	185	963	94	98	53	7	3
average		871.1		972.3	85.2		52.4	7.1	3.3
SD		6.7		10.9	7.6		0.6	0.1	0.1
variability		0.8		1.1	8.9		1.1	1.6	2.5

3.5 Discussion

The objective of this paper was to use the fuzzy image processing tools to analyse the pore structure of porous bone substitute, in addition, an algorithm was developed to calculate the average substitute interconnection size and distribution. The results obtained from the algorithm were first used to examine the reproducibility of the substitute fabrication.

Specifically, the emulsion method used allowed a large degree of design control, which is of interest to biomaterial scientists. For example, among the substitutes characterized in this paper, which all had a porosity of approximately 52%, the pore size varied by a factor of 7, interconnection size by a factor of 1.4 and specific surface by a factor of 4. This method could thus be a useful approach with which to investigate the interaction between the biological response to implantation and geometric features of the substitute.

As shown in Table 3-1, the small standard deviations showed little variation between the samples of each group. The variability (percentage ratio of the standard deviation to the mean value) in the geometric parameters of specimens within the groups was lower than 5.5% except for interconnection size of group D, which increased up to 8.9%. These small values and deviations between pore size and interconnection size distribution of specimens in each group (Figure 3-5 to Figure 3-8) are evidence of the reproducibility of fabrication method.

The algorithm increases the usefulness of μ CT to biomaterial scientists. By using μ CT, biomaterial scientists are now in position to acquire geometric parameters with good accuracy. The recent publication by van Lenthe et al. [15] describes this approach extensively. Our novel contribution in this field is the introduction of the FDT method, which enhances the accuracy of results due to the fuzzy nature of μ CT [24, 35]. Moreover, different approaches have been used to determine the pore size distribution and these different approaches and the corresponding results are discussed herein. Particular attention is also paid to the link between the threshold values and the results.

The main added value is the new thresholding technique, which provides a method to recognize the fuzzy border of objects by allowing for more accurate segmentation. FDT does this specifically by using, instead a single threshold for segmentation, as in DT, a lower and an upper threshold value for the fuzzy zone. Intelligent methods can then be used to segment this zone and calculate an FDT map. For small pore size samples where the pore size is in the same size range as the voxel size, selecting single threshold value based on grey value histogram to distinguish between an object (pore space) and a non-object (material) is particularly difficult, whereas selecting two threshold values enables a fuzzy interval to be shown between the object and non-object. The new FDT algorithm then calculates the shortest distance from each object voxel to non-object by considering the fuzzy interval or fuzzified values. Group A, which is the group with the smallest pore size, was sensitive to the threshold values. For example, reducing the lower threshold value of group A, Th_C , to a grey value of 30 led to a reduction in the average porosity of group A from $52 \pm 2\%$ to $40 \pm 1\%$ and of the pore size from 125 ± 3 to $108 \pm 1.9 \mu\text{m}$. Further, we applied to two samples of the small-size substitute groups A and B a well-established subvoxelization technique designed for accurate measurement of the limited-resolution trabecular bone images [36]. The principal strategy consists of subdividing voxels and assigning voxel intensities to each subvoxel on the basis of local neighbourhood criteria and strict mass conservation. Accordingly, the changes in porosity in both groups after subvoxelization are less than 5% (Table 3-2). However, the local measures of pore and interconnection size are reduced more substantially (Table 3-2). The reason for this reduction is that subvoxelization makes smaller pores and interconnections visible [36].

In addition to the introduction of fuzzy mapping of the pores, we applied a new algorithm, the so called max-min operator, which can identify individual pores and their interconnections; this is a new method to recognize pores and interconnections. Also it should be noted that by using the advance image-processing tools the results are reasonable for small pore sizes.

Table 3-2 Geometric properties before and after subvoxelization process.

Group	Sample Name	Before subvoxelization process			After subvoxelization process		
		Average maximum pore size (μm)	Average interconnection size (μm)	Porosity (%)	Average maximum pore size (μm)	Average interconnection size (μm)	Porosity (%)
A	Sample A-1	127.74 \pm 42.01	61.49 \pm 27.91	50.37	110.96 \pm 36.09	50.52 \pm 30.43	52.49
	Sample A-3	131.43 \pm 41.05	62.19 \pm 28.11	51.62	113.93 \pm 35.43	51.39 \pm 30.70	53.60
B	Sample B-1	193.29 \pm 38.20	62.38 \pm 27.56	51.93	170.62 \pm 43.23	51.39 \pm 32.01	52.84
	Sample B-2	195.32 \pm 37.71	65.86 \pm 30.10	53.54	172.31 \pm 42.06	55.12 \pm 34.37	54.33

Truncated pores at sample boundaries can affect the distribution and average pore size [37]. This effect is significantly increased when the volume of sample is limited in comparison with the pore size. In other words, by increasing the ratio of average pore size to sample size, the error resulting from the truncated pores raised. comparison of the average pore size before and after exclusion shows the different of 13%, 7%, 3% and 2% for average pore size of samples D, C, B and A respectively. As expected for the same sample size, the truncation effect is considerably increased for samples D and C and needs to be corrected. The exclusion criteria that are a part of our image processing algorithm make this correction to produce a reliable estimate of the average pore size.

Beside the geometric analysis, image processing tools allow the determination of the transport properties of the substitute which are often quoted to be very important for tissue engineering [8]; more details of this are provided in Ref. [38]. Specifically, the transport properties of our substitutes were calculated using the Lattice-Boltzmann simulation, the results of which are shown in Table 3-3. Figure 3-9 shows the velocity map resulting from fluid transport simulation. The stream lines which indicate the direction of flow through the structure are also shown in the same figure. Extracting the stream lines help us to estimate the tortuosity of a structure and thereby understand how much easily the fluid (nutrient and blood cells) can pass through the bone substitute.

Table 3-3 Summary of average, standard deviation and variation of permeability values of samples in each group

Permeability *10 ⁻¹⁰ (m ²)	Sample A	Sample B	Sample C	Sample D
Average	1.14	2.20	3.67	4.07
Standard deviation	0.19	0.39	0.44	0.75
Variation (%)	17.10	17.85	12.04	18.38

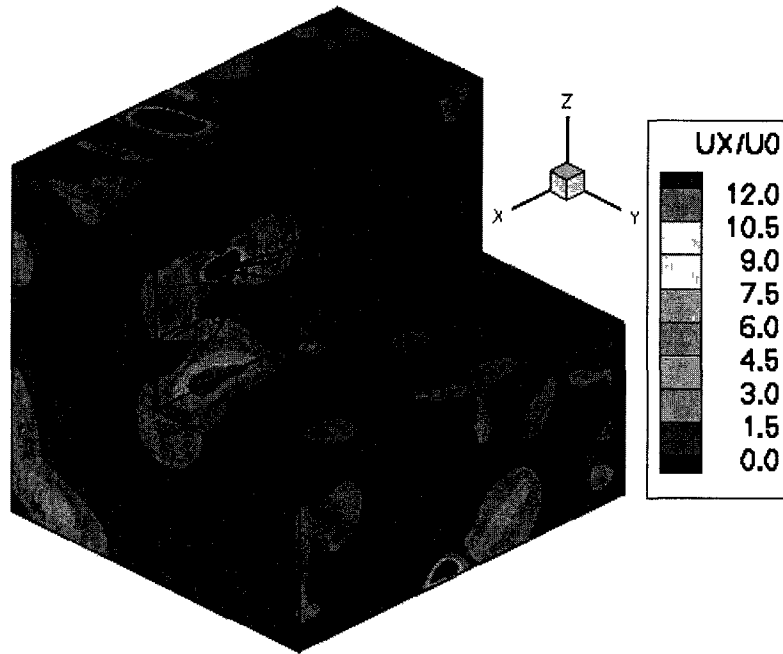


Figure 3-9 Velocity map of bone substitute (sample D-1) with stream lines show the flow direction through the bone substitute structure

Interestingly, for the substitutes with larger pore sizes (group C and D), a relatively large variation in pore size and distribution can be seen. In addition, several populations exist within their pore size distribution: for group C, there is one population around 250 μm and another one around 400 μm , while for group D these populations are around 250 μm and 900 μm . It is clear that the number of populations decreases the homogeneity of the structure. The distribution of pores in the case of substitutes with smaller pore size is narrower than that of the larger pore size samples and it is similar to normal distribution. These observations demonstrate that substitutes in group A and B have a more homogenous structure while the homogeneity is less in group C and D.

In order to compare the results based on FDT with results obtained from DT and Hildebrand method, which is based on the weighting the local size according to their volume fraction the volume-based average pore size was calculated. A close correlation was found between our results and earlier results presented in Ref. [8]. The distribution of

volume-based pore size presented in Figure 3-7 shows the volume-based calculation results in almost normal distribution of pore size among all samples.

The size of interconnections is assumed to have an important impact on nutrient transport, vascularization and bone migration. According to Lu et al. [3], an interconnection size of over 50 μm is suitable for bone formation inside the pores. The results of interconnection size distribution (Figure 3-8) indicate that more than 60% of interconnections in specimens of group D and 50% of interconnections in specimens of groups A, B and C are larger than 50 μm .

One of the important parameters reported to enhance the functionality of bone substitutes is surface area because it allows for cell interaction. A large surface to volume ratio would assist bone ingrowth. Peyrin et al. [21] observed that samples with larger surface-to-volume ratio and connectivity showed greater bone ingrowth. According to the results, the surface density of the substitutes decreased by increasing pore size (Figure 3-10). Also increasing the pore and interconnection sizes increased permeability (Figure 3-10). Both surface density and permeability are effective factors in bone substitute study, so designing bone substitutes with sufficient surface density and permeability needs to consider the geometry of bone substitute that shows the value of geometric characterization.

The characterization tools presented in this study to determine geometric parameters can be helpful in the design scaffolds. They can also help us to better understand the biological response and resorption behaviour of substitute [28], this will be our follow-up investigation.

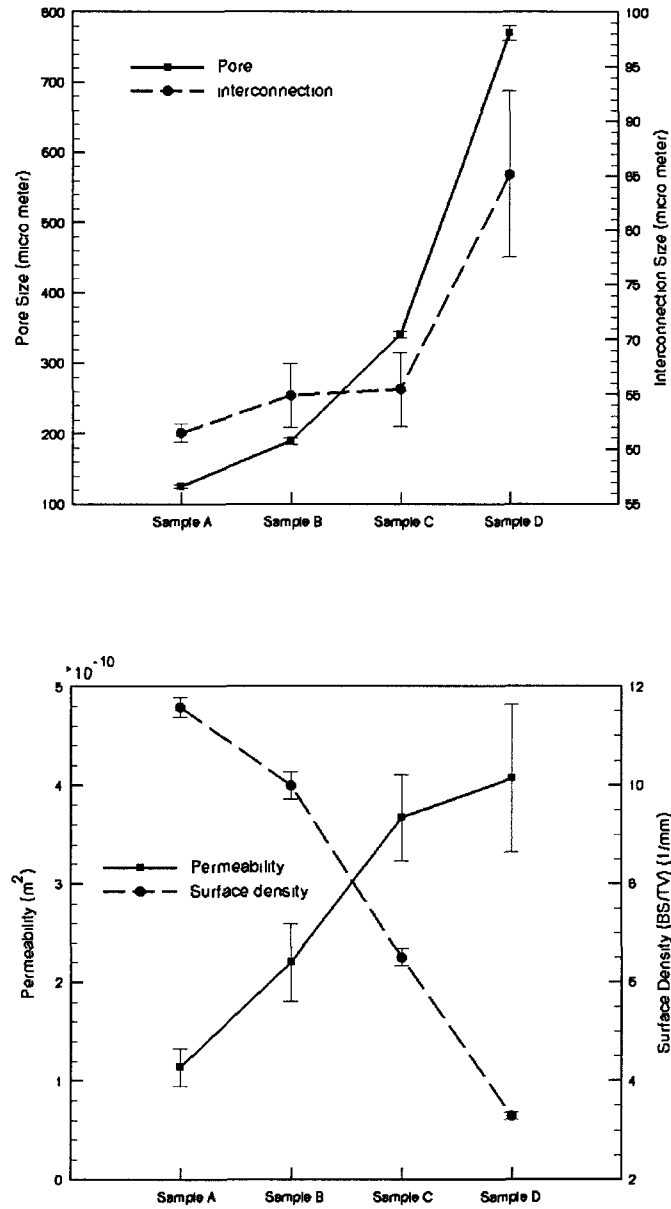


Figure 3-10 (a) Bone substitute average pore and interconnection size versus four different bone substitute groups. (b) Bone substitute permeability and surface density versus four different bone substitute groups.

The characterization tools presented in this study to determine the geometric parameters, can be helpful to design scaffolds and to better understand the biological response and resorption behaviour of substitute [28], this will be our follow-up investigation.

3.6 Reference

[1] Hutmacher DW, Scaffolds in tissue engineering bone and cartilage. *Biomaterials* 2000;21(24):2529-43.

[2] Agrawal CM, Ray RB, Biodegradable polymeric scaffolds for musculoskeletal tissue engineering. *J Biomed Mater Res* 2001,55(2):141-50.

[3] Lu JX, Flautre B, Anselme K, Hardouin P, Gallur A, Descamps M, et al. Role of interconnections in porous bioceramics on bone recolonization in vitro and in vivo. *J Mater Sci Mater Med* 1999;10(2):111-20.

[4] Mastrogiacomo M, Scaglione S, Martinetti R, Dolcini L, Beltrame F, Cancedda R, et al. Role of scaffold internal structure on in vivo bone formation in macroporous calcium phosphate bioceramics. *Biomaterials* 2006;27(17):3230-7.

[5] Gauthier O, Bouler JM, Aguado E, Pilet P, Daculsi G. Macroporous biphasic calcium phosphate ceramics: influence of macropore diameter and macroporosity percentage on bone ingrowth. *Biomaterials* 1998;19(1-3):133-9.

[6] Karageorgiou V, Kaplan D. Porosity of 3D biomaterial scaffolds and osteogenesis. *Biomaterials* 2005;26(27):5474-91.

[7] Li Sh, de Wijn JR, Li J, Layrolle P, de Groot K. Macroporous biphasic calcium phosphate scaffold with high permeability/porosity ratio. *Tissue Eng* 2003;9(3):535-48.

[8] Bohner M, van Lenthe GH, Gruenenfelder S, Hirsiger W, Evison R, Mueller R. Synthesis and characterization of porous β -tricalcium phosphate blocks. *Biomaterials* 2005;26(31):6099-105.

- [9] Jones JR, Poologasundarampillai G, Atwood RC, Bernard D, Lee PD. Non-destructive quantitative 3D analysis for the optimisation of tissue scaffolds. *Biomaterials* 2007;28(7): 1404-13.
- [10] Otsuki B, Takemoto M, Fujibayashi S, Neo M, Kokubo T, Nakamura T. Pore throat size and connectivity determine bone and tissue ingrowth into porous implants: three-dimensional micro-CT based structural analyses of porous bioactive titanium implants. *Biomaterials* 2006;27(35):5892-900.
- [11] Mathieu LM, Mueller TL, Bourban PE, Pioletti DP, Muller R, Manson JA. Architecture and properties of anisotropic polymer composite scaffolds for bone tissue engineering. *Biomaterials* 2006;27(6):905–16.
- [12] Ruegsegger P, Koller B, Müller R. A microtomographic system for the nondestructive evaluation of bone architecture. *Calcif Tissue Int* 1996;58(1):24–9.
- [13] Moore MJ, Jabbari E, Ritman EL, Lu L, Currier BL, Windebank AJ, et al. Quantitative analysis of interconnectivity of porous biodegradable scaffolds with micro-computed tomography. *J Biomed Mater Res* 2004;71(2):258-67.
- [14] Lin ASP, Barrows ThH, Cartmell SH, Guldberg RE. Microarchitectural and mechanical characterization of oriented porous polymer scaffolds. *Biomaterials* 2003;24(3):481-89.
- [15] van Lenthe GH, Hagenmueller H, Bohner M, Hollister SJ, Meinel L, Mueller R. Nondestructive micro-computed tomography for biological imaging and quantification of scaffold-bone interaction in vivo. *Biomaterials* 2007;28(15):2479-90.
- [16] Ho ST, Hutmacher DW. A comparison of micro CT with other techniques used in the characterization of scaffolds. *Biomaterials* 2006;27(8):1362-76.
- [17] Fierz FC, Beckmann F, Huser M, Irsen SH, Leukers B, Witte F, et al. The morphology of anisotropic 3D-printed hydroxyapatite scaffolds. *Biomaterials* 2008;29(28):3799-806.

- [18] Atwood RC, Jones JR, Lee PD, Hench LL. Analysis of pore interconnectivity in bioactive glass foams using X-ray microtomography. *Scripta Mater* 2004;51(11):1029–1033.
- [19] Hildebrand T, Rüegsegger P. A new method for the model-independent assessment of thickness in three-dimensional images. *J Microscopy* 1997;185:67-75.
- [20] Muller B, Beckmann F, Huser M, Maspero F, Szekely G, Ruffieux K, et al. Nondestructive three-dimensional evaluation of a polymer sponge by micro-tomography using synchrotron radiation. *Biomol Eng* 2002;19:73–8.
- [21] Peyrin F, Mastrogiacomo M, Cancedda R, Martinetti R. SEM and 3D synchrotron radiation micro-tomography in the study of bioceramic scaffolds for tissue-engineering applications. *Biotechnol Bioeng* 2007;97(3):638-48.
- [22] Martin-Badosa E, Elmoutaouakkil A, Nuzzo S, Amblard D, Vico L, Peyrin F. A method for the automatic characterization of bone architecture in 3D mice microtomographic images. *Computerized medical imaging and graphics* 2003;27:447-58.
- [23] Borgefors G, Svensson S. Fuzzy border distance transform and their use in 2D skeletonization. *IEEE* 2002;1:180-83.
- [24] Saha PK, Wehrli FW, Gomberg BR. Fuzzy distance transform: theory, algorithms and applications. *Comput Vis Image Understanding* 2002;86(3):171-90.
- [25] Sladoje N, Nystrom I, Saha PK. Measurements of digitized objects with fuzzy borders in 2D and 3D. *Image Vis Computing* 2005;23(2):123-32
- [26] Darabi A, Chandelie F, Baroud G. Thickness analysis and reconstruction of trabecular bone and bone substitute microstructure based on fuzzy distance map using both ridge and thinning skeletonization. *Can J Elect Compt Eng* 2009;34(1-2):57-62.
- [27] von Doernberg MC, von Rechenberg B, Bohner M, Gruenenfelder S, van Lenthe GH, Mueller R, et al. In vivo behavior of calcium phosphate scaffolds with four different pore sizes. *Biomaterials* 2006;27(30):5186-98.

- [28] Bohner M, Baumgart F. Theoretical model to determine the effects of geometrical factors on the resorption of calcium phosphate bone substitutes. *Biomaterials* 2004;25(17):3569-82.
- [29] Bohner M. Calcium phosphate emulsions: possible applications. *Key Eng Mater* 2001;192-195:765-8.
- [30] Niblack CW, Gibbons PB, Capson DW. Generating skeletons and centrelines from the distance transform. *Graphical models and image processing* 1992;54(5):420-37.
- [31] Haralick RM, Shapiro LG. *Computer and robot vision*. Addison Wesley Pub. Co. 1992-1993.
- [32] López AM, Lumbreras F, Serrat J, Villanueva JJ. Evaluation of methods for ridge and valley detection. *IEEE Transactions on Pattern Analysis and Machine Intelligence* 1999; 21(4):327-35.
- [33] Gagvani N, Silver D. Parameter-controlled volume thinning. *Graphical models and image processing* 1999;61(3):149-64.
- [34] Lorensen WE, Cline HE. Marching cubes: a high resolution 3D source construction algorithm. *Comput Graphics* 1987;21(4):163-9.
- [35] Darabi A, Chandelier F, Baroud G. Morphometric analysis of trabecular bone thickness using different algorithms. *Can J Elect Comput Eng* 2007; 32(3): 157-63.
- [36] Hwang SN, Wehrli FW. Subvoxel processing: a method for reducing partial volume blurring with application to in vivo MR images of trabecular bone. *Magnetic Resonance in Medicine* 2002;47(5):948–957.
- [37] Munch B, Gasser P, Holzer L, Flatt R. FIB-nanotomography of particulate systems - part II: particle recognition and effect of boundary truncation. *J Am Ceram Soc* 2006;89(8):2586–2595.

[38] Zeiser T, Bashoorzadeh M, Darabi A, Baroud G. Pore-scale analysis of Newtonian flow in the explicit geometry of vertebral trabecular bones using lattice boltzmann simulation. *J Eng Med* 2008;222(H2):185-94.

CHAPTER 4

Effect of subvoxel process on non-destructive characterization of bone substitutes

M. Bashoor-Zadeh¹, G. Baroud¹, M. Böhner²

(1) Laboratoire de Biomécanique, Département de Génie, Université de Sherbrooke,
Sherbrooke, QC, Canada J1K 2R1, (2) Dr Robert Mathys Foundation, Bettlach,
Switzerland

To be submitted to one of the field journals

Corresponding author:

Gamal Baroud, Ph.D., Tenured Professor

Canada Research Chair in Skeletal Reconstruction and Biomedical Engineering

Director, Biomechanics Laboratory

Tel.: (819) 821-8000 ext. 61344

Fax: (819) 821-7163

UNIVERSITE DE SHERBROOKE

Faculté de génie - Département de génie mécanique

2500 boul. Université, Sherbrooke, QC, Canada J1K 2R1

4.1 Abstract

Bone substitute are increasingly the gold standard in the bone repair and spinal fusion surgeries. Important geometric features of the bone substitute include pore size and interconnection between the pores. Calcium-phosphate Substitutes of four different pore sizes and interconnection, yet of constant porosity, produced by the emulsion method, and scanned with micro-computed tomography device, were the focus of this study. In the previous study, we introduce fuzzy-based image treatment methods to enhance the characterization accuracy. The fuzzy methods particularly improved the characterization accuracy for substitute featuring small pore sizes. This study resorts to numerical and hardware subvoxelization methods to further improve the characterization of bone substitutes in terms of the pore and interconnection sizes. Furthermore, we have observed some boundary effects due to the details obtained with the subvoxelization that can yield misleading results in the characterization process of the pore interconnection sizes. We also present in this article the approach to eliminate the boundary effects. Further, the hardware subvoxelization, i.e. the higher resolution scanning, significantly improves the histograms and therefore allowed for adequate segmentation and accurate pore size and interconnection characterization. Comparing the results obtained from numerical and hardware subvoxelization datasets revealed a minor difference of less than 2.5% for the porosity values. The difference for the pore sizes increased up to 10%. Considerable difference of up to 35-50% was found for interconnection sizes of samples. The results demonstrated significant improvement using both numerical and hardware subvoxelization. In particular, the subvoxelization yielded interconnection sizes significantly below 50 micron and yet in-vivo biological results of our earlier studies showed that these substitute showed adequate bone ingrowth. Material scientists should be aware of the complexity of pore sizes measurements and characterization and future work will show whether or not the 50-micron interconnection size is a pre-requisite for adequate bone repair.

4.2 Introduction

Geometric features of bone substitutes have been reported to have a great impact on the biological response of bone in the healing process. The accurate characterization of the substitute microstructure has therefore received significant attention for designing an effective scaffold for clinical application.

The use of micro-computed tomography (μ CT) has grown significantly for the non-invasive study of trabecular bone and porous bone substitutes [1-3]. Literature shows that the image resolution has a significant impact on accuracy of structural analysis [4]. In particular, when the voxel size is relatively large compared to the structure of interest, it becomes difficult to obtain accurate geometric information. Therefore, there is increased interest in studying the effect of resolution and segmentation methods on the accuracy geometric parameters of substitute.

In the following paragraphs, we briefly review the researches on the relation between voxel size and geometric parameters. A number of studies focused on the impact of voxel size on trabecular bone characterization using μ CT and/or magnetic resonance (MR) images [5-12]. In these comparative studies, the accuracy of trabecular bone structural parameters obtained from MR images were compared with high-resolution μ CT images as reference images [5-7]. Specifically, Majumdar et al. [5] scanned trabecular bone specimens with MR scanner at $156 \times 156 \times 300 \mu\text{m}$ voxel size and high resolution X-ray topographic microscopy scanner at $18 \mu\text{m}$ isotropic voxel size. They showed that structural parameters such as trabecular thickness and volume fraction tend to be increasingly overestimated with lower resolution. In the study of Last et al. [6], the architectural parameters of calcaneus specimens were measured by using MR images of $66 \mu\text{m}$ voxel size and high-resolution micro tomography images of $10 \mu\text{m}$ voxel size. The results showed that the parameters quantified from MR images were biased towards overestimation as compared to their corresponding values from micro tomography data.

Another approach taken in trabecular bone resolution studies has been often to acquire the high-resolution images by scanning the samples and then to subsequently produce

low-resolution images by artificial image degradation methods. The artificial image degradation methods combine a group of neighboring voxels into one voxel with intensity equal to the mean intensity of voxel group [8-11]. Tabor [8] studied the error of estimating the trabecular bone structural parameters as a function of pixel size. In this study, the original binary images with resolution of 30 μm were artificially degraded to larger pixel size of 150 μm . In the study of Kothari et al. [9] the original scanned images of 40 μm resolution were degraded in all direction to create low resolution images with isotropic and non-isotropic voxel size and then the dependency of bone structural parameters on slice thickness were investigated. Consistent with other studies [5-7], this study showed that trabecular thickness increased with increasing the slice thickness.

Muller et al. [11] used trabecular bone images scanned at 14 μm and then artificially increase the voxel size by the factors ranging from 2 to 20. They have shown the same trends of overestimation of trabecular thickness and size separation compared to Kothari [9]. The above-mentioned studies demonstrated that the index resolution significantly affect the evaluation of structural parameters of bone. Specifically, when using μCT at higher resolution, the effect of partial volume blurring is decreased and more accurate structural and geometric information is possible to obtain.

In addition to the use of fuzzy-based segmentation, two approaches can be used to improve the characterization of the structure of scaffolds: (i) scanning the sample directly at a higher resolution, leading to higher scanning cost and (ii) decreasing the voxel size artificially by using subvoxelization algorithms, in which the high resolution images are subsequently generated by dividing voxels into subvoxels. This does not cause any changes to the histograms in the images.

There exist a number of algorithms in the literature to decrease the voxel size. For example, the linear interpolation method calculates the material-volume fraction (MVF) of a voxel located between two adjacent voxels as the average MVF of the two voxels [4]. In addition the Bayesian subvoxel approach classified the subvoxels based on Gibbs prior distribution. According to this method the output is binarized image, in other words the subvoxels are assigned to object or non-object [13]. Hwang and Wehrli [4] also

developed the “subvoxel processing” algorithm to divide voxels into subvoxels. The intensity of each subvoxel is then calculated based on local neighboring intensities with due attention to conservation principles. The output of this algorithm is fuzzy images because the subvoxel processing assigned partial fraction to each subvoxel [4]. They also showed this method is superior to the interpolation method and therefore it is adopted in this study.

The previous studies have mainly investigated the impact of voxel size on quantification of trabecular bone structure. To our knowledge, no study has shown the relation between the voxel size and geometric parameters of bone substitutes, particularly the pore and interconnection size.

Generally, in porous bone substitutes, pores provide space for bone formation and cell attachment, while pore interconnections act as a path for cell movement, nutrient transport and vascularization [16, 22, 23]. The clinical observation showed that the cells could not penetrate to the pores that have narrow interconnections toward the periphery of scaffold [16]. Hence, an effective bone substitute should have interconnected structure with adequate interconnection size.

Therefore, due to significant effect of pore and interconnection size of a substitute on bone formation and cellular resorption, this article focused on improving the characterization of these parameters.

Further, in this study four classes of porous bone substitutes of variable geometric features were analyzed at different resolutions (generated artificially or by direct high resolution scanning) to examine the effect of spatial resolution on the pore size and interconnection size.

In our pilot studies, the subvoxel process algorithm of Hwang and Wehrli [4] was applied to the four classes of bone substitutes. Overall, the pore size decreased with decreasing the voxel size. However, we have observed surprising and confusing behaviour with respect to the interconnection size in that it showed different trends among classes. Specifically, the interconnection size appeared to reduce for small pore size samples with

a transient change towards high interconnection size for large pore samples. Therefore, the authors have decided to examine this observation by comparing the algorithm results with direct scanning results using of higher resolution, to further examine the interconnection size dependency upon voxel size. Our underlying hypothesis has been that some of the geometric features such as surface irregularities of the substitutes that may appear at higher resolution cause this conflicting result.

We follow these additional effects to clarify the confusion that is the interest of many material scientists to reach accurate pore size and interconnection characterization.

4.3 Material and Method

4.3.1 Scaffold fabrication and preparation

Four classes of porous β -tricalcium phosphate (β -TCP) bone substitutes were fabricated by the calcium phosphate emulsion method [18, 19]. Based on this method, the calcium phosphate cement pastes were produced by mixing the cement components, and then the oil droplets were dispersed in the resulting paste to form the pores and interconnections. Variations in emulsifier concentration led to different macropore sizes, while the volume fraction was constant. The resulting paste was then moulded, after hardening; the samples were cleaned, dried and sintered at 1250 °C. The samples were then machined to produce the cylinders with 8mm diameter and 13 mm height. Four samples of calcium phosphate bone substitutes with variable geometric features were randomly selected and analyzed at different resolutions to examine the effect of special resolution on the evaluation of structural parameters.

4.3.2 Image acquisition

Four cylindrical samples of β -TCP bone substitutes were scanned with SKYSCAN1172 μ CT scanner (Desktop x-ray micro tomography, Aartselaar Belgium). Each sample was scanned at three different resolution level to generate the 7.5, 15 and 30 μ m isotropic voxel size.

For all configurations the x-ray tube voltage and current were fixed at 55 Kv and 181 μ A, respectively. A copper plus Aluminum filter was used to cut the soft x-rays and consequently reduce the beam hardening effects. Also, a frame average of four and rotation step of 0.4 degree were set within an angular range of 360 degree, therefore, a total of 900 radiographic images were acquired for each sample at different resolution level. The total scanning time varied approximately from 30 to 100 min, depending on the resolution level. As the resolution increased, the acquisition time increased.

After acquiring the images, NRecon software (V15.1.5) was used to reconstruct 3D structure from 2D radiographic images and generate 2D cross sectional images.

4.3.3 Subvoxelization process

The low-resolution images (30 μ m) were submitted to a subvoxel-processing algorithm established by Hwang and his colleagues [4]. The basic assumptions used to define this algorithm are: (a) subvoxels can be assigned to higher volume fraction and (b) continuing of material phase [4, 20]. According to this algorithm, each reference voxel was divided into eight subvoxels and the allotted grey value of each subvoxel is determined by adjacent neighbouring values and strict conservation principles. The detail of the algorithm has been described in Ref [4]. Specifically, each subvoxel is weighted based on the value of adjacent voxels then the total value of original voxel is distributed between the subvoxels according to their normalized weight value. In agreement with the conservation principles, the average of the subvoxels' material volume fraction (in this study ceramic volume fraction, CVF) will be equal to the CVF of the original voxel. Based on this process, the images of 15 μ m resolution were artificially generated and then analyzed for the pore and interconnection sizes. The results obtained from artificial 15 μ m images compared with ones obtained from 15 μ m scanned images.

4.3.4 Thresholding

In general manner, the threshold values were selected using the histogram of images and visual inspection and comparison to the porosity values of substitute that are known to us prior to the thresholding process. Furthermore, the shape of histograms is changed

between the samples and resolution levels and therefore establishing a general rule to find the threshold values of all cases was difficult.

When increasing the resolution, the bimodal histograms show distinct phase of calcium material and void space as separate peaks. The valley between the two peaks is known as fuzzy zone which is corresponding to the intensities of voxels in the border of material and pores. The threshold values were selected around the minimum value of fuzzy zone to provide the appropriate porosity which is comparable to one measured experimentally. Therefore, in the high resolution scanning the threshold values were approximately set in the interval of $\pm 30\text{-}40\%$ of minimum value of fuzzy zone.

The threshold values of unimodal histograms were selected with respect to subjective visual inspection based on roundness and sphericity of pores and comparable porosity to the one measured experimentally.

4.3.5 Geometric analysis and verification

The method used for determining pore and interconnection has been described extensively in an earlier article of the authors [15]. Briefly, as a first step, the scanned images were fuzzified by a sigmoidal function with two threshold values for the calcium material and void space. Specifically, the two thresholds were selected via histograms and visual inspection of the fuzzing border between calcium material and void space. By applying the sigmoidal function, each voxel, x , of set X will be assigned by a value between 0 and 1 which called its membership value, $\mu(x)$.

$$\{(x, \mu(x)) \mid x \in X, \mu: X \rightarrow [0, 1]\} \quad (4.1)$$

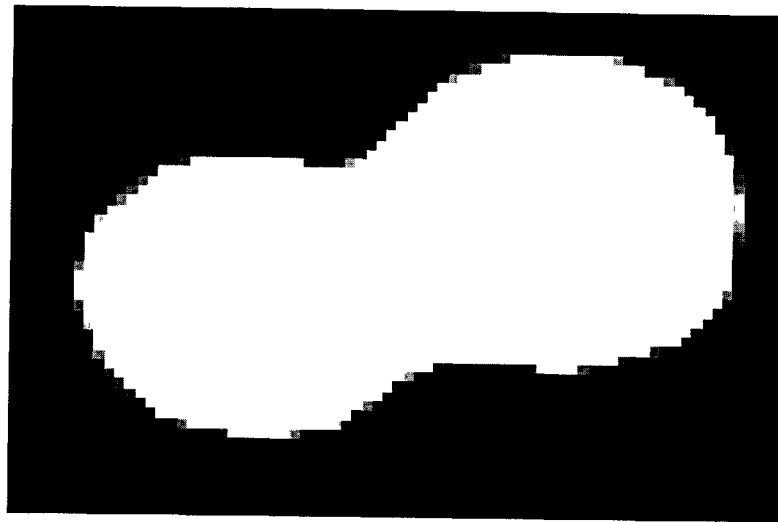
The membership value of voxel determines the fraction of its volume belonging to the object. Therefore, the volume of object is obtained as the sum of the membership values of all voxels in volume of interest (VOI). Since in this study the object of interest is void space, the summation of membership values is defined as the volume of void space. Hence the porosity was calculated as the ratio of volume of void space over the total number of voxels in VOI [21].

The object's voxel membership was also used to compute the fuzzy distance transform (FDT) map. The FDT value at each voxel is defined as the shortest fuzzy distance between that voxel and the background. For this purpose, we used the FDT algorithm published in Ref. [14].

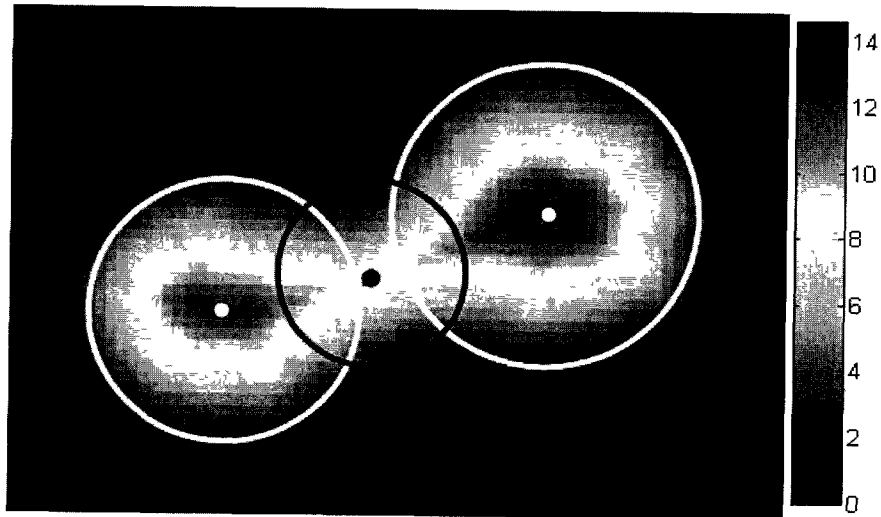
Once the FDT map was determined, the next step is the determination of geometric parameters, e.g. pore and interconnection size. Generally, the pore size was defined by the diameter of the maximum sphere that can be completely inscribed in a pore and the interconnection size was defined as the diameter of opening between two pores [15] (Figure 4-1).

Pore size and interconnection size were then obtained by applying the max-min detection algorithm to FDT map. With respect to FDT values, the algorithm finds the local maxima and saddle voxels of the FDT map. According to this algorithm, the maxima voxels have the largest FDT value among their neighbours and the saddle voxels have at least maximum FDT value in one direction and minimum value in the other directions. The FDT value at local maxima and saddles corresponds to the radius of pores and interconnection, respectively. The average pore size is then calculated using two definitions, arithmetic average value (Number-based) and volume weighted average value (Volume-based). The average interconnection size is calculated by arithmetic averaging the FDT value of saddle voxels.

When verifying the 2D image produced with high resolution we have noticed that decreasing voxel size leads to the detection of local irregularities on pores surface. The local surface irregularities affect on FDT values and consequently result in finding extra saddle voxels as representative of new interconnections. The extra saddle voxels which have a size in the range of local neighbouring maxima are known as virtual interconnections (Figure 4-2). Additional conditions have been applied to eliminate the effect of such virtual interconnections and modify the average interconnection size based on the real interconnections. These conditions exclude saddles which specific percentage of their sphere volume (overlapping volume) overlapped by a maxima sphere. The overlapping volume of 60, 70, 80 and 90 % were examined.



(a)



(b)

Figure 4-1 (a) Fuzzified image of an individual void space. (b) 2-D fuzzy distance transform map; The pore size and interconnection size is defined as the diameter of circles in 2-D (or spheres in 3-D) centered at local maxima (white points) and saddle voxels (black points), respectively

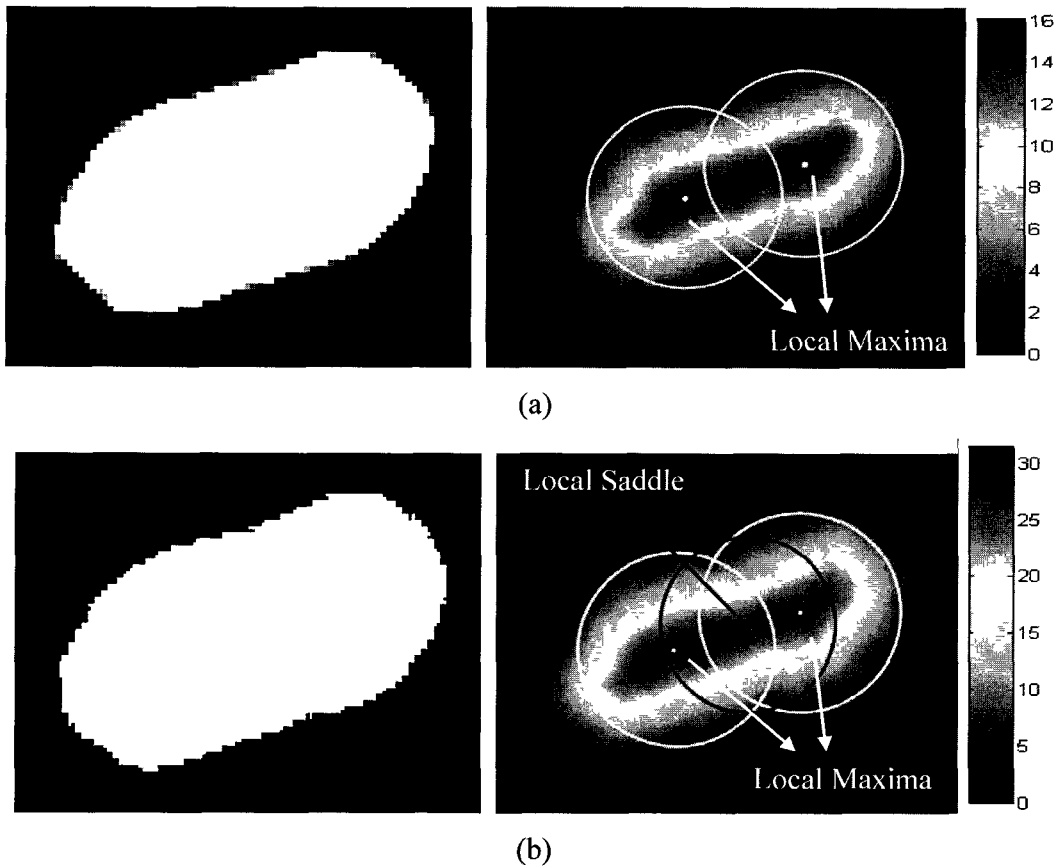


Figure 4-2 (a) Representative illustration of 2-D fuzzified image (left) and fuzzy distance transform (FDT) map (right) of individual void space extracted from images of 30 μm resolution. The local maximums are shown as white points in FDT map. (b) Corresponding illustration of 2-D fuzzified image (left) and FDT map (right) after applying subvoxel process. The surface irregularities are appeared by decreasing the voxel size. These irregularities caused generating local saddle point as representative of virtual interconnections in FDT map (black point).

4.4 Results

Four samples of different geometric features were analyzed. Figure 4-3 shows representative 2D cross sectional images of samples scanned at 30, 15 and 7.5 μm resolution. Visual comparison of 2D images showed that by decreasing the voxel size, pores achieve sharper and more spherical boundary, specifically for samples with small

pores (e.g. samples A and B). Hence providing more detail of structure leads to accurate measurement of structural parameters.

The gray-level histograms of samples obtained from scanned images of different resolutions are shown in Figure 4-4. The histograms of samples A and B show that the scan resolution had considerable impact on distinguishing of two phases (pore and material). By increasing the voxel size, the effect of partial volume blurring increased, specifically for samples A and B (with small pore size). These artificial effects caused two peaks of histogram get closer and /or merge together and the histogram became unimodal, Figure 4-4, histograms of samples A and B at 30 μm resolution. The histograms of samples C and D illustrated the existence of two peaks corresponding to pore and material phase for all configurations even for the 30-micron resolution.

The gray level histogram of images before and after applying subvoxel process were similar, in other words the intensity histograms of 30 μm scanned images and 15 μm artificially generated images presented similar manner. Due to this similarity, the same threshold values were used for analysis of both cases (Table 4-1).

The threshold values and geometric parameters of substitutes for different voxel size and methods are summarized in Table 4-1.

Generally, for all samples, the number-based (N-b) average pore size decreased as the voxel size decreased (Table 4-1). Comparing the pore size values calculated at 15 μm resolution exhibited small difference between the scan and artificial subvoxel process results (<10 %) (Table 4-2).

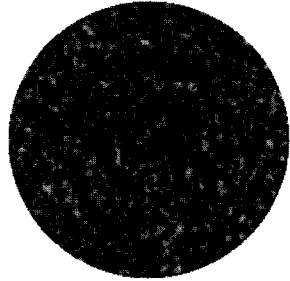
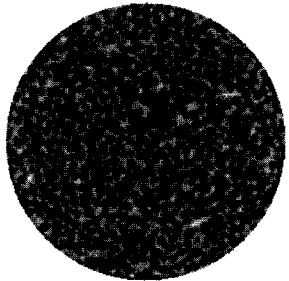
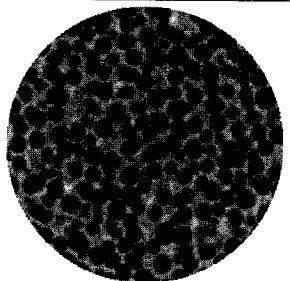
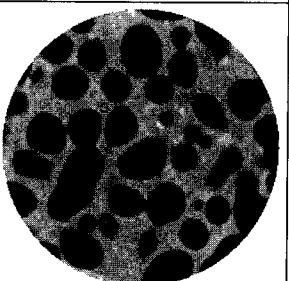
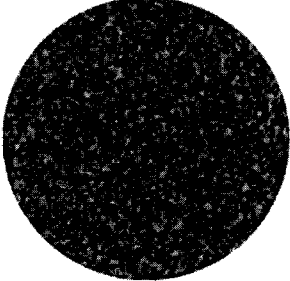
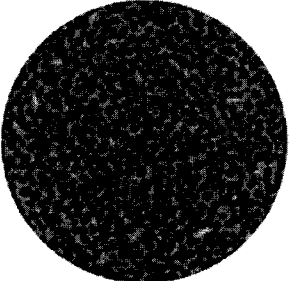
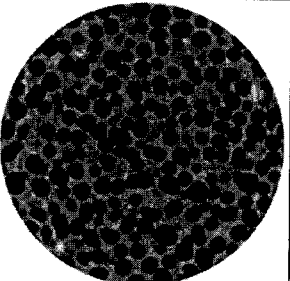
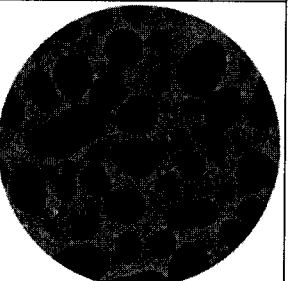
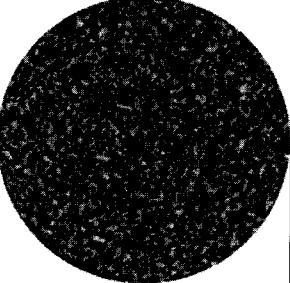
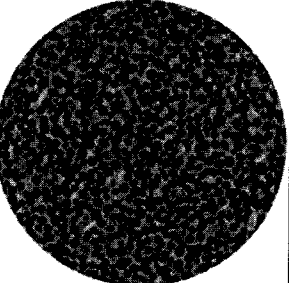
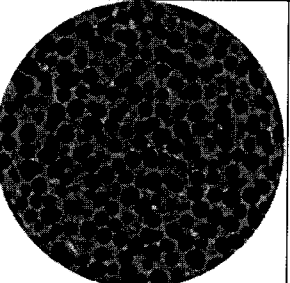
Voxel size	Sample A	Sample B	Sample C	Sample D
30 μm				
15 μm				
7.5 μm				

Figure 4-3 2-D representative μCT slices of samples A, B, C and D scanned at 30, 15 and 7.5 μm resolutions.

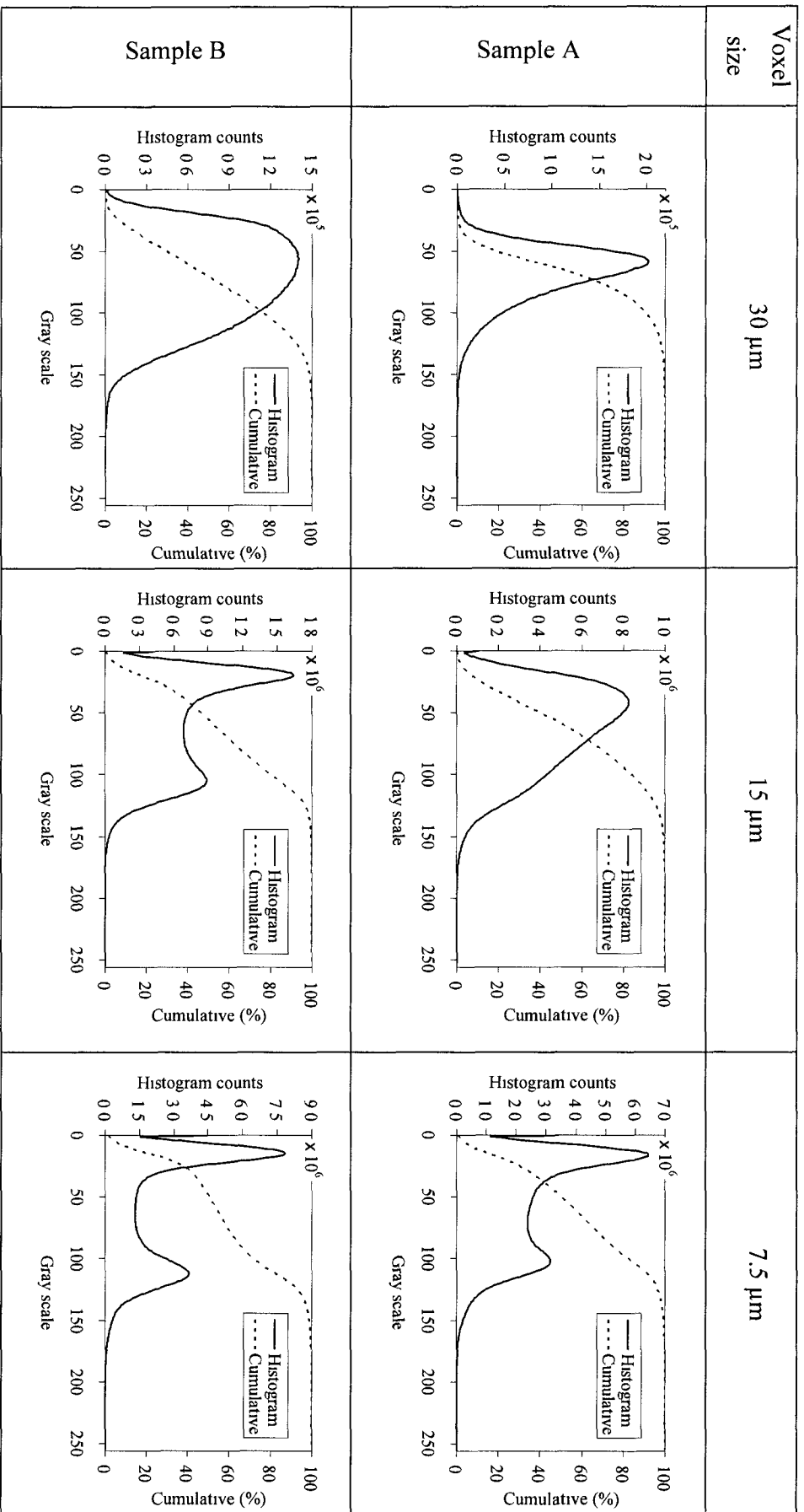


Figure 4-4 Intensity histograms of μCT images of samples A, B, C and D at various resolutions (Continue on next page).

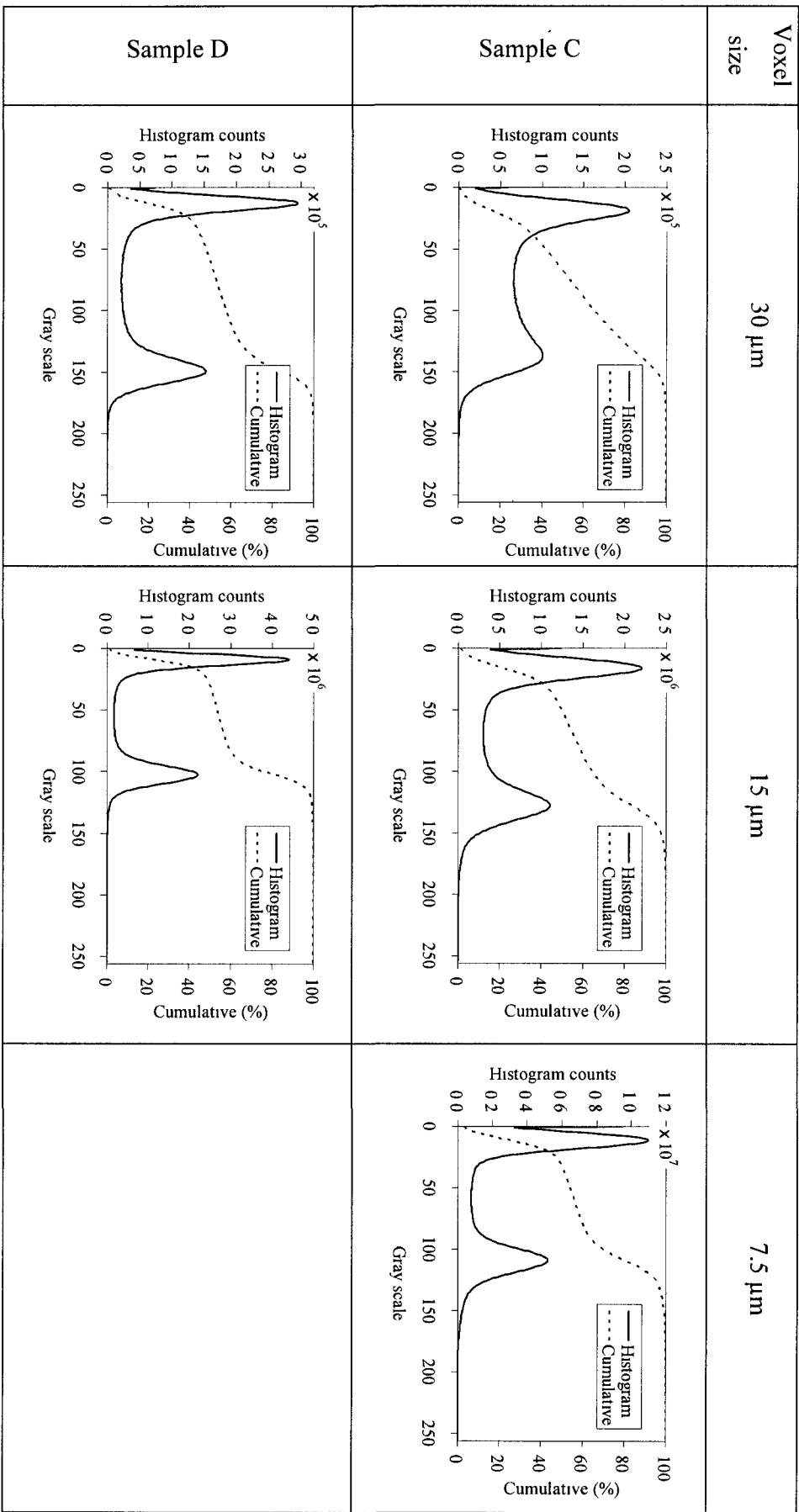


Figure 4-4- Continue

Table 4-1 Geometrical properties of bone substitutes presented as a function of resolution and method

Sample	Resolution	Method	Threshold values	Porosity	Number-based pore size (μm)	Volume-based pore size (μm)	Interconnection size (μm)
sample A	30	Scan	55-80	50	135 \pm 42	175 \pm 52	63 \pm 29
	15	Artificial(subvoxel)	55-80	52	118 \pm 37	152 \pm 47	54 \pm 32
	15	Scan	40-90	54	107 \pm 25	129 \pm 46	40 \pm 19
	7.5	Scan	40-80	55	94 \pm 34	138 \pm 67	22 \pm 13
sample B	30	Scan	50-100	52	193 \pm 39	217 \pm 44	63 \pm 28
	15	Artificial(subvoxel)	50-100	53	170 \pm 45	204 \pm 48	52 \pm 33
	15	Scan	45-85	54	181 \pm 53	220 \pm 48	36 \pm 23
	7.5	Scan	45-80	54	165 \pm 64	223 \pm 52	30 \pm 29
sample C	30	Scan	55-100	52	365 \pm 94	435 \pm 119	62 \pm 41
	15	Artificial(subvoxel)	55-100	54	330 \pm 108	428 \pm 134	66 \pm 70
	15	Scan	50-90	54	353 \pm 109	438 \pm 122	47 \pm 53
	7.5	Scan	40-75	55	337 \pm 125	439 \pm 124	66 \pm 89
sample D	30	Artificial(subvoxel)	50-110	53	909 \pm 226	1030 \pm 173	99 \pm 106
	15	Artificial	50-110	53	890 \pm 236	1019 \pm 176	234 \pm 284
	15	Scan	30-80	54	899 \pm 221	1015 \pm 172	154 \pm 217
	7.5	Scan					

Table 4-2 Comparing voxel size dependency of structural parameters obtained from scan and artificial datasets. Arrows (▲, ▼) indicate direction of change in parameters as voxel size decreased.

Sample	Method	Porosity	Pore size	Interconnection size
Sample A	15micron-Scan	▲	▼	▼
	15micron-Artificial (subvoxel)	▲	▼	▼
Sample B	15micron-Scan	▲	▼	▼
	15micron-Artificial (subvoxel)	▲	▼	▼
Sample C	15micron-Scan	▲	▼	▼
	15micron-Artificial (subvoxel)	▲	▼	▲
Sample D	15micron-Scan	▲	▼	▲
	15micron-Artificial (subvoxel)	▲	▼	▲
Difference between actual scan results and artificial subvoxel process results		< 2.5%	< 10%	35-50%

Figure 4-5 shows the pore size distribution of all samples at different scan and artificial resolutions. For the two smallest pore sizes (Samples A and B), the pore size distribution obtained from high resolution images demonstrated more detail of structure by appearing two peaks corresponding to different population of size inside the structure. Pore size distributions of sample A (7.5 μm), Figure 4-5a, reveals the two populations of pore size around 60 and 120 μm . In addition pore size distribution of sample B, Figure 4-5b, displays two populations of pores with two equal peaks at 15 and 7.5 μm resolutions. Decreasing the voxel size from 15 to 7.5 μm moves the first peak, as representative of

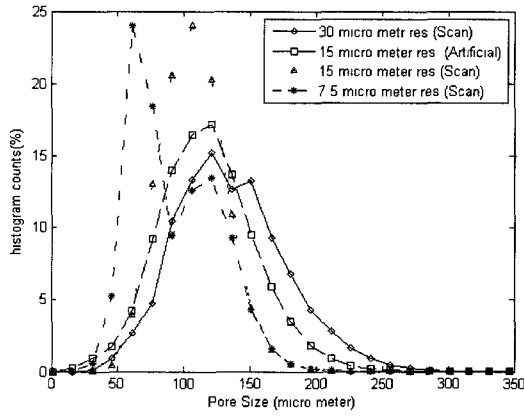
smaller pores, from 120 to 90 μm . Also as demonstrated in Figure 4-5c and Figure 4-5d, pore size distribution of samples C and D, the main peaks did not change with resolution for these samples.

The volume-base (V-b) average pore size values showed various trends when the voxel size decreased (Table 4-1).

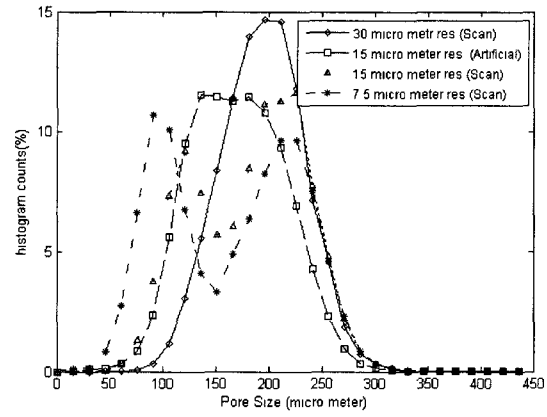
The average interconnection size showed contrary pattern between the samples. Decreasing the voxel size decreased the interconnection size in samples A and B but increased the size of interconnection in sample D.

For sample C, interconnection size obtained from scan and artificial datasets showed opposite trends, increasing with artificial dataset and decreasing with scan dataset. In addition, for scan dataset, the average interconnection size was dropped down to 47 μm at 15 μm resolution and then elevated to 66 μm at 7.5 μm resolution (Table 4-1).

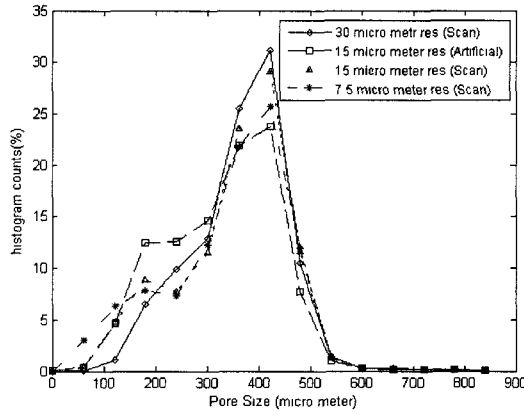
The interconnection size distributions of samples (Figure 4-6) show that all main interconnections are below 60 μm and also the main peaks shift to the left with decreasing the voxel size which made the average interconnection size got smaller. The interconnection size distribution of sample D (Figure 4-6d) also shows that the main peaks moved to smaller values with subvoxelization (scan and artificial). This means that the main features, here being interconnection, get smaller. On the other hand, the average interconnection value got larger for sample D, this could be because of the newly appearing the large interconnections (interconnections larger than 200 μm).



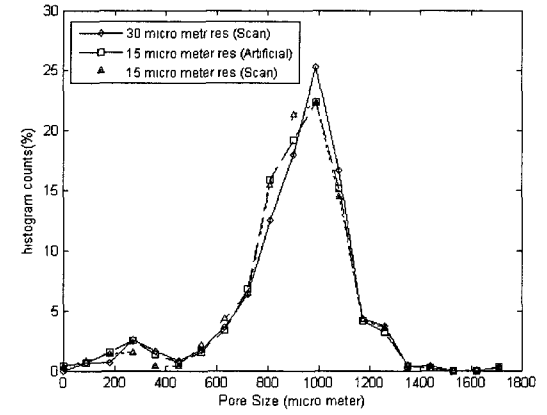
(a)



(b)



(c)



(d)

Figure 4-5 Number-based pore size distributions of (a) Sample A, (b) Sample B, (c) Sample C and (d) Sample D derived from max-min operation and FDT values at different scan and artificial resolutions.

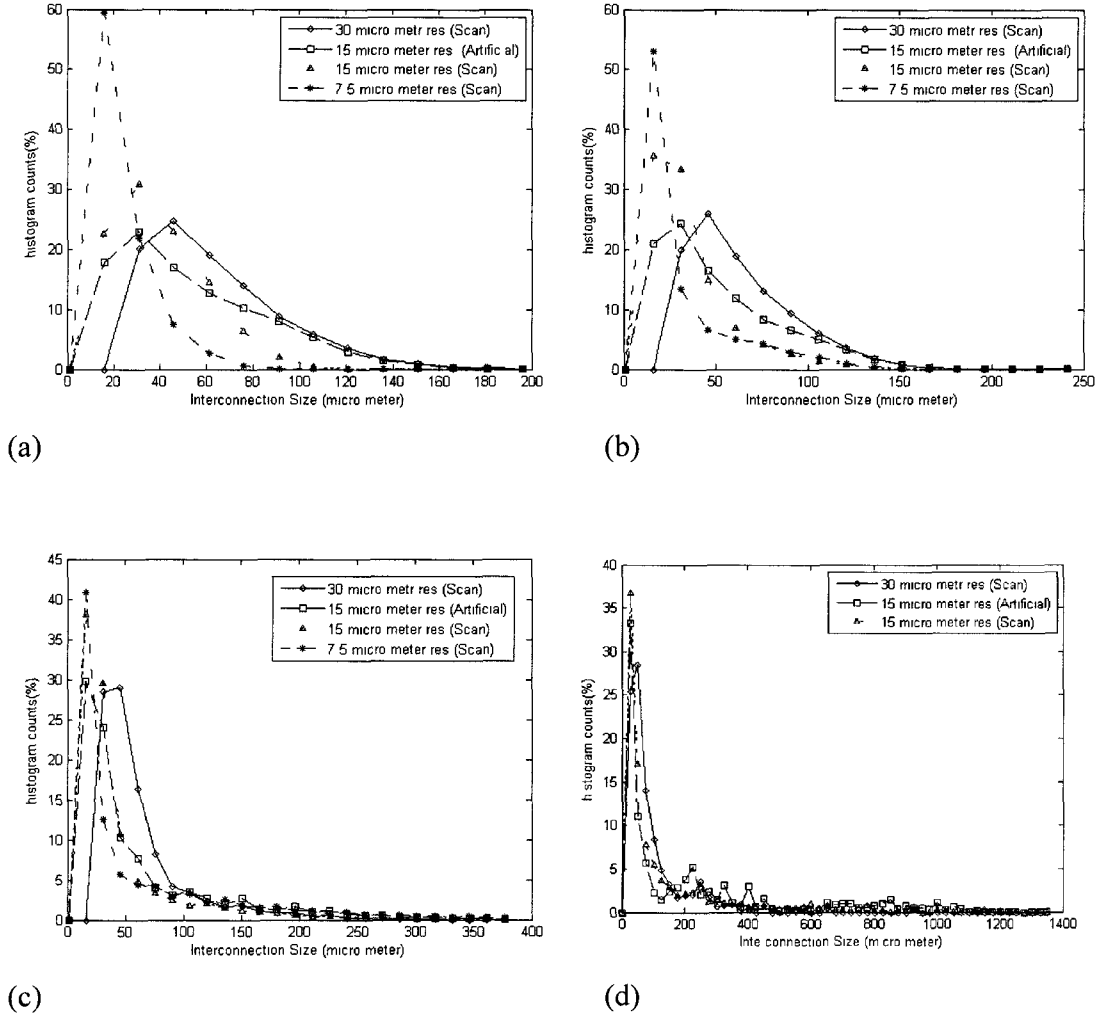


Figure 4-6 Interconnection size distributions of (a) Sample A, (b) Sample B, (c) Sample C and (d) Sample D derived from max-min operation and FDT values at different scan and artificial resolutions.

Additional conditions were applied to eliminate boundary effects appeared by decreasing the voxel size. Accordingly, the virtual interconnections with overlapping volume larger than X% (X: 60, 70, 80, 90%) were removed and average interconnection size were recalculated. In Figure 4-7, we show the modified average interconnection size versus various overlapping volume. Comparing the data of samples A and B (Figure 4-7a and Figure 4-7b) with similar results of samples C and D (Figure 4-7c and Figure 4-7d) show that the average interconnection size of samples A and B were less influenced by boundary effect at small voxel size.

For all overlapping volume (60-90%), the average interconnection size of sample C decreased as the voxel size decreased (Figure 4-7c). In addition, Figure 4-7d show that the average interconnection size of sample D (15 μm) (scan and artificial) considerably decreased after removing virtual interconnections (with decreasing the overlapping volume). Interconnection size distribution of sample D (15 μm) scan and artificial dataset, Figure 4-8a and Figure 4-8b, indicate the distributions of interconnections larger than 300 μm were mainly affected by removing the overlapping interconnections. In other words most of large interconnections were generated by boundary effect or surface irregularities. The interconnection size distributions of sample D(30 μm) (Figure 4-8c) show more stability in distribution of interconnections for all cases (60-90% overlapping).

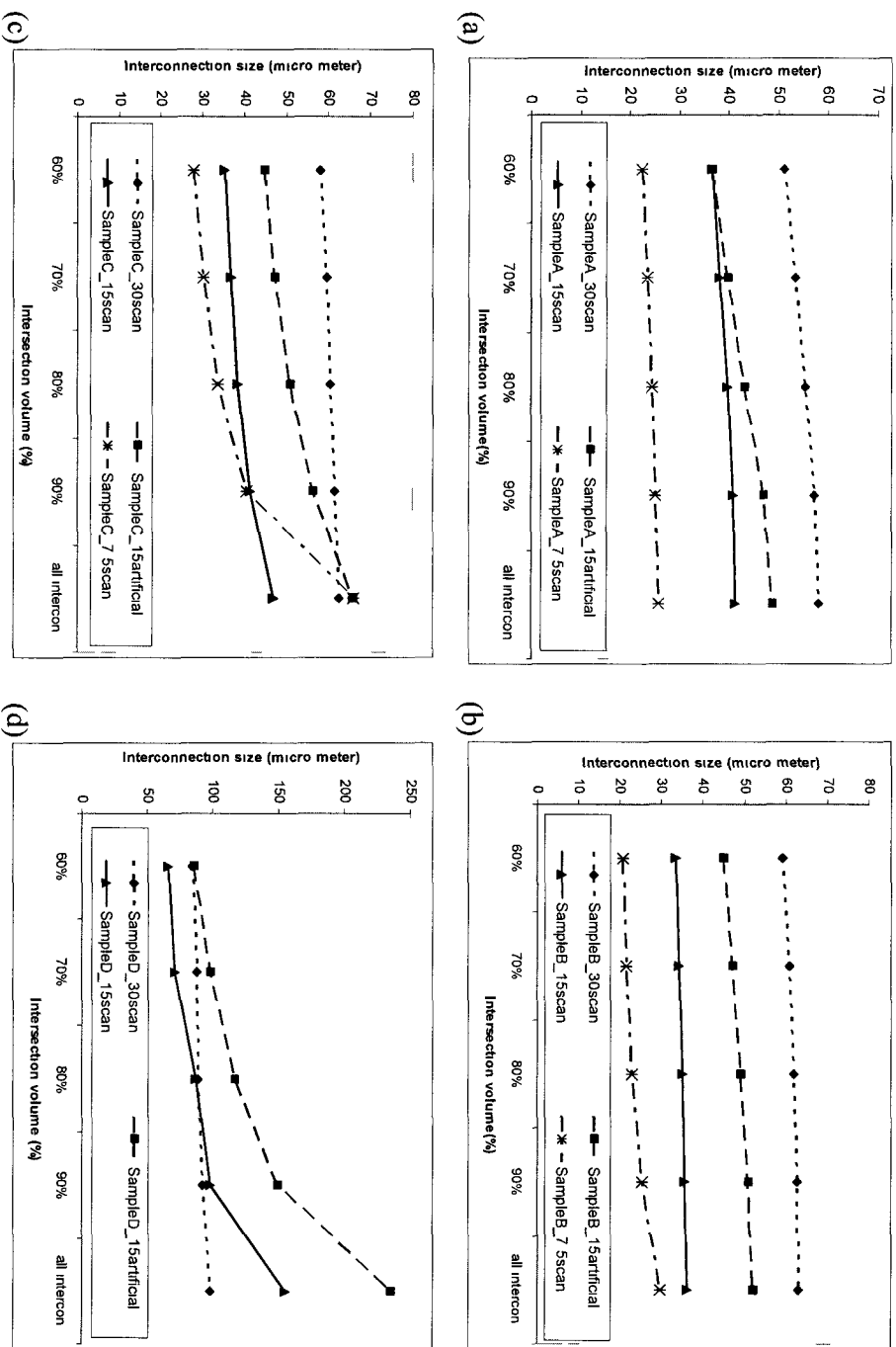


Figure 4-7 Average interconnection size versus intersected volume (a) Sample A, (b) Sample B, (c) Sample C and (d) Sample D. In each point, the virtual interconnection with intersected volume larger than X% (60-90%) were removed and average interconnection size was calculated.

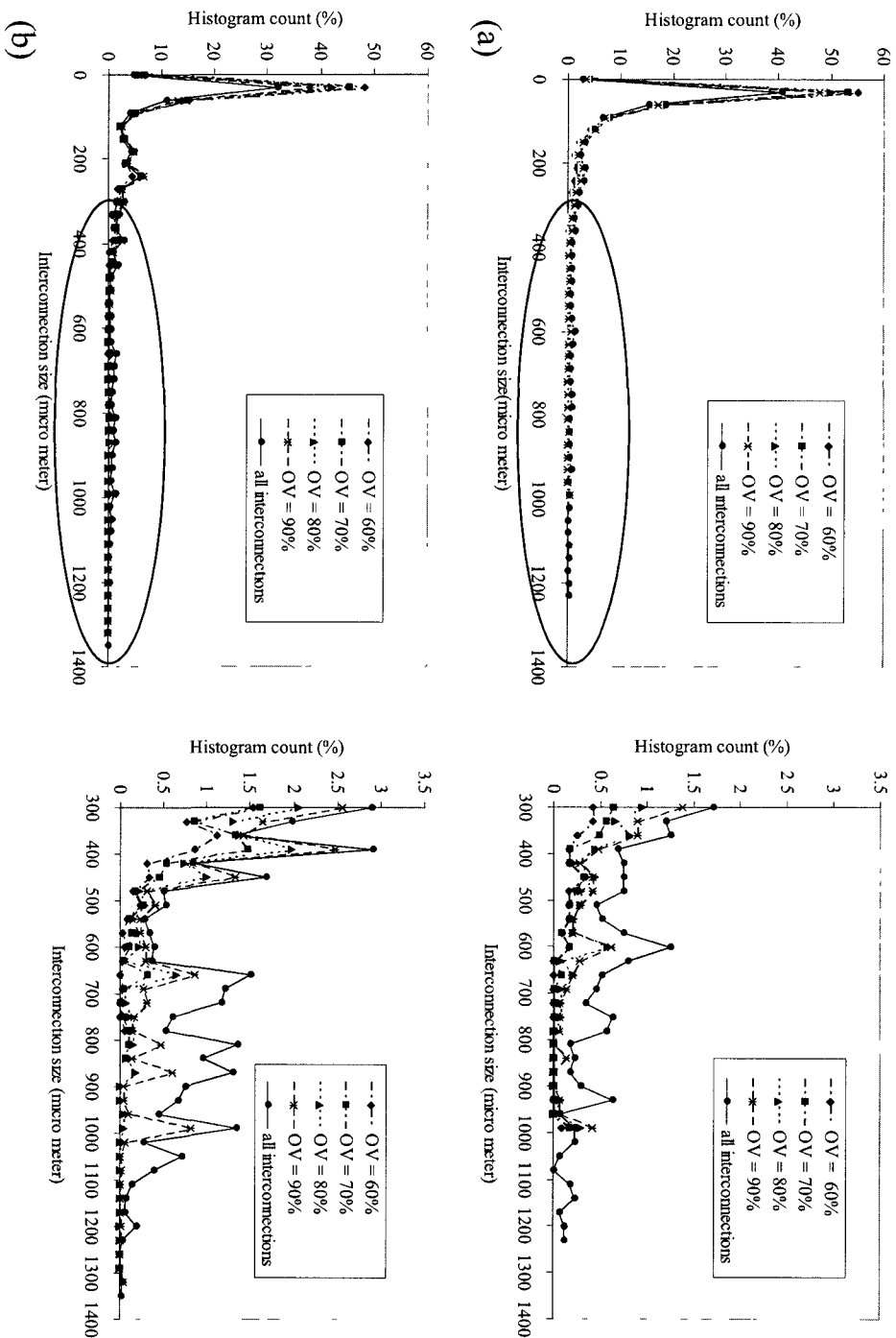


Figure 4-8 The impact of numerical effect on interconnection size distribution of (a) Sample D-15 μm scan, (b) Sample D-15 μm artificial and (c) Sample D-30 μm scan. Removing the virtual interconnections considerably affect on distribution of interconnections larger than 300 μm (Continue on next page). OV is overlapping volume.

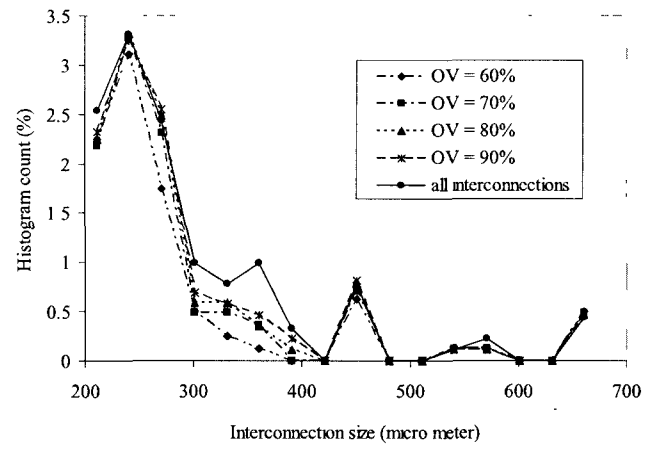
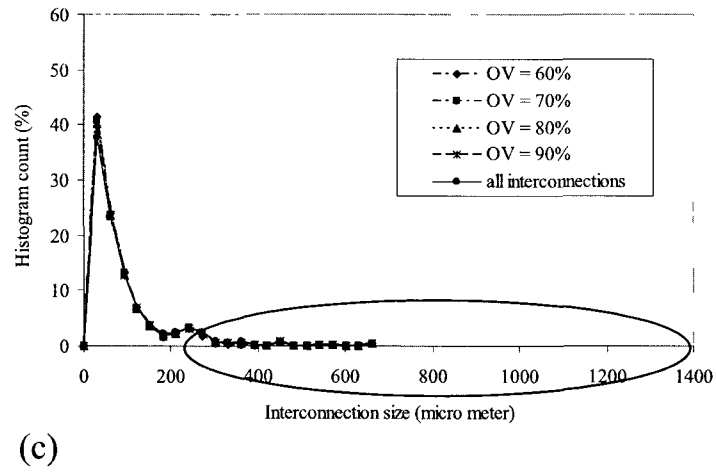


Figure 4-8 Continue

Figure 4-9 presents the difference between the pore size of each sample in terms of percent error from 7.5 and 15 μm scan. Small pore size samples with higher voxel / pore size ratio revealed larger differences.

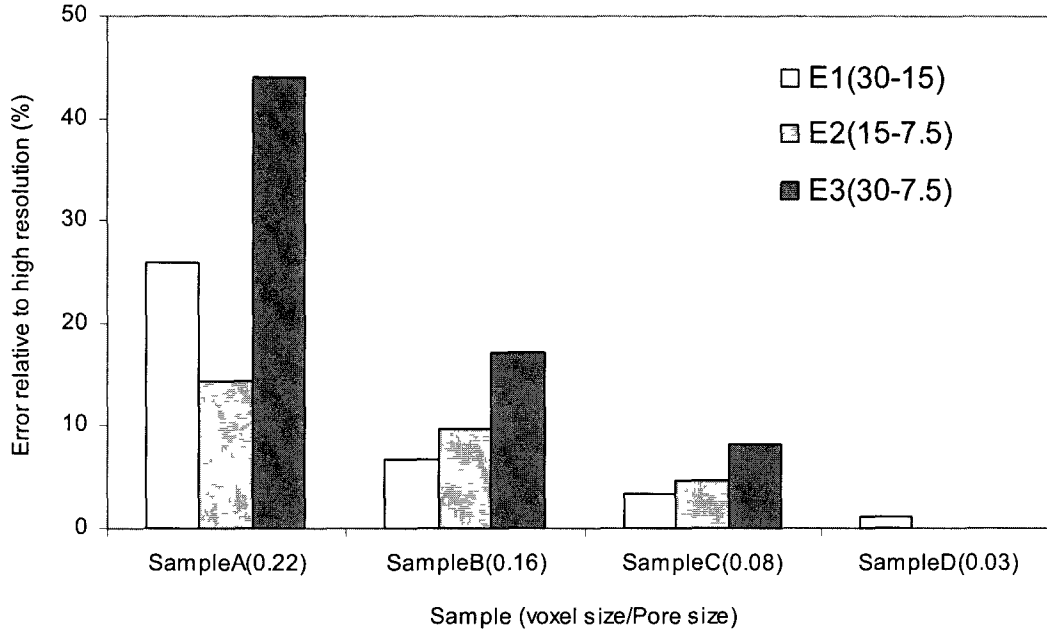


Figure 4-9 Percent errors relative to high resolution datasets versus four different bone substitute samples. Voxel size/pore size ratio calculated based on voxel size of 30 μm and corresponding computed pore size. E1 (30-15): represent the percent error between the pore size analysis at 30 μm and 15 μm . E2 (15-7.5): represent the percent error between the pore size analysis at 15 μm and 7.5 μm . E3 (30-7.5): represent the percent error between the pore size analysis at 30 μm and 7.5 μm .

4.5 Discussion

The objective of this study was to improve the characterization of pores and interconnections size of bone substitutes. Pore and interconnection size are reported to have a great impact on vascularization and new bone formation. In such porous material, pores provide a location for new bone cells and interconnections provide the ways for cell transports [22, 23]. In this study, we focused on the accurate characterization of the substitute structural parameters. The effort was to improve the characterization results by increasing the voxel resolution using both numerical methods and high-resolution scans.

Previous studies in the field of trabecular bone [4, 11, 12] demonstrated that the structural parameters are highly influenced by the voxel size. In particular, it was shown that higher resolution scans result in smaller and well defined features. Since the β -TCP bone substitutes have a porous structure, the structural parameters of substitute could be also affected by resolution of scanned images. For this purpose, the subvoxel algorithm [4] was applied to low resolution (30 μm) images of four types of bone substitutes to artificially generate the 15- μm resolution images. Analysis of artificially generated high resolution images indicated unexpected results with respect to the interconnection size in that the interconnection size has increased for samples C and D. This finding led us to scan the four samples at higher resolutions (15 and 7.5 μm) and to compare the results obtained from artificial and scanned datasets. We showed that decreasing the voxel size can lead to detect more features of structure and these new boundary features can be misleading with respect to interconnection size calculation. Furthermore, we have demonstrated how to overcome these boundary effects. The readers are advised that these effects do not influence the pore size characterization because the unique methods applied to find interconnections.

We have expanded our analysis and examined both the volume and number based averages. Both provide complementary information. The number based average is provided by the arithmetic mean. The volume based average takes into consideration the volume of each pore and thus the smaller pores are less important when calculating the mean.

Generally, due to inability to detect smaller pores in low-resolution images [11], the N-b average pore size increased with increasing the voxel size. Larger N-b average pore size can be also related to the loss of detecting smaller material parts, which result in larger void space in the structure [11, 12, 17]. Furthermore, the N-b average pore size showed the similar trend in relation to voxel size for all samples. However, the V-b average pore size showed inconsistent trends among the samples (Table 4-1). This unclear trend can be attributed to the definition of V-b averaging in which the pore sizes were weighted using the volume of respective sphere in order to calculate the average. It is evident that a small pore has less contribution in calculating V-b average pore size. Therefore depending on the size and number of small pores detected in high-resolution images the V-b average pore size showed various trends when voxel size reduced. The readers are strongly advised to review the pore distribution and to appreciate how the mean values are being calculated.

Furthermore, due to detecting small structures when using higher resolution images, particularly between pores [11], the interconnection size was expected to decrease, accordingly. The opposite direction of change in interconnection size of sample D (15 μm) and sample C (7.5 μm) were therefore surprising to us. It was hypothesized that the increasing of interconnection size of samples C and D was caused by the local irregularities and boundary effects appeared on the material surface in high resolution images. It is clear that detecting more details on the surface provides sharper and more irregular material surface [12]. These irregularities on the surface affect the FDT values and change the FDT map slightly.

According to the max-min algorithm, the saddle voxels were locally extracted based on the FDT values (Figure 4-7). Changes in FDT map affect the local numerical detection and result in finding new saddle voxels that represent new virtual interconnections. As shown in Figure 4-2, the sizes of these virtual interconnections are in the range of adjacent pores, therefore leading to an increase in the interconnection size. Intensive visual and numerical inspection of the images and related FDT maps made us believe that these irregularities and boundary effects are the cause for the increasing interconnection size in the high resolution images.

In order to examine the hypothesis, additional conditions were applied to eliminate the boundary effects and the distributions were carefully analyzed. In these added conditions, interconnections, which overlap with adjacent pores, were removed. As illustrated in Figure 4-7c and Figure 4-7d, removing interconnections overlapping with adjacent pores in samples C (7.5 μm) and D (15 μm), scan and artificial dataset, led to considerable decrease of the average interconnection size. These results confirm that removing of new overlapping interconnections significantly decreases the mean interconnection size and produces results that are consistent with the literature.

Analysis of interconnection size using the high-resolution images demonstrated that for samples A and B, the average interconnection size dropped from 63 μm to 21 and 29 μm , respectively. According to existing paradigms, a minimum interconnection size of 50 μm is generally required for bone ingrowth [22, 24, 25]. Accordingly, our results related to samples A and B may imply that these samples do not allow cell migration inside the structure. However the biological in-vivo outcomes obtained from implanting these samples in bone defects of sheep [26] revealed positive results in terms of good osteoconduction and bone formation in these samples. The discrepancy between biological results and interconnection size can be interpreted mechanisms following mechanisms. First, the properties of scaffold material and second, the effect of micropores on bone formation. Due to bioresorbability of scaffold material, the size of pores and interconnections are modified in the in vivo environment, over time. This fact leads to enlarge small interconnections or create new interconnections between pores. It is also in agreement with the description of Lu et al [22], in which they mentioned that “in resorbable material the density of pore and interconnection is more important than their size because the sizes are enlarged by degradation”.

In addition, a number of recent studies have shown that micropores (typically defined as pore sizes less than 10 μm) in the structure of CaP-based scaffolds can indeed support the bone ingrowth [27, 28, 29]. Levengood et al. [27] observed the presence of bone, osteoid and osteogenic cells in micropores. The migration of osteoprogenitor cells inside the micropores and the subsequent bone formation leads to ingrowth of bone through the scaffold material [27]. These findings indicate the development of bone inside micro size

void features. Consequently, the biological results of Samples A and B can be related to the combination of aforementioned mechanisms, including the bioresorbability of CaP components of scaffold material and development of bone ingrowth into micro size void space.

There is a third potential mechanism for explaining the biological results. Specifically the interconnection size distributions of samples A and B (Figure 4-6a and Figure 4-6b) show that 5% of all interconnections were above 50 μm and this can be sufficient to provide an interconnected network for bone cells to migrate into the structure. As a matter of fact the permeability estimation of the samples investigated in this study shows that the permeability values of all substitutes are in the same order of magnitude as published in Ref. [15].

Since the pore size and interconnection size of sample D at 30 μm and 15 μm resolution exhibited similar distributions and the average pore size and porosity were almost the same, we didn't examine the analysis of sample D at 7.5 μm .

The parameters calculated from scan and artificial dataset at 15 μm resolution exhibited similar pattern of resolution dependency between the samples. However the values obtained from each method (scan and artificial) were not identical. The error presented between the scan and artificial results (Table 4-2) can be described by the inability of subvoxelization process to present the details which were not detected in original low resolution images.

4.6 Conclusion

Micro-CT based scaffold characterization became an important mean for material scientists to understand the complexity of bone repair. Accuracy of the geometric characterization is a key in the process because of the existing paradigms interrelating microstructural features such as pore and interconnection size with bone repair and formation process. We have applied both numerical and physical subvoxelization to improve the characterization accuracy. Subvoxelization, in particular when using high resolution scanners, allows for more accurate descriptions but also can lead to undesired

boundary effects. We would like to draw the attention of the readers to this boundary effects that can influence the calculation of mean values. We have provided a mean to understand the boundary effects. Using the higher resolution images showed that the interconnection size in the scaffolds A and B reduced to around 20 μm and our in vivo data showed that these resorbable substitutes provided adequate vehicle for bone ingrowth. The paradigm of 50 μm being essential for adequate bone ingrowth needs to be evaluated in future research in the light of the results of this study and a new related literature in the field.

4.7 Reference

- [1] P. Ruegsegger, B. Kollar and R. Muller, A microtomographic system for the non-destructive evaluation of bone architecture, *Calcif. Tiss. Int.* 58 (1996). 24-25

- [2] Ho ST, Hutmacher DW. A comparison of micro CT with other techniques used in the characterization of scaffolds. *Biomaterials* 2006; 27(8):1362–76.

- [3] Van Lenthe GH, Hagenmueller H, Böhner M, Hollister SJ, Meinel L, Mueller R. Nondestructive micro-computed tomography for biological imaging and quantification of scaffold-bone interaction in vivo. *Biomaterials* 2007; 28(15):2479–90.

- [4] Hwang SN, Wehrli FW. Subvoxel processing: a method for reducing partial volume blurring with application to in vivo MR images of trabecular bone. *Magn Reson Med* 2002, 47(5):948–957.

- [5] Majumdar S, Newitt D, Mathur A, Osman D, Gies A, Chiu E, Lotz J, Kinney J, Genant H. Magnetic resonance imaging of trabecular bone structure in the distal radius: relationship with X-ray tomographic microscopy and biomechanics. *Osteoporos Int* 1996, 6(5):376_385.

- [6] Last D, Peyrin F, Guillot G. Accuracy of 3D MR microscopy for trabecular bone assessment: a comparative study on calcaneus samples using 3D synchrotron radiation microtomography. *Magma* 2005, 18 (1):26_34.
- [7] Pothuaud L, Laib A, Levitz P, Benhamou CL, Majumdar S. Three-dimensional-line skeleton graph analysis of high-resolution magnetic resonance images: a validation study from 34_microm-resolution microcomputed tomography. *J Bone Miner Res* 2002, 17(10):1883_1895
- [8] Tabor Z. Analysis of the influence of image resolution on the discriminating power of trabecular bone architectural parameters. *Bone* 2004, 34(1):170_179.
- [9] Kothari M, Keaveny TM, Lin JC, Newitt DC, Genant HK, Majumdar S. Impact of spatial resolution on the prediction of trabecular architecture parameters. *Bone* 1998, 22 (5):437_443.
- [10] Muller R, Koller B, Hildebrand T, Laib A, Gianolini S, Ruegsegger P. Resolution dependency of microstructural properties of cancellous bone based on threedimensional mu-tomography. *Technol Health Care* 1996, 4 (1):113_119.
- [11] Cooper d, Turinsky A. Sensen Ch, Hallgrimsson B. Effect of voxel size on 3D micro-CT analysis of cortical bone porosity. *Calcified Tissue Inc* 2007, 80 (3):211-219.
- [12] Peyrin F, Salome M, Cloetens P, Laval-Jeantet AM, Ritman E, Ruegsegger P. Micro-CT examinations of trabecular bone samples at different resolutions: 14, 7 and 2 micron level. *Technol Health Care* 1998, 6 (5-6):391_401.
- [13] Wu Z, Chung H-W, Wehrli FW. A Bayesian approach to subvoxel tissue classification in NMR microscopic images of trabecular bone. *Magn Reson Med* 1994; 31(3):302-308.

- [14] Darabi A, Chandelier F, Baroud G. Thickness analysis and reconstruction of trabecular bone and bone substitute microstructure based on fuzzy distance map using both ridge and thinning skeletonization. *Can J Elect Compt Eng* 2009; 34(1-2):57–62.
- [15] Bashoor-Zadeh M, Baroud G, Bohner M. Geometric analysis of porous bone substitutes using micro-computed tomography and fuzzy distance transform, *Acta Biomater* 2010; 6(3): 864-875.
- [16] Jones AC, Arns CH, Hutmacher DW, Milthorpe BK. The correlation of pore morphology, interconnectivity and physical properties of 3D ceramic scaffolds with bone ingrowth, *Biomaterials* 2009;30 (7):1440–1451.
- [17] Kim DG, Christopherson GT, Dong XN, Fyhrie DP, Yeni YN. The effect of microcomputed tomography scanning and reconstruction voxel size on the accuracy of stereological measurements in human cancellous bone. *Bone* 2004; 35 (6):1375_1382.
- [18] Bohner M, van Lenthe GH, Gruenenfelder S, Hirsiger W, Evison R, Mueller R. Synthesis and characterization of porous b-tricalcium phosphate blocks. *Biomaterials* 2005; 26(31):6099–105.
- [19] Bohner M. Calcium phosphate emulsions: possible applications. *Key Eng Mater* 2001; 192–195:765–8.
- [20] Wehrli FW, Saha PK, Gomberg BR, Song HK. Noninvasive assessment of bone architecture by magnetic resonance micro-imaging-based virtual bone biopsy. *Proc IEEE* 2003; 91(10):1520–1542.
- [21] Sladoje N, Nystrom I, Saha PK. Measurements of digitized objects with fuzzy borders in 2D and 3D. *Image Vis Comput* 2005; 23(2):123–32.

[22] Lu JX, Flautre B, Anselme K, Hardouin P, Gallur A, Descamps M, et al. Role of interconnections in porous bioceramics on bone recolonization in vitro and in vivo. *J Mater Sci Mater Med* 1999;10(2):111–20.

[23] Mastrogiacomo M, Scaglione S, Martinetti R, Dolcini L, Beltrame F, Cancedda R, et al. Role of scaffold internal structure on in vivo bone formation in macroporous calcium phosphate bioceramics. *Biomaterials* 2006;27(17): 3230–7.

[24] Chang B-S, Lee C-K, Hong K-S, Youn H-J, Ryu H-S, Chung S-S, Park K-W. Osteoconduction at porous hydroxyapatite with various pore configurations. *Biomaterials* 2000;21(12):1291–8.

[25] Otsuki B, Takemoto M, Fujibayashi S, Neo M, Kokubo T, Nakamura T. Pore throat size and connectivity determine bone and tissue ingrowth into porous implants: three-dimensional micro-CT based structural analyses of porous bioactive titanium implants. *Biomaterials* 2006;27(35):5892-900.

[26] von Doernberg MC, von Rechenberg B, Bohner M, Gruenenfelder S, van Lenthe GH, Mueller R, et al. In vivo behavior of calcium phosphate scaffolds with four different pore sizes. *Biomaterials* 2006;27(30):5186-98.

[27] Lan Levengood SK, Polak SJ, Wheeler MB, Maki AJ, Clark SG, Jamison RD, Wagoner Johnson AJ. Multiscale osteointegration as a new paradigm for the design of calcium phosphate scaffolds for bone regeneration. *Biomaterials* 2010;31(13):3552-63.

[28] Habibovic P, Sees TM, van den Doel MA, van Blitterswijk CA, de Groot K. Osteoinduction by biomaterials – physicochemical and structural influences. *J Biomed Mater Res A* 2006;77(4):747–62.

[29] Hing KA, Annaz B, Saeed S, Revell PA, Buckland T. Microporosity enhances bioactivity of synthetic bone graft substitutes. *J Mater Sci Mater Med* 2005;16(5):467–75.

CHAPTER 5

Simulation of cell-mediated resorption of porous bone substitutes

M. Bashoor-Zadeh¹, G. Baroud¹, M. Bohner²

(1) Laboratoire de Biomécanique, Département de Génie, Université de Sherbrooke,
Sherbrooke, QC, Canada J1K 2R1, (2) Dr Robert Mathys Foundation, Bettlach,
Switzerland

To be submitted to one of the field journals

Corresponding author:

Gamal Baroud, Ph.D., Tenured Professor

Canada Research Chair in Skeletal Reconstruction and Biomedical Engineering

Director, Biomechanics Laboratory

Tel.: (819) 821-8000 ext. 61344

Fax: (819) 821-7163

UNIVERSITE DE SHERBROOKE

Faculté de génie - Département de génie mécanique

2500 boul. Université, Sherbrooke, QC, Canada J1K 2R1

5.1 Abstract

A computer model was established to simulate the resorption process of calcium phosphate bone substitutes. The resorption simulation algorithm had two main steps: (1) colonization of pores by resorbing cells in which, the pores and interconnections are enlarged to enable ingrowth of blood vessels and (2) resorption of bone substitute material at interface surface which is accessible for blood vessels. Since the scaffold architecture was complex, μ CT data and novel fuzzy imaging techniques were combined to reconstruct the precise scaffold geometry and then new image processing operators such as labelling and skeletonization were developed to perform the resorption simulation steps. The proposed algorithm was verified by comparing its results with the analytical results of a simple geometry and experimental in-vivo data of β -TCP bone substitutes with more complex geometry. A correlation coefficient between the simulation results and both analytical and in-vivo data, was found to be greater than 0.9. Moreover, the resorption rate was measured in two ways; (1) ceramic volume fraction rate (volume resorption rate) in which the resorption rate has been calculated using prony's series to do fit the resorption data curve and (2) total resorbed thickness rate (linear resorption rate) which was measured by calculating the total thickness resorbed over time. In order to study the resorption process from the periphery to the center of substitutes, the resorption rate was calculated at different regions of scaffolds. Faster resorption in external region specifically at earlier resorption time was in agreement with the clinical outcomes. In addition, the effect of different conditions, including type of resorption (unidirectional or pluridirectional), minimum interconnection size required for cell ingrowth (50 or 100 μ m) and resolution of μ CT images (15 or 30 μ m), on prediction of model were studied.

5.2 Introduction

Porous ceramic bone substitutes have been widely used in orthopaedic applications to support healing of large bone defects [1-3]. Among the various materials that can be used, calcium phosphate ceramics have a special position for their similarity to bone mineral composition and their excellent biocompatibility, bioactivity, osteoconduction and osteointegration properties [1, 4-8]. However, there is still a need to improve these

ceramics to enhance their functionality and their ability to support the healing of large bone defects. One particular field of interest is the determination of the optimum porous architecture, for example for an effective bone ingrowth (formation) and ceramic resorption [3, 9-16]. Despite a large number of *in vivo* studies, there is still a large confusion even though a consensus seems to emerge that the level of porosity should be larger than 50-60%, the minimal interconnection size should be larger than 50-100 μm and the mean pore size should be between 100-500 μm [3, 8, 9, 17, 18].

So far, most approaches used to determine the optimum architecture have been pragmatic: samples were implanted and the biological response was analyzed. However, there has been a trend towards theory driven approaches: a model is proposed, samples are produced and characterized – for example using free form fabrication approaches [19] and micro-computed tomography [36, 39], an *in vivo* study is performed, and the biological response is evaluated based on the model [19-21]. For example, Bohner and Baumgart [22] proposed a few years ago a model to predict the impact of morphological parameters on cell mediated resorption of bone substitutes. The comparison between this model and *in vivo* results gathered with dense cylindrical or spherical bone substitutes demonstrated the model adequacy [22]. However, since most bone substitutes are porous and hence allow cell invasion into the bone substitute, it would be more relevant to test the model on the *in vivo* behaviour of porous bone substitutes. The aim of this manuscript is to fulfill this task by simulating the *in vivo* behaviour of 4 different β -tricalcium phosphate (β -TCP) scaffolds varying in mean macropore size [23, 24]. The latter scaffolds were implanted in a sheep model for 6, 12 and 24 weeks [15].

The details of the novel algorithm are described in the next section and followed by the results obtained from simulation analysis of four groups of β -TCP scaffolds. The simulation results were then compared with both analytical and *in vivo* experimental data in Ref [15].

5.3 Material and Method

5.3.1 Scaffold fabrication and Image acquisition

Four β -TCP bone substitutes varying in macropore size (a macropore is defined here as a pore with a mean diameter superior to 50 micrometers) were produced by the so-called calcium phosphate emulsion method [23, 25]. According to this method, variations in emulsifier concentration led to various macropore sizes (Figure 5-1) while the micropore size (a micropore is defined here as a pore with a mean diameter in the range of 100 nanometers to 50 micrometers) and porosity were constant (Figure 5-2). For all macropore sizes, the macroporosity, microporosity and total porosity were close to 21%, 54% and 75%, respectively [23]. Macropores were spherical and mostly interconnected [23], and had a mean diameter of 128, 196, 345 and 871 μm (as determined by μCT ; [24]). The samples were cylindrical with a diameter of 8mm and a height of 13 mm. Six samples of each macropore size were randomly selected and analyzed for resorption simulation.

For 3D non-destructive geometric and simulation analysis, the samples were scanned with a Scanco Medical AG μCT 40 (Bassersdorf, Switzerland) scanner at 30 μm isotropic resolution [23]. The images of cylindrical core of 7 mm diameter and 10.5 mm height were then selected as volume of interest.

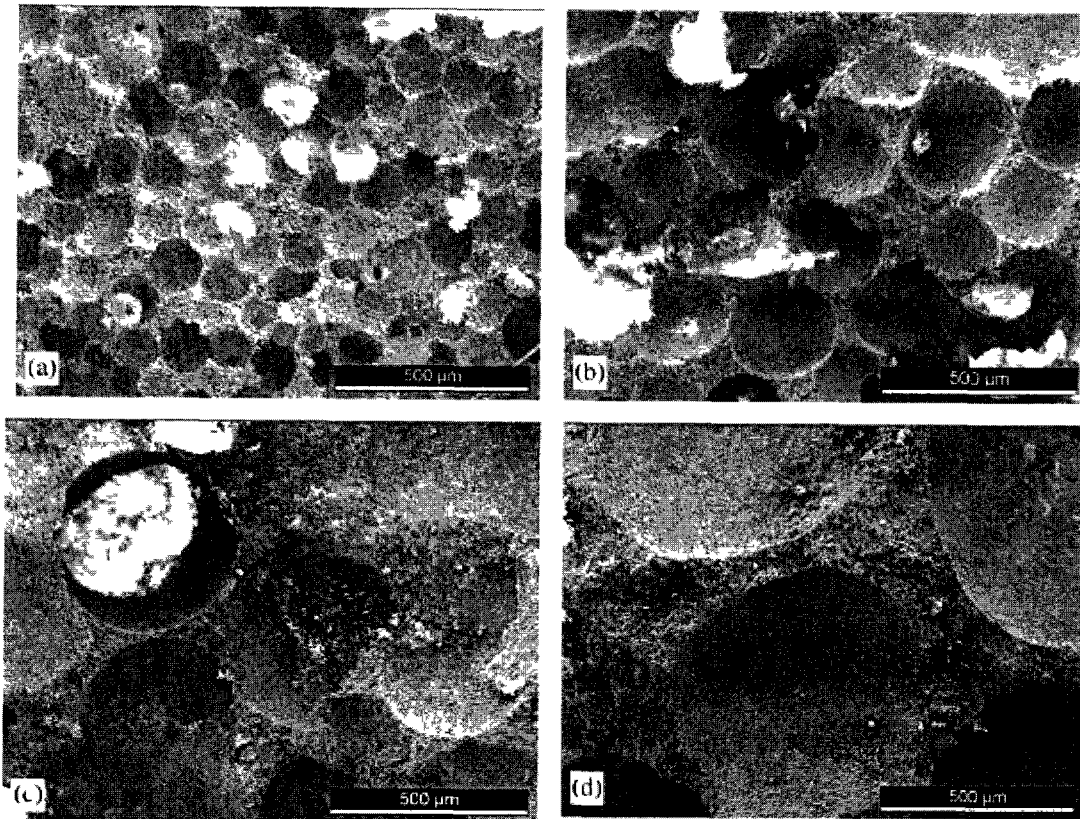


Figure 5-1 Representative SEM photos of the macropore structure of four groups of β -TCP scaffolds with different macropore sizes. (a) group A, (b) group B, (c) group C and (d) group D. The scale bar corresponds to 0.5 mm [23].

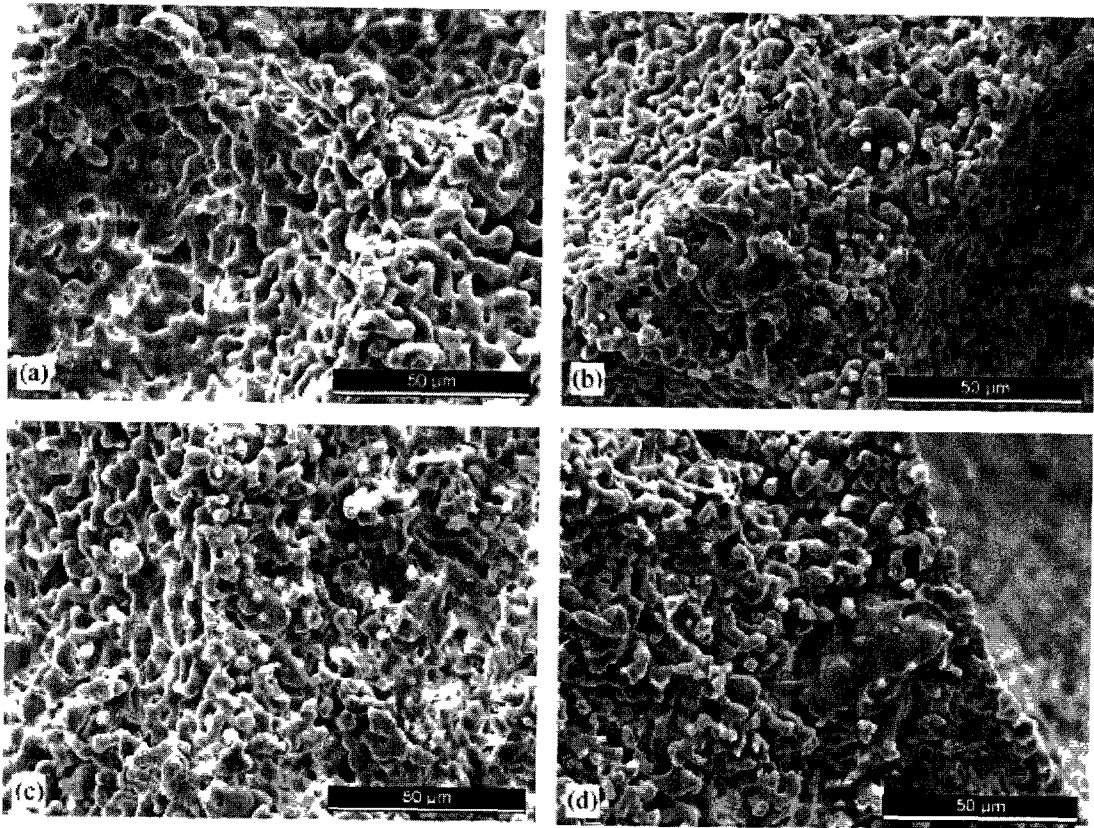


Figure 5-2 Representative SEM photos of the micropore structure of four groups of β -TCP scaffolds with different macropores sizes. (a) group A, (b) group B, (c) group C and (d) group D. The scale bar corresponds to 50 μm [23].

5.3.2 Application of the model on the *in vivo* data

Before going into the details of the simulation procedure, a few details must be given on the resorption model and the procedure used to apply the model on the *in vivo* data.

The two main assumptions of the model that are relevant here are that (a) material resorption occurs at a constant linear rate (i.e. one layer resorbed in each iteration) from the material surface, (b) provided the surface can be reached by blood vessels of 50 μm in diameter [14].

Since the scaffold architecture was complex and macropores were not fully interconnected, complex numerical algorithms had to be used. Specifically, μ CT data and novel fuzzy imaging techniques were combined to reconstruct the explicit and precise scaffold geometry. New image processing operators such as labelling and skeletonization were developed and introduced to perform the resorption simulation steps. In more details, the pores that could be colonized by resorbing cells had to be identified using the pores and interconnections analysis, and then resorption in those pores had to be simulated. The same procedure had to be applied after each iteration step until the entire material was resorbed. The simulated results could then be compared to the *in vivo* data to determine the adequacy of the model. The two parameters that could be varied were the minimum interconnection size that allows blood vessel ingrowth and the linear rate of (surface) resorption (material thickness resorbed in a time increment). The details of this approach are described in the next sections.

5.3.3 Geometric analysis

The geometric analysis algorithm is extensively described in Ref. [24]. Briefly, for geometric analysis, two threshold values corresponding to material and void space were selected via intensity histogram and visual inspection. To determine what was void (or object) and what was material (or non-object), the scanned images were fuzzified by a sigmoidal function based on the two pre-selected threshold values.

The latter results were then used to compute the fuzzy distance transform (FDT) map. The FDT value at each object's voxel was defined as the shortest fuzzy distance from that voxel to the non-object. In this study, the FDT algorithm introduced by Darabi et al. [26] was performed to calculate the FDT map. Once the FDT map was determined, the next step consisted in characterizing macropore and interconnection size by applying the max-min algorithm to FDT map [24]. This algorithm detects the local maxima (= pore size) and minima (= pore interconnection) of the FDT map.

5.3.4 Skeletonization and Reconstruction

The process of extracting central voxels of object (here is void space) is called skeletonization. In this study, a ridge detection algorithm was performed on FDT map to obtain the skeleton of void space of porous structure.

The algorithm mainly follows the theory and definition described by Niblac et al. [27] and Haralic and Shapiro [28]. The steps of skeletonization algorithm have been already described in Refs. [24, 26]. The skeleton is used to reconstruct the scaffolds. The void spaces are reconstructed by letting spheres grow around skeleton voxels with radius equal to their FDT value [29]. The main purpose of creating two phase sample based on skeletonization and reconstruction was to reserve more information by considering the fuzzy nature of scanned images.

The reconstructed samples were then used for resorption simulation. The skeleton is also used to control the size of void space and detect the accessible spaces for resorbing cells.

5.3.5 Creating models with FCC lattice of pores

The first step of this study was to validate the simulations presented here by comparing simulation with analytical results. In the cell-mediated resorption model proposed by Bohner and Baumgart [22], macropores were piled according to a face-centered cubic lattice (Figure 5-3). Therefore, in order to compare the simulation with analytical results [22], 3D cubical structures of pores were created by using image processing tools. A voxel size of 10 μm was set to form porous structures.

The block size, L , and the inter-pore distance, d , were set to be constant for all blocks and pore radius was increased from 100 to 500 μm .

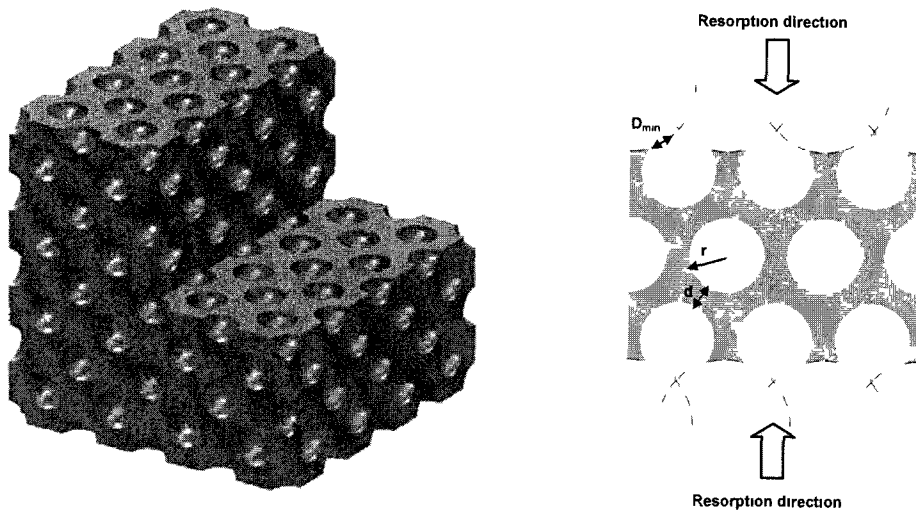


Figure 5-3 (a) Porous blocks with isolated spherical pores that are ordered in FCC lattice. (b) Schematic representation of blocks resorption. Resorption occurred from both sides of the blocks with perpendicular direction to block surface (arrows direction). The large circles, which were drawn by break lines, represent the pores that have been enlarged by resorption. r is the pore radius, d is the inter-pore distance and D_{min} is defined as the minimum interconnection size required for vascularization and migration of the cells into the porous structure.

5.3.6 Resorption simulation analysis

The resorption simulation was performed in two steps: (a) colonization of a pore by resorbing cells and (b) resorption of the bone substitute material.

Since vascularization inside the porous structure is essential for cellular resorption, some pores and pore interconnections had to be enlarged by resorption to enable blood vessels ingrowth. So, D_{min} was defined as the *minimum interconnection size* required for vascularization or in other words for the migration of the cells into the porous structure. To determine which macropore was invaded by cells, the algorithm looked at the size of pores and interconnections at each skeleton point and compared these values to the minimum interconnection size, D_{min} . This allowed the detection of all the pores that could be accessed by resorbing cells. Once defined, the walls of these pores and pore

interconnections were “resorbed” by one voxel size, i.e. the first voxel layer was moved from the “material” to the “void” space. This resorption enlarged all existing interconnections and created new interconnections. This procedure was repeated until all the material had been resorbed.

In the following, the specific steps of the resorption simulation algorithm are presented in detail.

1. Input the reconstructed structure and the skeleton voxels of void space (Skel) with corresponding FDT values;
2. Label the connected pores in the reconstructed structure (Figure 5-4a);
3. Find the skeleton voxels with FDT value less than $(D_{\min} / 2)$ (Figure 5-4b);

$$S_E = \{S \in Skel \mid FDT(S) \leq (D_{\min} / 2)\} \quad (5.1)$$

Where, S is a skeleton point.

4. Block the sample at S_E by growing the spheres (in 3D) centered at S_E with the radius equal to FDT value of that point (Figure 5-4c);
5. Find the pore which are accessible from outside, for this step the algorithm finds the skeleton branches corresponding to open pores with a diameter larger than D_{\min} (Figure 5-4d);
6. Colonization of the accessible pores by resorbable cells, (Figure 5-4e);
7. Resorbing one layer of bone substitute material at interface surface, (Figure 5-4f);
8. Output the resorbed structure at corresponding iteration;
9. Repeat step 5 to 8 for each pore until the structure is fully resorbed.

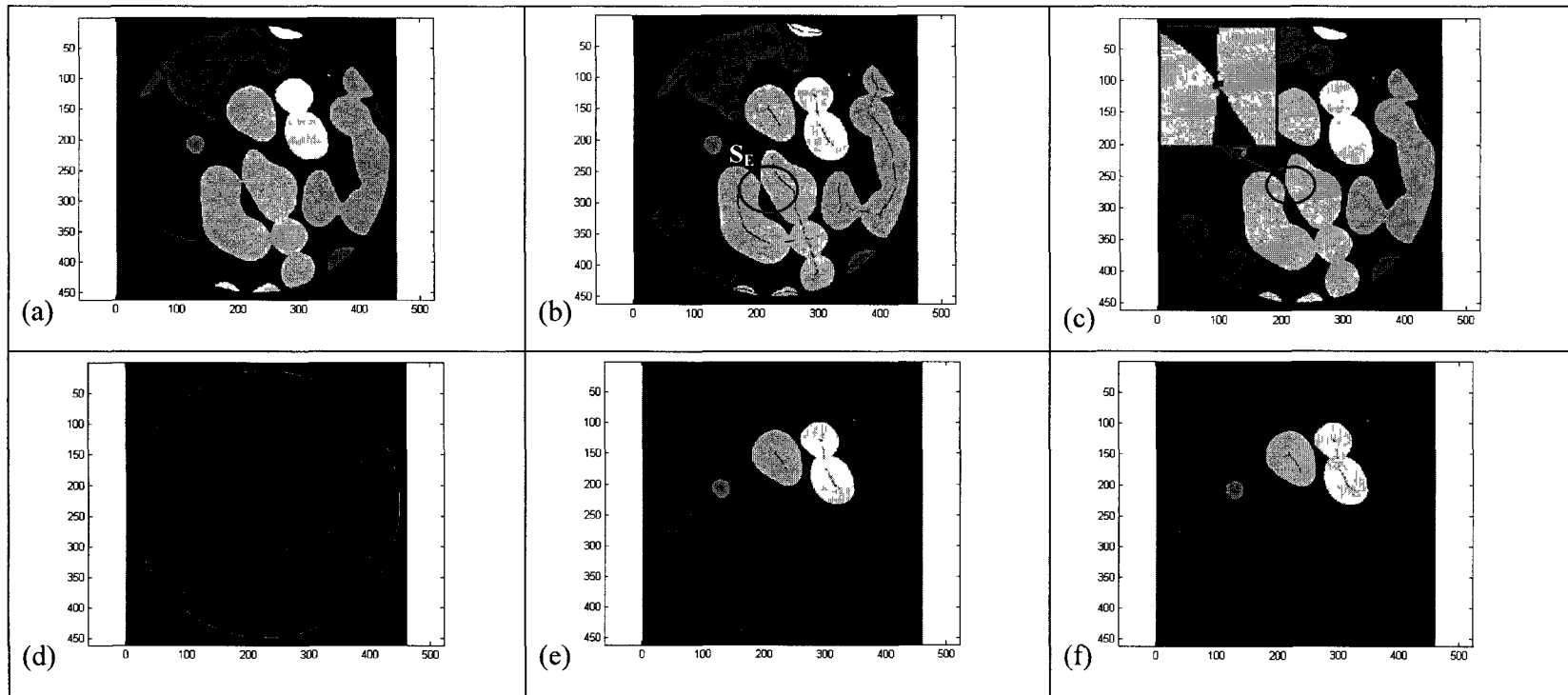



Figure 5-4 2-D representative of resorption steps, (a) Pores are labeled, (b) The skeleton point are extracted, S_E are skeletons with FDT value less than $D_{min}/2$, (c) Pores and interconnections with diameter less than D_{min} are blocked by growing the circles (or spheres in 3D) centered at S_E with the radius equal to FDT value of that point, (d) Skeleton branches corresponding to open pores with appropriate FDT value (i.e. larger than $D_{min}/2$), are detected (e) Pores that can be accessed from the outside are defined, (f) One voxel layer is “resorbed” or “removed” from the accessible surface. (The red lines “”, in figures (b), (d) and (f), are the skeleton voxels of non-resorbed pores)

5.3.7 Prony Method and Resorption Rate

The ceramic volume fraction (CVF) was calculated after each iteration. To compare with experimental data [15], the CVF decay was expanded in time until full ceramic resorption was achieved. The CVF decay results were fitted with the so-called Prony method which is based on a sum of exponential functions (Eq. 5.2):

$$f(t) = \sum_{i=1, 2, 3} K_i e^{-A_i t} \quad (5.2)$$

Where $f(t)$ is the percentage of CVF, t represents time (or iteration no.), K_i and A_i are constant and rate coefficients respectively. The rate of decreasing CVF as resorption rate was estimated using derivative of Prony-series ($f(t)$) with respect to time (an example is given in Figure 5-5).

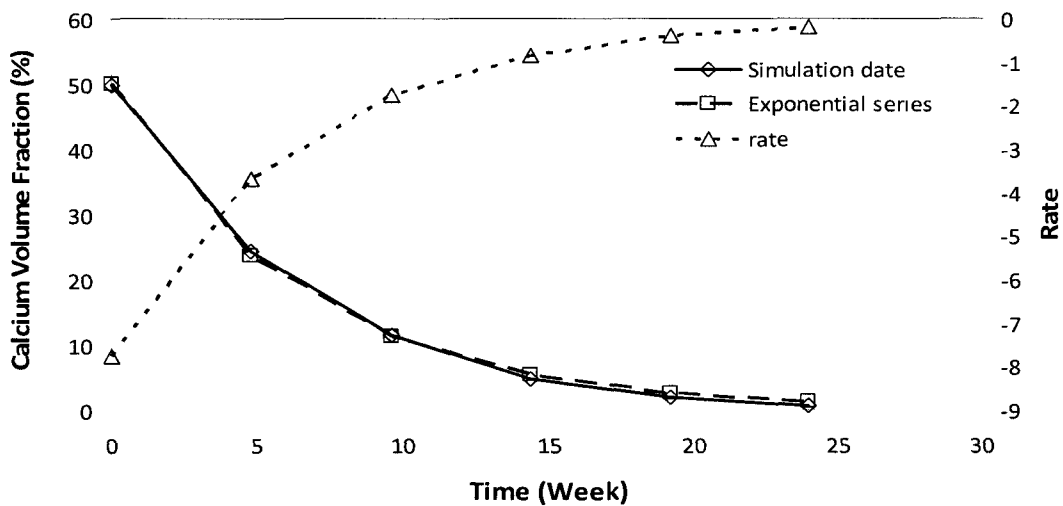


Figure 5-5 The left axis presents the simulation data (\diamond) and the exponential series approximation (Prony-series) of the simulation results (\square). The right axis presents the resorption rate data (Δ) which was obtained from the first derivative of Prony-series with respect to time.

5.3.8 Study design

As previously mentioned, the cell-mediated resorption algorithm of Bohner and Baumgart [22] has two variables: the minimum interconnection size required for blood vessel ingrowth (D_{\min}) and the linear resorption rate. Whereas the latter value was determined by experimental data fitting, the former value was set to a given value. Since authors generally consider that this value should be in the range of 50 to 100 μm [9], D_{\min} was either set at 50 μm or at 100 μm . Beside this parameter, resorption was assumed to proceed from two directions. Since a cylinder consist of three surface areas (side, bottom and top surface), the resorption direction was either set to be (a) unidirectional, i.e. the samples were resorbed through the cylindrical circular side or (b) pluridirectional, i.e. the samples were resorbed through all sides. Combination of D_{\min} values and resorption directions resulted in a total number of four simulation analysis for each sample.

Furthermore, in order to study the resorption from the periphery to the center of substitutes, the resorption rate was calculated at different regions of scaffolds. Accordingly, the scaffold was divided into three cylindrical zones (ROI1, ROI2 and ROI3) with an increasing radius (Figure 5-6).

5.3.9 Effect of voxel size on resorption simulation

To study the effect of voxel size on resorption simulation, one block of each group was selected and scanned at 30 μm and 15 μm resolution and the resorption behavior of block was analyzed for both cases. These blocks were scanned with a SKYSCAN1172 μCT scanner (Desktop x-ray micro tomography, Aartselaar, Belgium). In order to compare the simulation results, the CVF at each resorption iteration of low resolution blocks (30 μm) were compared with the CVF of corresponding even iteration number of high resolution blocks (15 μm).

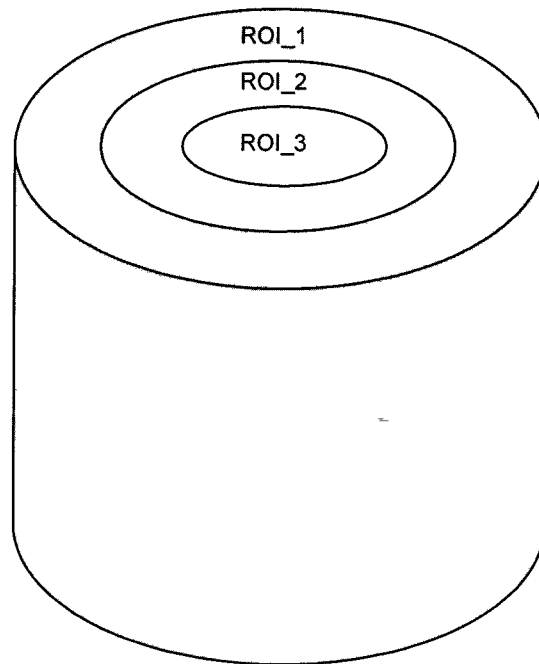


Figure 5-6 Schematic representation of three zones in cylindrical scaffold, ROI1: outer zone, ROI2: middle zone and ROI3: inner zone.

5.3.10 Computational platform

We used reconstructed images for resorption simulation analysis. All computations were performed on Mammouth supercomputers at “Réseau québécois de calcul de haute performance” as a part of “Compute Canada” facilities. Estimating the memory and the time required for analysis depend on the size of input data and complexity of analysis.

5.3.11 Provided in vivo data

The biological results used in this study were provided in collaboration with another research group in Switzerland (Dr Robert Mathys Foundation, Bettlach, Switzerland). The details related to the in vivo test, animal and implantation location were extensively described in Ref. [15]. Briefly, they used adult female Swiss Alpine sheeps of 3–4 years old with a body weight of 64–75 kg. The β -TCP blocks were implanted in long bones of

sheep (left and right proximal humerus, proximal femur, proximal tibia, and distal femur) for 6, 12 and 24 weeks [15].

5.4 Results

The results obtained from resorption simulation algorithm have been compared with the analytical results of FCC lattice geometry [22] and experimental data of more complex substitute structure [15].

Figure 5-7 shows and compares the simulation results of the resorption algorithm with those of the analytical model [22]. The porous blocks had a width of 5mm and an inter-pore distance of 22 μm ($L=5\text{mm}$, $d=22 \mu\text{m}$). The right axis shows the number of iterations required to achieve full resorption. This parameter was obtained by applying the simulation model to the various scaffold designs. The left axis presents the total layer thickness that has to be resorbed for to achieve full ceramic resorption. This parameter was calculated according to the analytical equations presented in Ref. [22], as follow:

$$th_{tot} = r(\sqrt{2} - 1) + d\left(\frac{\sqrt{2}}{2}\right) + \frac{\sqrt{r_i^2 + (2r + d - \sqrt{r^2 - r_i^2})^2} - r}{4r + 2d} L$$

$$\text{for } d > -2(r - \sqrt{r^2 - r_i^2}) \quad (5,3)$$

Where r is pore radius, d is the distance between the pores, r_i is the radius of interconnection (equal to $D_{min}/2$), L is the width of the block.

As depicted in Figure 5-7, , the discrepancy between simulation and analytical model decreased when the macropore size increased, and the data convergence was observed for blocks with macropore radii larger than 300 μm (i.e. 300, 400 and 500 μm). The correlation coefficient (R^2) between experimental and simulation data was superior to 0.9.

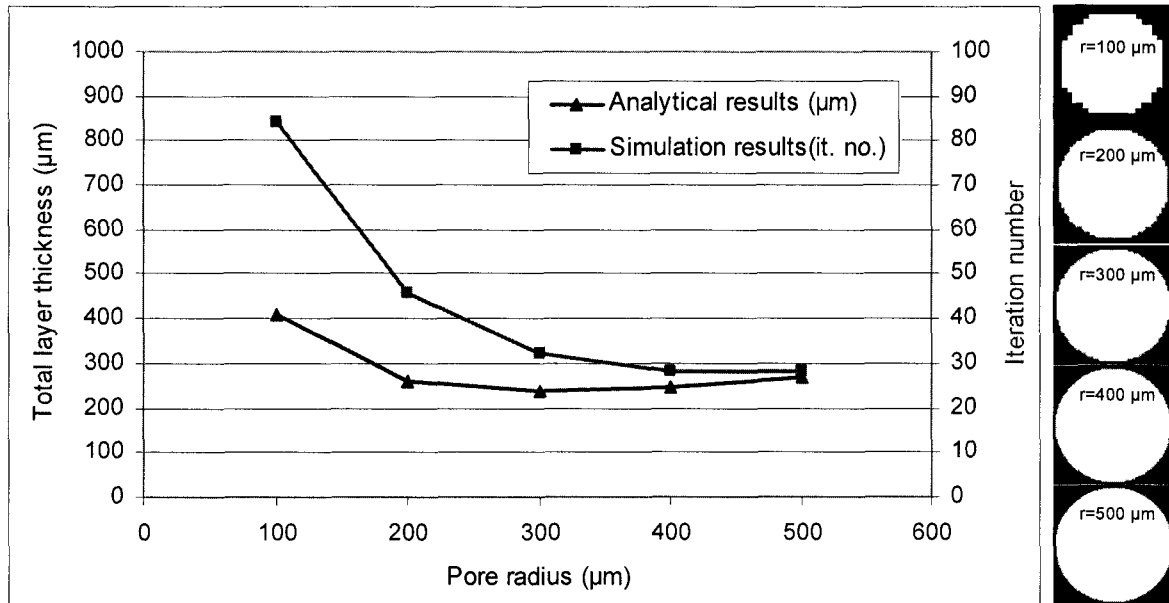


Figure 5-7 (▲)Analytical and (■) simulation results of FCC lattice of pores with various pore radius ranging from 100 to 500 µm. The porous blocks had a width of 5mm and inter-pore distance of 22 µm. A voxel size of 10 µm was set to create the blocks.

The mean macropore and interconnection size of the four scaffold types investigated in this study are summarized in Table 5-1 [24]. The porosity and interconnection size are rather constant from scaffold to scaffold since scaffold porosity is in the range of 50 to 54% and interconnection size lies between 62 and 85 µm. Contrary, the mean pore size varies sixfold between the smallest and largest size.

The resorption simulation analysis of the four scaffold types or groups showed the resorption direction had no effect on resorption time of the samples (Figure 5-8). Also for groups B, C and D, the total resorption duration was not affected by increasing D_{min} . However for group A, the resorption rate decreased with increasing D_{min} to 100 µm. In subsequent calculations, D_{min} is set to 50 µm.

Table 5-1 Geometrical parameters of bone substitutes obtained from μ CT data. The pore size calculated according to two definitions, number-base and volume-base. The surface density was calculated as the ratio of material surface to total volume, this parameter was computed by using CT-Analyzer software (CTAN).

Substitute group	Pore size number-base (μm)	Interconnection size (μm)	Pore size volume-base (μm)	Porosity (%)	Surface density (MS/TV) (mm ⁻¹)
A	128.1 \pm 2.6	61.7 \pm 0.5	170.3 \pm 1.7	50.2	11.5 \pm 0.2
B	195.8 \pm 4.8	64.9 \pm 2.9	217.3 \pm 5.2	52.7	10.0 \pm 0.3
C	364.7 \pm 5.1	65.5 \pm 3.4	415.8 \pm 18.8	53.7	6.5 \pm 0.2
D	871.1 \pm 6.7	85.2 \pm 7.6	972.3 \pm 10.9	52.4	3.3 \pm 0.1

To compare the simulation and biological results [15], the iteration numbers were matched to the period of times reported for completely resorption of ceramic bone substitute [15]. Figure 5-9 illustrates the simulation results and experimental data of the four bone substitute groups. The small standard deviation of simulation data (i.e. CVF) at each point of time shows how small the variation between the resorption behaviours of samples of each group was (SD of group: A<2.1%, B<1.3%, C<0.7%, D<0.6%). As depicted in Figure 5-9, the resorption data of the computational model compares well with the in vivo results, in particular for groups C and D where $r^2 > 0.99$.

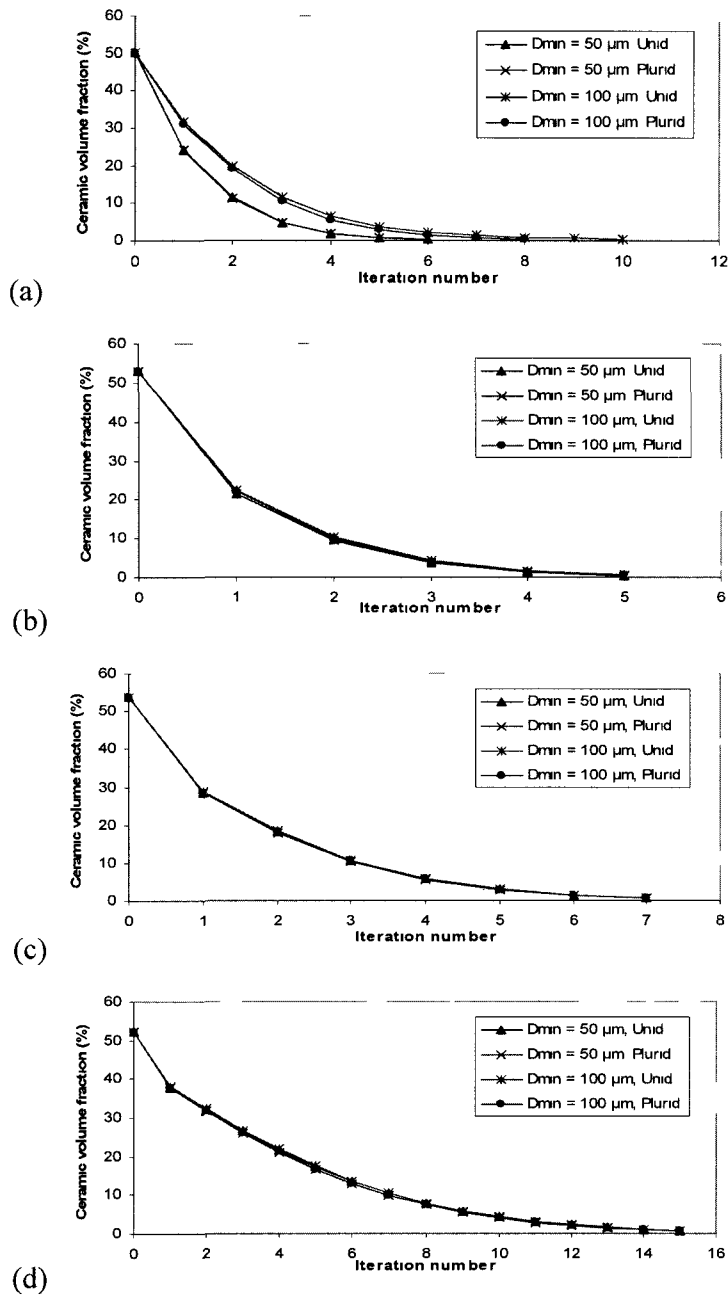


Figure 5-8 Resorption simulation of the four groups of scaffolds have been presented based on different setting conditions, (a) group A, (b) group B, (c) group C and (d) group D. Depending on the minimum interconnection size required for blood vessel ingrowth and the resorption direction, the resorption process of each group was analyzed four times. Dmin was either set to be 50 μm or 100 μm . the resorption direction was either set to be unidirectional or pluridirectional.

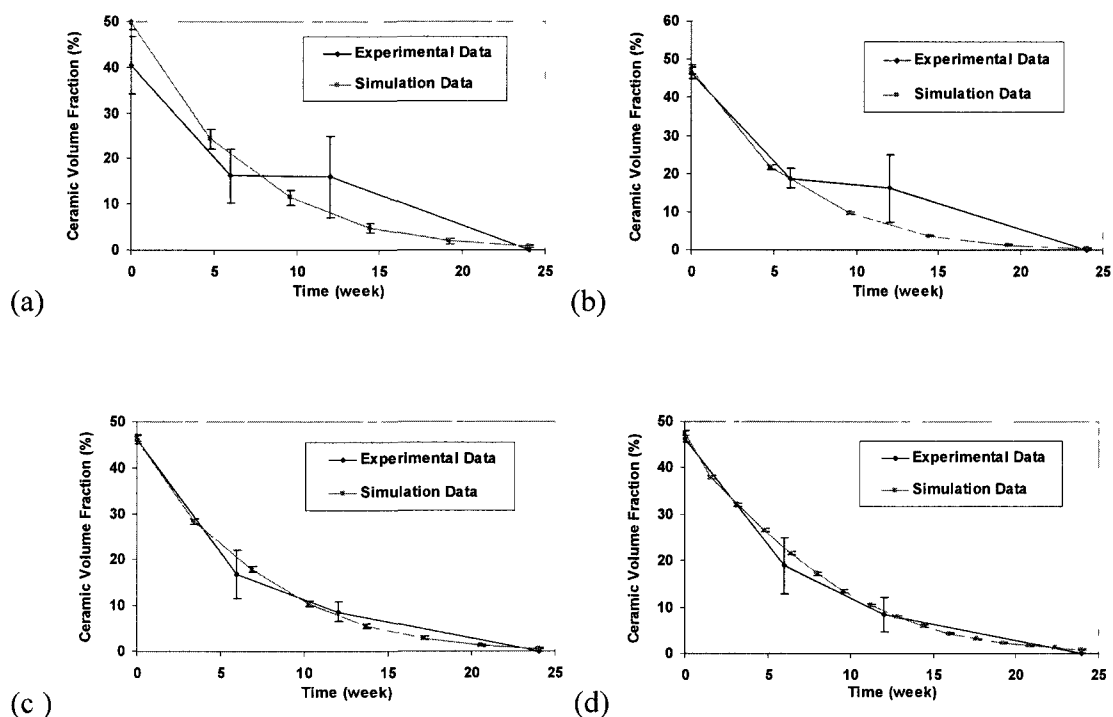


Figure 5-9 Simulation data of four scaffold groups were compared to experimental data. The experimental data were obtained from μ CT analysis of samples implanted in bone defects of sheep for 6, 12 and 24 weeks, (a) group A, (b) group B, (c) group C and (d) group D.

For more quantitative data, the simulation results were fitted with using the Prony method. Table 5-2 summarizes these results for the four bone substitute groups at three different remaining CVF values (30%, 20% and 10% - the initial value was close to 46-50% since macroporosity was comprised between 54 and 50%).). The volume resorption rate decreased with an increase of resorption time and was faster for group B and the slowest for group D. Contrarily, group D (largest pores) had the fastest linear resorption rate, followed by group C (Table 5-2). The two groups with the smallest pore size (group A and B) presented the lowest linear resorption rate.

Table 5-2 Volume and linear resorption rate at different remaining ceramic volume fractions (CVF), to investigate the pattern of resorption rate over time the resorption rate was calculated at different CVFs (30%, 20% and 10%). The calculation was done on 30 μm resolution images.

Scaffold group	Resorption function	Volume resorption rate (1 / Week)			Linear resorption rate (μm / Week)		
		CVF=30	CVF=20	CVF=10	CVF=30	CVF=20	CVF=10
		%	%	%	%	%	%
A	$f(t) = (50.03) * e^{-0.16t}$	4.65	3.10	1.55	3.13	3.13	3.13
B	$f(t) = (47.49) * e^{-0.17t}$	5.03	3.35	1.68	3.13	3.13	3.13
C	$f(t) = (46.65) * e^{-0.15t}$	4.45	2.97	1.48	4.38	4.38	4.38
D	$f(t) = (48.44) * e^{-0.14t}$	4.11	2.74	1.37	9.38	9.38	9.38

Figure 5-10 shows the resorption rate at different regions of scaffolds. For all groups, the volume resorption rate was slightly faster in the external zone (ROI1) than in the internal zones (ROI2 and ROI3) at early resorption time. At later time points, the volume resorption rates of the different zones reached identical values. In other words, the sensitivity of resorption rate to local regions decreased by time. However, the time to reach equivalence was increasingly long with a decreasing pore size. For example, the resorption rates of different zones in group D were almost similar after 6 weeks, whereas this time lasted approximately 10, 15 and 20 weeks for groups C, B and A, respectively.

All results presented so far are based on the assumption that the μCT resolution (30 μm) is good enough to detect scaffold architecture. To get an idea of the validity of this assumption, one block of each pore size was scanned at a higher resolution (15 μm) and the evolution of the ceramic volume fraction was calculated (Figure 5-11). The results show that there is only a difference for group A (smallest pore size) (Figure 5-11a). Table 5-3 summarized the volume and linear resorption rate of four blocks scanned at 15 μm resolution. Except for sample A which showed the fastest volume resorption rate at three different remaining CVF values, other samples presented the same pattern of change as 30 μm resolution blocks (Table 5-2). In addition, similar to 30 μm resolution blocks, the linear resorption rate increased with an increase of pore size (Table 5-3).

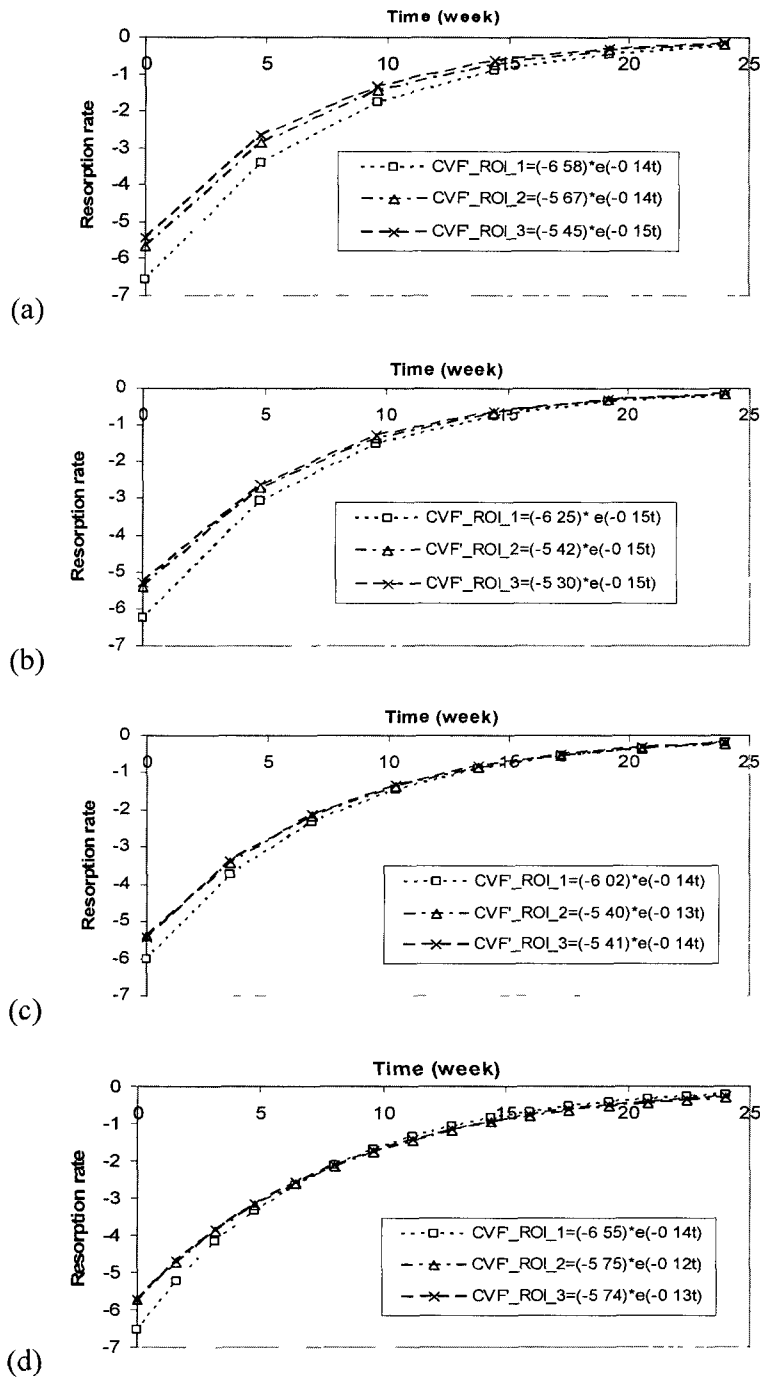


Figure 5-10 Volume resorption rate (CVF') at three different zones (ROI1, ROI2 and ROI3). of scaffold groups, (a) group A, (b) group B, (c) group C and (d) group D. The CVF'_ROI represents the volume resorption rate as a function of time for various location of scaffold.

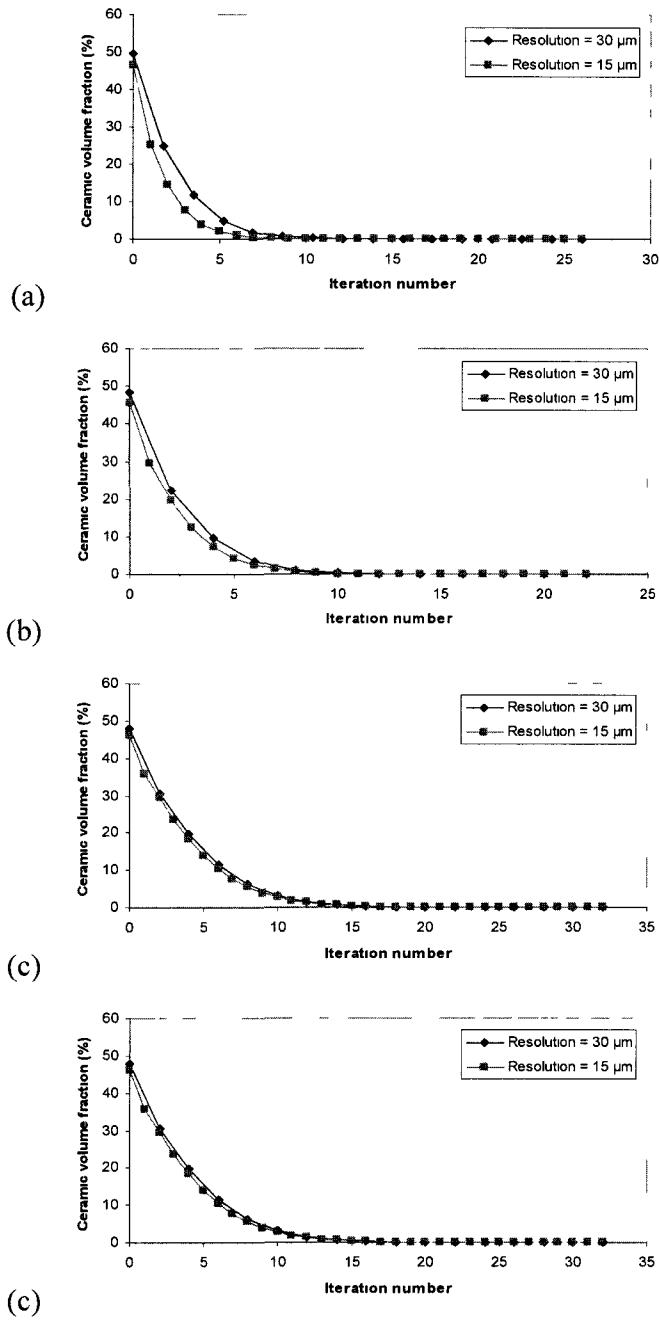


Figure 5-11 Resorption simulations of substitutes were processed based on two different voxel sizes (15 μm and 30 μm), (a) Sample A, (b) Sample C, (c) Sample D. The resorption simulation of small pore size samples, A and B, were affected by voxel size at earlier resorption time. The resorption simulation of samples C and D were not influenced by voxel size..

Table 5-3 Volume and linear resorption rate at different remaining ceramic volume fractions (CVF). To investigate the pattern of resorption rate over time the resorption rate was calculated at different CVFs (30%, 20% and 10%). The calculation was done on 15 μm resolution images.

Scaffold group	Resorption function	Volume resorption rate (1 / Week)			Linear resorption rate (μm / Week)		
		CVF=30	CVF=20	CVF=10	CVF=30	CVF=20	CVF=10
		%	%	%	%	%	%
A	$f(t) = (46.42) * e^{-0.20t}$	6.01	4.01	2.00	2.50	2.50	2.50
B	$f(t) = (45.97) * e^{-0.17t}$	5.07	3.38	1.69	2.81	2.81	2.81
C	$f(t) = (46.87) * e^{-0.17t}$	5.05	3.37	1.68	5.00	5.00	5.00
D	$f(t) = (47.05) * e^{-0.14t}$	4.30	2.87	1.43	10.00	10.00	10.00

5.5 Discussion

The objective of this study was to assess the validity of a recently-proposed resorption model to simulate the cell-mediated resorption of four different groups of bone substitutes consisting of β -TCP and varying in macropore size. The model assumes that (a) material resorption occurs at a constant linear rate (i.e. one layer resorbed in each iteration) from the material surface; (b) provided the surface can be reached by blood vessels of 50 μm in diameter [14]. The proposed assumptions are mainly based on the paradigms obtained from in vivo data [14]. Since the architecture of all tested scaffolds was complex, all scaffolds had to be scanned by μCT prior to implantation and after explantation. Also, since not all macropores were interconnected, complex algorithms had to be used to test the model validity and hence simulate the in vivo data. The resorption simulation algorithm was performed according to two main steps: (1) detection of the pores that can be reached by resorbing cells and (2) resorption of the pore surfaces which are accessible to resorbing cells, this resorption leading to a change of macropore and interconnection size. Prior to using the algorithm to apply the resorption model on in vivo data, the proposed algorithm was first tested by comparing its predictions with the analytical results obtained on scaffolds presenting a simple geometry (Figure 5-3).

Comparing the analytical and simulation results associated to blocks with different pore sizes showed that the iteration number was consistent with total layer thickness resorbed. The blocks with the largest pore size revealed a small difference between the data obtained from both methods however the data diverged for small pore size blocks (Figure 5-7). The discrepancy among the results can be justified by limitation of voxel size and resolution particularly for blocks with small pore radius (e.g. 100 μm and 200 μm). In other words, a voxel size of 10 μm is insufficient to perfectly depict the contour of 100 μm large macropores. This appears plausible in that the voxel size should be sufficiently small compared to the pore size and noticeable difference will be described below for the simulation of sample A. In addition we compared the simulation results of substitute groups with the experimental data obtained from replacing samples into the bone defects of sheep [15].

The comparison revealed that the simulation analysis compares well with the in vivo resorption behaviour of CaP substitutes. In particular, the correlation coefficient (R^2) between the experimental and simulation data of the two largest pore size groups (C and D) was above 0.99, whereas, this value was 0.92 and 0.94 for samples A and B, respectively.. For samples A and B the simulation data deviated from the experimental data beyond 6 weeks of implantation. The discrepancy between the results is likely related to some biological mechanism which can not be predicted by the algorithm. According to experimental data related to samples A and B, Figure 5-9a and Figure 5-9b, respectively, there was no significant changes in the amount of ceramics at weeks 6 and 12, whilst the simulation analysis showed a continues decrease of ceramics by time.

We also calculated the resorption rate of samples. The resorption rate was measured in two ways; (1) ceramic volume fraction rate (volume resorption rate) (2) total resorbed thickness rate (thickness or linear resorption rate). The volume resorption rate has been calculated using prony's series to do fit the resorption data curve. The linear resorption rate has been measured by calculating the total thickness resorbed over time.

Two different observations were obtained. The prony's method showed that the volume resorption rate was proportional to the accessible surface for resorbing cells. Samples

with small pore size had larger surface area than big pore size samples [24]. More surface area provides more cell adhesion [29, 30]. Therefore, according to surface accessibility of samples, groups B and A exhibited higher volume resorption rate than groups C and D. This observation is consistent with the clinical results presented in Ref. [31] in which the authors observed that the samples with higher surface area provided more bone ingrowth at the earlier implantation time. Moreover, due to decrease of surface area by time, the volume resorption rate decreased for all samples (Table 5-2).

The second method revealed that the linear resorption rate was proportional to the thickness of material. This observation could be attributed to the structure of sample. Since the porosity was constant between the samples (~50%), the ceramic thickness decreased with decreasing the pore size (thickness data not presented here) (Figure 5-1). Also considering that to resorb the constant ceramic volume, the amount of thickness resorbed from the interface surface of samples increased when the accessible surface decreased. Consequently, by decreasing the pore size, the linear resorption rate dropped down. In addition, due to the fact that the resorbed thickness is proportional to the resorption time [22], the linear resorption rate did not change by time for each sample (Table 5-2).

Moreover, although the simulation results were not identical between the samples, both methods (simulation and experimental) have demonstrated that resorption process did not considerably vary by pore size. Generally, the simulation and experimental data revealed no effect of pore and interconnection size on the resorption process of samples. In fact, for such ceramic substitutes, it didn't matter how much big the thickness were, the amount of material was important, so the resorption process was the same for large and small pore size. This observation could be related to the statement of Lu et al. [14] in which, for resorbable scaffolds, the density of pores and interconnections play more critical role than their size, because the sizes are changed by resorption.

Furthermore, we studied the effect of resorption direction and minimum interconnection size on resorption behaviour of bone substitute samples. According to the position of sample inside the bone, it could be colonized from different directions. Two resorption

directions were simulated; the samples were resorbed through (a) cylindrical circular side and (b) all sides. The simulation analysis exhibited no effect of resorption direction on simulation data (Figure 5-8). This fact could be attributed to the interconnectivity of macropores inside the structure. 3-D reconstructed structure of samples [23, 24] and interconnectivity analysis [23] demonstrated that the structures were mostly interconnected. Therefore, the resorption process should not be affected by colonization direction as long as the pores are interconnected and the interconnections sizes are large to allow movement of cells.

The formation of vascular network is important for the repair of bone defects with porous biomaterials [32, 33]. Particularly vascularization is known as prerequisite factor for bone formation and cellular resorption [22, 33]. The structural parameters affect on the degree of vascularization. Most specifically there has been relation between vascularization and interconnection size [31, 34]. Some studies [14, 35] have proposed a minimum interconnection size of 50 μm is adequate size whilst other authors [36, 37] mentioned a pore interconnection size of 100 μm . According to these studies we examined the effect of minimum interconnection size (D_{min}) on the resorption process of bone substitute samples.

The simulation analysis data did not show notable differences between the resorption behaviour of groups B, C and D with increasing D_{min} from 50 μm to 100 μm (Figure 5-8). However, increasing D_{min} reduced the resorption rate of group A (Figure 5-8a). This finding could be related to the 3D geometry of samples. The details of geometric parameters of substitutes used in this study have been presented in previous work of our group [24]. Geometric parameters indicated that the average interconnection size of all groups was in the range of 62-85 μm (Table 5-1); however the percentage of pores which had a size less than 100 μm is variable between the samples. The pore distribution of samples [24] showed that for groups B, C and D, only 0.1-4.5% of pores had a size less than 100 μm , while in group A 49-57% of pores were less than 100 μm in size.

Therefore, according to the number of small pores and interconnections, the resorption simulation was influenced by geometric parameters. In other words, if the pore size and interconnection size are less than D_{min} , more iteration number is required to open or

enlarge the pores. This fact was more obvious for group A, due to the large number of small pores available in the structure. However for other groups most of the pores were larger than D_{\min} and could be accessible after enlarging the narrow interconnections, so increasing D_{\min} did not considerably affect on resorption simulation of these samples.

The volume resorption rate was found to be faster in the external zone (ROI1) than internal zones (ROI2 and ROI3) at the earlier resorption time (Figure 5-10). In vivo results revealed that bone formation occurred initially at the periphery of substitute and decrease toward the center [3, 36]. Mastrogiacomo et al. [38] also demonstrated that there is an interrelationship between bone ingrowth and cellular resorption. In accordance with these studies, the simulation results in terms of faster resorption on the outside are consistent with biological results.

However, the difference between the resorption rate of various locations progressively decreased by time. For samples that have large pore and interconnection size such as sample D, the resorption rate of internal zones has been similar to the external zone after 6 weeks. This could be attributed to the size of pores and interconnections which provide fast accessibility to the center of substitutes. Hence, because the size of pores and interconnections and accessibility to pores grows over the resorption process, the resorption rate of various locations reached the same level towards the end of the process.

Moreover, decreasing the voxel size from 30 to 15 μm varied the resorption behaviour of sample A (Figure 5-11). Also sample A presented the fastest volume resorption rate and the slowest linear resorption rate at higher resolution, 15 μm (Table 5-3). This observation could be related to the effect of voxel size on geometrical parameters of sample A in which the average pore and interconnection sizes were highly influenced by resolution.

Our simulation model assumes that the resorbing cells move instantly into the pores and interconnections with size larger than D_{\min} . In reality, this assumption is not correct and might limit the validity and accuracy of simulation model. Therefore, a new condition which describes the movement of cells into the structure should be considered in

simulation model to modify the effect of instant colonization. This is the goal of future studies in development of resorption simulation model.

In this study, we used a global approach by looking at the mean resorption rate of four various blocks, to assess the model validity. The local approach can be also used to directly compare the resorption of one block at one location to the in vivo results. Since the later approach provides much more detail, we are going to consider it in our future works.

5.6 Conclusion

The resorption simulation algorithm helps understand the resorption behaviour of calcium phosphate bone substitutes. With this strengthening tool, we can determine resorption rate and follow the biological behaviour. The resorption rate was assessed in two ways, volume resorption rate and linear resorption rate. Two different observations were obtained; the volume resorption rate was proportional to accessible surface and decreased when the pore size increased, whereas the linear resorption rate was proportional to thickness of material and increased with increasing the pore size.

The resorption simulation data revealed no effect of resorption direction on resorption behaviour of samples as long as the pores are interconnected and the interconnection sizes are large to allow movement of cells. It was also found that the number of small pores and interconnections affect the resorption behaviour. For example resorption rate of group A with large number of small pores was more influenced by increasing D_{\min} to 100 μm . The results in terms of the fastest resorption rate on the outside are consistent with the biological results. Some differences between experiments and theory require further investigations to better understand the bone repair process.

The algorithm can also be used as a design tool to improve the geometrical parameters of bone substitutes.

5.7 Reference

- [1] Grynblas MD, Pilliar RM, Kandel RA, Renlund R, Filiaggi M, Dumitriu M. Porous calcium polyphosphate scaffolds for bone substitute applications in vivo studies. *Biomaterials* 2002;23(9): 2063-70.
- [2] Lu JX, Gallur A, Flautre B, Anselme K, Descamps M, Thierry B, Hardouin P. Comparative study of tissue reactions to calcium phosphate ceramics among cancellous, cortical, and medullar bone sites in rabbits. *J Biomed Mater Res* 1998;42(3): 357-67.
- [3] Gauthier O, Bouler JM, Aguado E, Pilet P, Daculsi G. Macroporous biphasic calcium phosphate ceramics: influence of macropore diameter and macroporosity percentage on bone ingrowth. *Biomaterials* 1998;19(1-3):133-9.
- [4] Yuan H, Yang Z, Li Y, Zhang X. Osteoinduction by calcium phosphate biomaterials. *J. Mater. Sci. - Mater. Med.* 1998;(9): 723-726.
- [5] Ohura K, Bohner M, Hardouin P, Lemaitre J, Pasquier G, Flautre B. Resorption of, and bone formation from, new btricalcium phosphate-monocalcium phosphate cements: an in vivo study. *J Biomed Mater Res* 1996;30:193-200.
- [6] Dong J, Uemura T, Shirasaki Y, Tateishi T. Promotion of bone formation using highly pure porous b-TCP combined with bone marrow-derived osteoprogenitor cells. *Biomaterials* 23 (2002) 4493-4502.
- [7] Daculsi G, Laboux O, Malard O, Weiss P. Current state of the art of biphasic calcium phosphate bioceramics. *J. Mater. Sci. - Mater. Med.* 2003, 14(3): 195-200.
- [8] Li Sh, de Wijn JR, Li J, Layrolle P, de Groot K. Macroporous biphasic calcium phosphate scaffold with high permeability/porosity ratio. *Tissue Eng* 2003;9(3):535-48.

- [9] Karageorgiou V, Kaplan D. Porosity of 3D biomaterial scaffolds and osteogenesis. *Biomaterials* 2005;26(27):5474-91.
- [10] Uchida A, Nade SM, McCartney EF, Ching W. The use of ceramics for bone replacement. A comparative study of three different porous ceramics. *J Bone Joint Surg Br* 1984;66(2): 269–75.
- [11] Klawitter JJ, Hulbert SF. Application of porous ceramics for the attachment of load bearing internal orthopedic applications. *J Biomed Mater Res Symp* 1971;2(1):161–229.
- [12] Egli PS, Mueller W, Schenk RK. Porous hydroxyapatite and tricalcium phosphate cylinders with two different macropore size ranges implanted in the cancellous bone of rabbits. *Clin Orthop* 1988;232:127–38.
- [13] Chang B-S, Lee C-K, Hong K-S, Youn H-J, Ryu H-S, Chung S-S, Park K-W. Osteoconduction at porous hydroxyapatite with various pore configurations. *Biomaterials* 2000;21:1291–8.
- [14] Lu JX, Flautre B, Anselme K, Hardouin P, Gallur A, Descamps M, Thierry B. Role of interconnections in porous bioceramics on bone recolonization in vitro and in vivo. *J Mater Sci Mater Med* 1999;10:111–20.
- [15] von Doernberg MC, von Rechenberg B, Bohner M, Gruenfelder S, van Lenthe GH, Mueller R, et al. In vivo behavior of calcium phosphate scaffolds with four different pore sizes. *Biomaterials* 2006;27(30):5186-98.
- [16] Navarro M, Valle SD, Martinez S, Zepetelli S, Ambrosio L, Planell JA, Ginebra MP. New macroporous calcium phosphate glass ceramic for guided bone regeneration. *Biomaterials* 25 (2004) 4233–4241

- [17] Flatley TJ, Lynch KL, Benson M. Tissue response to implants of calcium phosphate ceramic in the rabbit spine. *Clin Orthop* 1983;179:246-52.
- [18] Hulbert SF, Morrison SJ, Klawitter JJ. Tissue reaction to three ceramics of porous and non-porous structures. *J Biomed Mater Res* 1972;6:347-74.
- [19] Hollister SJ. Porous scaffold design for tissue engineering. *Nat. Mater* 2005; 4 (7): 518–524.
- [20] Sandino C, Checa S, Prendergast PJ, Lacroix D. Simulation of angiogenesis and cell differentiation in a CaP scaffold subjected to compressive strains using a lattice modeling approach. *Biomaterials*. 2010; 31(8):2446-52.
- [21] Byrne DP, Lacroix D, Planell JA, Kelly DJ, Prendergast PJ. Simulation of tissue differentiation in a scaffold as a function of porosity, Young's modulus and dissolution rate: application of mechanobiological models in tissue engineering. *Biomaterials*. 2007; 28(36):5544-54.
- [22] Bohner M, Baumgart F. Theoretical model to determine the effects of geometrical factors on the resorption of calcium phosphate bone substitutes. *Biomaterials* 2004;25(17):3569–82.
- [23] Bohner M, van Lenthe GH, Gruenenfelder S, Hirsiger W, Evison R, Mueller R. Synthesis and characterization of porous b-tricalcium phosphate blocks. *Biomaterials* 2005; 26(31):6099–105.
- [24] Bashoor-Zadeh M, Baroud G, Bohner M. Geometric analysis of porous bone substitutes using micro-computed tomography and fuzzy distance transform. *Acta Biomaterialia* 2010; 6(3); 864–875.

- [25] Bohner M. Calcium phosphate emulsions: possible applications. *Key Eng Mater* 2001; 192–195:765–8.
- [26] Darabi A, Chandelier F, Baroud G. Thickness analysis and reconstruction of trabecular bone and bone substitute microstructure based on fuzzy distance map using both ridge and thinning skeletonization. *Can J Elect Compt Eng* 2009;34(1-2):57–62.
- [27] Niblack CW, Gibbons PB, Capson DW. Generating skeletons and centerlines from the distance transform. *Graph Model Image Process* 1992;54(5):420–37.
- [28] Haralick RM, Shapiro LG. *Computer and robot vision*. Reading, MA: Addison Wesley; 1992–1993.
- [29] Gagvani N, Silver D. Parameter-controlled volume thinning. *Graph Model Image Process* 1999;61(3):149–64.
- [30] Yang Sh, Leong KF, Du Z, Chua ChK. Review, the design of scaffolds for use in tissue engineering. part I. traditional factors, *Tissue Eng*. 2001; 7 (6): 679-89.
- [31] Mastrogiacomo M, Scaglione S, Martinetti R, Dolcini L, Beltrame F, Cancedda R, et al. Role of scaffold internal structure on in vivo bone formation in macroporous calcium phosphate bioceramics. *Biomaterials* 2006;27(17):3230-7.
- [32] Klenke FM, Liu Y, Yuan H, Hunziker EB, Siebenrock KA, Hofstetter W. Impact of pore size on the vascularization and osseointegration of ceramic bone substitutes in vivo, *J. Biomed. Mater. Res. Part A* 2008; 85 (3): 777-786.
- [33] Hing KA, Bioceramic bone graft substitutes: influence of porosity and chemistry, *Int. J. Appl. Ceram. Technol.* 2005; 2 (3):184–199 (2005).

[34] Li JP, Habibovic P, van den Doel M, Wilson CE, de Wijn JR, van Blitterswijk CA, de Groot K, Bone ingrowth in porous titanium implants produced by 3D fiber deposition, *Biomaterials* 2007; 28:2810–282.

[35] Otsuki B, Takemoto M, Fujibayashi S, Neo M, Kokubo T, Nakamura T. Pore throat size and connectivity determine bone and tissue ingrowth into porous implants: three-dimensional micro-CT based structural analyses of porous bioactive titanium implants. *Biomaterials* 2006;27(35):5892-900.

[36] Jones AC, Arns Ch H, Sheppard AP, Hutmacher DW, Milthorpe BK, Knackstedt MA, Assessment of bone ingrowth into porous biomaterials using MICRO-CT. *Biomaterials* 28 (2007) 2491–2504.

[37] Jones AC, Arns ChH, Hutmacher DW, Milthorpe BK, Sheppard AP, Knackstedt MA, The correlation of pore morphology, interconnectivity and physical properties of 3D ceramic scaffolds with bone ingrowth, *Biomaterials* 2009; 30 (7): 1440–1451.

[38] Mastrogiacomo M, Papadimitropoulos A, Cedola A, Peyrin F, Giannoni P, Pearce SG, Alini M, Giannini C, Guagliardi A, Cancedda R, Engineering of bone using bone marrow stromal cells and a silicon-stabilized tricalcium phosphate bioceramic: Evidence for a coupling between bone formation and scaffold resorption, *Biomaterials* 2007;28 (7): 1376–1384.

[39] van Lenthe GH, Hagenmuller H, Bohner M, Hollister SJ, Meinel L, Muller R. Nondestructive micro-computed tomography for biological imaging and quantification of scaffold–bone interaction in vivo. *Biomaterials*. 2007; 28(15), 2479–2490.

CHAPTER 6

General discussion and conclusion

This research work has been concerned with an in-depth study of the accurate characterization and resorption assessment of β -TCP bone substitutes. μ CT images and novel fuzzy image processing techniques were combined and used for characterization and resorption simulation analysis.

This chapter discusses the findings and limitations, concludes the study, and makes suggestions for future research.

6.1 Image processing and geometric analysis

The μ CT images are fuzzy images and presented in gray levels. The assessment of porous structure based on μ CT images can be improved when fuzzy segmentation is performed. In particular, a significant improvement is found at low resolution images [Sladoje et al., 2005]. In this thesis, the introduced thresholding technique provided a method to identify the fuzzy border of objects and performed a fuzzy segmentation and subsequently increased the accuracy of structural analysis. Specifically, instead of single thresholding for binary segmentation, two threshold values were defined as representative of fuzzy interval between the object and non object. This can be very useful in segmentation of low resolution images where the voxel size is in the range of pore size. In such cases, single thresholding based on grey level histogram is a tough work and leads to inaccurate findings for further analysis. The threshold values were mainly selected based on gray level histogram of images, visual inspection and in comparison to the porosity values.

Moreover, the fuzzy distance transform technique was introduced to enhance the accuracy of results. Unlike the traditional distance transform method, the fuzzy distance transform does not require a binarization of the images and uses both distance and gray level values to calculate the shortest distance from the object's voxel to the background.

The added value reported by Saha and Wehrli [Saha and Wehrli, 2004] on the use of fuzzy distance transform compared to traditional distance transform were that it allowed for accurate geometric analysis, even if the resolution of the images was relatively low.

In addition to the introduction of fuzzy distance transform, this study used a new algorithm so called Max-Min operator to identify pores and their interconnections. This is a new method to recognize pores and interconnections. The Max-Min operator identified pores and interconnections based on FDT map and geometric definitions. The pore size and interconnection size were defined as the FDT value of the local maxima and saddle voxels in FDT map, respectively (Figure 6-1). The local maxima and saddle voxels were critical voxels of the so called 'skeleton'. Therefore, extracting only critical voxels instead of all skeleton voxels to measure the mean pore and interconnection sizes significantly reduced the computational time.

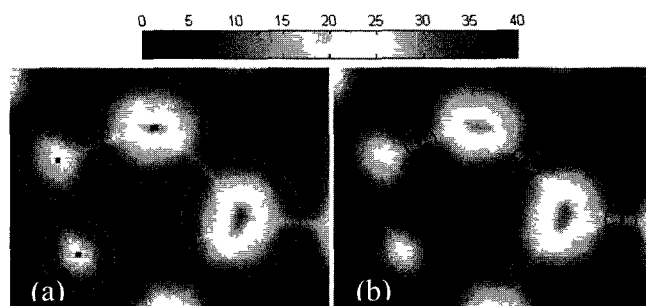


Figure 6-1 (a) 2D FDT map, local maxima as a representative of pore size are shown with dark points. (b) 2D FDT map, local saddles as a representative of interconnection size are shown with dark points.

In addition, this study used a new skeletonization method developed by the same group [Darabi et al., 2009; Bashoor-zadeh et al., 2009]. This method combined both fuzzy distance transform and ridge detection skeletonization. It should be mentioned that in this study, the skeletonization was not used for characterization of scaffold structure. The main goal of the skeletonization was to reconstruct the samples and create a binary model based on the fuzzy nature of images. The reconstructed model was generated by union of spheres centered at each skeleton voxels with radius equal to their FDT value. The accuracy of created binary model was examined by comparing the porosity of

reconstructed model with the porosity of fuzzified model. The difference between porosities of reconstructed and fuzzified models was found to be less than 5% (Table 6-1). The reconstructed models were utilized for fluid flow analysis, surface density calculation and resorption simulation.

Table 6-1 The porosity calculated based on fuzzified images and reconstructed images.

Sample	Porosity-fuzzy (%)	Porosity-reconstruct (%)
Sample A	50.2 ± 1.6	51.5 ± 2.0
Sample B	52.7 ± 1.3	54.9 ± 1.6
Sample C	53.7 ± 0.7	55.5 ± 0.7
Sample D	52.4 ± 0.6	54.4 ± 0.6

The surface area and surface density of scaffolds were measured based on marching cube algorithm. The results demonstrated that for scaffolds with constant porosity (52.3±1.5 %), the surface density of samples decreased from 11.5 to 3.3 mm⁻¹ when the pore size increased and revealed an inverse relation with permeability.

The geometric analysis revealed that the reproducibility of the fabrication method was high. The small variability, within 5-9%, between the geometric parameters of samples in each group confirmed this fact. In addition, the calcium phosphate emulsion method provided a high degree of design control. The porosity and pore size could be controlled by the amount of emulsifier concentration. The characterization of four groups of substitutes revealed that the samples with a constant porosity could be fabricated with different pore sizes varied by a factor of 7, interconnection sizes varied by a factor of 1.4 and surface densities varied by a factor of 4.

6.2 Fluid flow analysis

In collaboration with Regionales RechenZentrum Erlangen (RRZE), Germany, a well established Lattice Boltzmann method was performed to simulate the flow of a Newtonian fluid on pore scale level of the bone substitutes' structure. Lattice Boltzmann has already demonstrated to be useful and efficient for simulation of flow in complex porous structure [Succi S, 2001]. The transport properties of substitutes including the

pressure drop, local velocity and permeability were extracted from the results of the Lattice Boltzmann simulation. The permeability of samples was in the same order of magnitude and increased from 1.14×10^{-10} to $4.07 \times 10^{-10} \text{ m}^2$ with increasing the pore size. Therefore, all samples exhibited permeabilities larger than $3 \times 10^{-11} \text{ m}^2$ which was demonstrated to be adequate for vascularization and mineralization inside a porous implant [Hui et al.1996].

6.3 Effect of voxel size on geometric parameters

μ CT is an advanced tool to quantify geometric parameters of porous bone substitutes in 3-D. However, image resolution has a significant impact on accuracy of structural analysis. In particular, when the voxel size is relatively large compared to the structure of interest, it becomes difficult to obtain good geometric information. Therefore, decreasing the voxel size is the approach to attain the precise geometric characterization. Specifically, the gray level histograms were significantly improved when the voxel size decreased. The histogram of samples revealed the significant effect of voxel size on identification of different phases (e.g. material and void space) (Figure 6-2). The bimodal histograms with two separate peaks, corresponding to material and void space, were obtained by decreasing the voxel size. Therefore the thresholding process was simplified when using bimodal histograms instead of unimodal histograms.

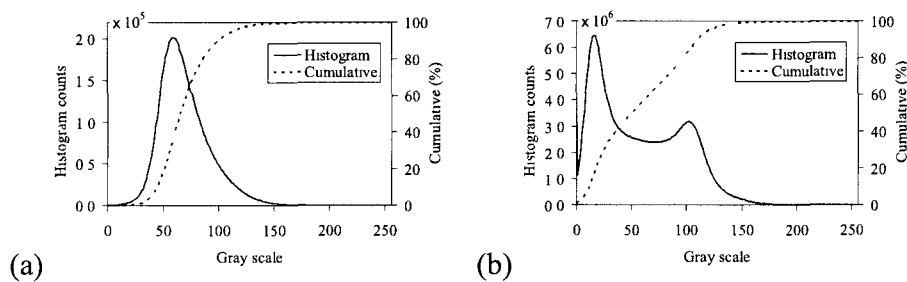


Figure 6-2 Gray level histograms of sample A (the small pore size sample) at (a) 30 μm resolution and (b) 7.5 μm resolution

Depending on the resolution of images and structural features of samples (pore size and interconnection size), the characterization of geometric parameters became sensitive to

threshold values. Increasing the ratio of voxel size to pore size caused more sensitivity to threshold values. For example, at 30 μm resolution, the geometric analysis of small pore size samples showed that if the lower threshold value decreased from 35 to 30, the porosity and pore size would decrease 20% and 16%, respectively. Sensitivity analysis of porosity to threshold values also indicated rapid decrease in porosity of small pore size samples (samples A and B) when the threshold domain decreased (Figure 6-3).

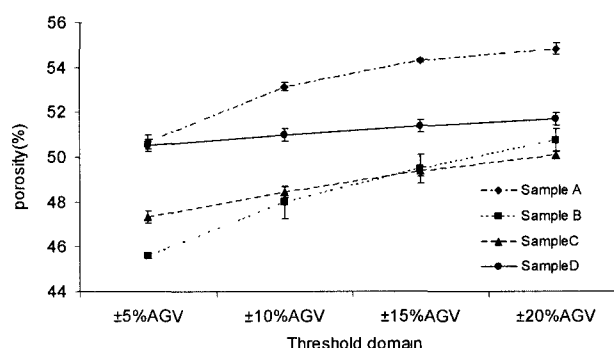


Figure 6-3 Sensitivity of samples' porosity to threshold values, AGV is the average gray level value. The threshold domains were selected as $\pm 5\%$, $\pm 10\%$, $\pm 15\%$ and $\pm 20\%$ of AGV.

The results demonstrated the high effect of voxel size on quantification of pore and interconnection sizes. Generally, due to detecting small structures when using high resolution images, the average pore and interconnection sizes were expected to decrease accordingly. However, an opposite trends were observed with respect to interconnection size. Specifically, the interconnection size appeared to reduce for small pore size samples with a transient change towards high interconnection size for large pore samples. It was shown that the increasing of interconnection size was caused by the local irregularities and boundary effects appeared on the material surface in high resolution images. Additional conditions were applied to eliminate the boundary effects and the distributions were carefully analyzed. In these added conditions, interconnections, which overlap with adjacent pores, were removed and therefore led to considerably decrease of average interconnection size. It should be noted that these effects did not influence the pore size characterization because the unique methods applied to find interconnections.

There was a remarkable decrease of interconnection size for small pore size samples when voxel size decreased. Specifically, analysis of interconnection size using high resolution images demonstrated that for small pore size samples, the average interconnection size decreased to 20-30 μm . According to existing paradigms, a minimum interconnection size of 50 μm is generally required for bone ingrowth [Lu et al., 1999; Chang et al., 2000; Otsuki et al. 2006]. However, biological in vivo data of implanted scaffold revealed positive behaviour of these samples [von Doernberg et al., 2006]. This findings and related literatures, showing effect of micropores on bone formation [Lan Levengood et al., 2010; Habibovic et al., 2006], allow for new debates in the future to evaluate the existing paradigms.

6.4 Cell-mediated resorption process

The resorption simulation algorithm presented in this study predicts the resorption behavior of calcium phosphate bone substitutes and helps to understand the biological results. With this tool, we can determine resorption rate and follow the biological behavior. The algorithm can also be used as a design tool to improve the geometric parameters of bone substitutes. The proposed algorithm was verified by comparing simulation results with the analytical results of a simple geometry and biological in vivo results of implanting β -TCP bone substitutes [von Doernberg et al., 2006]. A correlation coefficient between the simulation results and both analytical and experimental data was found to be larger than 0.9.

Skeletonization was shown to be a useful tool to perform the resorption steps. The skeleton points allowed comparing the size of void space, including pores and interconnections, with the minimum size required for migration of cells and finally found the accessible pores for cell invasion.

The resorption rate was calculated in two ways; (i) volume resorption rate in which the resorption rate was calculated using prony's series to do fit the resorption data curve and (ii) linear resorption rate which was measured by calculating the total thickness resorbed over time. Two different observations were obtained; the volume resorption rate was

proportional to accessible surface for cells and decreased when the pore size increased, while the linear resorption rate was proportional to thickness of material and increased with increasing the pore size.

In order to study the resorption process from periphery to the center of substitute, the volume resorption rate was calculated at various location of scaffold. The volume resorption rate was found to be faster in the external zone than internal zones at earlier resorption time. This finding was in agreement with in vivo observation. However, due to increasing the size of pores and interconnections, the accessibility to the center of substitute increased over time. Therefore the resorption rate of various locations reached the same level towards the end of the process.

The resorption simulation results revealed no effect of resorption direction on resorption behavior of samples as long as the pores were interconnected and the interconnection sizes were large to allow movement of cells. In addition, the effect of minimum interconnection size required for cell ingrowth (D_{min}) on prediction of model was studied. The resorption simulation of samples in group A (with the smallest pore size), was more influenced by D_{min} , as the resorption rate decreased with increasing D_{min} to 100 μm . The analysis of pore size distribution showed that 49-57% of pores in these samples are smaller than 100 μm . Therefore, it was found that the number of small pores and interconnections can also affect the resorption behaviour.

The resolution of images also affected the resorption simulation analysis of small pore size samples (sample A). Decreasing the voxel size from 30 to 15 μm changed the resorption behaviour of this sample. This observation can be related to the effect of voxel size on geometrical parameters of sample A in which the average pore and interconnection sizes were highly influenced by resolution.

Moreover, the results of both methods (simulation and experimental) have demonstrated that resorption process did not considerably vary by pore size. In fact, for such ceramic substitutes, it doesn't matter how much big the thickness are, the amount of material is important, so the resorption process is the same for large and small pore size.

6.5 Methodology-synthesis diagram

The following diagram (Figure 6-4) shows how different methods and analysis, used in this study, were combined together to create a methodology for accurate geometric, fluid flow and resorption simulation analysis of porous bone substitutes.

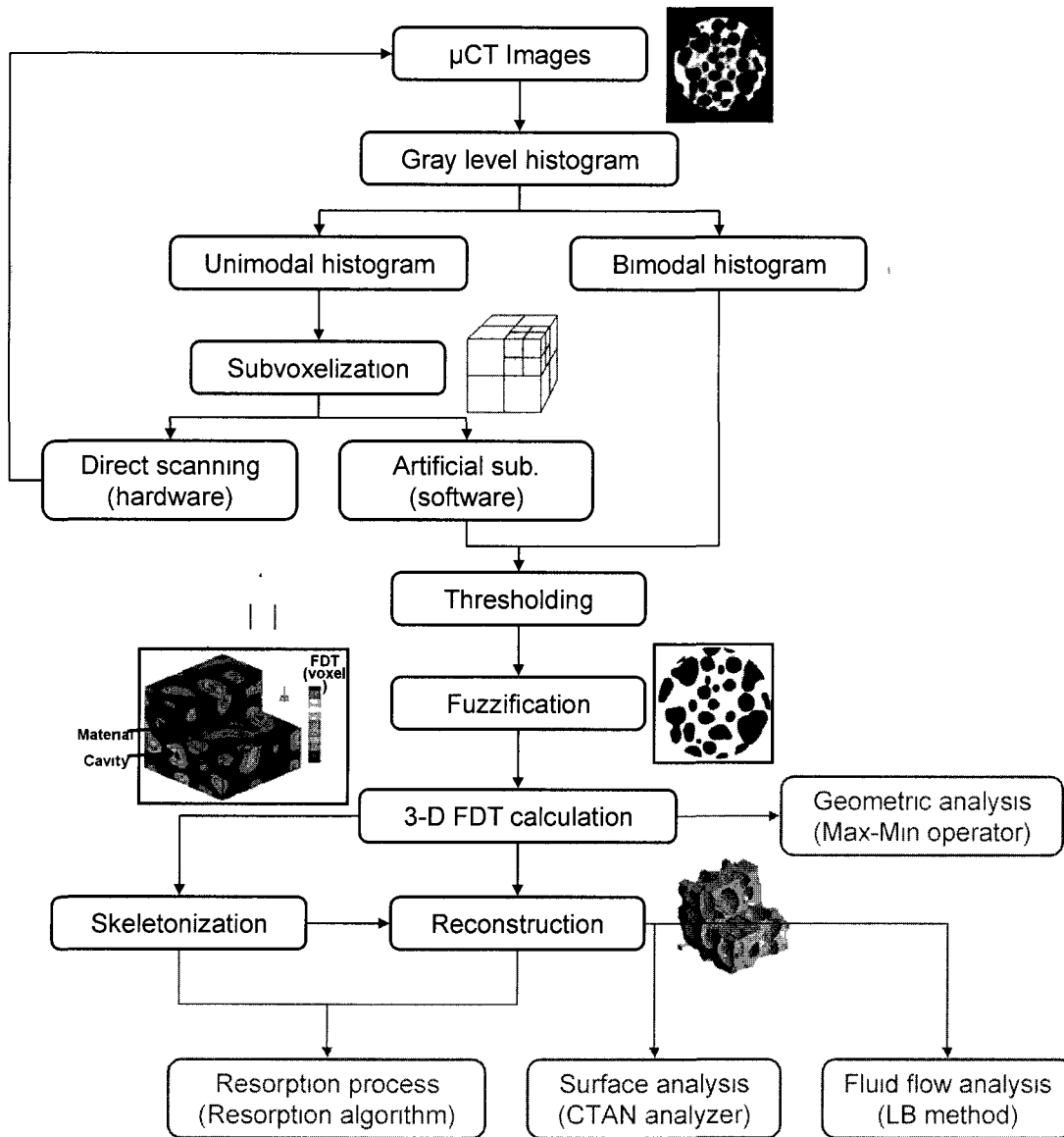


Figure 6-4 Methodology-Synthesis diagram, combination of methods and algorithm used for accurate geometric, fluid flow and resorption simulation analysis of bone substitutes

6.6 Contributions

Our contribution in this field is introducing fuzzy techniques in characterization of bone substitutes, which enhance the accuracy of results due to fuzzy nature of μ CT images. The fuzzy methods were combined with novel characterization algorithm to measure the structural parameter of bone substitutes.

Moreover, due to the important role of pore and interconnection sizes in vascularization and bone formation, this study mainly focused to provide accurate characterization of pore and interconnection sizes. The improvement was achieved using novel image treatment, developed algorithm and high resolution images.

The resorption model based on image processing tools is a novel contribution in the field of resorbable bone substitutes, which can help to predict and understand the biological response. Finally, it can be used as a tool to design an effective scaffold with appropriate properties.

6.7 Current limitation

Beside the advantage of introduced methods, there are some limitations to this study which should be considered for future investigations.

High resolution scanning provides more details of structural features; however, the scanning time significantly increases when the voxel size decreases. Also there is a challenge for data storage and data processing at high resolution scanning. It should be also noted that increasing the resolution will limit the field of view and reduce the scanning domain.

Increasing the resolution of μ CT images allows for more accurate characterization of geometric features, however, the amount of data is significantly increased. Extracting the relevant information from large data files is time extensive. Furthermore, computational limitation such as time and memory required for analyzing data is another restriction related to high resolution images.

According to Max-Min operator, the pore and interconnection sizes were defined as diameter of spheres which centered at local maxima and saddle voxels, respectively. Depending on the pores shape (spherical or semi-spherical), one or more maxima were found in the pores which their corresponding spheres overlapped each other. Therefore, due to the shape of pores, introducing an exact definition to measure average pore size and cover all condition, was not easy task. Therefore, this study introduced two definitions (Number-base and Volume-base) to calculate the average pore size and compared the average values. In addition, number of pores and interconnections can not be directly calculated based on the number of maxima and saddle points and need additional analysis.

Normally, the calculation methods used to analyze the μ CT data contain some error. Since there was not an exact geometric reference for characterization of pore and interconnection sizes, it was not possible to estimate the calculation error of the characterization tools utilized in this study.

Moreover, the characterization method introduced in this study is able to characterize the geometric parameters of porous structure with spherical or semi-spherical pores and may not be applied to characterize the geometric parameters of porous structures with different pore shape.

Decreasing the voxel size led to detect more details of the structure and caused some boundary effects that misled the results in terms of interconnection size. The characterization algorithm showed to be sensitive to these boundary effects. Therefore, additional condition was required to eliminate the boundary effects and modify the characterized parameters.

The gray level histograms of images become unimodal when the voxel size is in the range of pore and interconnection sizes, Thresholding and segmentation of unimodal histograms where the two peaks of histograms are merged together is very difficult and limits the accuracy of quantification analysis.

In order to compare the resorption simulation results with biological in vivo results, it is required to perform the in vivo tests. The biological results used in this study were provided in collaboration with another research group in Switzerland. Performing more animal experiments to investigate the effect of geometric parameters on biological response and study the prediction of simulation model is very expensive and time extensive task.

Micro mechanical environment including the stress and strain induced within tissue have been demonstrated to influence the cell penetration and bone formation [Jaecques et al. 2004; van Cleynenbreugel et al., 2006]. Mechanical signals affect the development and differentiation of bone tissue, the sign of strain will determine whether bone is resorbed or deposited. This thesis was devoted to study the effect of geometric parameters on resorption simulation and did not consider the mechanical environment which has significant effect on bone repair procedure.

The resorption model assumes that the resorbing cells instantly invade the accessible pores and interconnections. This assumption is not certainly correct. The movement and proliferation of cells depend on biological and mechanical environment. Therefore, movement of cells inside the porous structure should be considered to achieve more accurate resorption model.

6.8 Future work

The conclusions of this PhD thesis are not meant to be final; rather they are an outline of the significant results obtained from the research performed during the period of the thesis. There remain, some suggestions for future work following this project.

- Resorption model, proposed in this study, supposed that resorbing cells move instantly into the accessible pores and interconnections. In reality, the resorbing cells fill the pores gradually. Therefore, a new condition which describes the movement of cells into the structure should be considered in simulation model to modify the effect of instant colonization. This could be the subject of future work.

- Beside the geometry of scaffold, there are some biological mechanisms related to activity of biological cells such as osteoclasts, osteoblasts, growth factors and etc. that affect resorption kinetics. Considering such biological mechanisms in modeling of resorption process can develop the prediction of model.
- Mechanical environment and strain induced within the bone tissue have significant effect on the cell penetration inside the porous structure; these effects were eliminated in this study. Future work can be devoted to study the effect of both geometric and mechanical environment on bone formation and resorption behaviour of porous bone substitute.
- Decreasing the voxel size leads to detect more features of structure and creates some boundary effects. These boundary effects can be misleading with respect to interconnection size calculation. The characterization algorithm showed to be sensitive to these boundary effects. Therefore, developing an intelligent computer model which can be less affected by microstructures appeared in high resolution images, can be considered in future.

6.9 Discussion et conclusion (Français)

Ce travail de recherche s'est penché sur l'étude approfondie de la caractérisation et l'évaluation de la résorption de substituts osseux β -TCP. Des images μ CT et une nouvelle méthode de traitement d'images « fuzzy-based » ont été combinées et utilisées pour caractériser l'analyse de simulations de résorption.

Ce chapitre comprend une discussion générale des découvertes et les limitations des méthodes utilisées, les résultats obtenus, et la conclusion de l'étude ainsi que des recommandations pour les travaux ultérieurs.

Traitement d'image et analyse géométrique

Les images μ CT sont des images floues (« fuzzy ») en niveau de gris. L'analyse de la structure poreuse découlant de ces images peut être améliorée en effectuant une segmentation floue de l'image. Une amélioration significative est observée surtout pour les images basse résolution [Sladoje *et al.*, 2005]. Dans cette thèse, la technique de seuil limite présentée a fourni une méthode d'identification des contours flous d'objets et effectue une segmentation floue, améliorant la précision de l'analyse structurelle. Ainsi, au lieu d'utiliser un seul seuil limite pour une segmentation binaire, deux seuils limites ont été définis, représentant l'intervalle flou entre l'objet et le non objet. Ceci peut se révéler utile dans la segmentation d'images basse résolution, où la taille d'un voxel est de l'ordre celle d'un pore. Dans ce cas, la technique à un seul seuil limite avec un histogramme à niveaux de gris rend l'interprétation difficile et mène à des résultats imprécis. Les seuils limites ont été déterminés via l'histogramme en niveaux de gris de l'image, une inspection visuelle et la comparaison avec les valeurs de porosité.

Par la suite, la technique dite de transformée de distance floue (« Fuzzy Distance Transform » - FDT) a été introduite afin d'améliorer la précision des résultats. Contrairement à la méthode traditionnelle de transformée de distance, la transformée floue ne requiert pas la binarisation des images, et utilise deux paramètres, soit la distance et le niveau de gris, pour calculer la plus courte distance entre le voxel de l'objet l'arrière plan. La conclusion rapportée par Saha et Wehrli [Saha and Wehrli, 2004] sur

l'utilisation de la transformée de distance floue versus la méthode traditionnelle est la possibilité d'obtenir une analyse géométrique précise et ce, même avec des images de résolution relativement faible.

En plus de l'introduction de la transformée de distance floue, cette étude utilise un nouvel algorithme nommé opérateur Max-Min afin d'identifier les pores et leurs interconnexions. L'opérateur Max-Min identifie les pores et interconnexions en se basant sur la carte FDT et des définitions géométriques. La taille des pores et interconnexions ont été définies respectivement comme la valeur FDT du maximum local et des voxels points de selle dans la carte FDT (Figure 1). Les maxima locaux et points de selle sont des points critiques de la structure nommée « squelette ». Par la suite, afin de mesurer la taille moyenne des pores et interconnexions, on n'extrait que les voxels critiques au lieu de tous les voxels du squelette a grandement réduit le temps de calcul numérique.

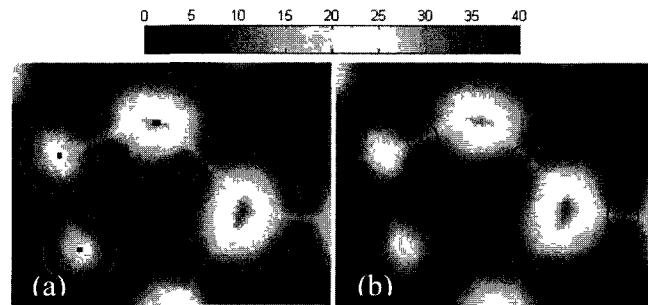


Figure 1. (a) Carte FDT 2D, les maxima locaux représentant la taille de pore sont montrés par des points foncés. (b) Carte FDT 2D, les points de selle représentant la taille des interconnexions sont montrés par des points foncés.

De plus, cette étude a mis en œuvre une nouvelle méthode de squelettisation développée par le même groupe [Darabi *et al.*, 2009, Bashoor-zadeh *et al.*, 2009]. Cette méthode combine la transformée de distance floue et la squelettisation de détection d'arête. Il est à noter que dans cette étude, la squelettisation n'a pas été utilisée pour caractériser la structure de greffe osseuse. Le but principal de la squelettisation était de reconstruire des échantillons et de créer un modèle binaire basé sur la nature floue des images. Le modèle de reconstruction a été généré par l'union de sphères centrées à chaque voxel du squelette, avec un rayon égal à leur valeur FDT. La précision du modèle binaire créé a été

examinée en comparant la porosité du modèle reconstruit avec le modèle flou. La différence de porosité entre les deux modèles a été évaluée sous 5% (Tableau 1).

Tableau 1. Porosité calculée pour le modèle flou et les images reconstruites.

Sample	Porosity-fuzzy (%)	Porosity-reconstruct (%)
Sample A	50.2 ± 1.6	51.5 ± 2.0
Sample B	52.7 ± 1.3	54.9 ± 1.6
Sample C	53.7 ± 0.7	55.5 ± 0.7
Sample D	52.4 ± 0.6	54.4 ± 0.6

La surface totale et la densité de surface des substituts osseux ont été mesurées par un calcul basé sur l'algorithme « marching cube ». Les résultats montrent que pour des substituts osseux de même porosité (52,3±1,5 %), la densité de surface des échantillons diminue de 11,5 à 3,3 mm⁻¹ lorsque la taille des pores augmente, révélant une relation inverse entre la taille des pores et la perméabilité.

L'analyse géométrique a révélé que la reproductibilité de la méthode de fabrication est élevée. La petite variabilité, de 5 à 9%, des paramètres géométriques de chaque groupe le confirme. De plus, la méthode d'émulsion de phosphate a produit un haut degré de control du design. La porosité et la taille des pores ont été contrôlées via la concentration d'émulsifiant. La caractérisation des quatre groupes de substituts a révélé que les échantillons de même porosité peuvent être fabriqués avec comme taille de pores possibles variant d'un facteur 7, la taille des interconnexions variant d'un facteur 1,4 et une densité de surface variant d'un facteur 4.

Analyse d'écoulement de fluide

En collaboration avec le Regionales RechenZentrum Erlangen (RRZE), la méthode bien connue de Lattice Boltzmann a été utilisée pour simuler l'écoulement d'un fluide Newtonien à l'échelle des pores de la structure d'un substitut osseux. Cette méthode s'est montrée utile et efficace pour la simulation d'écoulement dans une structure poreuse complexe [Succi S, 2001]. Les propriétés de transport de substituts, incluant la chute de pression, la vitesse locale et la perméabilité, ont été extraites des résultats de simulation

Lattice Boltzmann. La perméabilité des échantillons est restée du même ordre de grandeur, augmentant de $1,14 \times 10^{-10}$ to $4,07 \times 10^{-10}$ m² lorsque la taille des pores est augmentée. Ainsi, tous les échantillons ont démontré une perméabilité supérieure à 3×10^{-11} m², limite minimale démontrée pour la vascularisation et la minéralisation dans un implant poreux [Hui *te al.*, 1996].

Effet de la taille de voxel sur les paramètres géométriques

La μ CT est un outil avancé permettant de quantifier les paramètres géométriques de substituts osseux en 3D. Cependant, la résolution a un impact majeur sur la précision de l'analyse microstructurale. Il devient difficile d'obtenir de bonnes informations géométriques particulièrement lorsque le voxel est relativement large par rapport à la structure observée. Ainsi, réduire la taille de voxel est l'approche privilégiée pour obtenir une caractérisation géométrique précise. Plus spécifiquement, les histogrammes en niveaux de gris ont été grandement améliorés avec la diminution de taille des voxels. L'histogramme des échantillons révèle l'important effet de la taille de voxel sur l'identification des phases (matériel et vide) (Figure 2). L'histogramme bimodal avec deux pics séparés correspondant au matériel et au vide, ont été obtenus en réduisant la taille de voxel. Ainsi, l'utilisation de seuils limites a été simplifiée par l'utilisation d'un histogramme bimodal au lieu d'un monomode.

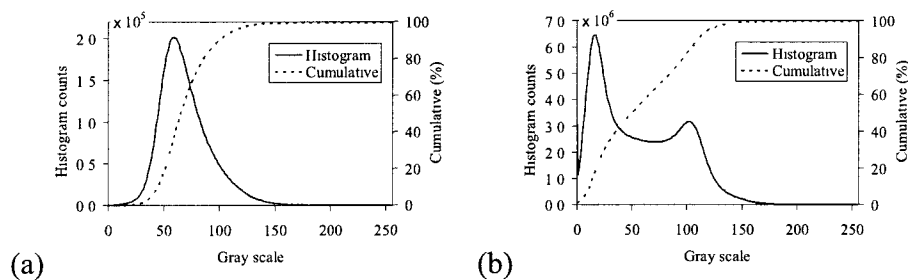


Figure 2. Histogrammes en niveaux de gris de l'échantillon A (petits pores) à (a) résolution de 30 μ m et (b) résolution de 7.5 μ m.

La caractérisation des paramètres géométriques est devenue sensible aux valeurs de seuils limites dépendamment de la résolution des images et de la structure de l'échantillon

mesuré. Une augmentation de la proportion « taille de voxel » sur « taille de pore » a augmenté la sensibilité. Par exemple, pour un échantillon à petits pores mesuré à une résolution de 30 μm , réduire le seuil limite bas de 35 à 30 a eu pour effet de réduire la porosité et la taille de pore de 20% et 16% respectivement. L'analyse de sensibilité de porosité par rapport aux seuils limites a aussi indiqué une rapide diminution de porosité pour les échantillons à petits pores (A et B) lorsque le domaine de seuils limites diminue (Figure 3).

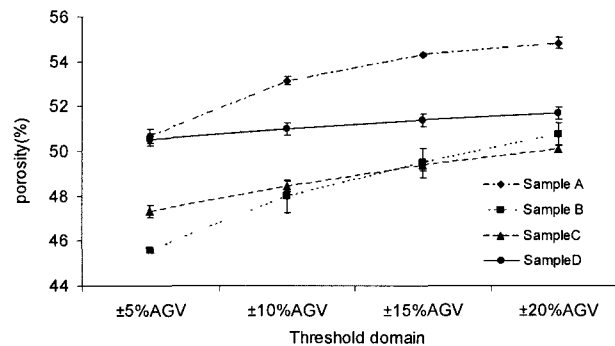


Figure 3. Sensibilité de la porosité des échantillons par rapport aux seuils limites. AGV est la valeur grise moyenne (Average Gray Value). Les domaines choisis pour les seuils sont $\pm 5\%$, $\pm 10\%$, $\pm 15\%$ and $\pm 20\%$ de AGV.

Les résultats ont démontré que la taille de voxel a un effet important sur la quantification de la taille de pore et d'interconnexions. Généralement, en détectant de petites formes en haute résolution, il est attendu que la taille des pores et des interconnexions diminue. Toutefois, l'inverse est observé pour la taille d'interconnexions. Effectivement, leur taille a paru diminuée pour les échantillons à petits pores, mais une variation vers les grandes tailles d'interconnexion est notée pour les échantillons à grands pores. Il a été montré que l'augmentation de la taille des interconnexions est causée par des irrégularités locales, et que des effets de bord apparaissent à la surface du matériau dans les images haute résolution. Des conditions additionnelles ont été appliquées pour éliminer les effets de bord, et les distributions ont été analysées avec précaution. Il est à noter que ces effets n'ont pas influencé la caractérisation de taille de pores car la méthode utilisée ne s'applique que pour les interconnexions.

Une importante réduction de taille des interconnexions a été notée lors d'une diminution de taille de voxel pour les échantillons à petits pores. Effectivement, l'analyse de la taille des interconnexions avec des images haute résolution a montré que pour les échantillons à petits pores, la taille moyenne d'interconnexions diminue à 20-30 μm . Selon les paradigmes existants, une taille minimale de 50 μm est généralement nécessaire pour la vascularisation adéquate et la formation d'os [Lu et al., 1999, Chang *et al.*, 2000, Otsuki *et al.* 2006]. Cette découverte permettra de nouveaux débats pour évaluer les paradigmes existants.

Processus de résorption assistée par les cellules

L'algorithme de simulation de résorption présenté dans cette étude prédit le comportement de résorption du substitut d'os en phosphate de calcium, et aide à la compréhension des résultats biologiques. À l'aide de cet outil, il est possible de déterminer le taux de résorption et de le faire correspondre au comportement biologique. L'algorithme peut aussi être utilisé comme outil de conception afin d'améliorer les paramètres géométriques des substituts osseux. L'algorithme proposé a été validé en comparant les résultats de simulations à des résultats analytiques de géométries simples, ainsi qu'aux résultats *in vivo* de substituts osseux β -TCP implantés [von Doernberg *et al.*, 2006]. Un coefficient de corrélation supérieur à 0,9 a été obtenu entre les résultats simulés, analytiques et expérimentaux.

La squelettisation s'est révélé un bon outil pour effectuer les pas de simulation de résorption. Les points du squelette ont permis de comparer la taille des espaces vides, incluant les pores et interconnexions, avec la taille minimale requise pour la migration des cellules, et ont enfin permis de trouver les pores accessibles à l'invasion cellulaire.

Le taux de résorption a été calculé de deux manières; (i) via le taux de résorption volumique, en utilisant les séries de Prony pour ajuster le modèle à la courbe de donnée et (ii) via le taux de résorption linéaire, mesuré en calculant l'épaisseur résorbée totale en fonction du temps. Deux observations différentes ont ainsi été obtenues, le taux de résorption volumique était proportionnel à la surface accessible aux cellules et diminuait

avec l'augmentation de taille des pores, alors que le taux de résorption linéaire était proportionnel à l'épaisseur du matériel et augmentait avec l'augmentation de la taille des pores.

Dans le but d'étudier le processus de résorption de la périphérie vers le centre du substitut, le taux de résorption volumique a été mesuré à différents endroits de substitut osseux. Il a été déterminé qu'après de faibles temps de résorption, le taux de résorption volumique était plus élevé en périphérie que vers le centre. Cette observation est en accord avec les résultats *in vivo*. Toutefois, l'accès au centre du substitut a augmenté avec le temps puisque la résorption augmente la taille des pores et interconnexions. Ainsi, vers la fin du processus, le taux de résorption volumique à différents sites de l'échantillon s'est vu nivelé.

Les résultats de simulation de résorption n'ont révélé aucun effet de la direction de résorption sur le déroulement du processus, tant que les pores étaient interconnectés et que les interconnexions étaient suffisamment larges pour permettre la migration cellulaire. De plus, l'effet sur le modèle prédictif de la taille minimale d'interconnexion requise pour la migration cellulaire et formation d'os (D_{min}) a été étudié. La simulation de résorption d'échantillons du groupe A (les plus petits pores) a été de plus influencée par D_{min} , car le taux de résorption était réduit avec un D_{min} augmentant jusqu'à 100 μ m. L'analyse de la distribution de taille des pores a montré que 49-57% des pores de cet échantillon étaient plus petits que 100 μ m. Il a donc été déterminé que le nombre de petits pores et interconnexions peut aussi avoir un effet sur le comportement de résorption.

La résolution des images obtenues a aussi modifié l'analyse de la simulation de résorption pour l'échantillon à petits pores (A). Réduire la taille de voxel de 30 à 15 μ m a changé le comportement de résorption de cet échantillon. Cette observation peut être reliée à l'effet de la taille de voxel sur les paramètres géométriques de l'échantillon A, pour lequel la taille moyenne de pore et interconnexion étaient hautement influencées par la résolution.

Ensuite, les deux méthodes, simulation et expérience, ont démontré que le processus de résorption ne variait pas considérablement avec la taille de pore. En fait, pour ce genre de

substitut en céramique, l'épaisseur n'a pas d'importance, alors que la quantité de matériau l'est, donc le processus de résorption est semblable pour des pores petits ou grands.

Diagramme de synthèse de la méthodologie

Le diagramme suivant (Figure 4) montre comment les différentes méthodes et analyses utilisées dans cette étude ont été combinées de façon à créer une méthodologie pour une analyse précise de substituts poreux pour l'os quant à la géométrie, l'écoulement de fluides et la simulation de résorption.

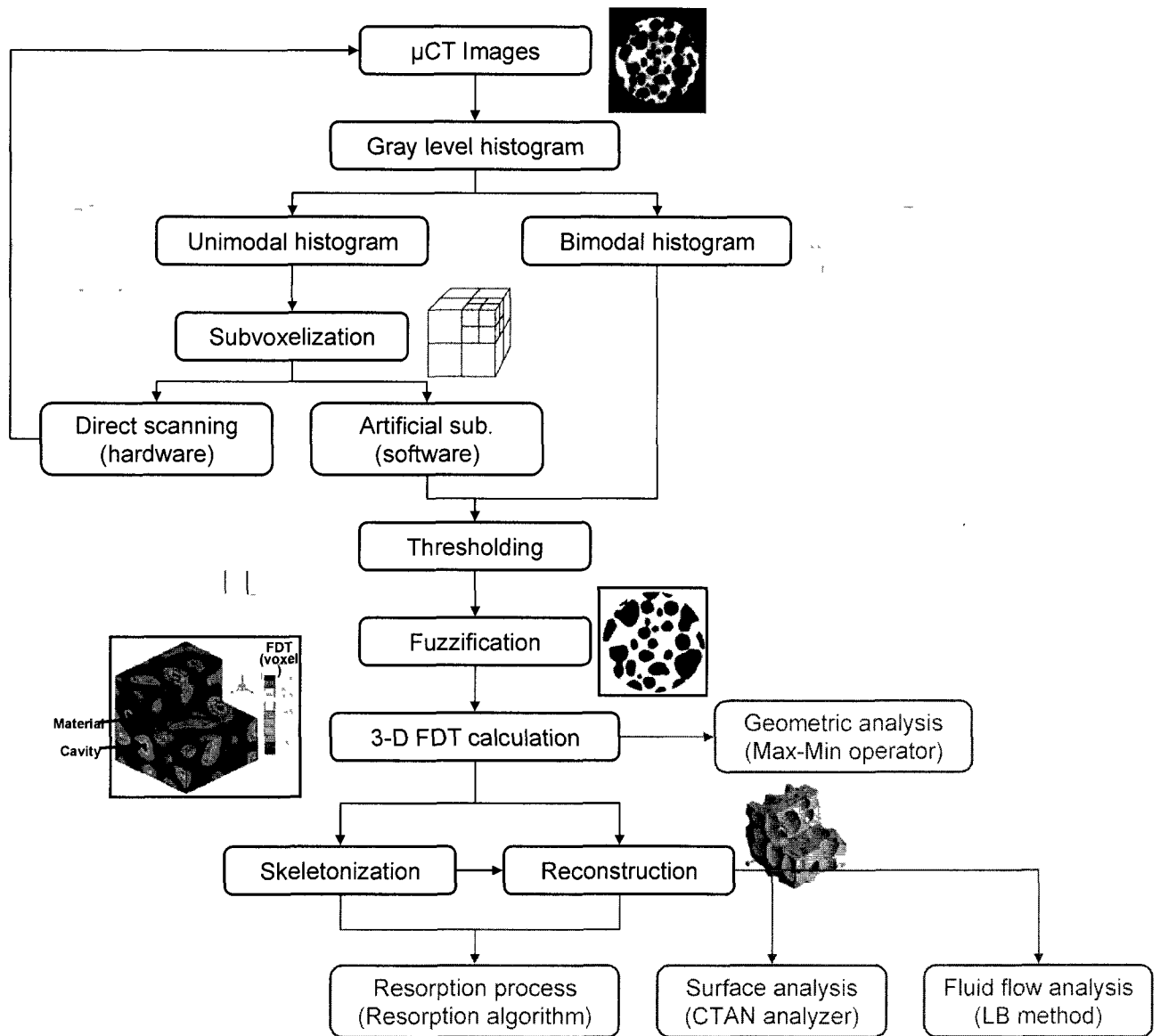


Figure 4. Diagramme de synthèse de la méthodologie, combinaison de méthodes et algorithmes utilisés pour une analyse précise de substituts poreux pour l'os quant à la géométrie, l'écoulement de fluides et la simulation de résorption.

Contributions

Notre contribution à ce domaine introduit les techniques de flou dans la caractérisation de substituts osseux, améliorant la précision des résultats étant donnée la nature floue des images μ CT. Les méthodes de flou ont été combinées à des algorithmes de caractérisation novateurs afin de mesurer les paramètres structuraux de substituts osseux.

Ensuite, étant donné l'important rôle de la taille des pores et interconnexions dans la vascularisation et la formation d'os, cette étude a principalement concentré ses efforts sur la caractérisation précise des tailles de pores et interconnexions. Cette amélioration a été obtenue en utilisant un traitement d'image novateur, en développant un nouvel algorithme ainsi que des images haute résolution.

Le modèle de résorption basé sur des outils de traitement d'image est une contribution originale dans le domaine de substituts osseux résorbables, ce qui aide à la prédiction et la compréhension de la réponse biologique. Enfin, le modèle peut être utilisé pour la conception d'un greffe osseuse efficace, avec les propriétés optimales.

Limitations actuelles

Au-delà des avantages avancés pour les méthodes présentées, certaines limitations de cette étude devraient être considérées lors de recherches ultérieures.

Les mesures haute résolution fournissent plus de détails structurels; toutefois, les temps d'acquisition augmentent significativement lorsque la taille de voxel est réduite. Aussi, il existe un défi au niveau de l'emmagasinage et le traitement des données haute résolution. Il est aussi à noter que l'augmentation de résolution limite le champ visuel et le domaine spatial mesurable.

Augmenter la résolution des images μ CT permet une plus grande précision de caractérisation des propriétés géométriques, au prix d'une augmentation significative de la quantité de données. L'extraction des données pertinentes depuis de lourds fichiers de données devient coûteuse en temps. Ainsi, des limitations de traitement informatique

telles le temps et la mémoire requise pour l'analyse des données devient une nouvelle restriction liée aux images haute résolution.

Selon l'opérateur Max-Min, la taille des pores et interconnexions ont été définies comme le diamètre de sphères centrées au maxima locaux et voxels de selle respectivement. Dépendamment de la forme des pores (sphérique ou semi-sphérique), plus d'un maximum peut se trouver dans un pore, avec leur sphère respective tel que défini, qui se recouvrent mutuellement. Ainsi, à cause de la forme des pores, il a fallu introduire une définition exacte pour mesurer la taille moyenne des pores, une tâche non triviale. Ensuite, cette étude a introduit deux définitions (« number-base » et « volume-base ») pour calculer la taille moyenne d'un pore et comparer les valeurs moyennes. De plus, la taille de plusieurs pores et interconnexions ne peut être calculée directement en se basant sur le nombre de maxima et points de selle, nécessitant une analyse supplémentaire.

Normalement, les méthodes de calcul utilisées pour l'analyse d'images μ CT engendrent certaines erreurs. Puisqu'il n'y avait aucune référence géométrique exacte pour la caractérisation de taille de pore et d'interconnexion, il était impossible d'estimer l'erreur de calcul générée par l'outil de caractérisation utilisé dans cette étude.

Ensuite, la méthode de caractérisation introduite dans cette étude permet de caractériser les paramètres géométriques d'une structure poreuse ayant des pores sphériques ou semi-sphériques, donc ne peut pas être appliquée à la caractérisation de structures ayant des pores de forme différente.

La réduction de la taille de voxel a mené à une détection plus détaillée de la structure, et a causé l'apparition d'effets de bords qui déroutaient les résultats au niveau des interconnexions. L'algorithme de caractérisation a montré une sensibilité à ces effets de bord. Ainsi, des conditions supplémentaires ont été nécessaires à l'élimination des effets de bord et à la modification des paramètres caractérisés.

Les histogrammes en niveaux de gris deviennent monomodes lorsque la taille de voxel est de l'ordre de la taille des pores et interconnexions. L'utilisation de seuils limites et de

la segmentation d'histogrammes monomodes où les deux pics sont confondus est très difficile et limite la précision de l'analyse quantitative.

Dans le but de comparer les résultats de simulation de résorption aux résultats biologiques *in vivo*, il faut effectuer des tests *in vivo*. Les résultats de tests biologiques utilisés dans cette étude ont amené une collaboration avec un autre groupe de recherche en Suisse. Effectuer plus d'expériences animales pour étudier l'effet des paramètres géométriques sur la réponse biologique et l'étude de prédiction du modèle de simulation est très coûteux en argent et en temps.

Il a été démontré que l'environnement micromécanique, incluant la contrainte et la tension dans le tissu, influence la pénétration des cellules et la formation d'os [Jaecques et al. 2004, Van Cleynenbreugel et al., 2006]. Les signaux mécaniques affectent le développement et la différenciation du tissu osseux, le signe de la tension déterminera si l'os est résorbé ou déposé. Cette thèse a été dédiée à l'étude de l'effet des paramètres géométriques sur la simulation de résorption, et n'ont pas pris en compte l'environnement micromécanique qui a un effet significatif sur le processus de réparation de l'os.

Le modèle de résorption considère que les cellules résorbant le tissu envahissent instantanément les pores et interconnexions accessibles. Cette considération n'est pas nécessairement correcte. Le mouvement et la prolifération des cellules dépendent de l'environnement biologique et mécanique. Ainsi, le mouvement des cellules dans une structure poreuse devrait être prise en compte afin d'obtenir un modèle plus réaliste.

Travaux ultérieurs

Les conclusions de cette thèse de doctorat n'ont pas pour but d'être définitives; elles font plutôt office de profil des principaux résultats obtenus en recherche effectuée durant la période de ce projet. Voici donc quelques suggestions concernant le travail faisant suite à ce projet.

- Le modèle de résorption proposé dans cette étude suppose que les cellules résorbant le tissu envahissent instantanément les pores et interconnexions accessibles. En

réalité, les cellules remplissent les pores graduellement. Ainsi, une nouvelle condition décrivant le mouvement des cellules dans la structure devrait être considérée dans le modèle de simulation pour modifier l'effet de la colonisation instantanée. Ceci pourrait être le sujet d'un travail ultérieur.

- Au-delà de la géométrie de la greffe osseuse, certains mécanismes biologiques liés à l'activité cellulaire biologique tels les ostéoclastes, ostéoblastes, facteurs de croissances, etc., ont un effet sur la cinétique de résorption. Considérer ce genre de mécanismes biologiques dans la modélisation du processus de résorption permettrait d'améliorer le caractère prédictif du modèle.
- L'environnement mécanique et la tension induite dans le tissu osseux ont un effet significatif sur la pénétration des cellules dans la structure poreuse; ces effets ont été ignorés dans cette étude. Un travail ultérieur pourrait cibler l'étude simultanée de l'effet des paramètres géométriques et de l'environnement mécanique sur le comportement de la formation osseuse et de la résorption du substitut poreux d'os.
- La réduction de la taille de voxel mène à une détection plus détaillée de la structure, mais génère des effets de bord. Ces effets de bord peuvent tromper les calculs de taille d'interconnexions. L'algorithme de caractérisation a montré une sensibilité à ces effets de bord. Ainsi, le développement d'un modèle numérique intelligent, moins affecté par les microstructures apparaissant dans les images haute résolution paraît intéressant comme travail futur.

Reference

- Aaltosalmi, U. (2005). Fluid flow in porous media the Lattice Boltzmann method. Doctora thesis, University of Jyväskylä, Jyväskylä, Finland, 82 p.
- Agrawal, C.M., McKinney, J.S., Lanctot, D. and Athanasiou, K.A. (2000) Effects of fluid flow on the in vitro degradation kinetics of biodegradable scaffolds for tissue engineering. *Biomaterials*, vol. 21, n° 23, p. 2443-2452.
- Agrawal, C.M. and Ray, R.B. (2001). Biodegradable polymeric scaffolds for musculoskeletal tissue engineering. *Journal of Biomedical Materials Research*, vol. 55, n° 2, p. 141-150.
- Ayers, R.A., Simske, S.J., Bateman, T.A., Petkus, A. Sachdeva, R.L. and Gyunter, V.E. (1999). Effect of nitinol implant porosity on cranial bone ingrowth and apposition after 6 weeks. *Journal of Biomedical Materials Research*, vol. 45, n° 1, p. 42-47.
- Baksh, D. (1999). A comparison of 3-dimensional calcium phosphate scaffolds for candidate bone tissue engineering. Doctorate thesis, University of Toronto, Toronto, Ontario, 181p.
- Balto, K., Muller, R., Carrington, D.C., Dobeck, J. and Stashenko, P. (2000). Quantification of periapical bone destruction in mice by microcomputed tomography. *Journal of Dental Research*, vol. 79, n° 1, p. 35-40.
- Baroud, G., Bohner, M., Heini, P. and Steffen, T. (2004). Injection biomechanics of bone cements used in vertebroplasty. *Bio-medical materials and engineering*, vol.14, n° 4, p. 487-504.
- Baroud, G., Cayer, E. and Bohner M. (2005). Rheological characterization of concentrated aqueous beta-tricalcium phosphate suspensions: the effect of liquid-to-powder ratio, milling time, and additives. *Acta Biomaterialia*, vol. 1, n° 3, p. 357-363.
- Baroud, G., Swanson, T. and Steffen, T. (2006). Setting properties of four acrylic and two calcium-phosphate cements used in vertebroplasty. *Journal of Long-Term Effects of Medical Implants*, vol. 16, n 1, p. 51-59.

- Barriga, A., Diaz-De-Rada, P., Barroso, J.L., Alfonso, M., Lamata, M., Hernaez, S., Beguiristain, J.L., San-Julian, M. and Villas, C. (2004). Frozen cancellous bone allografts: positive cultures of implanted grafts in posterior fusions of the spine. *European Spine Journal*, vol. 13, n° 2, p. 152–156.
- Bashoor-Zadeh, M., Baroud, G. and Böhner, M. (2010). Geometric analysis of porous bone substitutes using micro-computed tomography and fuzzy distance transform. *Acta Biomaterialia*, vol. 6, n° 3, p. 864-875.
- Bear, J. (1972). *Dynamics of fluids in porous media*. New York, Elsevier, 738p.
- Bentley, M.D., Ortiz, M.C., Ritman, E.L. and Romero, J.C. (2002). The use of microcomputed tomography to study microvasculature in small rodents. *American Journal of Physiology, Regulatory, Integrative and Comparative Physiology*, vol. 282, n° 5, p. 1267-1279.
- Bernsdorf, J., Lammers, P., Zeiser, T., Brenner, G. and Durst, F. (2000). A new tool for high performance CFD:Lattice Boltzmann Automata. *Berichtsband projects on the high performance computers of the Leibniz computing center 1997-1999*.
- Böhner, M. and Baumgart, F. (2004). Theoretical model to determine the effects of geometrical factors on the resorption of calcium phosphate bone substitutes. *Biomaterials*, vol. 25, n° 17, p.3569-3582.
- Böhner, M., van Lenthe, G.H., Gruenenfelder, S., Hirsiger, W., Evison, R. and Muller, R. (2005). Synthesis and characterization of porous b-tricalcium phosphate blocks. *Biomaterials*, vol. 26, n° 31, p. 6099–6105.
- Borgefors, G. and Svensson, S. (2002). Fuzzy Border Distance Transform and their use in 2D Skeletonization. In *proceedings, 16th International Conference on Pattern Recognition (ICPR)*, 11-15 Aug. 2002, Quebec, Canada, vol.1, n° 11-15, p.180-183.
- Cehreli, M., Sahin, S. and Akça, K. (2004). Role of mechanical environment and implant design on bone tissue differentiation: current knowledge and future contexts. *Journal of Dentistry*, vol. 32, n° 2, p. 123-132.
- Celil, A.B., Guelcher, S., Hollinger, J.O. and Miller, M. (2007). Tissue engineering applications — Bone. In Fisher, J.P., Mikos, A.G. and Bronzino, J.D., *Tissue engineering (chap. 21, p. 21.1-21.22)*. New York, Taylor & Francis Group.

- Chang, B.S., Lee, Ch.K., Hong, K.S., Youn, H.J., Ryu, H.S., Chung, S.S. and Park, K.W. (2000). Osteoconduction at porous hydroxyapatite with various pore configurations. *Biomaterials*, vol. 21, n° 12, p. 1291-1298.
- Charalambides, C., Beer, M. and Cobb, A.G. (2005). Poor results after augmenting autograft with xenograft (Surgibone) in hip revision surgery: a report of 27 cases . *Acta Orthopaedica*, vol. 76, n° 4, p. 544-549.
- Charles-Harris, M. (2007). Development and Characterization of Completely Degradable Composite Tissue Engineering Scaffolds. Doctorate thesis, Technical University of Catalonia (UPC), Barcelona, Spain ,326 p.
- Chor, M.V. and Li, W. (2007). A permeability measurement system for tissue engineering scaffolds. *Measurement Science and Technology*, vol. 18, n° 1, p. 208-216.
- Daculsi, G., Laboux, O., Malard, O. and Weiss, P. (2003). Current state of the art of biphasic calcium phosphate bioceramics. *Journal of Materials Science Materials in Medicine*, vol. 14, n° 3, p. 195-200.
- Darabi, A., Chandelier, F. and Baroud, G. (2007). Morphometric analysis of trabecular bone thickness using different algorithms. *Canadian Journal of Electrical and Computer Engineering*, vol. 32, n° 3, p 157-163.
- Darabi, A., Chandelier, F. and Baroud, G. (2009). Thickness analysis and reconstruction of trabecular bone and bone substitute microstructure based on fuzzy distance map using both ridge and thinning skeletonization. *Canadian Journal of Electrical and Computer Engineering*, vol. 34, n° 1/2, p. 57-62.
- Di Silvio, L. (2007). Bone tissue engineering and biomineralisation. In Boccaccini, A.R. and Gough, J.E., *Tissue engineering using ceramics and polymers* (chap. 15, p.319-334). Cambridge, Woodhead Publishing Ltd.
- Donath, S. (2004). On optimized implementations of the Lattice Boltzmann method on contemporary high performance architectures. Bachelor Thesis, Friedrich Alexander- Universitat, Erlangen, Nurnberg, 120 p.
- Dong, J., Uemura, T., Shirasaki, Y. and Tateishi, T. (2002). Promotion of bone formation using highly pure porous b-TCP combined with bone marrow-derived osteoprogenitor cells. *Biomaterials*, vol. 23, n° 23, p. 4493-4502.

- Dullien, F.A.L. (1979). *Porous Media, Fluid Transport and pore Structure*. New York, Academic Press Inc., 396 p.
- Finkemeier, C.G. (2002). Bone-grafting and bone-graft substitutes. *The Journal of Bone and Joint Surgery American Volume*, vol. 84, n° 3, p. 454-464.
- Frost, H.M. (1994). Wolff's law and bone's structural adaptations to mechanical usage: an overview for clinicians. *Angle Orthodontics*, vol. 64, n° 3, p. 175-188.
- Gagvani, N. and Silver, D. (1999). Parameter controlled volume thinning. *Graphical Models and Image Processing*, vol. 61, n° 3, p. 149-164.
- Gauthier, O., Bouler, J.M., Aguado, E., Pilet, P. and Daculsi, G. (1998). Macroporous biphasic calcium phosphate ceramics: influence of macropore diameter and macroporosity percentage on bone ingrowth. *Biomaterials*, vol. 19, n° 1-3, p. 133-139.
- Gauthier, O., Muller, R., von Stechow, D., Lamy, B., Weiss, P., Bouler, J.M., Aguado, E. and Daculsi, G. (2005). In vivo bone regeneration with Injectable calcium phosphate biomaterial: a three-dimensional micro-computed tomographic, biomechanical and SEM study. *Biomaterials*, vol. 26, n° 27, p. 5444–5453.
- Griffith, L.G. (2002). Emerging design principles in biomaterials and scaffolds for tissue engineering. *Annals of the New York Academy of Science*, vol. 961, p. 83-95.
- Grynepas, M.D., Pilliar, R.M., Kandel, R.A., Renlund, R., Filiaggi, M. and Dumitriu, M. (2002). Porous calcium polyphosphate scaffolds for bone substitute applications in vivo studies. *Biomaterials*, vol. 23, n° 9, p. 2063-70.
- Guldberg, R.E., Lin, A.S., Coleman, R., Robertson, G. and Duvall, C. (2004). Microcomputed tomography imaging of skeletal development and growth. *Birth Defects Research Part C Embryo Today: Reviews*, vol. 72, n° 3, p. 250–259.
- Goldberg, V.M. (1992). Natural history of autografts and allografts. In Older J., *Bone implant grafting* (p. 9-12). Berlin Heiideberg, Springer-Verlag.
- Goldberg, V.M. and Stevenson, S. (1993). The biology of bone grafts. *Seminars in Arthroplasty*, vol. 4, n° 3, p. 58-63.
- Habibovic, P., Sees, T.M., van den Doel, M.A., van Blitterswijk, C.A. and de Groot, K. (2006). Osteoinduction by biomaterials – physicochemical and structural

- influences. *Journal of Biomedical Materials Research Part A*, vol. 77, n° 4, p. 747–762.
- Haralick, R.M. and Shapiro, L.G. (1993). *Computer and robot vision*. Michigan, Addison-Wesley Pub. Co., 2 volumes, 630 p.
- Hench, L.L. (1980). *Biomaterials*. *Science*, vol. 208, n° 4446, p. 826-831.
- Hench, L.L. (1998). *Biomaterials: a forecast for the future*. *Biomaterials*, vol. 19, n° 16, p. 1419-1423.
- Hench, L.L. and Polak, J.M. (2002). *Third-generation biomedical materials*. *Science*, vol. 295, n° 5557, p. 1014-1017.
- Hildebrand, T. and Rügsegger, P. (1997). A new method for the model-independent assessment of thickness in three-dimensional images. *Journal of Microscopy*, vol. 185, n° 1, p. 67-75.
- Hing, K.A. (2004a). Bone repair in the twenty-first century: biology, chemistry or engineering. *Philosophical Transactions Series A Mathematical Physical and Engineering Sciences*, vol. 362, n° 1825, p. 2821-2850.
- Hing, K.A., Best, S.M., Tanner, K.E., Bonfield, W. and Revell, P.A. (2004b) Mediation of bone ingrowth in porous hydroxyapatite bone graft substitutes. *Journal of Biomedical Materials Research Part A*, vol. 68, n° 1, p. 187-200.
- Hing, K.A. (2005a). Bioceramic Bone Graft Substitutes: Influence of Porosity and Chemistry, *International Journal of Applied Ceramic Technology*, vol. 2, n° 3, p. 184-199.
- Hing, K.A., Annaz, B., Saeed, S., Revell, P.A. and Buckland, T. (2005b). Microporosity enhances bioactivity of synthetic bone graft substitutes. *Journal of Materials Science Materials in Medicine*, vol. 16, n° 5, p. 467–475.
- Ho, S.T. and Hutmacher, D.W. (2006). A comparison of micro CT with other techniques used in the characterization of scaffolds. *Biomaterials*, vol. 27, n° 8, p. 1362-1376.
- Hollister, S.J., Maddox, R.D. and Taboas, J.M. (2002). Optimal design and fabrication of scaffolds to mimic tissue properties and satisfy biological constraints. *Biomaterials*, vol. 23, n° 20, p. 4095-4103.

- Hu, Y., Grainger, D.W., Winn, S.R. and Hollinger, J.O. (2002). Fabrication of poly(alpha-hydroxy acid) foam scaffolds using multiple solvent systems. *Journal of Biomedical Materials Research*, vol. 59, n° 3, p. 563-72.
- Hui, P.W., Lmng, P. and Sher, A. (1996). Fluid conductance of cancellous bone graft as a predictor for graft-host interface healing. *Journal of Biomechanics*, vol. 20, n° 1, p. 123-132.
- Huiskes, R., Ruimerman, R., van Lenthe, G.H. and Janssen, J.D. (2000). Effects of mechanical forces on maintenance and adaptation of form in trabecular bone. *Nature*, vol. 405, n° 6787, p. 704-706.
- Hulbert, S.F., Morrison, S.J. and Klawitter, J.J. (1972). Tissue reaction to three ceramics of porous and non-porous structures. *Journal of Biomedical Materials Research*, vol. 6, n° 5, p. 347-374.
- Hutmacher, D.W. (2000). Scaffolds in tissue engineering bone and cartilage. *Biomaterials*, vol. 21, n° 24, p. 2529-2543.
- Hutmacher, D., Woodfield, T., Dalton P. and Lewis J. (2008). Scaffold design and fabrication. In van Blitterswijk, C., Thomsen, P., Lindahl, A., Hubbell, J., Williams, D., Cancedda, R., de Bruijn, J. and Sohier, J., *Tissue engineering* (chap. 14, p. 403-454). London, Academic Press.
- Innocentini, M.D.M., Pardo, A.R.F., Salvini, V.R. and Pandolfelli, V.C. (2002). Prediction of permeability constants through physical properties of refractory castables. *Ceramica*, vol. 48, n° 305, p. 5-10.
- Jaecques, S.V., van Oosterwyck, H., Muraru, L., van Cleynenbreugel, T., de Smet, E., Wevers, M., Naert, I. and Vander Sloten, J. (2004). Individualised, micro CT-based finite element modelling as a tool for biomechanical analysis related to tissue engineering of bone. *Biomaterials*, vol. 25, n° 9, p. 1683-1696.
- Jones, A.C., Arns, Ch.H., Sheppard, A.P., Hutmacher, D.W., Milthorpe, B.K. and Knackstedt, M.A. (2007). Assessment of bone ingrowth into porous biomaterials using MICRO-CT. *Biomaterials*, vol. 28, n° 15, p. 2491-2504
- Jones, A.C., Arns Ch. H, Hutmacher, D.W., Milthorpe, B.K., Sheppard, A.P. and Knackstedt, M.A. (2009). The correlation of pore morphology, interconnectivity

- and physical properties of 3D ceramic scaffolds with bone ingrowth. *Biomaterials*, vol. 30, n° 7, p. 1440-1451
- Jarcho, M. (1981). Calcium phosphate ceramics as hard tissue prosthetics. *Clinical Orthopedics and Related Research*, vol. 157, p. 259-78.
- Karageorgiou, V. and Kaplan, D. (2005). Porosity of 3D biomaterial scaffolds and osteogenesis. *Biomaterials*, vol. 26, n° 27, p. 5474-5491.
- Karande, T.S., Ong, J.L. and Agrawal, C.M. (2004). Diffusion in musculoskeletal tissue engineering scaffolds: Design issues related to porosity, permeability, architecture, and nutrient mixing. *Annals of Biomedical Engineering*, vol. 32, n° 12, p. 1728-1743.
- Kapur, J.N., Sahoo, P.K. and Wong, AKC. (1985). A new method for gray-level picture thresholding using the entropy of the histogram. *Computer Vision Graphics and Image Processing*, vol. 29, n° 3, p. 273-285.
- Kaviany, M. (1995). Principles of heat transfer in porous media. 2nd edition, New York, Springer, 708p.
- Khang, G., Kim, M.S. and Lee, H.B. (2007). A manual for biomaterials/scaffold fabrication technology. Singapore, World scientific publishing Co. Pte. Ltd, 2 volumes, 289p.
- Klenke, F.M., Liu, Y., Yuan, H., Hunziker, E.B., Siebenrock, K.A. and Hofstetter, W. (2008). Impact of pore size on the vascularization and osseointegration of ceramic bone substitutes in vivo. *Journal of Biomedical Materials Research Part A*, vol. 85, n° 3, p. 777-786.
- Körner, C., Pohl, T., Rüde, U., Thürey, N. and Zeiser T. (2005). Parallel lattice Boltzmann methods for CFD Applications. In Bruaset, A.M. and Tveito A., Numerical Solution of Partial Differential Equations on Parallel Computers (p. 439-465). Berlin Heidelberg, Springer.
- Kruyt, M.C., de Bruijn, J.D., Wilson, C.E., Oner, F.C., van Blitterswijk, C.A., Verbout, A.J. and Dhert, W.J.A. (2003) Viable osteogenic cells are obligatory for tissue-engineered ectopic bone formation in goats. *Tissue Engineering*, vol. 9, n° 2, p. 327-336.

- Kuboki, Y., Jin, Q. and Takita, H. (2001) Geometry of carriers controlling phenotypic expression in BMP-induced osteogenesis and chondrogenesis. *The Journal of Bone and Joint Surgery American volume*, vol. 83A, Suppl. 1(Pt 2), p. 105–115.
- Kujala, S., Ryhanen, J., Danilov, A. and Tuukkanen, J. (2003). Effect of porosity on the osteointegration and bone ingrowth of a weightbearing nickel–titanium bone graft substitute. *Biomaterials*, vol. 24, n° 25, p. 4691–4697.
- Langer, R. and Vicente, J.P. (1993). Tissue engineering. *Science*, vol. 260, n° 5110, p. 920-925
- Lan Levengood, S.K., Polak, S.J., Wheeler, M.B., Maki, A.J., Clark, S.G., Jamison, R.D. and Wagoner Johnson, A.J. (2010). Multiscale osteointegration as a new paradigm for the design of calcium phosphate scaffolds for bone regeneration. *Biomaterials*, vol. 31, n 13, p. 3552-3563.
- Laurencin, C.T., Ambrosio, A.M., Borden, M.D. and Cooper, J.A.Jr. (1999). Tissue engineering: orthopedic applications. *Annual Review of Biomedical Engineering*, vol. 1, p. 19-46
- Le Huec, J.C., Schaefferbeke, T., Clement, D., Faber, J. and Le Rebeller, A. (1995). Influence of porosity on the mechanical resistance of hydroxyapatite ceramics under compressive stress. *Biomaterials*, vol. 16, n 2, p. 113-118.
- Li, Sh., de Wijn, J.R., Li, J., Layrolle P. and de Groot, K. (2003). Macroporous biphasic calcium phosphate scaffold with high permeability/porosity ratio. *Tissue Engineering*, vol. 9, n° 3, p. 535-548.
- Li, J.P., Habibovic, P., van den Doel, M., Wilson, C.E., de Wijn, J.R., van Blitterswijk, C.A. and de Groot, K. (2007). Bone ingrowth in porous titanium implants produced by 3D fiber deposition, *Biomaterials*, vol. 28, n° 18, p. 2810-2820.
- Liebschner, M. and Wettergreen, M. (2003). Optimization of bone scaffold engineering for load bearing applications. In Ferretti, P. and Ashammakhi, N., *Topics in tissue engineering*. University of Oulu.
- Lin, A.S., Barrows, T.H., Cartmell, S.H. and Guldborg, R.E. (2003). Microarchitectural and mechanical characterization of oriented porous polymer scaffolds. *Biomaterials*, vol. 24, n° 3, p. 481–489.

- López, A.M., Lumbreras, F., Serrat, J. and Villanueva, J.J., (1999). Evaluation of Methods for Ridge and Valley Detection. *IEEE Transactions on Pattern Analysis and Machine Intelligence*, vol. 21, n° 4, p. 327-335.
- Lorensen, W.E. and Cline, H.E. (1987). Marching cubes: a High Resolution 3D surface Construction Algorithm. *Computer Graphics*, vol. 21, n° 4, p. 163-169.
- Lu, J.X., Flautre, B., Anselme, K., Hardouin, P., Gallur, A., Descamps, M. and Thierry, B. (1999). Role of interconnections in porous bioceramics on bone recolonization in vitro and in vivo. *Journal of Materials Science: Materials in Medicine*, vol. 10, n° 2, p. 111-120.
- Ma, B., Lin, L., Huang, X, Hu, Q. and Fang, M. (2006). Bone tissue engineering using B-Tricalcium Phosphate scaffolds fabricated via selective laser sintering. In Wang, K., Kovacs, G., Wozny, M. and Fang M., *Knowledge enterprise: intelligent strategies in product design, manufacturing and management* (p. 710-716). Boston, Springer.
- Maspero, F.A., Ruffieux, K., Muller, B. and Wintermantel, E. (2002). Resorbable defect analog PLGA scaffolds using CO₂ as solvent: structural characterization. *Journal of Biomedical Materials Research*, vol. 62, n° 1, p. 89–98.
- Mastrogiacomo, M., Muraglia, A., Komlev, V., Peyrin, F., Rustichelli, F., Crovace, A. and Cancedda, R. (2005). Tissue engineering of bone: search for a better scaffold. *Orthodontics and Craniofacial Research*, vol. 8, n° 4, p. 277-284.
- Mastrogiacomo, M., Scaglione, S., Martinetti, R., Dolcini, L., Beltrame, F., Cancedda, R. and Quarto, R. (2006). Role of scaffold internal structure on in vivo bone formation in macroporous calcium phosphate bioceramics. *Biomaterials*, vol. 27, n° 17, p. 3230–3237
- Mastrogiacomo, M., Papadimitropoulos, A., Cedola, A., Peyrin, F., Giannoni, P., Pearce, S.G., Alini, M., Giannini, C., Guagliardi, A. and Cancedda, R. (2007). Engineering of bone using bone marrow stromal cells and a silicon-stabilized tricalcium phosphate bioceramic: Evidence for a coupling between bone formation and scaffold resorption. *Biomaterials*, vol. 28, n° 7, p. 1376–1384.

- Mathieu, L.M., Mueller, T.L., Bourban, P.E., Pioletti, D.P., Muller, R. and Manson, J.A. (2006). Architecture and properties of anisotropic polymer composite scaffolds for bone tissue engineering. *Biomaterials*, vol. 27, n° 6, p. 905-916.
- Mei, R., Shyy, W., Yu, D. and Luo, L.S. (2000). Lattice Boltzmann method for 3-D flows with curved boundary. *Journal of Computational Physics*, vol. 161, n° 2, p. 680-699.
- Meyer, U. and Wiesmann, H.P. (2006). *Bone and Cartilage Engineering*. Germany, Springer, 264p.
- Miranda, P., Pajares, A., Saiz, E., Tomsia, A.P. and Guiberteau, F. (2008). Mechanical properties of calcium phosphate scaffolds fabricated by robocasting. *Journal of Biomedical Materials Research Part A*, vol. 85, n° 1, p. 218-227.
- Moon, H., Chellappa, R. and Rosenfeld, A. (2002). Optimal edge-based shape detection. *IEEE Transactions on Image Processing*, vol. 11, n° 11, p. 1209–1227.
- Moore, W.R., Graves, S.E. and Bain, G.I. (2001). Synthetic bone graft substitute. *ANZ Journal of Surgery*, vol. 71, n° 6, p. 354-361.
- Moore, M.J., Jabbari, E., Ritman, E.L., Lu, L., Currier, B.L., Windebank, A.J. and Yaszemski, M.J. (2004). Quantitative analysis of interconnectivity of porous biodegradable scaffolds with micro-computed tomography. *Journal of Biomedical Materials Research Part A*, vol. 71, n° 2, p. 258-267.
- Moroni, L., de Wijn, J.R. and van Blitterswijk, C.A. (2006). 3D fiber-deposited scaffolds for tissue engineering: influence of pores geometry and architecture on dynamic mechanical properties. *Biomaterials*, vol. 27, n° 7, p. 974-985.
- Muller, R., Hildebrand, T., Hauselmann, H.J. and Ruegsegger, P. (1996). In vivo reproducibility of three-dimensional structural properties of noninvasive bone biopsies using 3D-pQCT. *Journal of Bone and Mineral Research*, vol. 11, n° 11, p. 1745–1750.
- Niblack, C.W., Gibbons, P.B. and Capson, D.W. (1992). Generating skeletons and centerlines from the distance transform. *Graphical Models and Image Processing*, vol. 54, n° 5, p. 420-437.
- Ogniewics, R.L. and Kubler, O. (1995). Hierarchic Voronoi skeletons. *Pattern Recognition*, vol. 28, n° 3, p. 343-359.

- Ohura, K., Bohner, M., Hardouin, P., Lemaitre, J., Pasquier, G. and Flautre, B. (1996). Resorption of, and bone formation from, new btricalcium phosphate-monocalcium phosphate cements: an in vivo study. *Journal of Biomedical Materials Research*, vol. 30, n° 2, p.193-200.
- Otsu, N. (1979). A threshold selection method from gray level histograms. *IEEE Transactions on Systems, Man, and Cybernetics*, vol. 9, n° 1, p. 62-66.
- Otsuki, B., Takemoto, M., Fujibayashi, Sh., Neo, M., Kokubo, T. and Nakamura, T. (2006). Pore throat size and connectivity determine bone and tissue ingrowth into porous implants: Three-dimensional micro-CT based structural analyses of porous bioactive titanium implants, *Biomaterials*, vol. 27, n° 35, p. 5892-5900.
- Parikh, S.N. (2002). Bone graft substitutes: past, present, future. *Journal of Postgraduate Medicine*, vol. 48, n° 2, p. 142-148.
- Polly, D.W. and Kuklo, T.R. (2002). Bone Graft Donor Site Pain. Presented at the 44th Annual Meeting of the Society of Military Orthopaedic Surgeons, San Diego, California, 9-14 December.
- Palágyi, K. (2008). Skeletonization, University of Szeged. (online). <http://www.inf.u-szeged.hu/~palagyi/skel/skel.html#Distance> (page modified at Jun 21, 2008)
- Rajagopalan, S., Lu, L., Yaszemski, M.J. and Robb, R.A. (2005). Optimal segmentation of microcomputed tomographic images of porous tissue-engineering scaffolds. *Journal of Biomedical Materials Research Part A*, vol. 75, n° 4, p. 877-887.
- Ridler, T.W. and Calvard, S. (1978). Picture thresholding using an iterative selection method. *IEEE Transactions on Systems Man and Cybernetics*, vol. 8, p. 630-632.
- Rosenfeld, A. and Torre, P. (1983). Histogram concavity analysis as an aid in threshold selection. *IEEE Transactions on Systems Man and Cybernetics*, vol. 13, p. 231-235.
- Ruhe, P.Q., Wolke, J.G.C., Spauwen, P.H.M., Jansen, J.A. (2007). Calcium phosphate ceramics for bone tissue engineering. In Fisher, J.P., Mikos, A.G. and Bronzino, J.D., *Tissue engineering* (chap. 21, p. 21.1-21.22). New York, Taylor & Francis Group.
- Roy, T.D., Simon, J.L., Ricci, J.L., Rekow, E.D., Thompson, V.P. and Parsons, J.R. (2003). Performance of degradable composite bone repair products made via

- three-dimensional fabrication techniques. *Journal of Biomedical Materials Research Part A*, vol. 66, n° 2, p. 283-291.
- Rubin, P.A., Popham, J.K., Bilyk, J.R. and Shore, J.W. (1994). Comparison of fibrovascular in-growth into hydroxyapatite and porous polyethylene orbital implants. *Ophthalmic Plastic and Reconstructive Surgery*, vol. 10, n° 2, p. 96-103.
- Saha, P.K., Chaudhuri, B.B. and Majumder, D.D., (1997). A new shape preserving parallel thinning algorithm for 3D digital images. *Pattern Recognition*, vol. 30, n° 2, p. 1939-1955.
- Saha, P.K., Wehrli, F.W. and Gomberg, B.R. (2002). Fuzzy distance transform: theory, algorithms and applications. *Computer Vision and Image Understanding*, vol. 86, n° 3, p. 171-190.
- Saha, P.K. and Wehrli, F. (2004). Measurement of trabecular bone thickness in the limited resolution regime of in vivo MRI by fuzzy distance transform. *IEEE Transactions on Medical Imaging*, vol. 23, n° 1, p. 53–62.
- Sandino, C., Planell, J.A. and Lacroix, D. (2008). A finite element study of mechanical stimuli in scaffolds for bone tissue engineering. *Journal of Biomechanics*, vol. 41, n° 5, p. 1005-1014.
- Scheidegger, A.E. (1960). *The physics of flow through porous media*. Toronto, University of Toronto Press, 313p.
- Sikavitsas, V.I., Temenoff, J.S. and Mikos, A.G. (2001). Biomaterials and bone mechanotransduction. *Biomaterials*, vol. 22, n° 19, p. 2581-93.
- SKYSCAN 1172 (2005). *Desktop X-ray microtomograph, Instruction Manual*. Manufactured by SkyScan N.V. Aartselaar, Belgium.
- Sladoje, N., Nystrom, I. and Saha, P.K. (2005). Measurements of digitized objects with fuzzy borders in 2D and 3D. *Image and Vision Computing*, vol. 23, n° 2, p. 123-32.
- Street, J., Bao, M., de Guzman, L., Bunting, S., Peale, F.V.Jr., Ferrara, N., Steinmetz, H., Hoeffel, J., Cleland, J.L., Daugherty, A., van Bruggen, N., Redmond, H.P., Carano, R.A. and Filvaroff, E.H. (2002). Vascular endothelial growth factor stimulates bone repair by promoting angiogenesis and bone turnover. *Proceedings*

- of the National Academy of Sciences of the United States of America, vol. 99, n° 15, p. 9656–9661.
- Succi, S. (2001). *The lattice Boltzmann equation for fluid dynamics and beyond*. New York, Oxford university press, 288 p.
- Taché, A., Gan, L., Deporter, D. and Pilliar, R.M. (2004). Effect of surface chemistry on the rate of osseointegration of sintered porous-surfaced Ti-6Al-4V implants. *The international Journal of Oral and Maxillofacial Implants*, vol. 19, n° 1, p. 19-29.
- Tanck, E., Homminga, J., van Lenthe, G.H. and Huiskes, R. (2001). Increase in bone volume fraction precedes architectural adaptation in growing bone. *Bone*, vol. 28, n° 6, p. 650–654.
- Thamaraiselvi, T.V. and Rajeswari, S. (2004). Biological evaluation of bioceramic materials - a review. *Trends in Biomaterials and Artificial Organs*, vol. 18, n° 1, p. 9-17.
- van Cleynenbreugel, T., Schrooten, J., van Oosterwyck, H. and Vander Sloten, J. (2006). Micro-CT-based screening of biomechanical and structural properties of bone tissue engineering scaffolds. *Medical and Biological Engineering and Computing*, vol. 44, n° 7, p. 517-25.
- van Lenthe, G.H., Hagemuller, H., Bohner, M., Hollister, S.J., Meinel, L. and Muller, R. (2007). Nondestructive micro-computed tomography for biological imaging and quantification of scaffold-bone interaction in vivo. *Biomaterials*, vol. 28, n° 15, p. 2479-2490.
- van Gaalen, S., Kruyt, M., Meijer, G., Mistry, A., Mikos, A., van den Beucken, J., Jansen, J., de Groot, K., Cancedda, R., Olivo, C., Yaszemski, M. and Dhert, W. (2008). Tissue engineering of bone, In van Blitterswijk, C., Thomsen, P., Lindahl, A., Hubbell, J., Williams, D., Cancedda, R., de Bruijn, J., Sohier, J., *Tissue Engineering* (chap. 19, p. 560-610). London, Academic Press.
- van Doernberg, M.C., von Rechenberg, B., Bohner, M., Gruenenfelder, S., van Lenthe, G.H., Mueller, R., Gasser, B., Mathys, R., Baroud, G. and Auer, J. (2006). In vivo behavior of calcium phosphate scaffolds with four different pore sizes. *Biomaterials*, vol. 27, n° 30, p. 5186–5198.

- Wagoner Johnson AJ, Herschler BA. A review of the mechanical behavior of CaP and CaP/polymer composites for applications in bone replacement and repair. *Acta Biomater* (2010), doi:10.1016/j.actbio.2010.07.012
- Wehrli, F.W., Song, H.K., Saha, P.K. and Wright, A.C. (2006). Quantitative MRI for the assessment of bone structure and function. *NMR in Biomedicine*, Vol. 19, n° 7, p. 731–764.
- Wellein, G., Zeiser, T., Hager, G. and Donath, S. (2006). On the single processor performance of simple lattice Boltzmann kernels. *Computers & Fluids*, vol. 35, n° 8-9, p. 910-919.
- White, J.M. and Rohrer, G.D. (1983). Image thresholding for optical character recognition and other applications requiring character image extraction. *IBM Journal of Research and Development*, vol. 27, n° 4, p. 400–411.
- Will, J., Melcher, R., Treul, C., Travitzky, N., Kneser, U., Polykandriotis, E., Horch, R. and Greil, P. (2008). Porous ceramic bone scaffolds for vascularized bone tissue regeneration. *Journal of Materials Science Materials in Medicine*, vol. 19, n° 8, p. 2781-2790.
- Woźniak, P. and El Haj, A.J. (2007). Bone regeneration and repair using tissue engineering. In Boccaccini, A.R. and Gough, J.E., *Tissue engineering using ceramics and polymers* (chap. 14, p.294-318). Boca Raton, CRC Press LLC.
- Yang, Sh., Leong, K.F., Du, Z. and Chua, Ch.K. (2001). Review, The Design of Scaffolds for Use in Tissue Engineering. Part I. Traditional Factors. *Tissue Engineering*, vol. 7, n° 6, p. 679-689.
- Yarlagadda, P.K., Chandrasekharan, M. and Shyan, J.Y. (2005). Recent advances and current developments in tissue scaffolding. *Bio-Medical Materials and Engineering*, vol. 15, n° 3, p. 159-177.
- Yu, D., Mei, R., Luo, L.S. and Shyy, W. (2003). Viscous flow computations with the method of lattice Boltzmann equation. *Progress in Aerospace Sciences*, vol. 39, p. 329-367.
- Yuan, H., Yang, Z., Li, Y. and Zhang, X. (1998). Osteoinduction by calcium phosphate biomaterials. *Journal of Materials Science Materials in Medicine*, vol. 9, n° 12, p. 723-726.

- Zeltinger, J., Sherwood, J.K., Graham, D.A., Muller, R. and Griffith, L.G. (2001). Effect of pore size and void fraction on cellular adhesion, proliferation and matrix deposition. *Tissue Engineering*, vol. 7, n° 5, p. 557-572.
- Zeiser, T., Wellein, G., Hager, G., Donath, S., Deserno, F., Lammers, P. and Wierse, M. (2004). Optimized Lattice Boltzmann kernels as testbeds for processor performance. Technical Report, RRZE-Erlangen, Germany.
- Zhou, Y. and Toga, A.W. (1999). Efficient Skeletonization of Volumetric Objects, *IEEE Transaction Visualization and Computer Graphics*, vol. 5, n° 3, p. 196-209.

Permission to reprint published materials:

- Figures 2-3, 2-12, 5-1 and 5-2 were reprinted from: “Bohner, M., van Lenthe, G.H., Gruenenfelder, S., Hirsiger, W., Evison, R. and Muller, R. (2005). Synthesis and characterization of porous b-tricalcium phosphate blocks. *Biomaterials*, vol. 26, n° 31, p. 6099–6105.”, with permission from “Elsevier”.
- Figure 2-11 was reprinted from: “Hildebrand, T. and Rüeggsegger, P. (1997). A new method for the model-independent assessment of thickness in three-dimensional images. *Journal of Microscopy*, vol. 185, n° 1, p. 67-75.”, with permission from “John Wiley and Sons”.
- Chapter 3 was reprinted from: “Bashoor-Zadeh, M., Baroud, G. and Bohner, M. (2010). Geometric analysis of porous bone substitutes using micro-computed tomography and fuzzy distance transform. *Acta Biomaterialia*, vol. 6, n° 3, p. 864-875.”, with permission from “Elsevier”.
- Table 2-1 was reprinted from: “Di Silvio, L. (2007). Bone tissue engineering and biomineralisation. In Boccaccini, A.R. and Gough, J.E., *Tissue engineering using ceramics and polymers* (chap. 15, p.319-334). Cambridge, Woodhead Publishing Ltd.”, with permission from “Woodhead Publishing Ltd.”

Annexe A

Additional scientific contributions

A.1 Journal publications

- Stähli C., Bohner M., Bashoor-Zadeh, M., Doebelin, N. and Baroud, G. (2010). Aqueous impregnation of porous beta-tricalcium phosphate scaffolds. *Acta Biomaterialia*, vol. 6, n° 7, p. 2760-2772.
- Bashoor-Zadeh, M., Baroud, G. and Bohner, M. (2010). Geometric analysis of porous bone substitutes using micro-computed tomography and fuzzy distance transform. *Acta Biomaterialia*, vol. 6, n° 3, p. 864-875.
- Zeiser, T., Bashoor-Zadeh, M., Darabi, A. and Baroud, G. (2008). Pore-scale analysis of Newtonian flow in the explicit geometry of vertebral trabecular bones using lattice Boltzmann simulation. *Proceedings of the Institution of Mechanical Engineers, Part H: Journal of Engineering in Medicine*, vol. 222, n° 2, p.185-94.

A.2 Conference/Proceeding publications

- Bashoor-Zadeh, M., Stähli, C., Doebelin, N., Bohner, M. and Baroud, G. (2010). Characterization of Porous Calcium Phosphate Substitutes using Micro-Computed Tomography and Fuzzy Image Processing Methods. In proceeding of the 20th GRIBOI Conference (interdisciplinary research conference on Injectable biomaterial/biomechanics for minimally invasive clinical Application), 25-27 March 2010, Turin, Italy. (Oral presentation)
- Bashoor-Zadeh, M., Bohner, M. and Baroud, G. (2010). Resorption Simulation of Porous Substitutes for Repair. In proceeding of the 20th GRIBOI Conference, 25-27 March 2010, Turin, Italy. (Oral presentation)

- Bashoor-Zadeh, M., Bohner, M. and Baroud, G. (2009). Simulation of cell mediated resorption of porous bone substitute. In proceeding of the 19th GRIBOI conference, 23-27 March 2009, Martinique, France. (Oral presentation)
- Bashoor-Zadeh, M., Bohner, M. and Baroud, G. (2009). Effect of Subvoxel Process on Non-destructive Characterization of Bone Substitute. In proceeding of the 19th GRIBOI Conference, 23-27 March 2009, Martinique, France. (Oral presentation)
- Bashoor-Zadeh, M., Bohner, M. and Baroud, G. (2008). Enhancing non-destructive characterization of porous bone substitutes. In proceeding of the 18th GRIBOI Conference, 5-6 May 2008, Montreal, Canada. (Poster presentation)
- Perrot, C., Chevillotte, F., Bashoor-Zadeh, M., Darabi, A., Panneton, R. and Baroud, G. (2008). Towards periodic unit cell reconstruction of trabecular bone structure. In proceeding of the 18th GRIBOI Conference, 5-6 May 2008, Montreal, Canada. (Poster presentation)
- Bashoor-Zadeh, M., Darabi, A., Bohner, M. and Baroud, G. (2007). Geometric and Fluid Transport Analysis of Calcium-Phosphate Scaffolds. In proceeding of the 17th GRIBOI Conference, 1-3 April 2007, Oxford, United Kingdom. (Oral presentation)